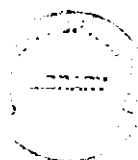# A STUDY OF A PLUNGING JET
BUBBLE COLUMN

A thesis submitted for
the degree of
DOCTOR OF PHILOSOPHY

by

GEOFFREY MICHAEL EVANS

Department of Chemical Engineering
THE UNIVERSITY OF NEWCASTLE, N.S.W.

January, 1990

I hereby certify that the work
embodied in this thesis is the
result of original research and
has not been submitted for a
higher degree to any other
University or Institution.

(Signed) _Geoffrey Evans_

ACKNOWLEDGEMENTS

ABSTRACT

The hydrodynamic phenomena occurring inside the enclosed downcomer
section of a plunging jet bubble column are described in this study.

The gas entrainment rate for a plunging liquid jet was found to consist
of two components, namely the gas trapped within the effective jet
diameter at the point of impact, and the gas contained within the film
between the jet and induction trumpet surface at the point of rupture.
Entrainment within the effective jet diameter has been examined by
McCarthy (1972). In this study, a model has been developed to predict
the rate of filmwise entrainment. The model was supported by the
experimental results, provided the film attained a region of constant
thickness. When the induction trumpet was ruptured prior to a constant
film thickness being reached, the measured rate of filmwise entrainment
was higher than the prediction.

Filmwise entrainment was found to be initiated once a critical velocity
along the surface of the induction trumpet was reached. The critical
velocity was a function only of the liquid physical properties and was
independent of the jet conditions and downcomer diameter. The velocity
of the free surface of the induction trumpet was obtained from the
velocity profile for the recirculating eddy generated by the confined
plunging liquid jet.

The jet angle used to describe the expansion of the submerged jet inside
the downcomer was predicted from the radial diffusion of jet momentum
into the recirculating eddy. The model was able to predict the jet angle
when it was assumed that the radial diffusion of jet momentum was a
function of the Euler number based on the jet velocity and absolute
pressure in the headspace at the top of the downcomer.

The model was also developed to predict the maximum stable bubble
diameter generated within the submerged jet volume, where the energy
dissipation attributed to bubble breakup was given by the energy mixing
loss derived for the throat section of a liquid-jet-gas-pump. Good
agreement was found between the measured and predicted maximum bubble

diameter values. The average experimental Sauter mean/maximum diameter ratio was found to be 0.61, which was similar to that for other bubble generation devices.

It was found that for turbulent liquid conditions in the uniform two-phase flow region, a transition from bubbly to churn-turbulent flow occurred at a gas void fraction of approximately 0.2 when the gas drift-flux was zero. Under laminar liquid flow, this transition took place at a gas void fraction above 0.3.

For the bubbly flow regime the Distribution parameter C_o used by Zuber and Findlay (1965) to describe the velocity and gas void fraction profile, was found to be a function of the liquid Reynolds number. For laminar liquid flow, values of C_o greater than unity were obtained. As the liquid Reynolds number was increased it was found that C_o decreased, until a constant value of unity was obtained for fully turbulent flow.

For the churn-turbulent regime it was found that the gas void fraction measurements for all of the experimental runs could be collapsed onto a single curve when a modified gas void fraction was plotted against the gas-to-liquid volumetric flow ratio. The modified gas void fraction included a correction factor to account for the difference in the bubble slip velocity between the experimental runs. The experimental results also indicated that the value of the constant in the gas void fraction correction factor was different for laminar and turbulent flow.

Prior to bubble coalescence, it was found that the experimental drift-flux curves could be predicted from the measured bubble diameter, using the separated flow model developed by Ishii and Zuber (1979). After the onset of coalescence the drift flux measurements departed from the original drift-flux curves at a rate which increased linearly with increasing gas void fraction. It was found that the slope of the line fitted to the coalesced region of the drift-flux curves increased with increasing liquid Reynolds number and reached a constant value under fully turbulent flow conditions.

The model developed, together with the implications of the experimental results, are discussed with regard to optimising the design of an industrial plunging jet bubble column.

TABLE OF CONTENTS

NOMENCLATURE

A   Area, (m^2)

b   Cross-sectional area ratio, (A_j/A_c)

C_0 Distribution parameter defined by (6.16)

D   Diameter, (m)

$\mathcal{D}$ Dispersion coefficient, $(m^2 s^{-1})$

d   Diameter, (m)

E   Energy dissipation rate, $(kgm^2 s^{-3})$

e   Energy dissipation, $(kgm^2 s^{-2})$

F   Force, $(kgms^{-2})$

f   Friction factor

G   Circulation strength, (s^{-1})

g   Acceleration due to gravity, (ms^{-2})

J   Total volumetric flux, (ms^{-1})

j   Volumetric flux (or superficial velocity), (ms^{-1})

k   Frictional loss coefficient

L   Length, (m)

M   Momentum, $(kgms^{-1})$

N   Number

P   Pressure, $(kgms^{-2})$

Q   Volumetric flowrate, $(m^3 s^{-1})$

R   Radius, (m)

r   Radial co-ordinate, (m)

S   Surface roughness (defined in Figure 4.4), (m)

T   Film thickness, (m)

T_c Film thickness in constant film thickness region, (m)

t   Time, (s)

V   Volume, (m^3)

V	Voltage, (volts)
v	Linear velocity, (ms^{-1})
W	Mass flowrate, (kgs^{-1})
y	Length from column wall, (m)
z	Axial length, (m)

GREEK SYMBOLS

β	Submerged jet angle, (degrees)
γ	Axis ratio, (length of maximum axis/length of minimum axis)
δ	Dirac delta function
ε	Gas void fraction
η	Energy transfer efficiency, (defined in 5.47)
θ	Nozzle contraction angle, (degrees)
κ	Film thickness ratio, (defined in 4.32)
μ	Absolute viscosity, (Pa-s)
ν	Kinematic viscosity, (m^2s^{-1})
Ω	Packing parameter, (used in 6.50)
ρ	Density, (kgm^{-3})
σ	Surface tension, (Nm^{-1})
τ	Shear stress, $(kgm^{-1}s^{-2})$
ø	Angle of inclination from horizontal plane, (degrees)
Ψ	Stream function
ω	Shear rate. (s^{-1})

SUPERSCRIPTS

*	Dimensionless quantity
'	Drift quantity

SUBSCRIPTS

B	Boundary layer
b	Bubble
c	Column
d	Droplet
e	Recirculating eddy
F	Film
f	Froth
G	Gas
I	Entrained gas component inside effective jet diameter
i	Interface
j	Jet
L	Liquid
M	Molecular
MZ	Mixing zone
m	Mean
N	Nozzle
o	Orifice
p	Pipe
r	Radial
S	Slip
s	Specific
T	Turbulent
VS	Volume-surface, or Sauter mean
w	Wall
z	Axial

DIMENSIONLESS NUMBERS

We   Weber number, $\dfrac{\rho v^2 d}{\sigma}$.

Re   Reynolds number, $\dfrac{\rho v d}{\mu}$.

Ca   Capillary number, $\dfrac{\mu v}{\sigma}$.

N_H Hill number, $\dfrac{Q}{\sqrt{2\pi}\, r\sqrt{\dfrac{M}{\rho}}}$.

C_T Crayer-Curtet number, $\sqrt{\dfrac{2(N_H)^2}{1-(N_H)^2}}$.

Fr   Froude number, $\dfrac{v^2}{gD}$.

N_{Eu} Euler number, $\dfrac{P_o}{v^2}$.

Chapter 1

INTRODUCTION

1.1 BACKGROUND TO THE STUDY

This study has developed from research into methods of improving the
recovery of fine material in the flotation industry. Ahmed (1983) found
the recovery of particles with a diameter range of 4 μm to 40 μm was
increased fifty fold when the bubble diameter was reduced from 650 μm to
75 μm. This result showed that fine particles were best recovered by
using small bubbles.

Allum and Jameson (1984) surveyed the range of bubble sizes produced in
flotation circuits operating throughout Australia. They found the mean
bubble diameter was approximately 500 μm which gave low recoveries for
the fine particles. The results of the survey highlighted the inability
of the existing mechanically agitated flotation cells to produce the
small bubbles necessary for the efficient recovery of fine particles.
For this reason a totally different flotation device was considered. The
device considered was a bubble column, chosen because more effective
means than mechanical stirring could be utilised for fine bubble
production. An additional advantage of bubble columns over the
conventional flotation cell was they did not require a mechanical
agitator to suspend the solids.

Most bubble columns operate countercurrently with the gas entering the
base of the column through a sparger where bubbles are formed. The
bubbles then rise inside the column and contact the downflowing liquid

stream. The contact area between the two phases is determined by the gas flowrate and the bubble diameter with smaller bubbles beneficially producing a greater surface area per unit volume. With countercurrent flows, however, the operation is restricted to a minimum bubble size limited by the superficial velocity of the downflowing liquid and the rise velocity of the bubble.

An alternative bubble column design has both the gas and liquid entering at the top of the column. The liquid is introduced as a high velocity jet which entrains gas from the head-space at the top of the column. The entrained gas is then broken into very fine bubbles by the shearing forces generated by the jet plunging into the receiving liquid. The gas and liquid then flow cocurrently down the column where they are discharged at the bottom. The major advantage of this method over countercurrent bubble column operation is the elimination of the minimum bubble size constraint, thereby increasing the potential for producing greater interfacial areas. Also, the mixing ability of the jet is more efficient than for sparger systems. This is reflected by significantly lower residence times for the jet system and consequently, much smaller equipment is needed, which represents a substantial saving in capital investment.

The plunging jet bubble column used in this study had the downcomer closed to the atmosphere which resulted in a reduction in pressure in the vicinity of the plunging jet. The reduction in pressure inside the downcomer caused it to fill with a dense froth as shown in Figure 1.1.

At low rates of air injection to the top of the column, the level of froth is sustained just below the level of the nozzle, as shown in Figure 1.1(a). As the gas rate is increased the gas void fraction of the froth also increases. However, as the gas supply is increased a point is reached where the jet can no longer entrain all of the gas. The build-up of gas in the top of the column increases the local pressure in the head-space, which results in a drop in the froth level inside the column and a subsequent increase in the length of the free jet. The entrainment ability of the plunging jet is directly related to the free jet length and a new equilibrium froth height is reached, as shown in Figure 1.1(b).

The new froth height marks the position where the jet can effectively entrain all of the gas entering the top of the column. Because the gas entrainment rate increases with free jet length, the froth is able to stabilise at any level in the downcomer. However, at high gas rates the froth does eventually collapse to the base of the downcomer, as shown in Figure 1.1(c).

(a)   (b)   (c)
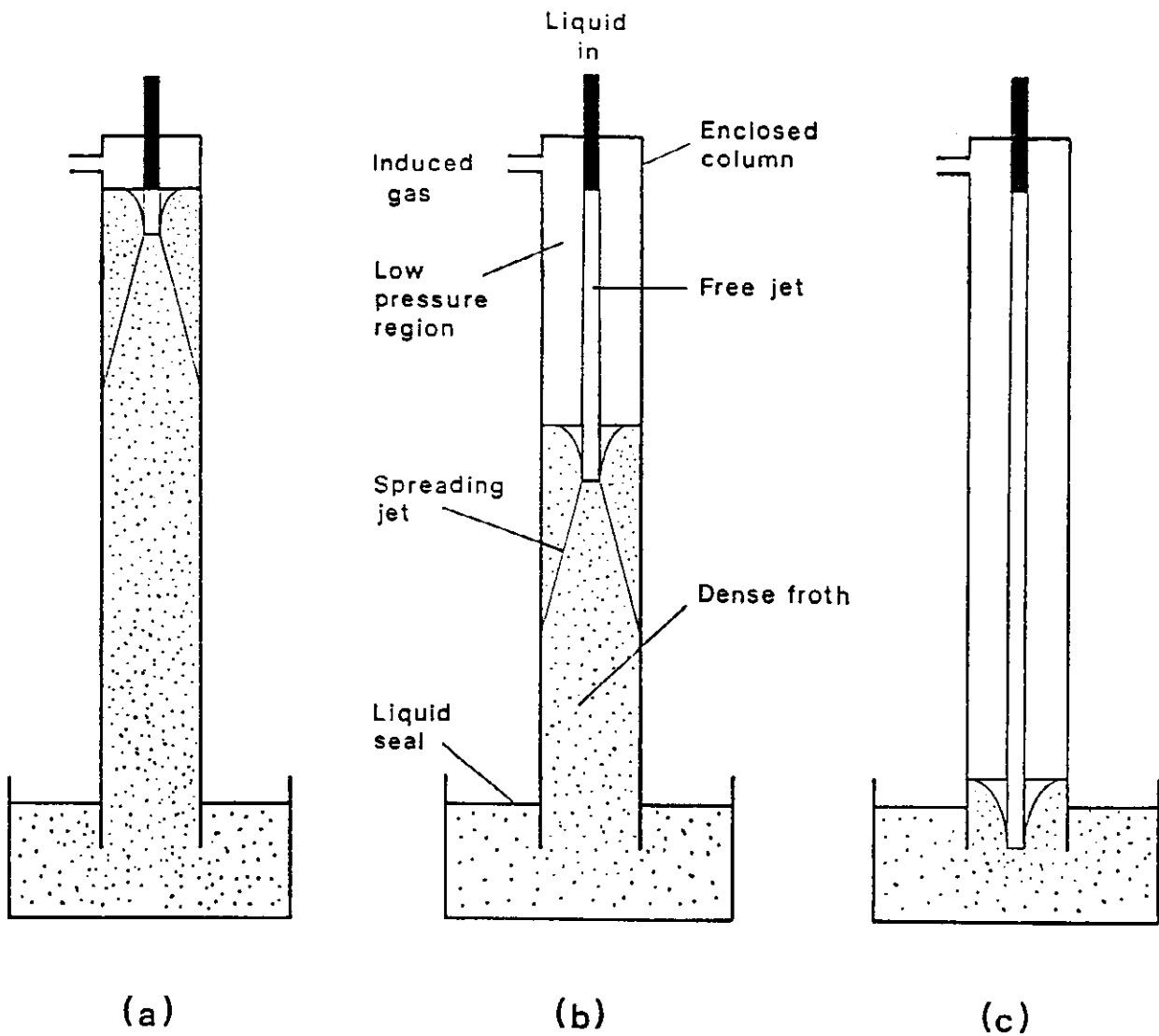
Figure 1.1   Downcomer section of a plunging jet bubble column

The design of bubble columns to date has been primarily empirical
(Herbrechtsmeier et al, 1985; Clark and Flemmer, 1985; Reilly et al,
1986; Guy et al, 1986; Dobby et al, 1986; Otake et al, 1981) relying
heavily on experimental data for the scale-up of equipment. The
hydrodynamic models[1] which have been developed to predict the gas void
fraction and velocity profiles inside the bubble column have been
restricted to conventional systems where the gas flow is vertically
upwards. No attention has been given to the situation where both the gas
and liquid phases flow cocurrently downwards inside the column.

The bubble formation process inside the bubble column is another
important aspect which has not been considered to date. Most models have
assumed a particular bubble profile and have limited their analysis to
the homogeneous two-phase flow region. They have not considered the
interaction which takes place between the bubble generation region and
the two-phase flow region.

The aim of this study is firstly, to investigate the bubble generation
mechanism for the plunging liquid jet bubble column and secondly, to
determine the hydrodynamic interactions which take place, in order to be
able to predict the overall behaviour of the column.

Even though the idea of a plunging jet bubble column was first developed
to improve the recovery of fine material in the flotation process, the
method has a wide range of applications in the gas-liquid contacting
field. It is hoped that the knowledge gained in this study will lead to
a clearer understanding of the basic mechanisms present and the effect of
the operating parameters on the column performance which will lead to a
greater utilisation of the device.

---

[1]Chapter 2 contains a review of the main classes of hydrodynamic
models which have been developed for conventional countercurrent bubble
column operation.

1.2 DEFINITION OF PROBLEM

In order to develop a hydrodynamic model for the plunging jet bubble
column, the processes taking place must first be defined. Ogawa (1982)
described two distinct flow regions which interact with each other to
determine the overall hydrodynamics of the bubble column. The first flow
region is the bubble production zone where the liquid jet plunges into
the column and expands until it strikes the wall of the column. It is in
this region the shearing forces are at a maximum and the bubble size is
determined. Below the region of jet influence is the uniform two-phase
zone where there is a net movement of gas and liquid in a downward
direction. Barnea (1987) has shown that the type of flow in this region
can be either bubbly, churn-turbulent or slug flow, depending on the
superficial gas and liquid velocities and the bubble diameter inside the
column.

The type of two-phase flow is very important for bubble column operation.
Bubbly flow is most desirable because it produces the greatest surface
area for a given gas to liquid ratio and it also provides for stable
bubble column operation. With churn-turbulent and slug flow, larger
bubbles with rise velocities greater than the net downward motion are
able to return to the top of the column and be re-entrained by the jet.
The recirculation of gas inside the column reduces the operating range of
the gas-to-liquid volumetric flow ratio and it also leads to instability
and eventual collapse of the column of froth inside the downcomer.

The hydrodynamic model for downcomer section of the plunging jet bubble
column therefore should be able to predict:-

  The quantity of gas which can be entrained initially for a given
  plunging liquid jet system.

  The size and shearing strength of the submerged region which is
  created by the plunging jet once it enters the receiving liquid
  inside the downcomer. From this knowledge the bubble diameter can be
  calculated.

The type of flow which is produced in the uniform two-phase flow region. This is a function of the gas and liquid rates and also the bubble size produced by the forces associated with the plunging jet.

The quantity of gas which is recirculated within the downcomer and its effect on the stability of the column of froth.

The model should be able to predict the effects of variables such as jet and column diameter, jet velocity, and liquid physical properties on the operation of the plunging jet bubble column.

1.3 RESEARCH PROGRAMME

The research programme was restricted to the hydrodynamic modelling of the downcomer section of the plunging jet bubble column illustrated in Figure 1.1. The work was carried out by firstly defining the zones within the downcomer which could be described as a single physical process which was essentially independent of what takes place within the remaining sections of the downcomer. The four separate zones inside the downcomer were defined as shown in Figure 1.2.

In Figure 1.2. the "free jet" zone is where the liquid jet passes through the gas space at the top of the downcomer prior to plunging into the receiving liquid. The "plunging jet" zone is defined as the region where the free liquid jet plunges into the column of froth and entrained gas is carried below the fluid surface. The region around the plunging jet zone is the "mixing" zone and includes the recirculating eddy and the submerged jet as it expands to reach the wall of the downcomer. Inside this zone there is intensive mixing and bubble generation takes place. Finally, the "uniform two-phase flow" zone is where the liquid turbulence is at a minimum and the bubbles and liquid travel downward as a uniform two-phase flow.

Once the different zones within the downcomer were defined, the hydrodynamic behaviour within each zone was investigated, and parameters such as the entrainment rate, bubble diameter and gas void fraction were related to the physical properties of the system.
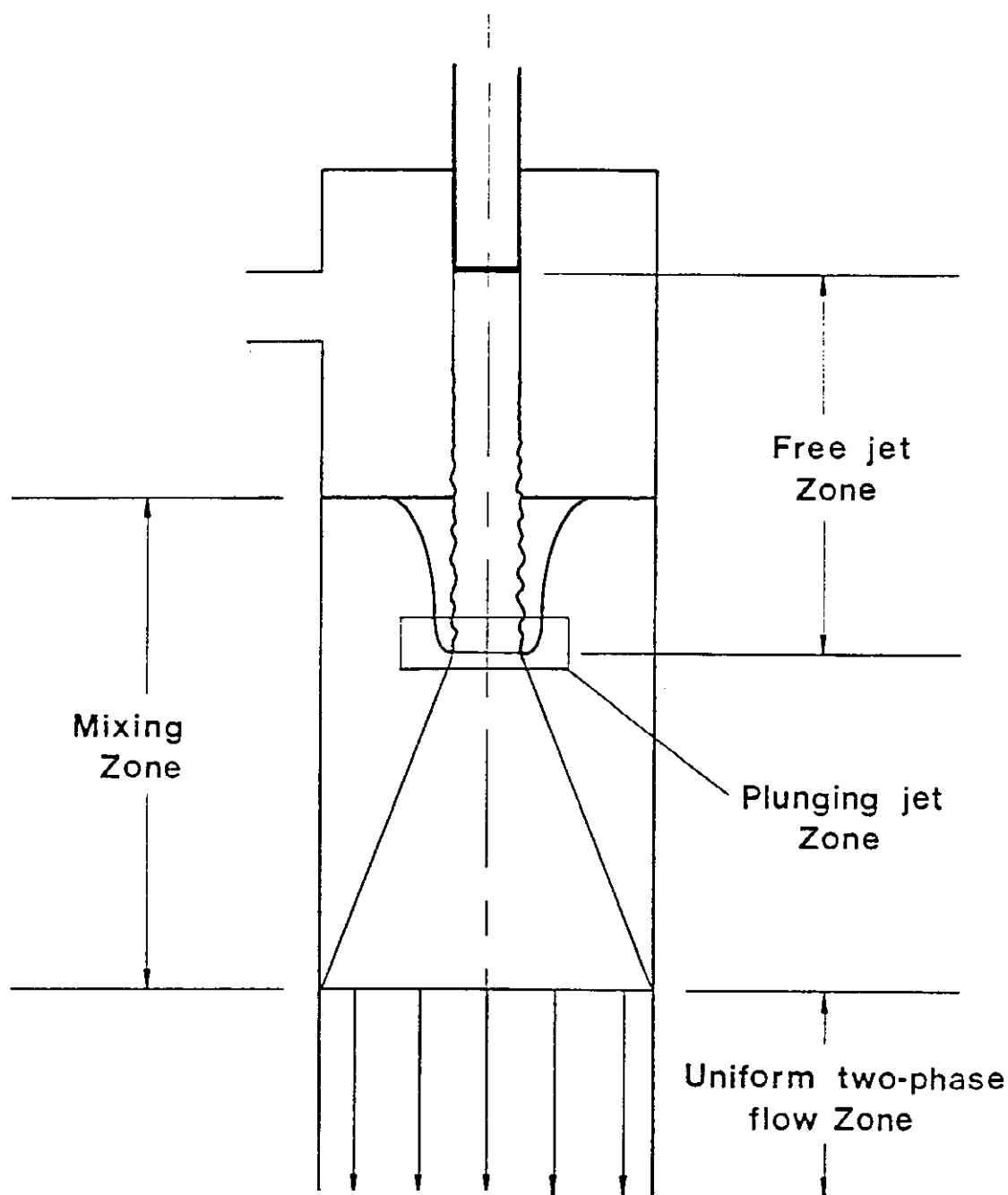
Figure 1.2 Definition of hydrodynamic zones inside the downcomer
section of the plunging liquid jet bubble column

A flowsheet of the model developed to describe the hydrodynamic characteristics for the downcomer section is given in Figure 1.3. The four zones defined in Figure 1.2 are shown inside the boxes and the parameters influencing the behaviour of the system are given inside the circles. The parameters include:-

stability - which determines the characteristics of the free jet such as the increase in its diameter with increasing jet length, or whether the free surface of the jet is rough or smooth.

expansion - the expansion in the free jet diameter as it passes through the head-space at the top of the downcomer determines the area of impact between the plunging jet and the receiving liquid.

energy dissipation - determines the rate of radial transfer of jet momentum and also the angle of spread for the submerged jet.

liquid circulation - a recirculating eddy is generated within the receiving liquid by the action of the liquid jet plunging into a confined volume.

gas entrainment - the interaction between the plunging jet and the receiving liquid surface controls the rate of gas entrainment.

volume - the volume of the mixing zone determines the energy dissipation rate per unit volume for the submerged jet.

gas/liquid ratio - determines the density of the two-phase mixture inside the recirculating eddy which influences the expansion of the submerged jet.

bubble diameter - the size of bubbles produced in the mixing zone is a function of the energy dissipation rate per unit volume.

slip velocity - the slip velocity between the bubbles and the downflowing liquid determine the gas void fraction inside the downcomer.

flow regime - determines whether the flow is bubbly or churn turbulent. The type of flow has a major influence on the stability of operation.

void fraction - influences the rate of bubble coalescence and the transition from bubbly to churn-turbulent flow.

gas recirculation - reduces the entrainment capacity of the plunging jet which can lead to the collapse of the column of froth.
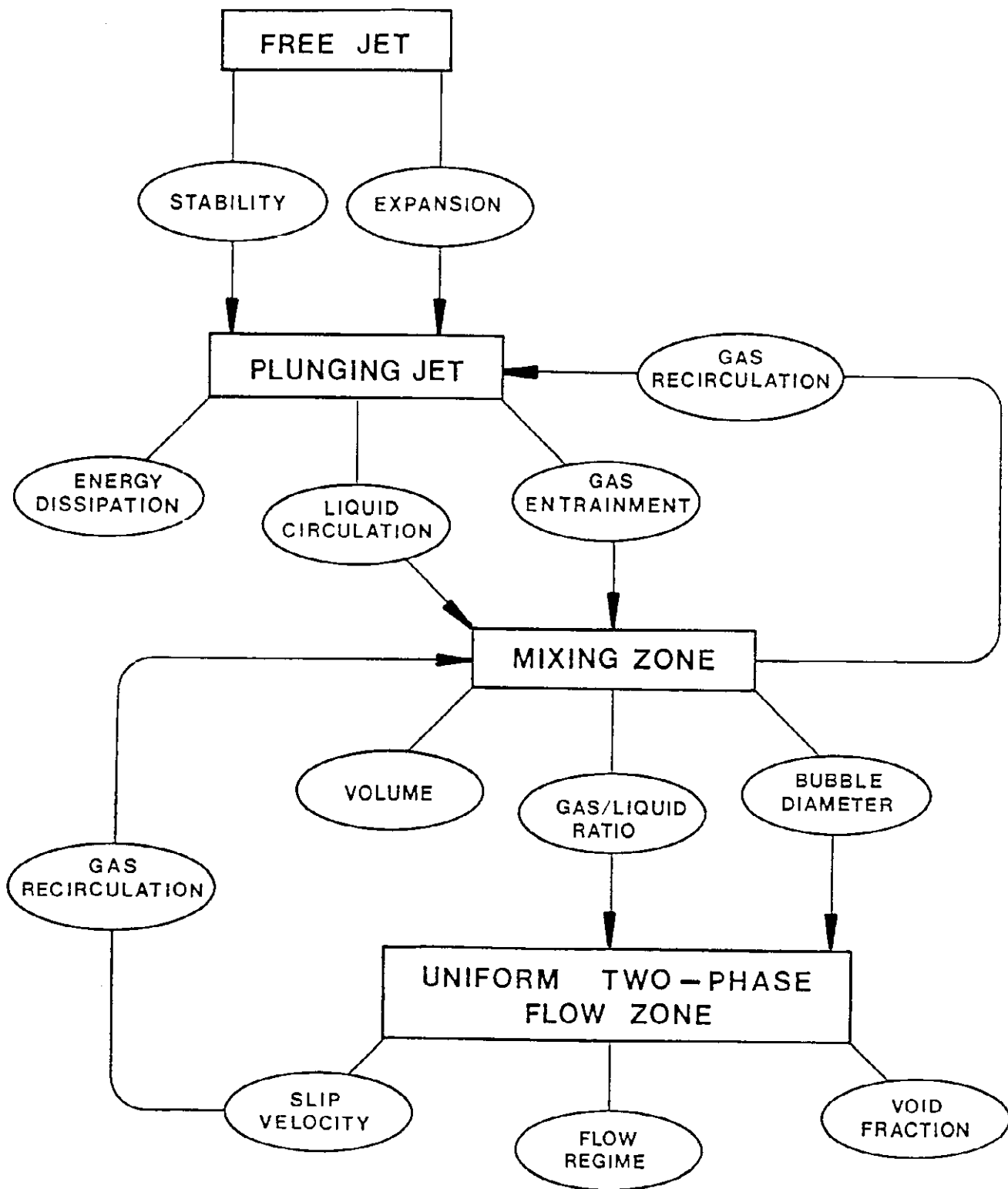
Figure 1.3 Schematic of hydrodynamic model developed for downcomer
section of plunging liquid jet bubble column

1.4 FORMAT OF THE THESIS

The different designs and operating principles of bubble columns are presented in Chapter 2, which also includes a review of the hydrodynamic models used to describe liquid circulation and gas void fraction inside bubble columns.

Chapter 3 contains a description of materials used, the experimental apparatus and the procedures implemented in undertaking this study.

In Chapter 4 a theoretical model is derived to predict the quantity of gas entrained by the jet as it plunges into the froth at the top of the downcomer section of the bubble column. Predictions from the model are compared with experimental results.

An analysis of the submerged jet or mixing zone at the top of the downcomer is presented in Chapter 5, which includes the derivation of a model used to predict the expansion of a submerged jet inside a confined region. The energy dissipation rate within the mixing zone is calculated and used to predict the resultant bubble diameter. The results from the model are compared with experimental bubble diameter measurements.

In Chapter 6 the experimental values of the gas void fraction, bubble diameter and flow type for the uniform two-phase flow zone are compared with predictions from two-phase flow theory. The quantity of gas which returns to the mixing zone as a result of the net upward motion of bubbles is also calculated.

In Chapter 7 the interactions taking place between the processes occurring in the downcomer of the plunging jet bubble column are discussed. Attention is given to the overall stability of the froth column and also the effect of gas recirculation on the quantity of gas which can be introduced to the top of the column.

The conclusions drawn from this study and recommendations for further work are presented in Chapter 8.

Chapter 2

BUBBLE COLUMNS: THEIR DESIGN
AND HYDRODYNAMIC MODELLING

2.1 INTRODUCTION

A number of different methods have been developed to contact gas and
liquid phases in the process industry. The method used depends on
whether the liquid or the gas is required to form the continuous phase.
For systems where the gas needs to be dispersed as bubbles in the liquid
phase either a mechanically stirred vessel, loop reactor or bubble column
can be used.

The effectiveness of any gas-liquid contacting process is measured by the
amount of interfacial area which is generated within the reactor for a
given power input per unit volume. The interfacial area is determined by
the size and number of the bubbles present which are also closely related
to the gas void fraction of the system which is equal to the ratio of the
volume occupied by the gas phase to the entire volume of the system.

This chapter describes the different types of gas-liquid contacting
devices which are available, with emphasis placed on bubble columns. A
review of the hydrodynamic models developed to predict the gas void
fraction for bubble columns is also presented.

2.2 TYPES OF GAS-LIQUID CONTACTING DEVICES

Gas-liquid contacting devices may be classified into three main groups
depending upon the distribution of the gas and liquid phases. The
different groups are:-

1. Liquid is present as discrete drops which are distributed within a
   continuous gas phase. Examples of this system are spray towers
   and atomiser units.

2. Both the liquid and gas are present as separate continuous phases
   with a single contact boundary surface. An example of this system
   is a falling film reactor.

3. The gas is dispersed as bubbles within a continuous liquid phase.
   Examples of these systems are mechanically aerated reactor vesels
   such as flotation cells, air-lift reactors and bubble columns.

In this chapter only those devices which operate with the gas dispersed
as bubbles within a continuous liquid phase are considered.

2.3 MECHANICALLY AGITATED REACTOR VESSELS

In mechanically agitated gas-liquid reactor vessels the gas is usually
introduced through a sparger or distributor at the bottom of the vessel.
The gas is then broken up and dispersed as fine bubbles by the shearing
force and pumping action of the rotating impeller. The pumping action of
the impeller uniformly distributes the gas phase throughout the vessel
and it also ensures the suspension of solid particles in three-phase
systems. For a comprehensive review of mechanically agitated gas-liquid
reactors see Joshi et al (1982).

A variation of this type of reactor vessel uses a self-inducing impeller
which requires no sparger and draws a continuous supply of gas from the
surrounding atmosphere. The hollow shaft of the self-inducing impeller
allows gas to be drawn into the low pressure region behind the back of
the rotating blades which then breaks up the gas into fine bubbles.

2.4 REACTOR VESSELS WITHOUT MECHANICAL AGITATORS

Gas-liquid contacting devices which are not equipped with mechanical
agitators for the production and dispersion of bubbles can be classified
generally as either loop reactors or bubble columns. The basic design
differences between these two devices are illustrated in Figure 2.1.
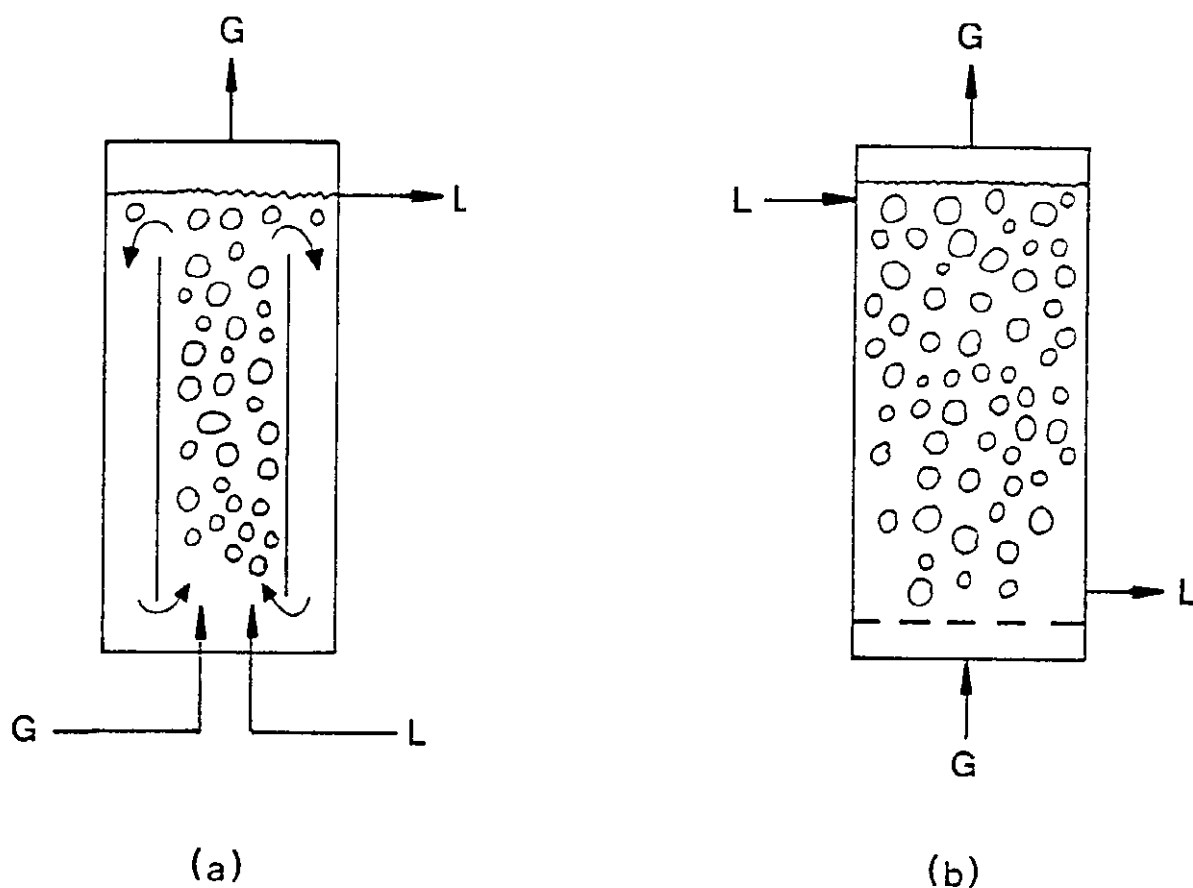
Figure 2.1. Schematic of (a) loop reactor and (b) bubble column

The loop reactor consists of two connected vertical legs which allow both
the gas and liquid to circulate within the reactor. The bubble column
consists of a single vertical leg where gas-liquid contact occurs. In
addition to the basic design difference just mentioned between bubble
columns and loop reactors, there are also operational differences, such

as the use of different rates of aeration and superficial gas and liquid velocities. These differences in operation are discussed in detail by Weiland and Onken (1981).

2.5   BUBBLE COLUMNS

2.5.1 Reactor Design

In a typical bubble column operation the gas is introduced through a distributor in the base of the column which is usually a porous sparger or perforated plate. The bubbles which are generated by the distributor then rise to the top of the column where they can disengage from the liquid and be removed from the system. The driving forces which are utilised in the operation of a bubble column are gravity, which causes the liquid to fall from the top of the column and exit through the outlet at the bottom, and buoyancy, which is associated with the bubbles and forces them to rise inside the column. The net result of these two forces is a countercurrent flow of gas and liquid inside the bubble column. (Shah et al, 1982; Walter and Blanch, 1983; Buchholz et al, 1983; Hikita et al, 1980; Yianatos et al, 1985; Iodogawa et al, 1986).

In addition to the conventional countercurrent flow bubble column design a number of different designs are shown in Figure 2.2. In the downflow bubble column, gas is injected into the top, usually through a porous sparger, and the bubbles produced are transported in a downward direction by the moving liquid. The gas and liquid are then separated in a disengagement zone at the base of the column (Herbrechtsmeier et al, 1981: Friedal et al, 1980; Herbrechtsmeier and Schäfer, 1982).

In the jet ejector bubble column both gas and liquid enter the bottom of the column through a jet ejector device. The high shearing forces present within the ejector produce very small bubbles which rise to the top of the column where they are removed from the system. A constant liquid level is maintained inside the column by an overflow weir situated at the top of the column (Nishikawa et al, 1976; Weisweiler and Rosch, 1978; Otake et al, 1981; Weisweiler et al, 1982; Ogawa et al, 1982).
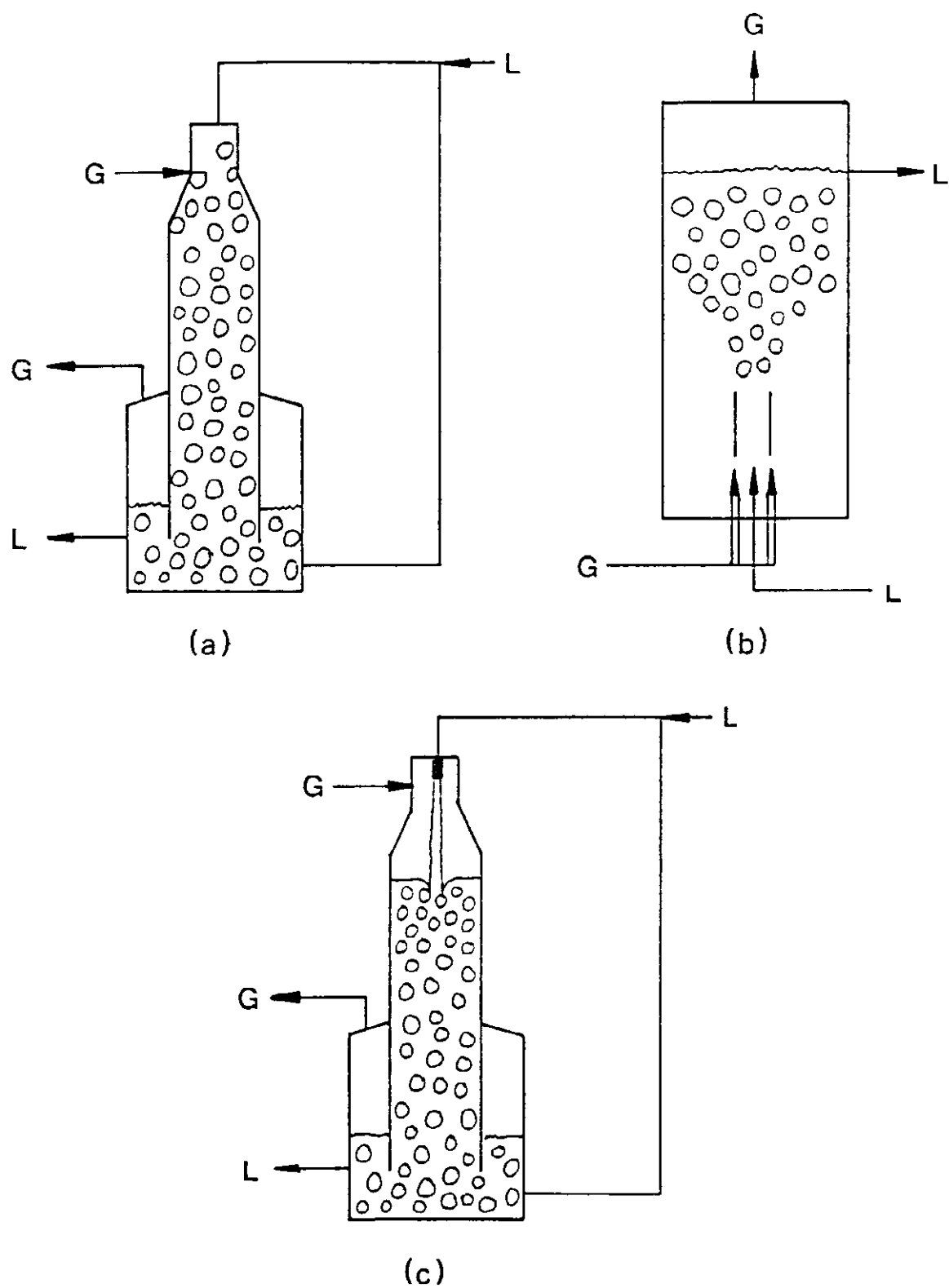
Figure 2.2   Alternative bubble column designs (a) downflow
(b) jet ejector (c) plunging jet

As shown in Figure 2.2(c), in the plunging jet bubble column a liquid jet plunges through a gas cavity at the top of the column. The jet entrains gas which forms very small bubbles that travel in a downward direction with the liquid. At the base of the column is a disengagement zone which allows the gas to be separated from the liquid phase. The advantage of this method is that gas compression is unnecessary because the gas is naturally entrained into the column due to the low pressure created by the liquid jet (van de Donk, 1979; Ohkawa et al, 1985a, 1985b, 1986, 1987; Bando et al, 1988; Evans and Jameson, 1988).

2.5.2 Hydrodynamic models

An important parameter in the operation of a bubble column is the gas void fraction, ϵ, which is defined as the ratio of the volume occupied by the gas to the total volume of the system. In most situations where bubble columns are used it is desirable to maximise the gas void fraction and for this reason hydrodynamic models have been developed in order to predict the gas void fraction as a function of the physical properties of the system.

The hydrodynamic models which have been developed to describe the flow inside a bubble column can be classified as either "single mixture", "separated flow", "circulating flow" or empirical. In single mixture models the two phases are treated as a single homogeneous pseudofluid with average properties. With these models only four equations are required to define the system, namely, the equations of continuity, momentum, and energy for the mixture, and the equation of continuity for one of the phases.

In separated flow models both phases are considered separately and their interaction at the interfacial boundary is described by use of constitutive equations. These models require the equations of continuity, momentum, and energy to be determined for both phases in order to describe the properties of the mixture. Consequently, separated flow models are considerably more complicated than the single mixture models but they do have the advantage of being able to describe non-equilibrium conditions within the system.

Both the single mixture models and the separated flow models apply generally to two-phase plug flow and a detailed analysis of the theoretical development of these two types of models is given in Chapter 6 of this study.

Diagram removed for
copyright reasons

Figure 2.3   Two-dimensional "gulf stream" flow inside a bubble
column described by Freedman and Davidson (1969)

A major factor which influences the performance of a bubble column is the amount of recirculation of the gas and liquid phases. Circulating flow models take into consideration the recirculation of the liquid phase caused by the uneven distribution of the gas phase due to bubbles rising along preferential paths inside the column. In these regions, liquid is entrained in the wakes of the rising bubbles, causing the establishment of one or more eddies which recycle the liquid inside the column. The size and strength of the recirculating eddies has a significant effect on the gas void fraction and operating range of the bubble column.

Freedman and Davidson (1969) modelled the liquid circulation strength caused by the "gulf-stream" effect created by bubbles rising inside a two-dimensional bubble column. They assumed that for low gas rates the liquid was circulated within a double vortex in the manner shown in Figure 2.3. By applying a pressure balance across the system they were able to determine the circulation strength of the vortex from inviscid flow theory, and from this information they calculated the mean gas void fraction inside the bubble column.

Rietema and Ottengraph (1970) examined liquid circulation for laminar flow of a highly viscous liquid inside a cylindrical bubble column. They based their prediction on the principle of minimum energy dissipation which states that for viscous systems, where inertia terms can be neglected, the steady state velocity field corresponds to a minimum viscous dissipation of energy. From this principle they applied a pressure balance across the column to predict the velocity field, liquid circulation and gas void fraction profiles inside the column.

Wijffels and Rietema (1972a, 1972b) modelled the circulatory behaviour observed in spray columns based on the assumption that there was a droplet free layer near the wall of the column and a homogeneous core of turbulent dispersion in the centre. Unlike Rietema and Ottengraph (1970), they found that axisymmetric circulation in the form of a double vortex was the dominant mode of motion inside the spray column. Wijffels and Rietema (1972a) calculated the dispersed liquid void fraction by carrying out a pressure balance across the column in a manner similar to Rietema and Ottengraph (1970).

Whalley and Davidson (1974) extended the work of Freedman and Davidson (1969) by deriving the inviscid flow model for the liquid circulation inside a three-dimensional axisymmetrical bubble column. In their analysis they applied an energy balance instead of a pressure balance across the column, arguing that this method gave greater insight into the forces acting within the system. The energy input associated with the gas phase was equated to the energy dissipation in the wake behind the rising bubbles and also in the hydraulic jump associated with the surface of the "gulf stream" illustrated in Figure 2.3. From the energy balance Whalley and Davidson calculated the circulation strength of the formed vortex to obtain a value for the mean gas void fraction.

Hills (1974) presented a theory of circulation based on the momentum transfer inside a bubble column. His model assumed that the driving force for circulation was the radial variation in the gas void fraction which was opposed by the radial dispersion of the liquid phase. A force balance applied to an annular element within the column gave the result

$$\frac{d}{dR^*}\left(R^* \mathcal{D}_R^* \frac{d\upsilon_L^*}{dR^*}\right) - R^*\left(\frac{1}{\rho_L g}\frac{dP}{dz}\right) - R^*(1-\epsilon) = 0 \;, \qquad (2.1)$$

where R^* is the dimensionless radius based on the radius of the column, i.e. $R^* = r/R_c$. In (2.1) dP/dz is the axial pressure gradient inside the bubble column, and υ_L^* and $\mathcal{D}_R^*$ are the dimensionless linear liquid velocity and dimensionless radial dispersion coefficient respectively, based on the linear liquid velocity, υ_L, and liquid radial dispersion coefficient, $\mathcal{D}_R$, i.e.

$$\upsilon_L^* = \frac{\upsilon_L}{(R_c g)^{1/2}} \qquad ; \qquad (2.2)$$

$$\mathcal{D}_R^* = \frac{\mathcal{D}_R}{(R_c^3 g)^{1/2}} \qquad . \qquad (2.3)$$

Hills measured the radial variation in the gas void fraction, and by using reported values for the local radial dispersion coefficient, he was able to determine the radial velocity profile from (2.1). His predicted values agreed reasonably well with the experimental results.

Joshi and Sharma (1979) noted that the energy balance method proposed by Whalley and Davidson (1974) gave much higher predicted circulation velocities than were measured experimentally. From this observation Joshi and Sharma concluded there were additional mechanisms for energy dissipation not already considered by Whalley and Davidson in their single circulating eddy model. They calculated the value of the circulation strength, G, as a function of the ratio of the column height to column diameter as shown in Figure 2.4 and found the circulation strength was a minimum when the length of the bubble column L_c was equal to the bubble column diameter D_c.

Diagram removed for copyright reasons

Figure 2.4 Effect of bubble column height to diameter ratio on liquid recirculating strength calculated by Joshi and Sharma (1979)

Joshi and Sharma combined the results from Figure 2.4 with the earlier finding of Whalley and Davidson (1974) that the number of circulation cells in the axial direction resulted in a minimum vorticity value, to conclude the circulation consisted of a number of vortices in series with the axial length of each circulation cell being equal to the column diameter. This model is shown graphically in Figure 2.5.

Diagram removed for copyright reasons

Figure 2.5 Multiple circulation cell model for the bubble column proposed by Joshi and Sharma (1979)

Joshi and Sharma (1979) found that for a vertical bubble column, the axial component of the local linear liquid velocity $v_L(z)$ is given by

$$v_L(z) = \frac{2G}{L_1 k_2 D_c} \left[\left\{ \frac{\pi \Psi^*(r)}{L_2 R^*} \cos(\pi z^*) \right\}^2 + \left\{ \frac{2}{D_c R^*} \cdot \frac{d\Psi^*}{dR^*} \sin(\pi z^*) \right\}^2 \right]^{1/2} , \quad (2.4)$$

where L_1 is the distance between the column axis and the point of maximum vorticity. In (2.4) k_2 is a constant with units of m^{-4}, and z^* is the dimensionless length based on the column length. Also in (2.4) L_2 is the clear liquid height and G is the circulation strength whose value is determined by applying an energy balance across the column diameter. The dimensionless radial stream function $\Psi^*(r)$ is defined as

$$\Psi^*(r) = \frac{\Psi(r)}{\Psi_{max}} , \quad (2.5)$$

where $\Psi(r)$ is the radial stream function and Ψ_{max} is the maximum value of the radial stream function, i.e.

$$\Psi_{max} = \frac{D_c^2}{5.4} \left\{ g D_c (j_G - \epsilon (v_b)_\infty) \right\}^{1/3} . \quad (2.6)$$

In (2.6) j_G is the gas volumetric flux and $(v_b)_\infty$ is the velocity of a single bubble rising in a quiescent liquid.

Joshi and Sharma also found the mean recirculation velocity inside the eddy, $(v_e)_m$, by integrating across the downward velocity path of a circulation cell, i.e.

$$(v_e)_m = 3 \left\{ g D_c \left(j_G - \epsilon (v_b)_\infty \right) \right\}^{1/3} . \quad (2.7)$$

They also determined $(v_e)_M$ was given by

$$(v_e)_m = \frac{j_G + \epsilon (v_b)_\infty}{\epsilon \left(\frac{2}{\pi}\right)} \cdot \qquad (2.8)$$

The average gas void fraction was found implicitly by solving (2.7) and (2.8) simultaneously.

Figure 2.6 Liquid flow profile inside a bubble column proposed by Ueyama and Miyauchi (1979)

The liquid circulation inside a bubble column has also been analysed by Ueyama and Miyauchi (1979). They assumed the radial velocity profile shown in Figure 2.6, in which the liquid flow in the central region of the column is fully turbulent and directed upwards. Outside this region the direction of flow is reversed with a transition from turbulent to laminar flow taking place near the wall of the column.

Ueyama and Miyauchi neglected the laminar sublayer and proceeded to solve the time averaged equation of motion, i.e.

$$-\frac{1}{r}\frac{d}{dr}\left(r\tau\right) = \frac{dP_o}{dz} + \left(1-\epsilon\right)\rho_L g \quad , \qquad (2.9)$$

where P_o is the the axial static pressure component; τ is the shear stress and is equal to

$$\tau = -\left(\nu_M + \nu_T\right)\rho_L \frac{d\nu_L}{dr} \quad . \qquad (2.10)$$

In (2.10) ν_M is the molecular kinematic viscosity and is negligible compared with the turbulent kinematic viscosity, ν_T, which is given by (2.29). Assuming ν_T is constant across the column, and the radial gas void fraction $\epsilon(r)$ is given by

$$\frac{\epsilon(r)}{\epsilon_m} = \frac{n+2}{n}\left\{1-\left(R^*\right)^n\right\} \quad , \qquad (2.11)$$

where ϵ_m is the mean gas void fraction and n is an exponent whose value can be taken as equal to 2 (Kato et al, 1975), Ueyama and Miyauchi solved (2.9) using the following boundary conditions:-

(i) $\quad \frac{d\nu_L}{dr} = 0 \quad \quad (at \; r=0) \quad ;$

(ii) $\quad |v_L| = -11.63 \left(\dfrac{T_w}{\rho_L} \right)^{1/2} \quad (\text{at } r = R_c) \quad ,$

where $|\ |$ indicates an absolute value and T_w is the shear stress in the liquid at the wall of the column. The solution to (2.9) gave

$$\frac{v_L(r) + |v_L(R_c)|}{v_L(0) + |v_L(R_c)|} = \left\{ 1 - (R^*)^2 \right\}^2 \quad , \qquad (2.12)$$

where

$$v_L(0) + \left| v_L(R_c) \right| = \frac{g R_c^2 \epsilon_m}{8 \, \nu_T} \quad , \qquad (2.13)$$

and from Shyu and Miyauchi (1971)

$$\left| v_L(R_c) \right| = 1.42 \, (j_G)^{0.43} (D_c)^{0.28} \quad . \qquad (2.14)$$

Sekizawa et al (1983) extended the analysis presented by Ueyama and Miyauchi (1979) by defining the apparent bubble slip-velocity $(v_s)_b$ for circulatory turbulent flow, i.e.

$$(v_s)_b = \frac{j_G}{\epsilon_m} - \frac{j_L}{1 - \epsilon_m} \quad , \qquad (2.15)$$

where j_L is the liquid volumetric flux. Seikizawa et al used the model developed by Ueyama and Miyauchi (1979), to calculate the mean slip velocity $(v_s)_m$ i.e.

$$(v_s)_m = (v_G - v_L)_m + 0.615 \, \frac{\epsilon_m}{1 - \epsilon_m} \, (g \, D_c)^{1/2} \quad . \qquad (2.16)$$

In (2.16) v_G and v_L are the velocities for the gas and liquid phases respectively; $(v_G - v_L)_m$ is the mean relative velocity between the gas and liquid phases and was found experimentally to be described by

$$(v_G - v_L)_m = 37 \cdot 125 \left(\epsilon_m\right)^{0.44} \left(1 - A_F\right)^{5.5} \pm 0 \cdot 0174 \left|j_L\right|^{1.74} , \qquad (2.17)$$

where the positive sign refers to $j_L > 0$, and the negative sign refers to $j_L < 0$. In (2.17) A_F is the free area fraction of the gas distributor. Sekizawa et al (1983) solved (2.15)-(2.17) to determine the mean gas void fraction for the bubble column.

Viswanathan and Subba Rao (1983) applied inviscid flow theory to obtain an analytical solution for calculating the liquid circulation and radial velocity profile inside a cylindrical bubble column. They found the mean radial profile of the axial liquid velocity $(v_L)_m$ was given by

$$(v_L)_m = \frac{1 \cdot 2 \, k_1}{R_c^2} \left\{ 1 + 0 \cdot 6 \left(R^*\right)^2 - 3 \cdot 32 \left(R^*\right)^4 - 0 \cdot 92 \left(R^*\right)^6 \right\} , \qquad (2.18)$$

where k_1 is a constant and is given by

$$k_1 = d_1 L_1 \left(v_b\right)_\infty \left\{ \frac{g L_1 j_G}{d_3 R_c^2 \left(v_b\right)_\infty^3} \right\}^{1/d_2} . \qquad (2.19)$$

In this expression L_1 is either the diameter or length of column, whichever is the smaller, and d_1, d_2 and d_3 are constants[2] for the system.

---

[2] See Viswanathan and Subba Rao (1983) for numerical values of d_1, d_2, and d_3.

In contrast to the numerical methods applied earlier by Whalley and Davidson (1974), Clark et al (1987)[3] modelled the turbulent liquid circulation inside bubble columns by relating the radial variation of the axial liquid velocity to the shear stress developed within the liquid phase. They calculated the shear stress using the expression

$$\tau(r) = \tau_w \left[1 + g\left\{ \frac{\rho_m(R_c) - \rho_m(r)}{2\tau_w} \right\} R_c \right] R^* \ , \qquad (2.20)$$

where $\tau(r)$ is the radial variation of the axial shear stress and $\rho_m(R_c)$ is the mean density of the mixture across the column; $\rho_m(r)$ is the average density within a central cylinder of radius, r, such that

$$\rho_m(R) = \frac{1}{\pi R^2} \int_0^R 2\pi \rho(r) r \, dr \ . \qquad (2.21)$$

From Schlichting (1968) the axial shear stress is given by

$$\tau(r) = -\rho_m(r)\left\{ l(r) \right\}^2 \frac{d\upsilon_L}{dr} \left| \frac{d\upsilon_L}{dr} \right| \qquad (2.22)$$

where $l(r)$ is equal to the mixing length for flow through a pipe having a diameter equal to r. Clark et al equated (2.20) and (2.22) and integrated the result to obtain an expression for the radial profile of the liquid axial velocity, i.e.

$$\upsilon_L(r) = \int_{R_c - y_w}^0 \frac{1}{l(r)} \left\{ \frac{1}{\rho_m(r)} \right\}^{1/2} \left[\tau_w\left(1 + g\left\{ \frac{\rho_m(R_c) - \rho_m(r)}{2\tau_w} \right\} R_c \right) R^* \right]^{1/2} dr , \quad (2.23)$$

where y_w is some finite distance from the wall where the liquid velocity

---

[3]Equations 2.20 - 2.23 have been corrected for errors contained in the original reference.

is taken as zero. For a smooth-walled vessel y_w is approximately equal
to

$$y_w \doteq \frac{0.111 \mu_L}{\rho_L} \left(\frac{\rho_L}{|T_w|}\right)^{1/2} .$$ (2.24)

In order to obtain a liquid velocity profile from (2.23) Clark et al
assumed a void fraction and density distribution, and a mixing length
equal to that for single phase flow through a pipe which is given by
Nikuradse[4] as

$$\frac{l(r)}{R_c} = 0.14 - 0.08(R^*)^2 - 0.06(R^*)^4.$$ (2.25)

Using the results from (2.23) and (2.24) equation (2.23) was solved
numerically to obtain the axial velocity profile across the bubble
column.

Wachi et al (1987) modelled the turbulent liquid circulation inside a
bubble column with a continuous liquid feed by extending the analysis of
Ueyama and Miyauchi (1979). From the time-average equation of motion
Wachi et al (1987) obtained the axial pressure gradient, i.e.

$$- \frac{dP_0}{dz} = -\frac{2T_w}{R_c} + (1-\epsilon_m)\rho_L g ,$$ (2.26)

where the shear stress at the wall is given by

$$T_w = \frac{\rho_L}{(11.63)^2} . v_L(R_c) |v_L(R_c)| .$$ (2.27)

Wachi et al eliminated the pressure gradient term from (2.26) and
integrated the result to obtain the local liquid velocity, i.e.

---

[4]see Schlichting (1968), P. 568.

$$v_L(r) = \frac{T_w R_c}{2\nu_T \rho_L}\left\{1-(R^*)^2\right\} + \frac{g R_c^2}{8\nu_T}\left\{1-(R^*)^2\right\}^2 + v_L(R_c) \quad, \quad (2.28)$$

where the turbulent kinematic viscosity is approximately given by

$$\nu_T \doteq 0.0345 \left(j_G\right)^{0.167}\left(D_c\right)^{1.5} \quad. \tag{2.29}$$

The linear liquid velocity at the wall of the column is approximately equal to

$$v_L(R_c) \doteq \frac{j_L}{1-\epsilon_m} - \frac{T_w R_c}{12\rho_L \nu_T}\left\{\frac{3-4\epsilon_m}{1-\epsilon_m}\right\}$$

$$- g\frac{R_c^2 \epsilon_m}{48\nu_T}\left\{\frac{2-3\epsilon_m}{1-\epsilon_m}\right\} \quad. \tag{2.30}$$

The mean gas void fraction was then obtained from a mass balance for the gas phase. i.e.

$$\rho_G \pi R_c^2 j_G = \int_0^{R_c} \rho_G 2\pi r \left\{v_L(r) + (v_s)_b\right\} \epsilon(r)\, dr \quad, \tag{2.31}$$

where $(v_s)_b$ is the slip velocity of the bubble relative to the liquid phase. Equation (2.31) was integrated to give the following correlation containing the mean void fraction:

$$\frac{j_G}{\epsilon_m} = \frac{T_w R_c}{12\rho_L \nu_T}\left\{\frac{1}{1-\epsilon_m}\right\} + \frac{g R_c^2 \epsilon_m}{48\nu_T}\left\{\frac{1}{1-\epsilon_m}\right\}$$

$$+ \frac{j_L}{1-\epsilon_m} + (v_s)_m \quad, \tag{2.32}$$

where values of $(v_s)_m$ could be obtained experimentally or from the correlation proposed by Sekizawa et al (1983), which is given by (2.16).

<div style="border:1px solid">

**Diagram removed for
copyright reasons**

</div>

Figure 2.7   Effect of superficial liquid velocity on the mean
             gas void fraction (after Wachi et al, 1987)

Figure 2.7 shows the comparison between the experimentally measured mean
gas void fraction values and those predicted by (2.32). The theoretical
calculation gives slightly larger values at higher liquid flowrates, and
slightly smaller values at lower liquid flowrates. The theoretical curve
does show, however, good agreement over a wide range of liquid flowrates.

Chapter 3

EXPERIMENTAL EQUIPMENT
AND PROCEDURE

This chapter outlines the experimental programme carried out to study the hydrodynamic characteristics of the downcomer section of the plunging liquid jet bubble column. The equipment and materials used are described including the experimental procedures adopted.

3.1 EXPERIMENTAL PROGRAMME

The experimental programme was divided into the following two major sections:-

Section 1 involved measuring the expansion of the free liquid jet as it passed through the gas phase at the top of the column prior to it plunging into the liquid phase. These measurements were necessary in order to be able to quantify the entrainment rates for the plunging jet. Appendix 2 contains the experimental results for the free jet study.

Section 2 of the experimental programme involved monitoring the hydrodynamic response of the plunging jet bubble column for a range of conditions. The variables which were measured included the gas entrainment rate for the plunging jet, free jet length, gas void fraction, and the bubble size.

Table 3.1 contains a list of the variables and their range of values used in this study. A summary of the experimental conditions for all runs is contained in Appendix 1.

TABLE 3.1   Variables studied and their range of values

Variable	Range
Nozzle Diameter	2.38 – 7.12 mm
Velocity	7.80 – 15.00 m/s
Column Diameter	44.20 – 95.40 mm
Length	1.00 m
Liquid Surface Tension	48 – 62 mN/m
Viscosity	0.85 – 2.85 mPa-s
Density	780 – 1114 kg/m^3

3.2   MATERIALS

3.2.1   Frother

The frother Teric 407 produced by Imperial Chemical Industries (ICI) was used throughout the experimental programme to control the surface tension of the liquid. The standard liquid was tap water which was chosen in preference to distilled water because of the large volumes required for each experimental run (150 litres). A listing of the physical properties of Teric 407 is given in Table 3.2.

TABLE 3.2 Physical properties of Teric 407

Chemical composition	Polyoxypropylene glycol ether
Average molecular weight	280
Active content (% W/w min)	99%
Freezing point	-20° C
Flash point	210° C
Specific gravity (25°C)	0.936
Viscosity (25°C)	25 cP
Solubility – water – kerosene	32 g/litre infinite

The addition of Teric 407 to tap water had a neglibible effect on the viscosity and density of the solution. In figure 3.1 the effect of frother concentration on the surface tension is given where the surface tension was measured using the du Noy ring method. Concentrations of 10, 150 and 1000 ppm Teric 407 were used to vary the surface tension over the range 48 - 62 mN/m which represented a realistic surface tension range encountered in most bubble column operations.

3.2.2 Aqueous sucrose solution

Aqueous sucrose solutions were used to vary the viscosity of the liquid. Two sucrose solutions were used and these were 16% and 28% by weight sucrose. Table 3.3 contains a list of the physical properties of these two solutions. The surface tension of each was adjusted to 62 mN/m by the addition of Teric 407.
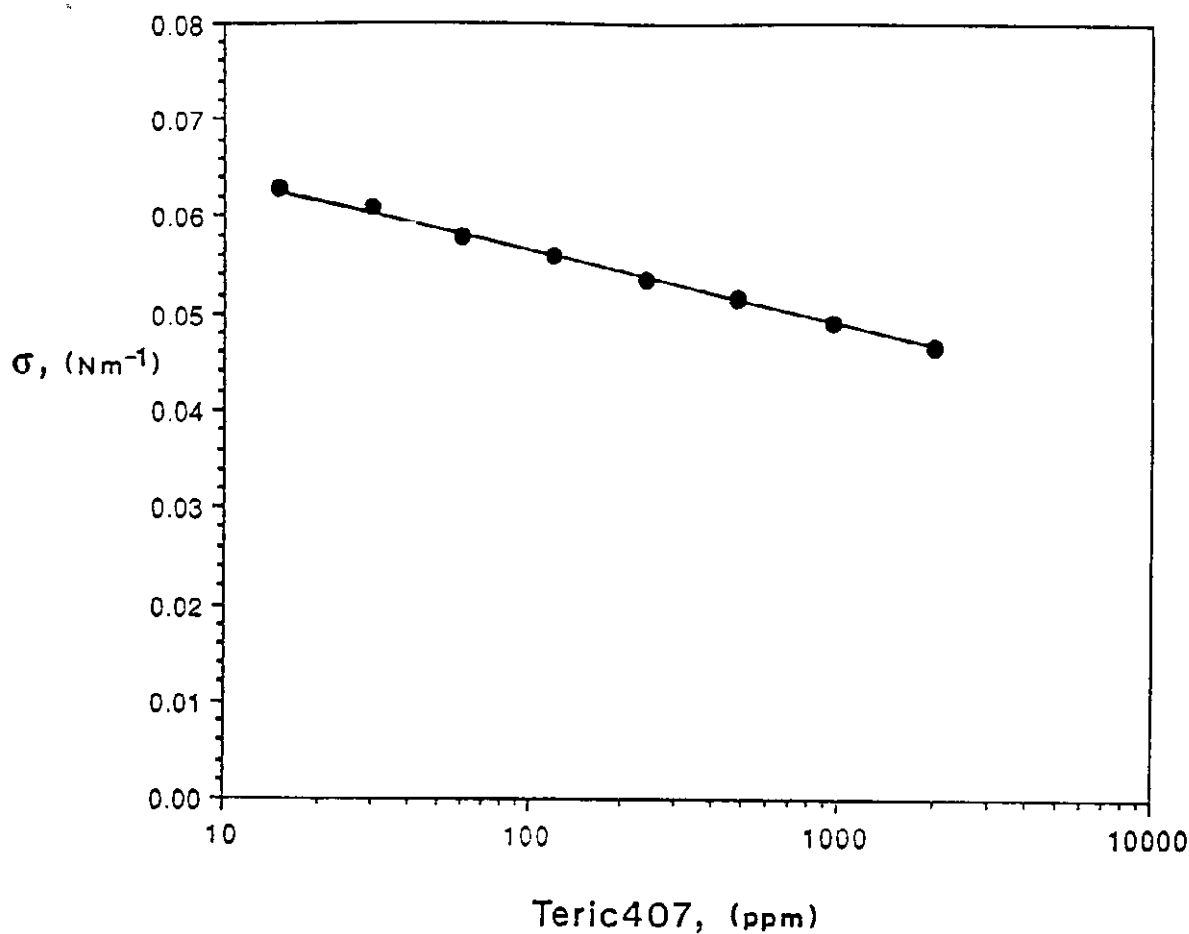
Figure 3.1   Effect of Teric 407 concentration
on surface tension of tap water

3.2.3   Kerosene

Kerosene was used in a limited number of experimental Runs as an
alternative to water-based solutions.   The kerosene was difficult to work
with as it caused the acrylic column to become brittle and fracture after
a period of time.   The kerosene also attacked the rubber seals inside the
pump and the silicone rubber seals on the column itself.   The physical
properties of kerosene are listed in Table 3.3.

TABLE 3.3   Physical properties of aqueous sucrose
solutions and kerosene used in the study

Liquid	Viscosity (cP)	Density (kg/m^3)	Surface Tension (mN/m)
16 wt% Sucrose	1.653	1064	62
28 wt% Sucrose	2.854	1114	62
Kerosene	2.12	784	24

3.3   EQUIPMENT

3.3.1   Apparatus

A general layout of the experimental apparatus is given in Figure 3.2.
It consisted of a vertically positioned perspex column with its base
extending 25 mm below the surface of a constant level bath. The top of
the column was sealed from the atmosphere allowing air to pass into the
column only through an inlet at the top. The air flowrate into the
column was measured using a network of calibrated rotameters.

The jet nozzle shown in Figure 3.2 was fixed at the top of the column so
that the liquid stream was directed along the vertical axis of the column
and plunged into the constant level bath below. The overflow from the
constant level bath was collected in a much larger vessel from which a
Mono pump was used to pump liquid through a rotameter and back to the
nozzle.

The flow through the nozzle was coarsely adjusted by changing the pulley
diameter on the drive shaft for the pump. Fine adjustments were made
using the control valve on the by-pass line from the pump outlet and back
into the reservoir. A Mono pump was used because it provided a constant
flowrate over a wide range of operating pressures without causing
excessive heating of the liquid. The liquid temperature remained
essentially constant for each experimental run.

gas inlet

sealed glass chamber

gas

nozzle

50

acrylic column

pressure tappings
(connected to pressure
manifold as shown in
Figure 3·4)

1000

constant level
tank

by-pass line

reservoir
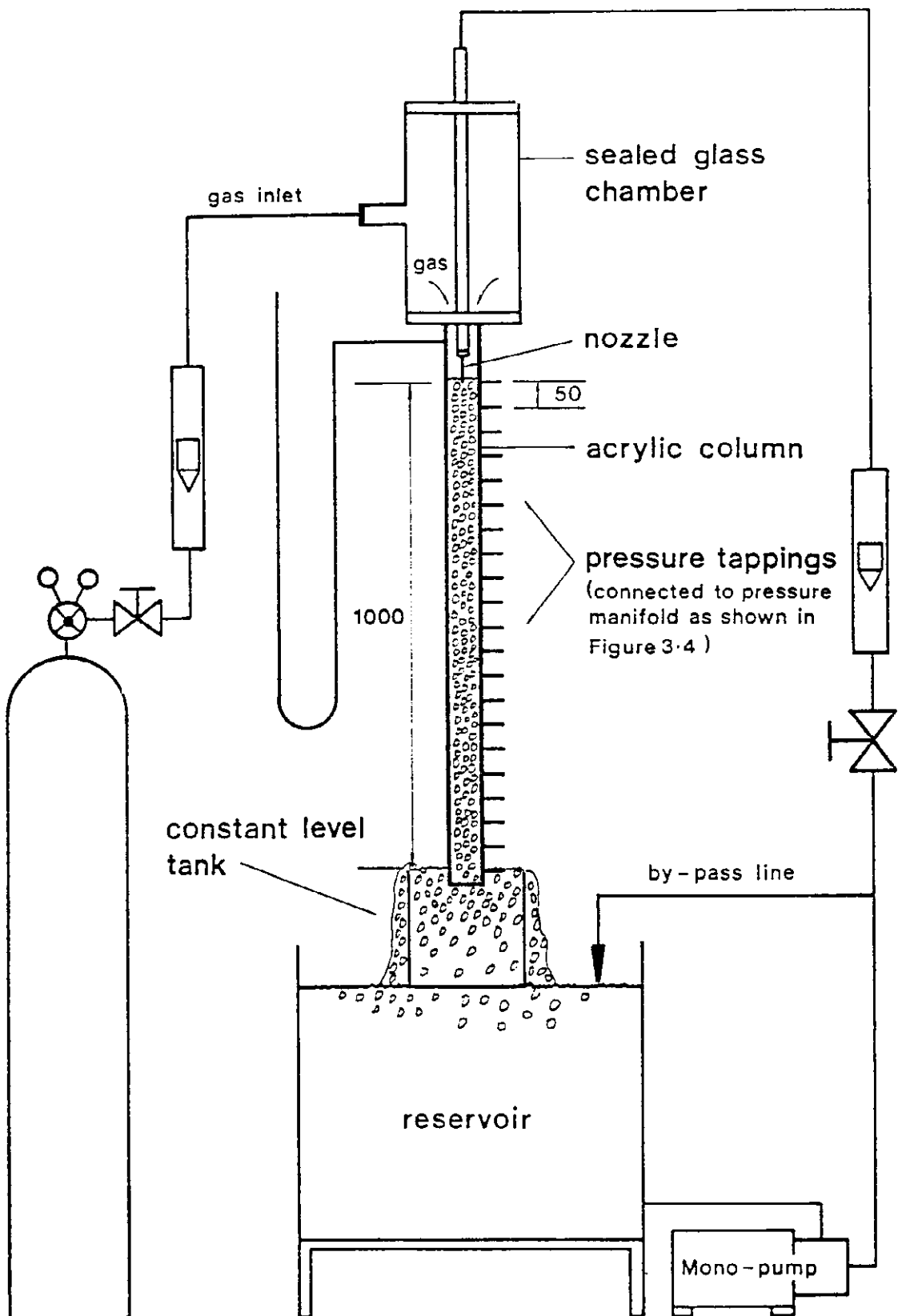
Mono-pump

Figure 3.2 General arrangement of the experimental apparatus

The main limitation associated with using a Mono pump (or any other pump) is that only jets with rough surface characteristics can be achieved. The reason for this is the pump generates disturbances within the liquid flow field which are amplified on the jet surface after it leaves the nozzle. For this study a pump delivery system was suitable because it was appropriate to use only rough jets. If smooth jets were required, a pressurised delivery system such as that used by McCarthy (1972) would be needed. The limitation of using a pressurised delivery system is that it is essentially a batch process and thus requires an extremely large holding vessel in order to maintain jet operation for sufficient time to allow the bubble column to reach equilibrium.

The jet flowrate was measured using a rotameter which was experimentally calibrated for each liquid. A flexible high pressure hose connected the rotameter to a 600 mm length of 12 mm inside diameter stainless steel delivery tube located at the top of the column. Inside the tube a 20 mm length of thin aluminium strip was inserted just above the nozzle assembly in order to reduce the amount of rotation within the liquid. The delivery tube was held in place at the top of the column by two sliding supports which allowed the nozzle to be moved into position at the zero mark at the top of the column. When the nozzle was in the correct position the assembly was fixed in place by tightening the mounting nut which forced the 'O' ring hard against the delivery tube and thus creating an air-tight seal.

The nozzle assembly was fixed onto the end of the delivery tube which allowed different nozzles to be used. The nozzle could be changed simply by unscrewing the holding nut and removing the nozzle which fitted neatly inside the delivery tube. The new nozzle could then be fitted into the end of the delivery tube and fixed into position by screwing down the holding nut.
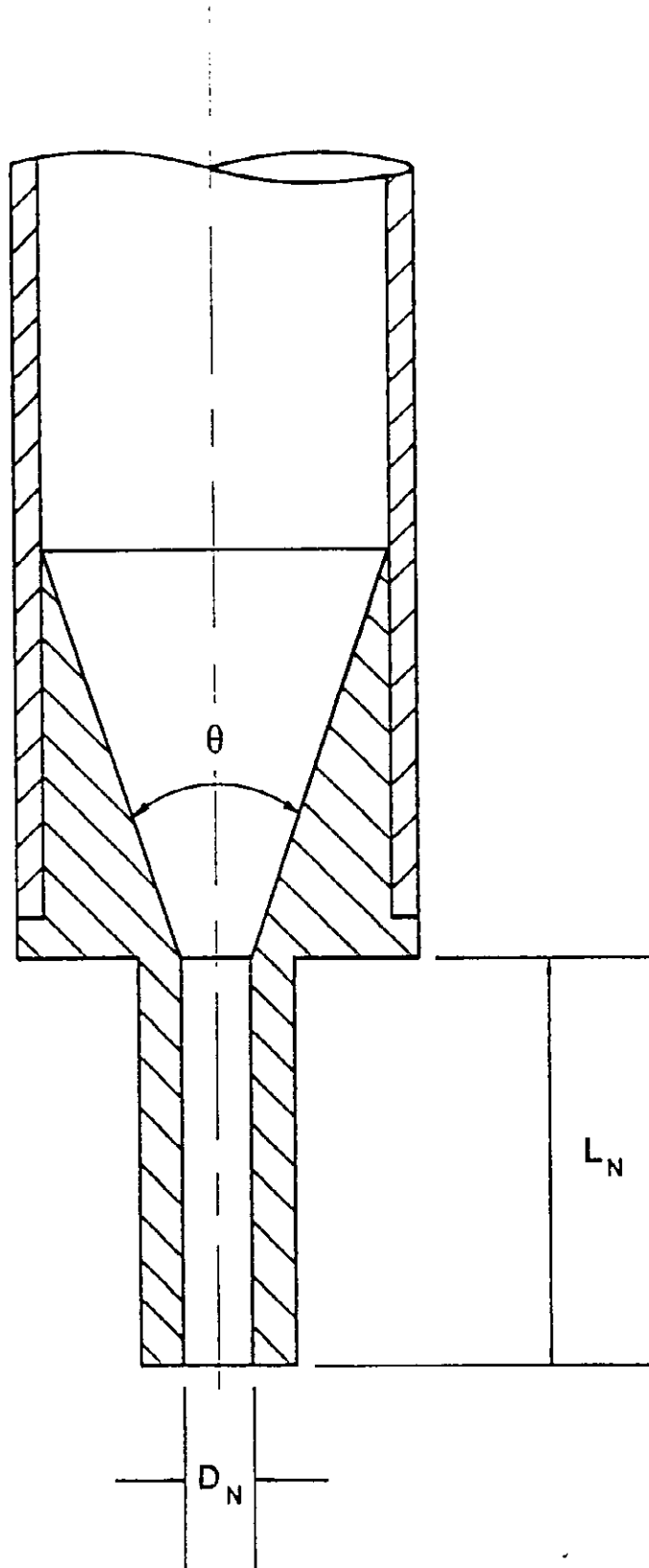
Figure 3.3 Nozzle design

3.3.2 Nozzle Design

The design which was used for all nozzles is shown in Figure 3.3. Each nozzle was constructed of brass and consisted of a tapered machined entrance section which fitted neatly inside the nozzle delivery tube giving a smooth transition. The tapered entrance led to the throat of the nozzle which consisted of a straight length of precision-bore brass tubing.

Most[5] of the experiments performed in this study examined only the influence of the nozzle diameter on the behaviour of the bubble column. The nozzles used all had the same throat length to diameter ratio and were designed[6] such that a fully turbulent velocity profile was developed in the throat of the nozzle.

The length necessary to ensure fully developed turbulent flow inside the throat of the nozzle was calculated from the entry length formula given by Latzko (1921),

$$\frac{L_N}{D_N} = 0.693 \left(Re_N\right)^{0.25} ,$$

$$(3.1)$$

where the Reynolds Number, Re_N, is based on the liquid physical properties, nozzle diameter and the liquid velocity through the nozzle.

---

[5] Appendix 2 contains tne results of a range of experiments where the throat length of the nozzle was varied to check the assumption that entrainment was maximised for fully developed flow conditions inside the nozzle.

[6] A fully developed turbulent velocity profile within the throat of the nozzle was chosen as a design criterion because it has been proposed that this condition maximised entrainment (McCarthy, 1972). He suggested the increased rate of entrainment was due to the relaxation of the velocity profile within the jet which takes place once the constraint of the nozzle is removed. The velocity relaxation results in a lateral movement of liquid which continues past the original boundary of the jet, resulting in a highly irregular or rough surface which increases the entrainment characteristics of the jet.

Table 3.4 contains the characteristic dimensions for the three nozzles used in the gas entrainment experiments performed in this study.

TABLE 3.4   Nozzle Dimensions

Nozzle No.	Diameter (mm)	Throat Length[1] (mm)	Contraction Angle (deg)
1	2.38	35.5	82
2	4.76	78	103
3	7.12	124	67

[1]The throat length was calculated from (3.1) with a liquid velocity of nominally 40 m/s.

3.3.3   Column Design

The experimental apparatus was designed to allow different diameter columns to be bolted onto the lower section of the bubble column. Three columns were used in the study and their inside diameter measurements were 44, 74 and 95 mm respectively. All three columns were identical in design and were constructed from clear perspex and consisted of a flanged section at the top which bolted onto the lower part of the chamber at the top of the bubble column. Below the flange was a straight length of clear perspex tube of length 1040 mm. Along the wall of the tube were 21 pressure tappings evenly spaced at 50 mm intervals. The pressure tappings started 15 mm below the flange and continued down the side of the column for a length of 1000 mm. The top pressure tapping was set as the zero mark for the bubble column and the tip of the nozzle was positioned level to this point. The bottom tapping was then fixed at a position level with the surface of the liquid in the constant level tank, leaving the base of the column 25 mm below the liquid surface in the constant level tank.

For a number of experimental runs, vertical baffles were installed inside the column to reduce the amount of swirl generated by the plunging jet. For these runs three radial baffles were fitted equidistantly around the inside perimeter and ran down the entire length of the column. The width of each baffle was equal to one third of the column diameter.

3.3.4 Pressure Sensing Equipment

The pressure tappings located down the side of the bubble column were connected to a dual manifold arrangement as shown in Figure 3.4. Each manifold was constructed from a 150 mm length of 50 mm diameter clear perspex rod which had a 12 mm diameter hole bored along the entire length of its vertical axis. A stop-cock was tapped into the top of each manifold which could be used to remove air trapped inside the system. Clear perspex was chosen for the manifold material because it allowed any gas cavities to be easily detected. The manifolds were also designed to minimise the liquid volume in the system in order to decrease the response time of the system.

The pressure tappings from the column were connected to stop-cocks which were tapped into the side of each manifold. The tappings were connected so that each alternative tapping was connected to the same manifold which allowed differential pressure readings to be made at 50 mm intervals along the entire length of the column.

Two-way valves were fitted to the bottom of each manifold and these were connected to the top ports of the high and low pressure legs of a Honeywell differential pressure transducer which had a variable differential range of 1 - 400 inches water gauge pressure. The two-way valves allowed the pressure pulse from the manifold to be transmitted to the appropriate side of the pressure transmitter. The bottom ports of the high- and low-pressure legs of the pressure transmitter were connected to a head tank which was used to purge liquid through the system to ensure the removal of any gas buildup in the transmitter lines prior to taking a pressure reading. Finally, the voltage output from the pressure transmitter was converted to a pressure value using the procedure outlined in Section 3.4.3.

For a number of experimental runs, vertical baffles were installed inside the column to reduce the amount of swirl generated by the plunging jet. For these runs three radial baffles were fitted equidistantly around the inside perimeter and ran down the entire length of the column. The width of each baffle was equal to one third of the column diameter.

3.3.4   Pressure Sensing Equipment

The pressure tappings located down the side of the bubble column were connected to a dual manifold arrangement as shown in Figure 3.4. Each manifold was constructed from a 150 mm length of 50 mm diameter clear perspex rod which had a 12 mm diameter hole bored along the entire length of its vertical axis. A stop-cock was tapped into the top of each manifold which could be used to remove air trapped inside the system. Clear perspex was chosen for the manifold material because it allowed any gas cavities to be easily detected. The manifolds were also designed to minimise the liquid volume in the system in order to decrease the response time of the system.

The pressure tappings from the column were connected to stop-cocks which were tapped into the side of each manifold. The tappings were connected so that each alternative tapping was connected to the same manifold which allowed differential pressure readings to be made at 50 mm intervals along the entire length of the column.

Two-way valves were fitted to the bottom of each manifold and these were connected to the top ports of the high and low pressure legs of a Honeywell differential pressure transducer which had a variable differential range of 1 - 400 inches water gauge pressure. The two-way valves allowed the pressure pulse from the manifold to be transmitted to the appropriate side of the pressure transmitter. The bottom ports of the high- and low-pressure legs of the pressure transmitter were connected to a head tank which was used to purge liquid through the system to ensure the removal of any gas buildup in the transmitter lines prior to taking a pressure reading. Finally, the voltage output from the pressure transmitter was converted to a pressure value using the procedure outlined in Section 3.4.3.

Figure 3.4 Arrangement of pressure measurement equipment
(connections are shown for only 2 tappings)

3.4 EXPERIMENTAL PROCEDURE

3.4.1 Jet diameter measurement

Photographs were taken of the free liquid jet in order to determine the expansion in jet diameter. The moving jet was photographed under natural lighting conditions using a Linhoff Polaroid camera fitted with a 156 mm telephoto lens and an extension bellows. The aperture setting was f5.6 for all runs with a shutter speed of 1/60 second which gave a time-average outline of the jet diameter. Agfa Type 55 positive-negative polaroid instant film was chosen because it produced a negative, as well as a positive image, which gave high quality 10" x 8" print enlargements.

From the 10" x 8" print enlargements jet diameter measurements were made by placing the print onto a Summographics digitiser pad which was interfaced to a microcomputer. The print was positioned on the digitiser tablet so that the jet axis was aligned in the vertical direction. The position of the tip of the nozzle was then recorded and used as a zero reference for the jet length measurements. The length scale was determined by calibrating the digitiser pad using the graduated ruler positioned to the side of the jet which also appeared on the print. Once the jet axis of the print had been vertically aligned on the tablet and the digitiser pad length scale calibrated, the diameter measurements were made. A mouse was used to record the outer surface of one side of the jet and the measurement was completed with the aid of an indicator on the screen monitor which showed when the mouse was correctly positioned in the horizontal plane on the other side of the jet. Diameter measurements were taken at single nozzle-diameter length increments for each jet. Appendix 2 contains a listing of the measured jet diameter readings.

Photographs of the free jet were also taken to examine the surface structure of the jet. A black background was placed behind the jet and the light source was a 10 µs duration flash which was mounted to the side at 45° to the vertical focal plane of the Linhoff camera. A white reflecting screen was placed on the opposite side of the camera to the flash to obtain a more even lighting of the jet. The camera used was again the Linhoff with the bellows extension and a 150 mm telephoto lens, using an aperture setting of f5.6. The shutter speed was increased to 1/250 second and the photographs were taken in a darkened room to

eliminate any influence of ambient light. It was found that the 10 µs flash was able to freeze the motion of the jet, which allowed qualitative comments to be made about the characteristics of the jet surface.

3.4.2   Jet length measurement

The length of the free jet was measured starting from the tip of the nozzle to the point where the jet penetrated the froth. The penetration point was determined to be at the interface between the low and high density froth phases at the top of the column. The position of this interface was found[7] by shining a light through the column which highlighted the difference in the optical density between the two froth phases.

3.4.3   Gas void fraction measurement

The gas void fraction ϵ averaged over the entire height of the froth inside the column was determined by measuring the froth height and the suction at the top of the column once the system had reached equilibrium. From these measurements the gas void fraction is given by

$$\epsilon = \frac{L_f - L_L}{L_f} \quad , \tag{3.2}$$

where L_f is the height of froth inside the column given by

$$L_f = L_c - L_j \quad . \tag{3.3}$$

---

[7]In a limited number of cases the interface was impossible to distinguish and the jet length was measured from the tip of the nozzle to the very top of the froth. This procedure was necessary for those Runs where the superficial downward liquid velocity was significantly lower than the rise velocity of the bubbles inside the column.

In (3.3) L_c is the height of the column measured from the tip of the nozzle to the surface of the liquid in the constant level reservoir; L_j is the length of the free jet measured using the procedure outlined in Section 3.4.2.

In (3.2) L_L is the length of the column of froth occupied by the liquid phase and its value was calculated from a differential pressure reading measured across the column using a monometer filled with water. The expression for L_L is given by

$$L_L = \Delta L \left\{ \frac{\rho_{H_2O}}{\rho_L} \right\} , \qquad (3.4)$$

where ΔL is the differential pressure reading, in metres of water, between the measured pressure at the top of the column and the ambient pressure. The ratio $\{\rho_{H_2O}/\rho_L\}$ accounted for any density difference between the water in the manometer and the test liquid inside the column.

The gas void fraction at different axial positions along the column of froth was calculated from pressure readings obtained using the tappings located along the wall of the column. The gas void fraction is given by

$$\xi(z) = \frac{\Delta L}{L_2 - L_1} , \qquad (3.5)$$

where L_1 and L_2 are the lengths from the tip of the nozzle to the nearest and furthest pressure tappings respectively. In (3.5) ΔL is the equivalent heigth of water for the differential pressure between two tappings and was calculated using the expression

$$\Delta L = \left\{ \frac{L_{max} - L_{min}}{1.6} \right\} V + \left(1.25 L_{min} - 0.25 L_{max} \right) , \qquad (3.6)$$

where V is the voltage output from the pressure transducer and the constant 1.6 (units of volts) is the transmitter output.

In (3.6) L_{max} and L_{min} are the respective maximum and minimum values of the range setting of the transducer measured in metres.

Equation (3.5) applies only to water systems where there is no detected dynamic pressure drop associated with the liquid flow. To include those runs where the density of the liquid being used was different from that of water, (3.5) was modified to become

$$\epsilon(z) = \frac{\Delta L}{L_2 - L_1} \left\{ \frac{\rho_{H_2O}}{\rho_L} \right\} , \tag{3.7}$$

where ΔL was calculated from (3.6).

The effect of the liquid flow on the pressure reading was accounted for by measuring the voltage output, V_o, from the transducer when only liquid was flowing down the column. The voltage component, V_D, as a result of the dynamic pressure drop due to the liquid flow is given by

$$V_D = V_o - 0.4 , \tag{3.8}$$

where the 0.4 value corresponds to the zero pressure differential voltage output from the transmitter. The value of V_D was subtracted from the voltage reading when gas was present to obtain the differential pressure reading between the two tappings due to the gas void fraction alone, i.e.

$$(\Delta L)_{top} = \left\{ \frac{L_{max} - L_{min}}{1.6} \right\} (V - V_D) + \left(1.25 L_{min} - 0.25 L_{max} \right) . \tag{3.9}$$

For cases when the froth level was between two pressure tappings, the gas void fraction was given by

$$\epsilon(z) = \frac{L_L - (L_j - L_1)}{L_2 - L_j} , \tag{3.10}$$

where L_L is given by (3.4)

column

Linhoff camera
with bellows

flash

A

flow-through cell

A

PLAN: SHOWING CAMERA AND FLASH LOCATION

to vacuum
pump

bubbles

2mm grid

200

bubble-free
liquid

SECTION A—A: FLOW-THROUGH CELL ARRANGEMENT
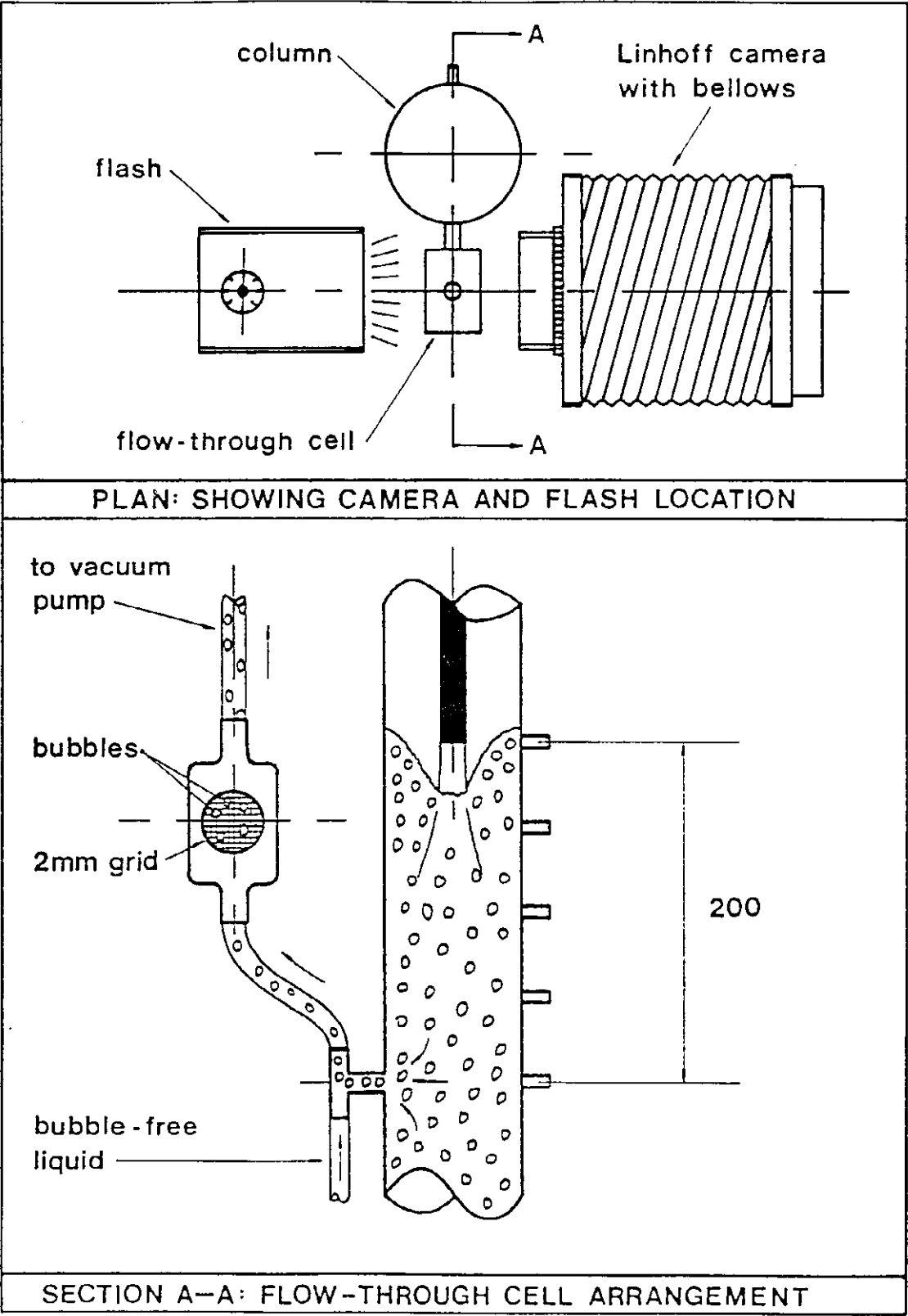
Figure 3.5 Arrangement for taking bubble photographs

3.4.4 Bubble diameter measurement

The bubble diameter distribution inside the column was measured at distances of 200 mm and 800 mm from the zero pressure tapping located at the top of the column. These two locations were chosen as being representative sample points to take bubble diameter measurements for the "mixing zone" (200 mm location), where the bubbles were being generated, and the "uniform two-phase flow zone" (800 mm location), where the mean bubble diameter was constant.

The arrangement for taking a sample of the two-phase mixture from inside the column is shown in Figure 3.5. The sample ports fitted into the side of the column consisted of 3/8" plastic 'T' fittings where the lower leg was connected via a valve to a small centrifugal pump and the upper leg was connected to the inlet at the base of the flow-through optical cell. The outlet at the top of the cell was then connected to a liquid-jet ejector pump.

Details of the flow-through optical cell are given in Figure 3.6. The cell consisted of a rectangular metal body which housed two parallel glass optical windows spaced 2 mm apart. A 2 mm grid was attached to the inside surface of the rear window which provided a calibration scale for the bubble diameter measurements. The scale also acted as a focussing object when setting up the camera.

The bubble photographs were taken using the same camera assembly which was used for the jet photography. The shutter speed was set at 1/250 second with an aperture setting of f5.6. Backlighting to the flow-through cell was provided by an Olympus flash unit operating at a power ratio of 1/128. Tracing paper was used to cover the flash to provide a more even background lighting for the bubble photographs.

The procedure for taking a bubble photograph involved starting the ejector pump which sucked froth from inside the column through the optical cell. The centrifugal pump was then switched on and the liquid flowrate through the cell was adjusted using the throttling valve on the pump outlet until a steady stream of discrete bubbles with a minimum amount of overlap passed through the photographic frame. When this was achieved the photograph was taken.

3.4.4 Bubble diameter measurement

The bubble diameter distribution inside the column was measured at distances of 200 mm and 800 mm from the zero pressure tapping located at the top of the column. These two locations were chosen as being representative sample points to take bubble diameter measurements for the "mixing zone" (200 mm location), where the bubbles were being generated, and the "uniform two-phase flow zone" (800 mm location), where the mean bubble diameter was constant.

The arrangement for taking a sample of the two-phase mixture from inside the column is shown in Figure 3.5. The sample ports fitted into the side of the column consisted of 3/8" plastic 'T' fittings where the lower leg was connected via a valve to a small centrifugal pump and the upper leg was connected to the inlet at the base of the flow-through optical cell. The outlet at the top of the cell was then connected to a liquid-jet ejector pump.

Details of the flow-through optical cell are given in Figure 3.6. The cell consisted of a rectangular metal body which housed two parallel glass optical windows spaced 2 mm apart. A 2 mm grid was attached to the inside surface of the rear window which provided a calibration scale for the bubble diameter measurements. The scale also acted as a focussing object when setting up the camera.

The bubble photographs were taken using the same camera assembly which was used for the jet photography. The shutter speed was set at 1/250 second with an aperture setting of f5.6. Backlighting to the flow-through cell was provided by an Olympus flash unit operating at a power ratio of 1/128. Tracing paper was used to cover the flash to provide a more even background lighting for the bubble photographs.

The procedure for taking a bubble photograph involved starting the ejector pump which sucked froth from inside the column through the optical cell. The centrifugal pump was then switched on and the liquid flowrate through the cell was adjusted using the throttling valve on the pump outlet until a steady stream of discrete bubbles with a minimum amount of overlap passed through the photographic frame. When this was achieved the photograph was taken.

60

6

B   B

GLASS WINDOWS

15

70   36

2mm GRID (glued onto
inside face of the rear
window)

15

A

FRONT VIEW: SECTION A-A   SIDE VIEW: SECTION C-C

C   CROSS-SECTION OF FLOW AREA

2   20

C

TOP VIEW: SECTION B-B

Figure 3.6   Detail of flow-through optical cell

The equatorial bubble diameter was obtained by enlarging the Polaroid
negative onto a 10" x 8" print. The diameters of the bubbles appearing
in the photograph were measured with the aid of the Summographics
digitiser pad which was interfaced to a microcomputer. The digitiser pad
was first calibrated using the scale which appeared on the print and then
the bubble diameters for at least 250 bubbles were recorded for each run.
The arithmetic and Sauter mean diameters for the bubble distribution were
also calculated.

Chapter 4

ENTRAINMENT BY
A PLUNGING LIQUID JET

4.1 INTRODUCTION

In this chapter the entrainment mechanisms for a vertical plunging liquid
jet are investigated. A survey of earlier entrainment models is given
for systems where the jet plunges through an unconfined gas space and
into a receiving vessel where the ratio of the jet diameter to vessel
diameter is very small. In these cases the receiving vessel diameter has
an insignificant[8] influence on the entrainment rate.

A model is developed in this chapter which includes the effect of the
receiving vessel diameter on the entrainment mechanism. The model is
verified experimentally by measuring the entrainment rate for a liquid
jet plunging through a confined gas space and into a receiving column of
liquid where the diameter of the column was varied to determine its
influence on the entrainment rate for a range of jet velocity and
diameter values, and liquid physical properties.

---

[8]An exception is the case reported by McCarthy (1972) who observed
that even in a very large diameter receiving vessel localised vorticity
was generated which increased the entrainment rate by an order of
magnitude. This occurred when the vorticity was localised at the point
of impact of the jet with the bath.

4.2   LITERATURE REVIEW OF PLUNGING LIQUID JET SYSTEMS

Studies into plunging liquid jet systems can be broadly divided into
those which examine the mechanism by which entrainment is initiated, and
those which attempt to quantify the entrainment process once it has
commenced. The present study falls into the latter category, focussing
on the process of entrainment after it has been initiated, as distinct
from the mechanism of initiation itself. The conditions under which
entrainment will take place will not be dealt with in any detail in this
study; some major studies of the initiation of entrainment include
Lin (1963), Sheridan (1966), Perry (1967), McCarthy (1972),
Wilkinson (1975), Kennedy and Burley (1977), Bolton and Middleman (1980),
McKeogh and Irvine (1981), Scriven (1982), Kumagai and Endoh (1983a),
Burley and Jolly (1984), Buonopane et al (1986), Sene (1988), Bin (1988).

The results reported by Sheridan (1966) and by McCarthy (1972) are of
particular interest to the present study. Sheridan proposed that
entrainment was initiated by an instability formed on the surface of the
meniscus at the point of contact between the jet and the receiving
liquid. The instability on the meniscus was caused by the downward force
exerted by the motion of the gaseous boundary layer being dragged along
by the free surface of the jet. He calculated the resultant meniscus
profile as a function of increasing jet velocity as shown in Figure 4.1,
and used the criterion that entrainment was initiated at a jet velocity
of 2.35 m/s when the meniscus profile contained a maximum. As can be
seen from Figure 4.1 Sheridan's experimental results supported the
predicted value of 2.35 m/s as the diameter of the jet approached zero.
His results also showed that the entrainment velocity was a function of
the jet diameter which was not predicted by the theory.

The entrainment initiation results reported by Sheridan (1966) were not
in agreement with the observations of McCarthy (1972). He produced very
smooth surface plunging jets and found that entrainment was not initiated
until jet velocities of the order of 6 m/s were reached.

Figure 4.1   Variation of critical entrainment velocity
with jet diameter observed by Sheridan (1966)

The first significant study quantifying the entrainment of a gaseous
phase by a plunging liquid jet was carried out by Mertes (1938), in his
patent application for a chemical reactor. The reactor consisted of a
plunging jet device with recycle of the jet liquid. In his patent
application Mertes described the entrainment process as being a film of
gas which was formed in the region immediately adjacent to the liquid
jet. The gas film then travelled at the same velocity as the jet, and
after being brought below the surface of the receiving fluid, the gas

film was sheared from the jet. The gas film was then distributed as bubbles throughout the liquid.

Shirley (1950) measured air entrainment rates for inclined plunging water jets for a range of jet diameter and velocity values. He found that the entrainment rate could not be determined from the jet diameter and velocity alone. Although not able to quantify his results, Shirley reported that both the roughness of the free surface of the jet and also the degree of turbulence present in the receiving fluid had a marked effect on the rate of entrainment.

Oyama, Takashima and Idemura (1953) examined the entrainment process for turbulent water jet systems. They proposed that the roughness on the surface of the jet caused gas to be entrained at a rate given by the correlation

$$\frac{Q_G}{Q_L} = 0.75 \left[\frac{v_j^2}{g L_j} \right]^{-0.447} \cdot \left\{ \frac{D_N v_j \rho_L}{\mu_L} \right\}^{1.33} \cdot \left\{ \frac{\mu_L}{(\sigma \rho_L D_N)^{1/2}} \right\}^{2.18} \cdot \left\{ \frac{L_j}{D_N} \right\}^{0.218} , \quad (4.1)$$

where Q_G and Q_L are the gas and liquid volumetric flowrates respectively; D_N is the nozzle diameter and v_j and L_j are the velocity and free length of the jet respectively. The liquid density, dynamic viscosity and surface tension are given by ρ_L, μ_L and σ. Equation (4.1) represents the first attempt to utilise dimensional analysis in order to correlate the entrainment process.

Lin and Donnelly (1966) also applied dimensional analysis to their experimental results to obtain the incipient entrainment velocity for a plunging jet. They found that the following relationship was valid for viscous, laminar jets:

$$We_{incip} = 10 \left\{ Re_{incip} \right\}^{0.74} . \quad (4.2)$$

where Re_{incip} and We_{incip} are the Reynolds and Weber numbers for the onset of entrainment based on the liquid physical properties, jet velocity and jet diameter at the plunge point.

Lin and Donnelly (1966) were also the first workers to differentiate between the entrainment mechanisms for laminar and turbulent jets. Although not able to quantify their results Lin and Donnelly were able to describe qualitatively the entrainment process. They found that for laminar jets entrainment was caused by the breakup of a thin film of gas which was carried along by the free jet surface. The gas film extended below the surface of the receiving liquid and broke up as a result of oscillations generated at the base of the film. The oscillations were created from instabilities associated with the jet after it had entered the receiving liquid. For turbulent jets instabilities were created within the jet as it passed through the gas phase. These instabilities created disturbances on the free surface of the jet resulting in air being mixed into the jet stream prior to it entering the receiving liquid. No surrounding gas film extending below the surface of the receiving liquid was observed for turbulent jets.

De Frate and Rush (1969) measured entrainment rates for turbulent water jets with Reynolds numbers greater than 20,000. They concluded that entrainment was caused by deformations on the surface of the jet and that the entrainment ratio was given by

$$\frac{Q_G}{Q_L} = 10^{-6} We .$$

(4.3)

The Weber number, We, in (4.3) is calculated using the liquid physical properties, the jet velocity and the free jet length. From their observations De Frate and Rush (1969) described three different mechanisms of increasing entrainment. At low velocities the liquid jet remained as a continuous liquid stream and entrainment occurred as bubbles detached themselves from the base of the gas film extending below the surface of the receiving liquid. This process of entrainment was similar to the mechanism described by Lin and Donnelly (1966) for laminar jets. When the velocity was increased the jet became sinuous and eventually disintegrated into droplets at longer jet-lengths. Gas was entrained below the receiving liquid surface due to gas being trapped inside the cavities which were formed by the impact of the droplets. For still higher velocities the amplitude of the sinuous motion of the jet increased, creating a greater impact area between the jet and the

receiving liquid surface. Entrainment was at a maximum under these conditions. Although able to describe the three different mechanisms by which entrainment could take place, De Frate and Rush were not able to quantify the conditions where a transition between mechanisms occurred.

The first theoretical prediction for the entrainment rate was made by Szekely (1969) who assumed the entrainment rate was equivalent to the quantity of gas contained within the gaseous film adjacent to the free surface of the jet. Szekely used the boundary layer profile derived by Glauert and Lighthill (1955) in order to calculate the mass flux of gas in the boundary layer. The following equation results:

$$\frac{W_G}{W_L} = \frac{4\rho_G}{\rho_L D_N^2}\left\{\frac{3\nu_L L_j}{\rho_G \nu_j} + 1.73\left(\frac{\nu_L L_j}{\nu_j}\right)^{1/2}\right\} \quad , \tag{4.4}$$

where W_G and W_L are the mass flowrates of the gas and liquid phases respectively and ν_L is the kinematic viscosity of the liquid phase. In his analysis Szekely did not differentiate between laminar and turbulent jets, or consider the effect of the disturbances present on the free surface of the jet.

McCarthy (1972) examined plunging jet systems for a wide range of liquid physical properties and nozzle designs. He found that for rough surface jets the basic entrainment mechanism was due to the interaction between the irregularities on the free surface of the jet and the surface of the receiving liquid. As a result of this interaction cavities formed which filled with gas and then dispersed as bubbles. McCarthy quantified the entrainment process using the jet volumetric flowrate Q_L and the effective jet diameter $D_j(z)$ for a vertical distance z from the nozzle, i.e.

$$\frac{(Q_G)_I}{Q_L} = \left\{\frac{D_j(z)}{D_N}\right\}^2 - 1 \quad , \tag{4.5}$$

where $(Q_G)_I$ is the quantity of gas trapped within the boundary of the jet, and the effective jet diameter is defined as shown in Figure 4.2.

Figure 4.2 Effective jet diameter defined by McCarthy (1972)

McCarthy found the effective jet diameter was a function of the surface roughness, which in turn was a function of the disturbances generated within the liquid by the jet delivery system and also the nozzle design. However, he was not able to predict values for the surface roughness, and relied on a photographic technique to measure the effective jet diameter as a function of the free jet length.

McCarthy (1972) also observed for smooth-surface plunging jets of moderate to high viscosity, a gas film formed around the free surface of

the jet below the surface of the receiving liquid. He suggested
entrainment was due to the generation of instabilities on the annular
film surface resulting in the periodic dispersion of the gas film into
bubbles. McCarthy therefore concluded that the thickness of the gas
annulus was the most significant factor in determining the entrainment
rate.

McCarthy (1972) also mentioned a phenomenon which he described as "vortex
amplification", which occurred when the point of impact of the plunging
jet became the site of a free surface vortex. The free surface vortex
was the localisation of the energy which was transferred to the receiving
liquid by the jet as a result of momentum exchange. The centripetal
forces created by the free surface vortex caused the surface of the
annular gas film to expand resulting in an increase in the entrainment
rate.

Ciborowski and Bin (1972) presented an empirical correlation for the
entrainment ratio for a plunging liquid jet system:-

$$\frac{W_G}{W_L} = 5 \times 10^{-11} D_N^4 \left\{ Fr_j - A_1 \right\} \left(\frac{L_j}{D_N} \right)^{1 \cdot 8} , \qquad (4.6)$$

where the Froude number Fr_j is based on the liquid physical properties,
the jet velocity and the free jet length. The coefficient A_1 in (4.6) is
a function of liquid physical properties, the jet diameter, and the free
jet length. Ciborowski and Bin concluded that the jet velocity, or more
specifically, the kinetic energy associated with the jet, was the most
important parameter affecting the entrainment rate.

Van de Sande (1974) and van de Sande and Smith (1973, 1976) observed
entrainment mechanisms for turbulent water jets. They made a distinction
between the mechanisms for those of low velocity (v_j < 5 m/s) and high
velocity ($v_j > \left\{ 10 \sigma/(\rho_G D_j) \right\}^{1/2}$) jets. At low velocities van de Sande found
the entrainment rate was determined by the surface deformities on the jet
and also the physical properties of the receiving liquid.

—

Figure 4.3 Theoretical relationship for the volume of gas contained within the boundary layer being carried along by the surface of the liquid jet (after van de Sande, 1974)

For high velocity jets van de Sande (1974) found the volumetric gas entrainment rate was given by the combined total of the gas contained inside the boundary layer $(Q_G)_B$ which was dragged along by the free surface of the jet, together with the gas trapped inside the boundary of the effective jet diameter $(Q_G)_I$, i.e.

$$Q_G = (Q_G)_B + (Q_G)_I \ .$$

(4.7)

In (4.7) $(Q_{\varepsilon})_{I}$ is calculated from (4.5) and the effective jet diameter is given by van de Sande (1974) as

$$\frac{D_{J}(z)}{D_{N}} = 0.125 \left\{ Re_{j} \, We_{B} \right\}^{1/6} . \qquad (4.8)$$

The Reynolds number in (4.8) is based on the liquid physical properties, the jet velocity and the free jet length, and the Weber number is based on the gas physical properties, the jet velocity and the nozzle diameter. Equation (4.8) was found to be valid for ($Re_{j} \, We_{B}$) > 7 x 10^5.

Van de Sande (1974) calculated the volumetric flux of gas in the boundary layer by assuming a laminar velocity profile suggested by Rotte (1969), and integrating across its thickness. The graphical solution which gives $(Q_{\varepsilon})_{B}$ is presented in Figure 4.3.

Diagram removed for copyright reasons

Figure 4.4 Surface disturbance defined by McKeogh and Irvine (1981)

McKeogh and Irvine (1981) found that the turbulence level of the plunging jet determined the mechanism for gas entrainment. For air/water systems they found the air entrainment ratio was best described by the expression

$$\frac{Q_G}{Q_L} = 1.4 \left\{ \left(\frac{2S}{D_N}\right)^2 + \left(\frac{S}{D_N}\right) - 0.1 \right\}^{0.6} ,$$
(4.9)

where S is equal to the magnitude of the surface disturbance on the free surface of the jet as shown in Figure 4.4. Equation (4.9) included the volume of gas which was trapped within the undulations on the free surface of the jet and also that which was contained within the boundary layer being carried along by the jet.

Kumagai and Endoh (1982, 1983a, 1983b) observed four distinct entrainment regions for a plunging liquid jet as shown in Figure 4.5, where (I) is the initial entrainment region; (II) is the low jet velocity region; (III) is the transition region; and (IV) is the high jet velocity region. In Figure 4.5 p_1, p_2, and p_3 are the transition points and, unlike van de Sande (1974), Kumagai and Endoh found that the transition points were functions of the kinematic liquid viscosity. They also found that the entrainment rate was independent of the surface tension, which was in contrast to all previous observations.

Figure 4.5 Definition of gas entrainment regions
described by Kumagai and Endoh (1983)

Thomas et al (1984) studied the mechanism whereby gas was entrained by a
.sheet of liquid travelling down an inclined surface and into a pool of
liquid as illustrated in Figure 4.6. They found that gas bubbles were
entrained via a layer of foam on the free surface of the receiving
liquid. The bubbles were then transported in discrete clusters
travelling within the shear layers between the submerged jet and the

receiving liquid. Thomas et al attributed the clustering phenomena to the bubbles becoming captured within the large eddies travelling along the edge of the jet. No attempt was made to quantify the entrainment rate.

Figure 4.6 Schematic showing air entrainment mechanism by an inclined plunging liquid jet

Ohkawa et al (1986) carried out an extensive study of entrainment rates for plunging jet systems which employed a downcomer arrangement as shown in Figure 4.7.

Figure 4.7   Schematic of the downcomer arrangement
used by Ohkawa et al (1986)

In Figure 4.7 the diameter of the downcomer was only an order of magnitude larger than the jet diameter which was different from all previous designs, where the dimensions of the receiving liquid vessel had been increased as much as possible to reduce the influence of swirl generated by the action of the plunging jet. The downcomer effectively concentrated the swirl at the point of impact of the plunging jet which resulted in higher rates of entrainment.

Sene (1988) studied planar and circular plunging jet systems for both low (v_j < 6 m/s) and high (v_j > 10 m/s) velocity jets. He found for low impact velocities the entrainment rate varied to the one third power of the impact velocity, and depended strongly on the magnitude of the disturbances on the free jet surface. The size of the disturbances were limited by the diameter of the jet and also by the surface tension effects resulting from the high curvature of small diameter circular jets. Both of these effects acted to decrease the gas entrainment rate when the jet diameter was less than a few centimetres.

For high velocity jets Sene found the gas was entrained in the form of a continuous layer at the plunge point which supported the idea of a boundary layer entrainment mechanism. He found for high impact velocities the entrainment rate varied to the three halves power. Sene also suggested that for high jet velocities the entrainment rate should be independent of the surface tension. He commented, however, for jet diameters less than a few centimetres the surface tension force may limit the thickness of the gas boundary layer thus reducing the amount of entrainment. The condition for which surface tension might limit the rate of entrainment was given by Sene (1988) as

$$D_j < \frac{2\sigma}{\rho_L g L_j \sin\phi} \quad , \tag{4.10}$$

where ϕ is the angle of inclination of the jet from the horizontal surface and L_j is the length along the surface of the jet.

Figure 4.8 Arrangement of entrainment guide
used by Funatsu et al (1988)

Funatsu et al (1988) examined the entrainment characteristics for
plunging water jet systems for a range of jet velocities between 4.4 and
26.5 m/s. They installed an entrainment guide to their system by
allowing the plunging jet to pass through a length of vertical pipe which
extended below the receiving liquid surface as shown in Figure 4.8.

The entrainment guide was thought to concentrate the energy dissipation of the jet at the plunge point thereby reducing the amount of energy required by the system to achieve a given gas entrainment rate. Funatsu et al found the entrainment rate was a function of $W_L\left(v_j^2+2gL_j\right)$, L_j, and D_N. No attempt was made to determine the influence of altering the entrainment guide geometry on the gas entrainment rate.

The studies outlined in this review have shown the entrainment mechanism to be either discontinuous or continuous depending upon the velocity of the jet. The jet velocity and, to a lesser extent, the nozzle geometry, have been found to have a strong influence on the surface characteristics of the jet. Generally it has been accepted that for a jet which has a smooth free surface, entrainment occurs in the form of a gas boundary layer which is dragged below the surface of the receiving liquid by the free surface of the jet. For jets which have a rough free surface the total entrainment rate is the sum of the gas contained within the boundary layer plus the gas which is trapped inside the surface irregularities of the jet. In most studies[9] the diameter of the receiving vessel was made very large in order to eliminate any effect on the entrainment rate due to energy buildup in the receiving liquid. No attempt has been undertaken to understand the influence of the diameter of the receiving vessel on the entrainment rate.

Before a model can be developed to include the effect of the receiving vessel diameter on the entrainment rate for a plunging liquid jet, it is necessary to present some basic concepts and principles describing the hydrodynamics of confined jets. These are presented in Section 4.3.

---

[9]The exceptions are Ohkawa et al (1986) and Funatsu et al (1988)
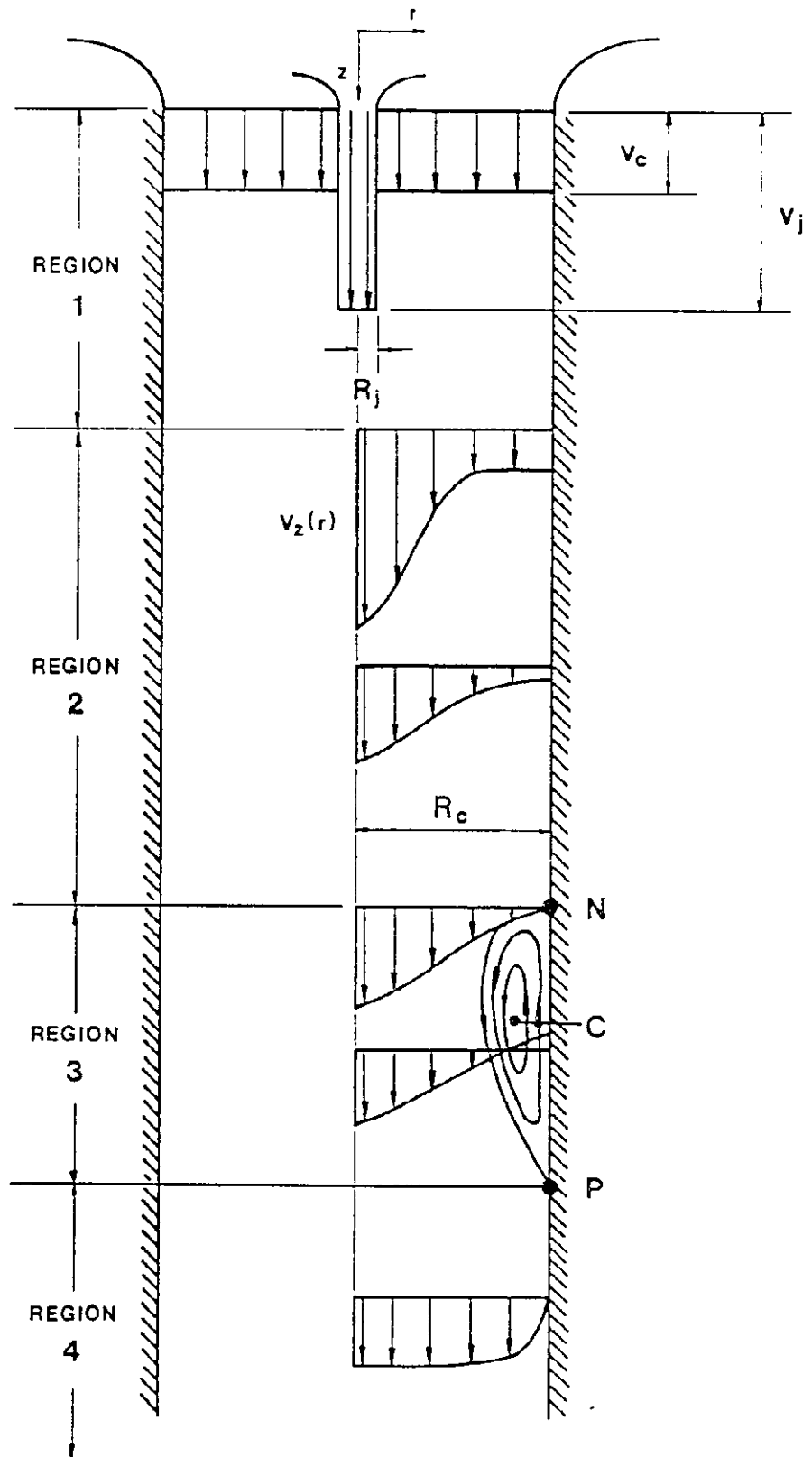
Figure 4.9 Circular confined jet issuing into a coaxial column

4.3 MODELLING OF CONFINED JETS

The expansion of a confined jet is influenced by the interaction of the
fluid inside the jet with the body of fluid between the jet boundary and
the duct wall as illustrated in Figure 4.9. It can be seen from the
diagram the expansion of the confined jet can be classified into four
regions. These are:-

Region 1 - is where the potential core of the primary jet is completely
consumed as the secondary stream loses a portion of its flow to the
primary stream due to entrainment.

Region 2 - is where the secondary stream is completely consumed.

Region 3 - is where both positive and negative velocities (from left to
right and right to left) are observed. Some of the mean streamlines
take the form of a closed loop or "recirculating eddy" and the distance
between the points N and P in Figure 4.9 represents the length of the
recirculating zone. The point C corresponds to the centre of the eddy
and is measured from the tip of the primary stream nozzle.

Region 4 - is the region of fully developed pipe flow.

For the jet system illustrated in Figure 4.9 the change in the total
volumetric flow in the axial direction is zero, i.e.

$$\frac{dQ}{dz} = 0 \quad,$$

(4.11)

where Q is the volumetric flow, and is given by

$$Q = \int_{0}^{R_c} 2\pi r \, v_z(r) \, dr \quad,$$

(4.12)

in which $v_z(r)$ is the linear velocity in the axial direction.

For the jet system shown in Figure 4.9 the change in the pressure plus momentum integral, M, along the axial direction is also zero, i.e.

$$\frac{dM}{dz} = O \quad .$$

(4.13)

If the pressure term in (4.13) is negligible, the momentum integral is given by

$$M = \int_o^{R_c} 2\pi r \left\{ U_z(r) \right\}^2 \rho_L \, dr \quad .$$

(4.14)

When (4.12) and (4.14) are combined they form the dimensionless parameter known as the Hill number N_H, which is often used to characterise confined jet systems and is defined by Rajaratnam (1976) as

$$N_H = \left\{ \frac{1}{2\pi} \right\}^{1/2} \frac{Q}{R_c \left\{ \frac{M}{\rho_L} \right\}^{1/2}} \quad .$$

(4.15)

Curtet and Ricou (1964) suggested another dimensionless variable known as the Crayer-Curtet number C_T, which is related to the Hill number by the expression

$$C_T = \left\{ \frac{2 N_H^2}{1 - N_H^2} \right\}^{1/2} \quad .$$

(4.16)

The significance of the Crayer-Curtet number becomes apparent when analysing experimental observations. Barchilon and Curtet (1964) found that the recirculating flow in Region 3 of Figure 4.9 was a function of the Crayer-Curtet number. At low values of C_T the recirculation was high. The recirculation then decreased with increasing C_T until a critical Crayer-Curtet number of 0.976 was reached, beyond which no

recirculation was observed. Becker et al (1962) reported a value of 0.75 for the critical Crayer-Curtet number.

Barchilon and Curtet (1964) quantified the recirculation as a function of Crayer-Curtet number as shown in Figure 4.10. It can be seen from the graph that the ratio of the maximum recirculation flowrate $(Q_e)_{max}$ to the volumetric flowrate of the primary jet Q_L was found to be inversely proportional to C_T.

Diagram removed for copyright reasons

Figure 4.10 Maximum recirculation flowrate as a function of Crayer-Curtet number (Barchilon and Curtet, 1964)

Liu and Barkelew (1986) have also measured the recirculating flowrates for confined jets and they found for $\left(1/C_T\right) > 2$ the relationship

$$\frac{(Q_e)_{max}}{Q_L} = \frac{0.37}{C_T} - 0.64 \quad , \qquad (4.17)$$

correlated their results, which also corresponded to the actual[10] measurements made by Barchilon and Curtet (1964).

4.4   THEORETICAL DEVELOPMENT

4.4.1   General description of the entrainment model

The entrainment model which has been developed is based on the assumption that the total rate of entrainment is equal to the sum of the amount of gas $(Q_G)_I$ trapped within the boundary of the effective jet diameter plus the amount of gas $(Q_G)_F$ contained within a thin gas film adjacent to the jet free surface, i.e.

$$Q_G = (Q_G)_I + (Q_G)_F \qquad (4.18)$$

where $(Q_G)_I$ is given by (4.5) and the effective jet diameter can be found either by direct measurement or from (4.8).

The film component of the entrainment rate is a function of the velocity profile of the gas inside the film. It is also a function of the film thickness which is determined by the forces acting within the receiving liquid at the plunge point of the jet. It is important to mention at this stage that the quantity of gas inside the entrained film is not equal to the volumetric flux of gas inside the boundary layer being dragged along by the free jet surface. This point is illustrated in Figure 4.11 where it can be seen that only part of the gas boundary layer

---

[10]shown as closed circles in Figure 4.10

contributes to the gas film and the rest of the gas in the boundary layer travels radially out along the surface of the receiving liquid.
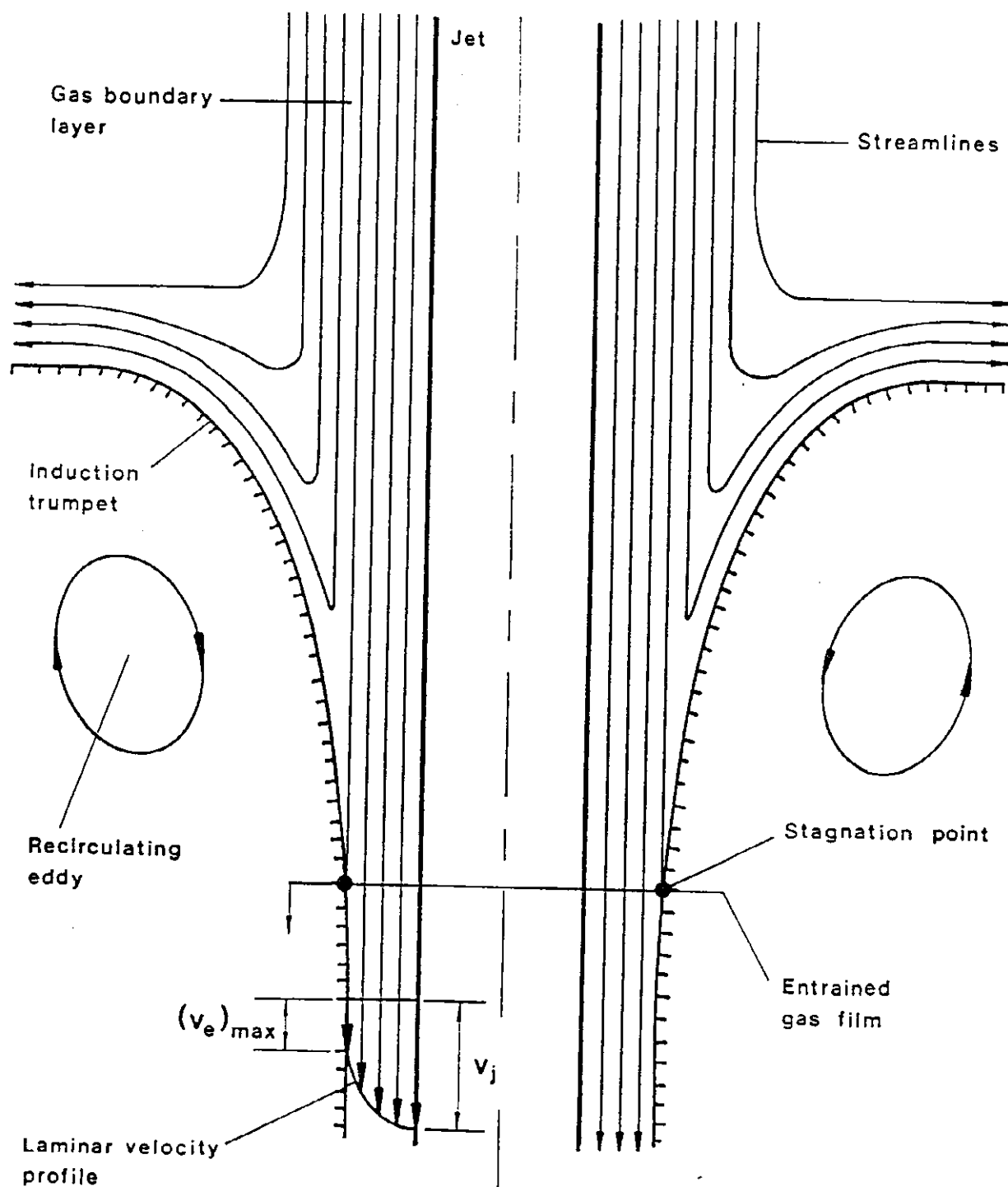
Figure 4.11 Streamlines showing only a portion of the gas boundary layer entrained by the plunging jet

It can also be seen from Figure 4.11 the presence of a depression in the free surface of the receiving liquid caused by the impact of the plunging jet. This depression is known as the "induction trumpet" and it is through the induction trumpet that entrainment of the gas film occurs. Below the free surface of the receiving liquid a recirculating eddy is generated whose outer boundary follows the free surface profile of the induction trumpet. The recirculating eddy is also bounded below the receiving liquid surface by the submerged jet as it expands towards the wall of the column as a result of the dissipation of the jet energy.

4.4.2 Calculation of the free-surface velocity of the induction trumpet

In order to quantify the gas entrainment rate for the plunging liquid jet the total volumetric flowrate inside the recirculating eddy is required. The maximum volumetric flowrate inside the recirculating eddy is calculated from (4.17) where the Crayer-Curtet number for systems where the secondary flow is zero is equal to

$$C_T = \frac{R_j}{\left\{ R_c{}^2 - \frac{1}{2} R_j{}^2 \right\}^{1/2}} \quad . \qquad (4.19)$$

If the three dimensional recirculation eddy is considered to be a torus whose inner radius is equal to the diameter of the jet at the plunge point and the outer radius is equivalent to the diameter of the column, the volumetric flowrate inside the recirculating eddy will also be given by

$$(Q_e)_{max} = 2\pi \left\{ \frac{R_c}{2} \right\} \int_0^{R_c/2} v_e(r) \, dr \quad , \qquad (4.20)$$

where πR_c is the linear length of the cylinder which would be formed if the torus was sliced in the radial direction and straightened out. The integral term in (4.20) represents the two-dimensional flow rotating within the radial cross-section of the eddy.

The angular velocity, v_e, in the radial cross-section of the eddy is obtained from

$$\frac{d}{dr}\left\{\frac{1}{r}\frac{d}{dr}(r v_e)\right\} = 0 \quad , \tag{4.21}$$

where it has been assumed the liquid recirculation in the radial plane of the eddy has the same velocity profile as that for a free vortex. Upon integration, (4.21) gives

$$c_1 = \frac{1}{r}\frac{d}{dr}(r v_e) \quad , $$

or

$$\frac{c_1 r^2}{2} = r v_e + c_2 \quad . $$

The boundary conditions for (4.21) are:-

(i) $\quad v_e = 0 \quad\quad\quad (at\ r = 0) \quad ;$

(ii) $\quad v_e = (v_e)_{max} \quad\quad (at\ r = R_c) \quad ,$

where $(v_e)_{max}$ is the maximum value of the velocity component tangential to the outer boundary of the recirculating eddy. Applying the boundary conditions to (4.21) gives

$$v_e(r) = \left\{\frac{2(v_e)_{max}}{R_c}\right\} r \tag{4.22}$$

Substituting v_e from (4.22) into (4.20), the maximum recirculating flow inside the recirculating eddy is given by

$$(Q_e)_{max} \doteqdot 2\pi \int_0^{\frac{R_c}{2}} (v_e)_{max} \, r \, dr \quad ,$$

which upon integration gives

$$(Q_e)_{max} \doteqdot \frac{\pi R_c^2}{4} \cdot (v_e)_{max} \quad , \tag{4.23}$$

or

$$(v_e)_{max} \doteqdot \frac{4}{\pi R_c^2} (Q_e)_{max} \quad . \tag{4.24}$$

From (4.24) the recirculating eddy maximum velocity, which is equal to the velocity of the free surface of the induction trumpet, can be found once $(Q_e)_{max}$ is calculated from (4.17).

4.4.3 Calculation of entrained film volumetric flux

The velocity profile of the gas film entrained by the plunging jet is found by applying a momentum balance over a volume of fluid flowing between two coaxial cylinders both of which are moving. The inside cylinder is moving at the jet velocity v_j and the outer cylinder is moving at a velocity equal to the tangential velocity of the recirculating eddy $(v_e)_{max}$, which is given by (4.24).

An order of magnitude calculation shows the Reynolds number in the gaseous film is of order 100. Hence by assuming the flow is laminar and there is no radial velocity component, the velocity profile inside the film is given by Bird et al (1960) as

$$\frac{d}{dr}\left(r\tau_{rz}\right) = \left\{\frac{\Delta P}{L}\right\} r \quad, \tag{4.25}$$

where τ_{rz} is the axial component of the radial shear stress and ΔP is the change in pressure over a length L, which is given by

$$\frac{\Delta P}{L} = \rho_L g \quad. \tag{4.26}$$

Substituting (4.26) into (4.25), we have

$$\frac{d}{dr}\left(r\tau_{rz}\right) = \rho_L g r \quad, \tag{4.27}$$

which on integration yields

$$r\tau_{rz} = \frac{\rho_L g r^2}{2} + C_1 \tag{4.28}$$

where C_1 is the constant of integration. Its value can be found by applying Newton's Law of Viscosity to the gas film, i.e.

$$\tau_{rz} = -\mu_G \frac{dv_z}{dr} \quad, \tag{4.29}$$

where μ_G is the gas absolute viscosity and dv_z/dr is the gradient of axial velocity in the radial direction.

Combining (4.28) and (4.29) gives

$$(-\mu_G r)\frac{dv_z}{dr} = \frac{\rho_L g r^2}{2} + c_1 .$$

(4.30)

When (4.30) is integrated the axial velocity as a function of radial position is obtained, i.e.

$$v_z(r) = -\frac{1}{\mu_G}\left[\frac{\rho_L g r^2}{4} + c_1 \ln r + c_2\right]_{BC(ii)}^{BC(i)} .$$

(4.31)

The constants of integration c_1 and c_2 can be found by applying the following boundary conditions to (4.31):-

(i) $v_z(r) = v_j$ (at $r = R_j$) ;

(ii) $v_z(r) = (v_e)_{max}$ (at $r = X R_j$) ,

in which

$$X = \frac{R_j + T_c}{R_j} ,$$

(4.32)

where T_c is the thickness of the gas film once it has obtained a constant thickness. The values for c_1 and c_2 are:-

$$c_1 = \frac{4\mu_G\left[v_j - (v_e)_{max}\right] + \rho_L g R_j^2(1-X^2)}{4\left\{\ln(X R_j) - \ln(R_j)\right\}} ;$$

$$c_2 = -\mu_G v_j - \frac{\rho_L g R_j^2}{4} - c_1 \ln(R_j) .$$

The volumetric flowrate inside the gas film is found by integrating the velocity profile across the film thickness, i.e.

$$(Q_G)_F = \int_0^{2\pi} \int_{R_j}^{XR_j} v_z(r) \, dr \, d\theta \quad , \tag{4.33}$$

where v_z is given by (4.31). When the expression for v_z is substituted into (4.33) then

$$(Q_G)_F = \left(\frac{-2\pi}{\mu_G}\right) \cdot \int_{R_j}^{XR_j} \left\{ \frac{\rho_L g r^2}{4} + C_1 \ln(r) + C_2 \right\} r \, dr \quad . \tag{4.34}$$

Integrating (4.34) gives

$$(Q_G)_F = \frac{-2\pi}{\mu_G} \left[\frac{\rho_L g r^4}{16} + C_1 \left\{ \frac{r^2}{2} \ln(r) - \frac{r^2}{4} \right\} + C_2 \frac{r^2}{2} \right]_{R_j}^{XR_j} \quad ,$$

and finally

$$(Q_G)_F = -\frac{2\pi R_j^2}{\mu_G} \left\{ \frac{\rho_L g R_j^2}{16}(X^4 - 1) + \frac{C_1}{2} \left[X^2 \ln(XR_j) - \ln(R_j) \right] \right. $$

$$\left. + \left[\frac{C_2}{2} - \frac{C_1}{4} \right] (X^2 - 1) \right\} \tag{4.35}$$

Equation (4.35) represents the volumetric rate of gas which is entrained as a gas film adjacent to the free surface of the jet at the point of impact with the receiving liquid. The entrainment rate can be calculated from (4.35) only if the film thickness and velocities of the jet and the receiving liquid surface at the point of impact are known. The jet velocity is easily determined from the volumetric liquid flowrate and a knowledge of the effective jet diameter at the point of impact. The receiving liquid surface velocity $(v_e)_{max}$, is found from (4.24). Therefore, the only unknown variable in (4.35) is the thickness of the gas film.

Jet

Air

Region 3

Receiving
liquid

Region 2

Region 1

T_c
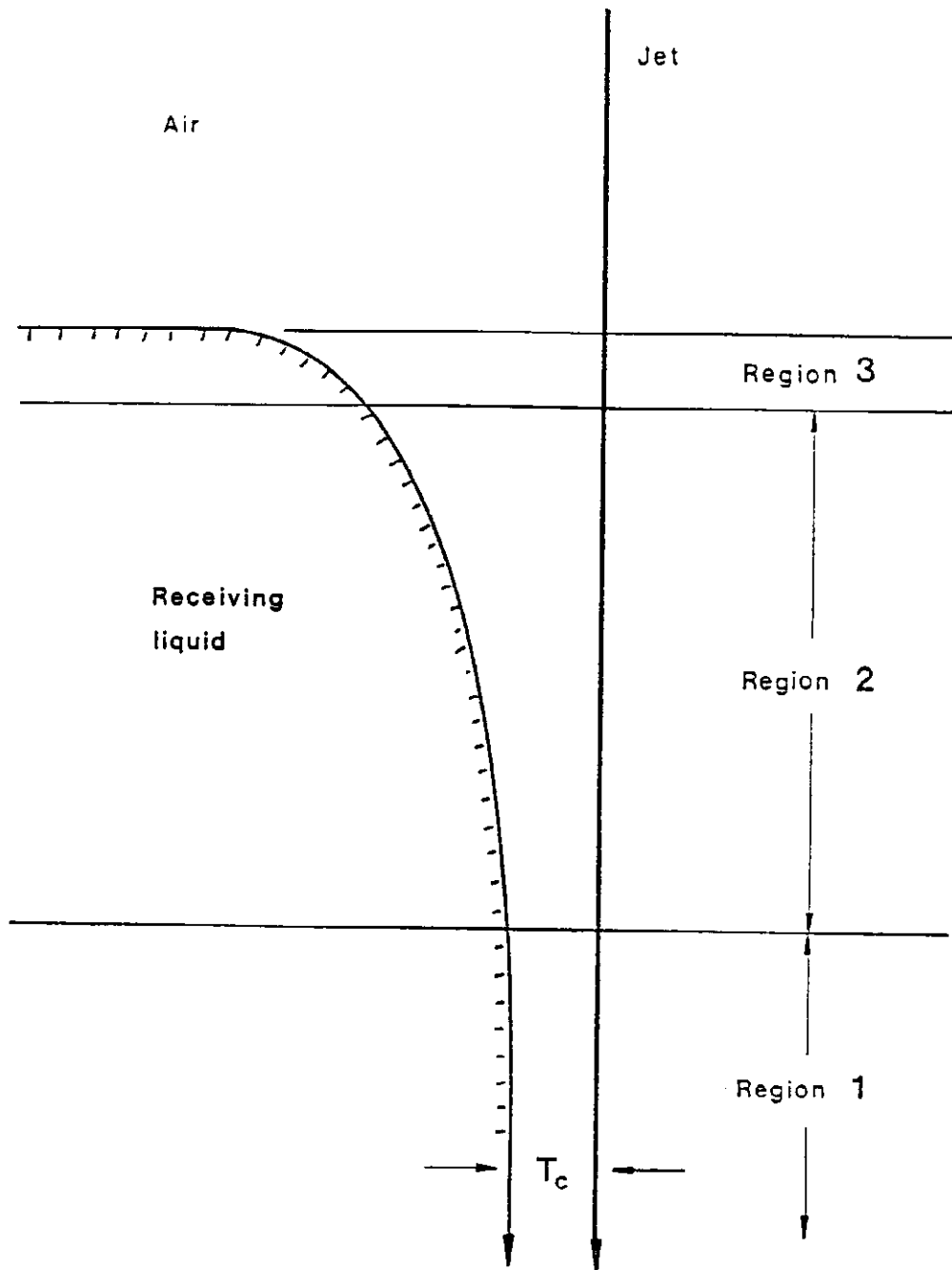
Figure 4.12   Induction trumpet profile

4.4.4 Prediction of the gas film thickness

The gas film thickness T_c can be predicted if the profile of the induction trumpet is known. The resultant profile of the induction trumpet, as illustrated in Figure 4.12, can be divided into three distinct regions. These regions are:-

Region 1 - is the region far from the surface of the receiving liquid where the film thickness becomes constant. Only the viscous and gravity forces influence the film thickness in this region.

Region 2 - is the dynamic meniscus region where the film thickness varies with height due to the influence of the viscous, gravity and interfacial forces.

Region 3 - is the region close to the surface of the receiving liquid where the liquid profile is influenced only by the interfacial forces.

If the gas flow inside the induction trumpet is in slow steady-state motion, the simplified form of the Navier-Stokes equation for thin-film flow is given by Levich (1962) as

$$\left(\frac{\sigma}{\rho_L}\right)\frac{d^3 T}{dz^3} + \left(\frac{\mu_L}{\rho_L}\right)\frac{\partial^2 U_z}{\partial L^2} + g = 0 \; , \qquad (4.36)$$

where T is the film thickness at a vertical depth of z from the receiving liquid surface. Equation (4.36) applies to all regions within the film, and Spiers et al (1974) have solved (4.36) for the film of liquid which adheres to a wire while it is being withdrawn vertically from a bath of liquid. For this case, their solution to (4.36) for the constant thickness region of the adhered film is

$$T^* = \frac{3^{1.5}}{2^{1/2}} f(Ca, T^*) \left\{ 1 - (T^*)^2 \right\}^{2/3} Ca^{1/6} \; , \qquad (4.37)$$

where $f(Ca, T^*)$ is a function and is found by numerical integration.

In (4.37) T^* is the dimensionless film thickness and is given by

$$T^* = T_c \left\{ \frac{\rho_L g}{\mu_L \upsilon_w} \right\}^{1/2} ,$$ (4.38)

where T_c is the constant film thickness and υ_w is the withdrawal velocity of the wire. The Capillary number Ca in (4.37) is given by

$$Ca = \frac{\mu_L \upsilon_w}{6} .$$ (4.39)

Even though equations (4.37) - (4.39) have been derived for the withdrawing wire case, it may be possible to apply them directly to the constant film thickness region of the induction trumpet by direct substitution of the buoyancy force in place of the gravity component in (4.36). If the velocity of the free surface of the induction trumpet is used instead of υ_w then (4.38) and (4.39) become

$$T^* = T_c \left\{ \frac{\rho_L g}{\mu_L (\upsilon_e)_{max}} \right\}^{1/2} ,$$ (4.40)

and

$$(Ca)_{trumpet} = \frac{\mu_L (\upsilon_e)_{max}}{6}$$ (4.41)

Equations (4.40) and (4.41) have been derived assuming the liquid is continuous. However, if gas bubbles are present near the induction trumpet surface then this assumption is no longer valid and the mixture viscosity would be higher than μ_L. To overcome this departure from the ideal case the mixture viscosity μ_m has been used in (4.40) and (4.41). Note also that (4.37) applies only to the constant film thickness region. If the film is ruptured prior to attaining this condition, the film thickness will always be greater than T_c as indicated in Figure 4.12.

4.5 EXPERIMENTAL DESCRIPTION

The apparatus used to determine the gas entrainment rate for a plunging jet system is shown in Figure 3.2. and the range of variables studied is summarised in Table 3.1.

The experimental procedure involved selecting a gas flowrate into the top of the column for a given set of jet operating conditions. Once the column had reached equilibrium operation the free jet length was measured in accordance with Section 3.4.2. This procedure was repeated for a number of different gas flowrates for the same jet system in order to produce a profile of the gas entrainment rate as a function of the free jet length. In addition, the jet diameter was measured as a function of free jet length for the liquid jets used in the entrainment studies.

4.6 RESULTS AND DISCUSSION

A summary of the conditions for each of the experimental runs is contained in Appendix 1. The experimental values for the gas entrainment rate and free jet length are also contained in Appendix 1. In Appendix 2 the jet expansion measurements are reported as a function of free jet length.

4.6.1 Effect of free jet length on the gas entrainment rate

The normalised entrainment rate Q_G/Q_L is plotted against the normalised jet length L_j/D_N in Figure 4.13. The shape of the curve is typical for all experimental runs carried out in this study where it can be seen that the rate of increase in Q_G/Q_L is linear for the region close to the nozzle. Beyond this region the rate of increase of Q_G/Q_L gradually becomes less until an almost constant value is obtained.
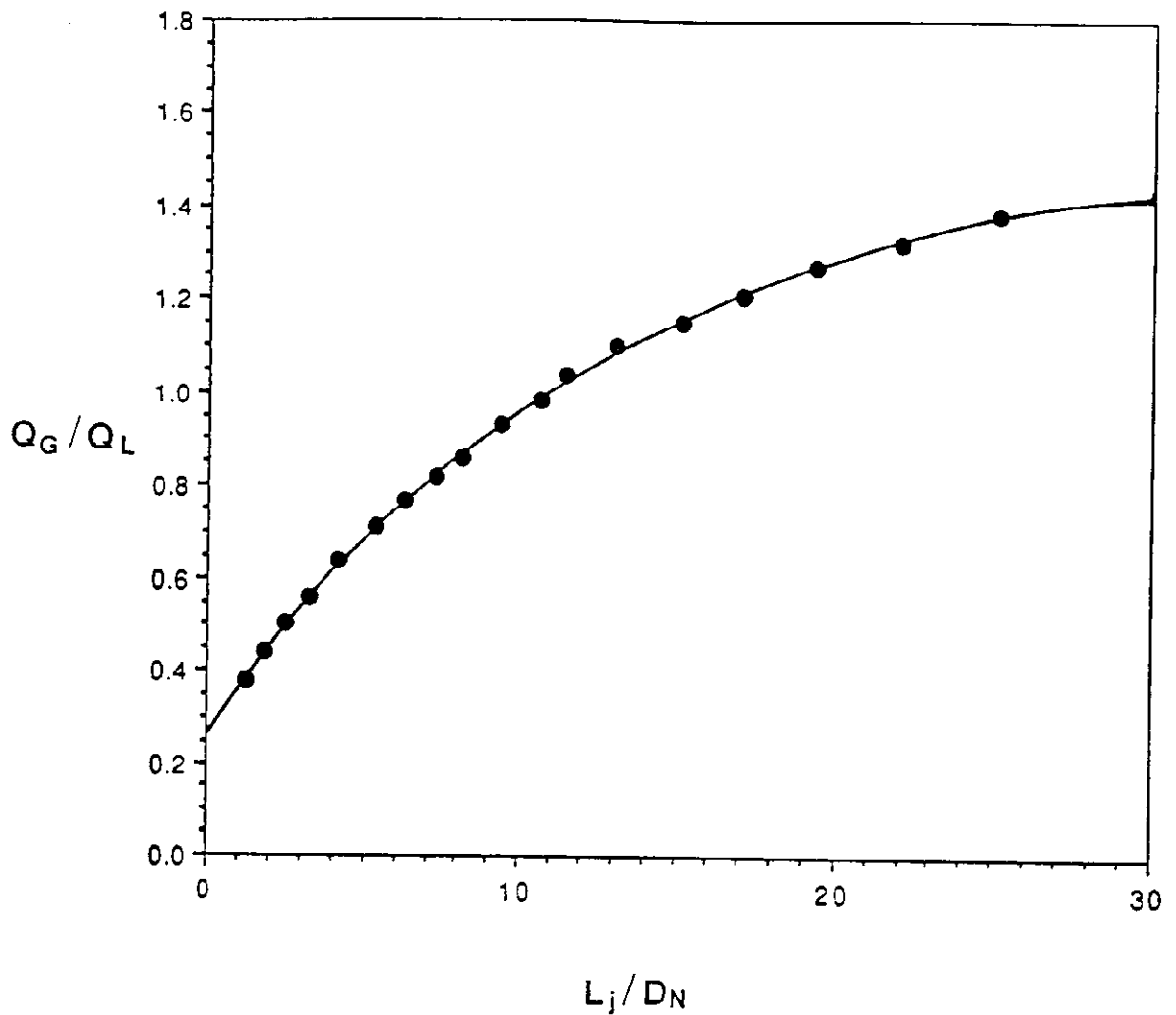
Figure 4.13 Normalised entrainment rate vs normalised jet length
(Run 1: D_c = 44 mm; D_j = 7.12 mm; υ_j = 15 m/s;
ρ_L = 1000 kg/m³; μ_L = 0.0009 Pa-s; G = 0.048 N/m)

Although Figure 4.13 illustrates the relationship which is characteristic
of the entrainment process taking place, it does not provide any insight
as to why the entrainment rate changes with changing jet length. The
variable directly controlling the entrainment rate is the effective jet
diameter $(D_j)_z$, which is a function of the free jet length, as shown in
Figure 4.14.
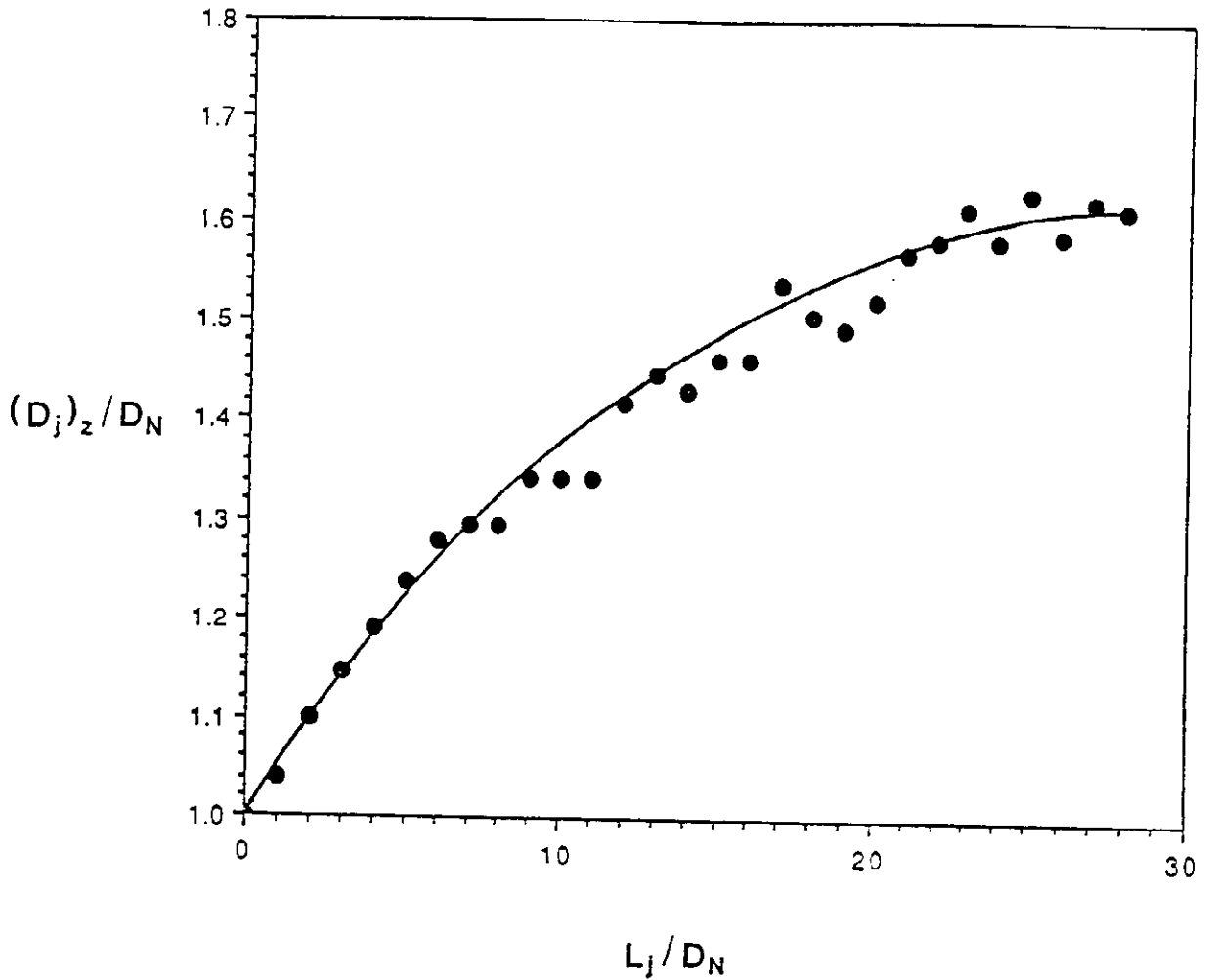
Figure 4.14   Normalised jet diameter vs normalised jet length
(Run 1: D_c = 44 mm; D_j = 7.12 mm; v_j = 15 m/s;
ρ_L = 1000 kg/m³; μ_L = 0.0009 Pa-s; σ = 0.048 N/m)

In Figure 4.14 the normalised jet diameter $(D_j)_z/D_N$ has been plotted against the normalised jet length L_j/D_N. It can be seen from the graph that for values of L_j/D_N below 5 the expansion in jet diameter with increasing distance from the nozzle is linear. For L_j/D_N above 5 the rate at which the jet diameter expands decreases with increasing jet length until a normalised length approximately equal to 25 is reached. Beyond this length $(D_j)_z/D_N$ becomes constant.

4.6.2 Effect of jet expansion on the gas entrainment rate

The effect of jet expansion on the gas entrainment rate is found by combining Figures 4.13 and 4.14 such that the normalised entrainment rate is plotted against the jet expansion, as given in Figure 4.15. It can be seen from the graph that for $(D_j')_z / D_N$ values less than 1.58, the gas entrainment rate is a linear function of the jet expansion. However, it can be seen from the graph that while $(D_j')_z / D_N$ remains constant at a value of 1.58 (L_j / D_N = 25) the entrainment rate continues to increase, even though effective jet diameter has not increased.
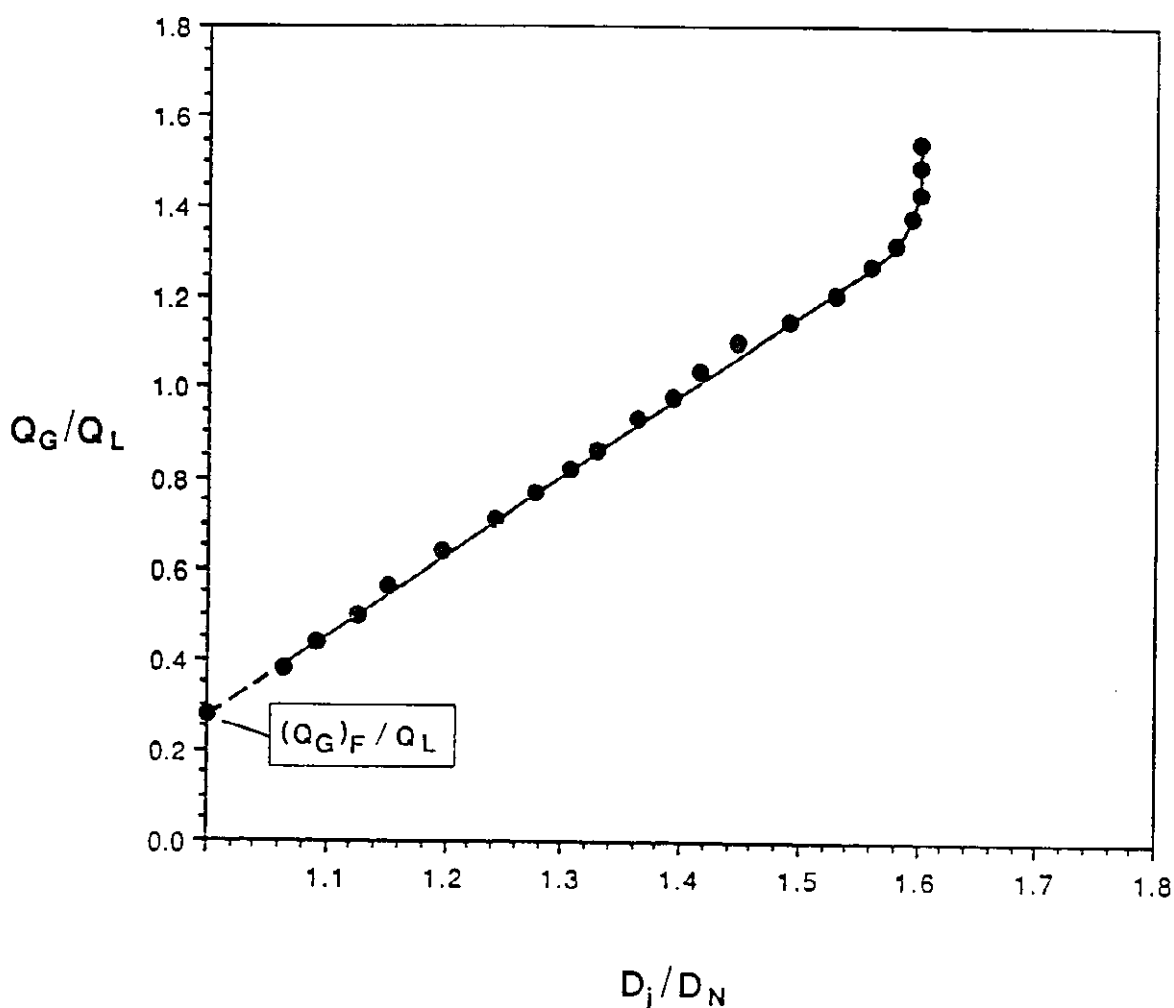
Figure 4.15 Normalised entrainment rate vs normalised jet diameter
(Run 1: D_c = 44 mm; D_j = 7.12 mm; v_j = 15 m/s;
ρ_L = 1000 kg/m³; μ_L = 0.0009 Pa-s; σ = 0.048 N/m)

If the entrainment rate consisted only of the quantity of gas captured within the boundary of the measured jet diameter at a given jet length, then Q_G/Q_L should remain constant once a constant value of $(D_j)_z/D_N$ is reached. The observation from Figure 4.15 that the normalised entrainment rate increases even after the jet diameter has ceased to expand, suggests the entrainment rate cannot be quantified solely by the amount of gas trapped within the irregularities on the free surface of the jet.

The additional entrainment component was thought to be attributed to the gas in the film adjacent to the surface of the jet at the point of impact with the receiving liquid.

4.6.3 Determination of gas film entrainment rate

The quantity of gas contained in the thin film $(Q_G)_F$ entrained by the jet as it plunges into the receiving liquid, can be directly determined from Figure 4.15. The entrainment curve can be extrapolated to the point where the jet expansion is zero, i.e. $(D_j)_z/D_N$ is equal to unity. At this point the jet must be a solid stream of liquid with no gas trapped within its boundary. The measured rate of entrainment therefore can be due only to the gas contained within the entrained film.

It is necessary, however, to comment on the use of the condition of zero jet expansion to determine the gas film component of the entrainment rate. From Figure 4.14, zero jet expansion occurs only at the tip of the nozzle. At this point the gas boundary layer has had no time to develop and its thickness must therefore be equal to zero. Subsequently, there would be no moving gas stream to occupy the entrained gas film, and hence the gas film entrainment rate would also be equal to zero.

The experimental observations represented in Figure 4.15, however, do indicate a non-zero film entrainment component even though the gas boundary layer adjacent to the jet free surface has had no time to develop. The reason for this was thought to be due to reported jet length values being measured from the tip of the nozzle to the interface between the low and high density froth zones at the top of the column.

The point where the actual mechanism of entrainment takes place is possibly a short distance below this interface. However, there is still sufficient time to allow the formation of a gas boundary layer adjacent to the free surface of the jet without any observable increase in the jet diameter. This would explain why a non-zero gas film component of the entrainment rate is obtained when the experimental total entrainment curve is extrapolated to the point of zero jet expansion.

4.6.4 Effect of jet Weber number on the gas film component of the entrainment rate

In Figure 4.16 the normalised film entrainment component $(Q_G)_F/Q_L$ has been plotted against the jet Weber number We_j. It can be seen from the graph that for $We_j < 10000$ the normalised gas film entrainment rate and We_j appear to be linearly related as shown by the solid line. This result can be written as

$$\frac{(Q_G)_F}{Q_L} \propto We_j \quad . \tag{4.42}$$

If the jet velocity and diameter are constant then (4.42) becomes

$$\frac{(Q_G)_F}{Q_L} \propto \frac{\rho_L}{\sigma} \quad . \tag{4.43}$$

From (4.43) it can be seen that the gas film entrainment rate is directly proportional to the liquid density and and inversely proportional to the liquid surface tension.
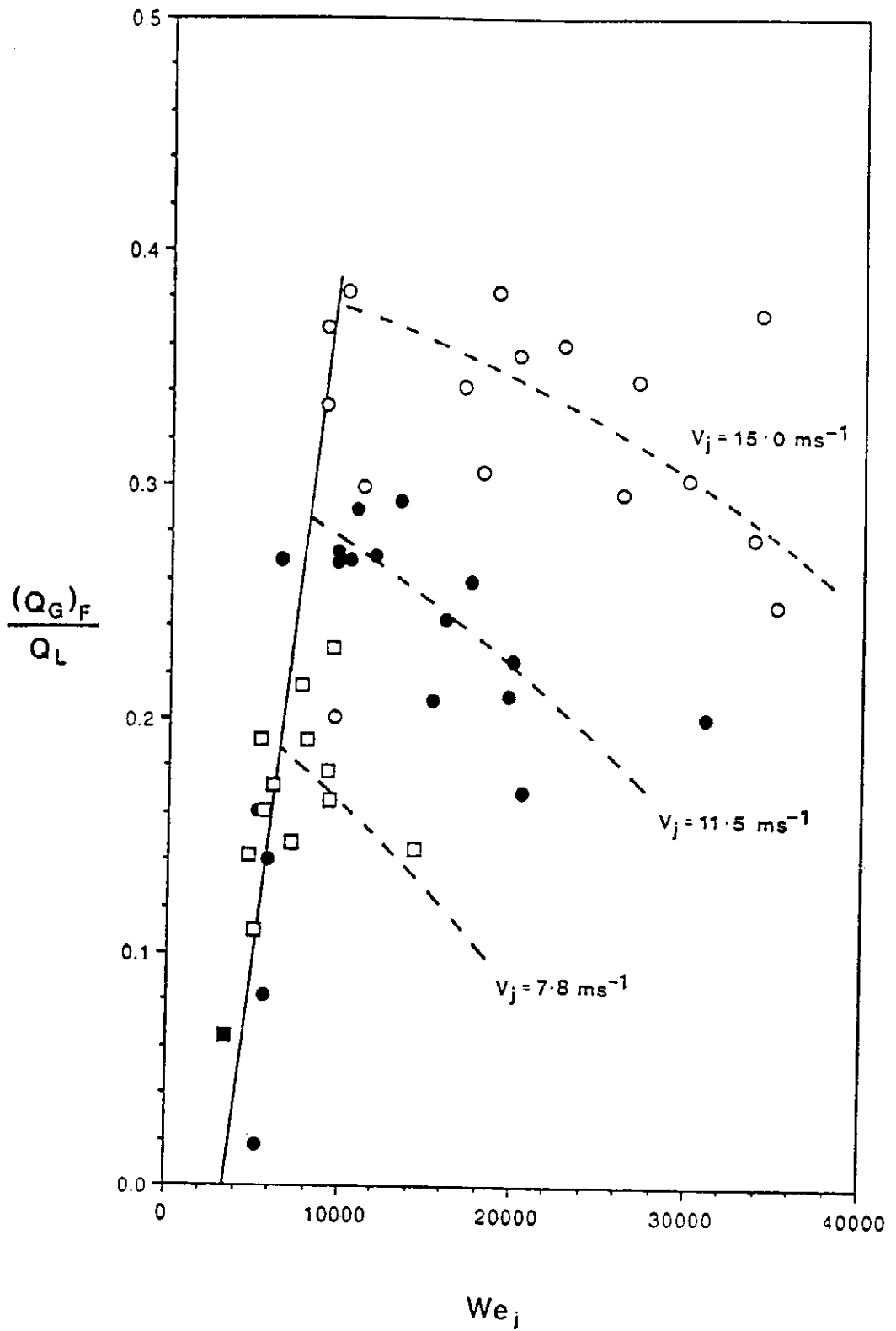
Figure 4.16 Normalised gas film entrainment rate vs jet Weber
number for 44 mm diameter column (V_j = 5.13 (■);
7.8 (□); 11.5 (●); and 15 (○) m/s)
[See Appendix 5 for calculations]

It also can be seen from the dotted curves given in Figure 4.16 that, for a given jet velocity, $(Q_G)_F/Q_L$ passes through a maximum when plotted against increasing We_j. This experimental observation is not in agreement with (4.42). One possible explanation can be found by considering the induction trumpet in the receiving liquid. The opening of the induction trumpet can act as a throttling valve regulating the flow of the gas boundary layer into the gas film which is ultimately entrained below the receiving liquid surface. When the opening is wide, more gas will enter the film than when the opening is narrow.

The size of the opening of the induction is determined by the balance between the interfacial and buoyancy forces acting on the free surface of the receiving liquid. The radius of curvature of the induction trumpet profile decreases with increasing interfacial force resulting in a narrowing of the opening. Subsequently, the rate of entrainment decreases with increasing interfacial force, i.e. decreasing values of liquid surface tension.

The interfacial force is opposed by the buoyancy force of the displaced liquid which resists the formation of the induction trumpet. The buoyancy force is proportional to the liquid density, where the size of the induction trumpet opening decreases with increasing liquid density Subsequently, the rate of entrainment decreases with increasing liquid density. The relationship between the gas film entrainment rate and the density and surface tension of the receiving liquid is therefore

$$\frac{(Q_G)_F}{Q_L} \propto \frac{6}{\rho_L} .$$

(4.44)

By comparing (4.44) with (4.43) it can be seen that a maximum in the normalised entrainment rate will exist when it is plotted against jet Weber number. If We_j is increased by varying 6 and ρ_L only, then $(Q_G)_F$ will increase according to (4.43). However, when the entrainment process is controlled by the forces acting within the receiving liquid the entrainment rate will decrease with increasing We_j according to (4.44). The value of We_j at which the maximum in the entrainment rate occurs is a function of the inertial force of the jet, or more specifically the jet velocity, as indicated by the dotted curves given in Figure 4.16.
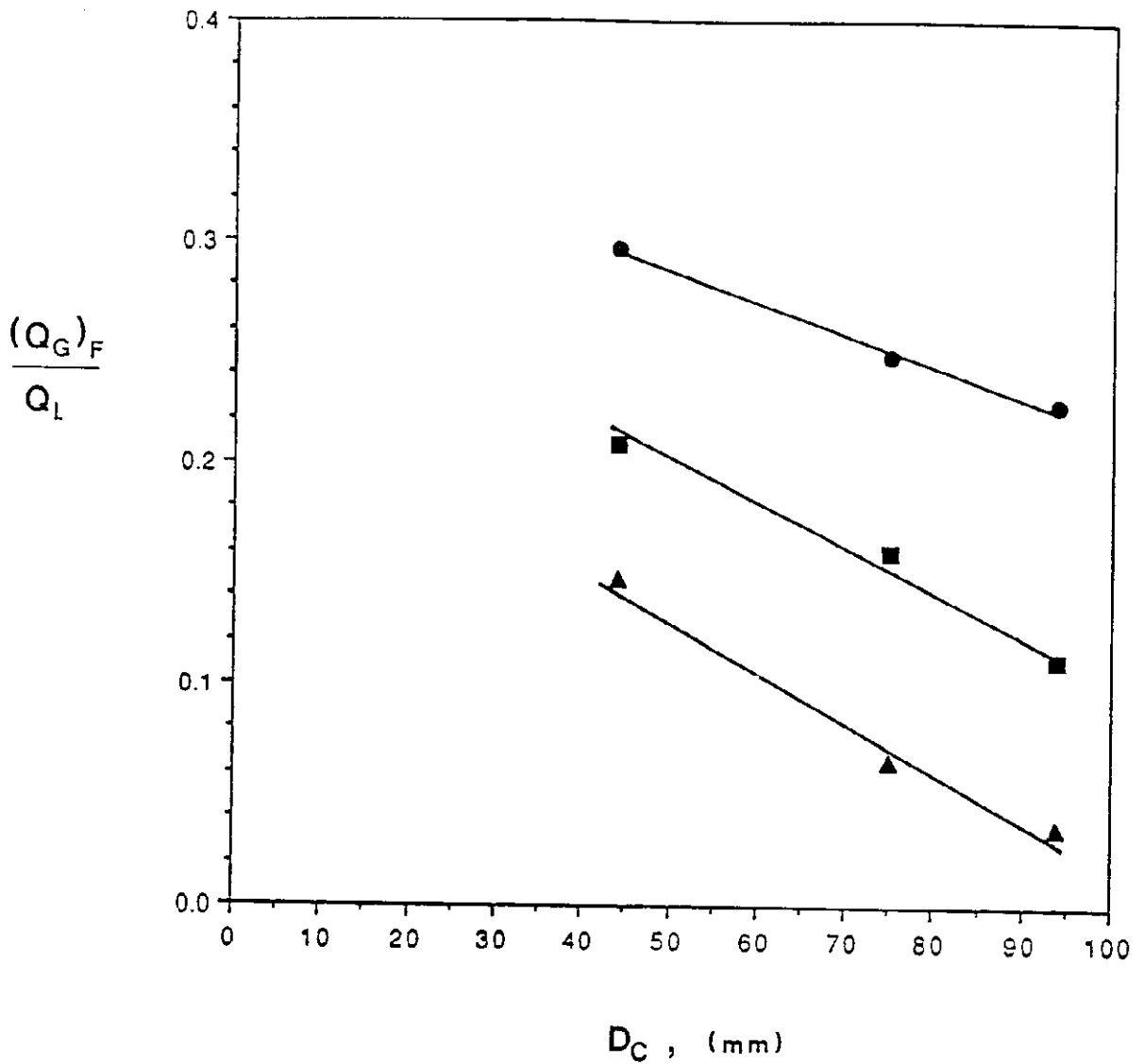
Figure 4.17 Normalised gas film entrainment vs column diameter
for jet velocity values of 7.8 (▲), 11.5 (■), and
15.0 (●) m/s (ρ_L = 1000 kg/m³; μ_L = 0.0009 Pa-s;
σ = 0.062 N/m; D_j = 7.12 mm)

4.6.5 Effect of column diameter on gas film entrainment

The effect of column diameter on the gas film entrainment rate was
examined for a range of jet conditions. Firstly, the jet diameter was
held constant and the normalised gas film entrainment rate was measured

as a function of column diameter for jet velocity values of 7.8, 11.5 and 15 m/s. The results are given in Figure 4.17, where it can be seen that $(Q_G)_F/Q_L$ decreases with increasing D_c for all three jet velocities. Also, it can be seen that $(Q_G)_F/Q_L$ increases with increasing V_j for a fixed column diameter.
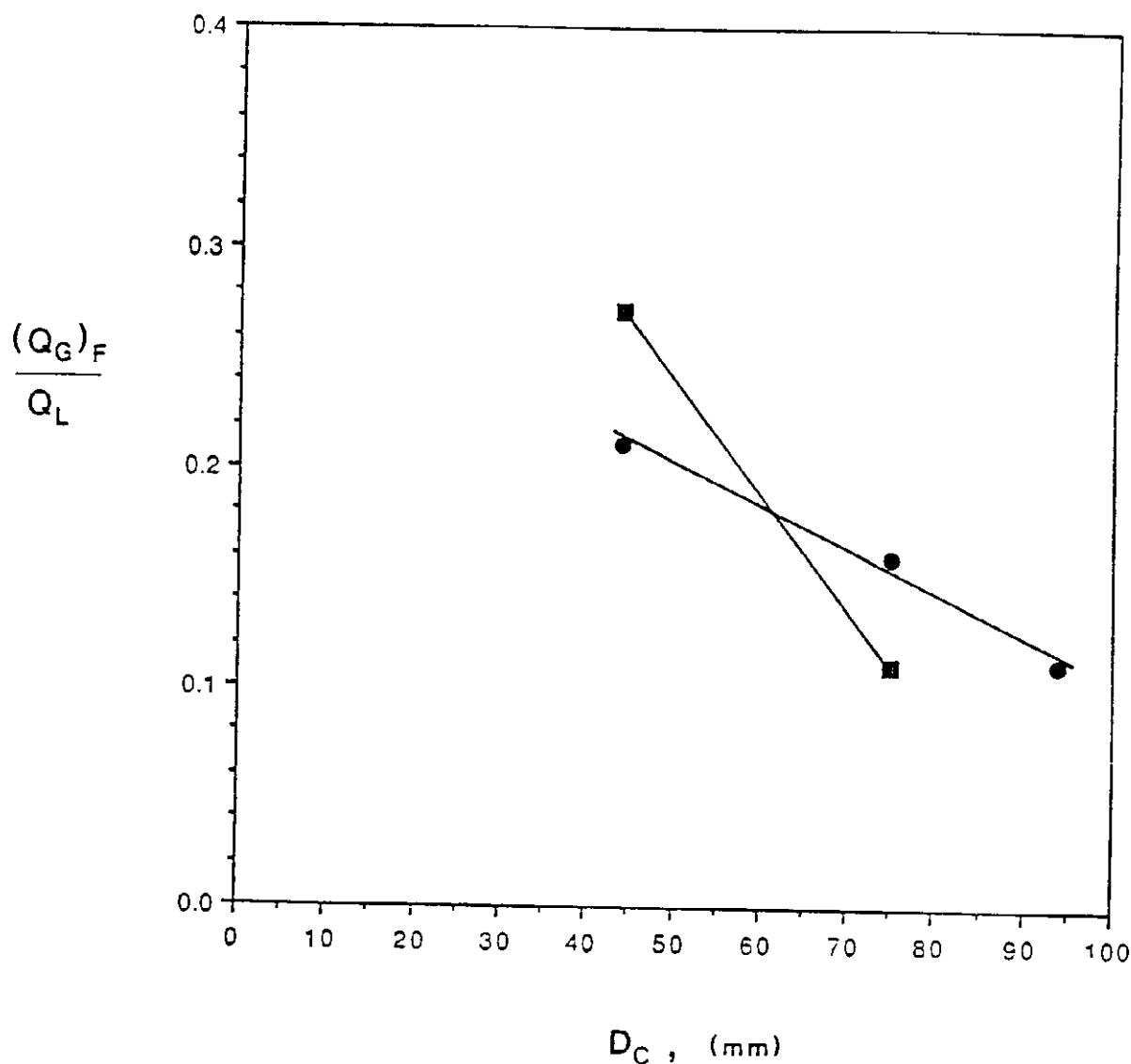
Figure 4.18   Normalised gas film entrainment vs column diameter for jet diameter values of 4.76 (■) and 7.12 (●) mm (Q_L = 1000 kg/m³; μ_L = 0.0009 Pa-s; G = 0.063 N/m; V_j = 11.5 m/s)

Secondly, the jet velocity was held constant and the normalised gas film entrainment rate was measured as a function of column diameter for jet diameter values of 4.76 and 7.12 mm. The results are plotted in Figure 4.18 where it can be seen that $(Q_G)_F/Q_L$ decreases with increasing D_C for both jet diameters.
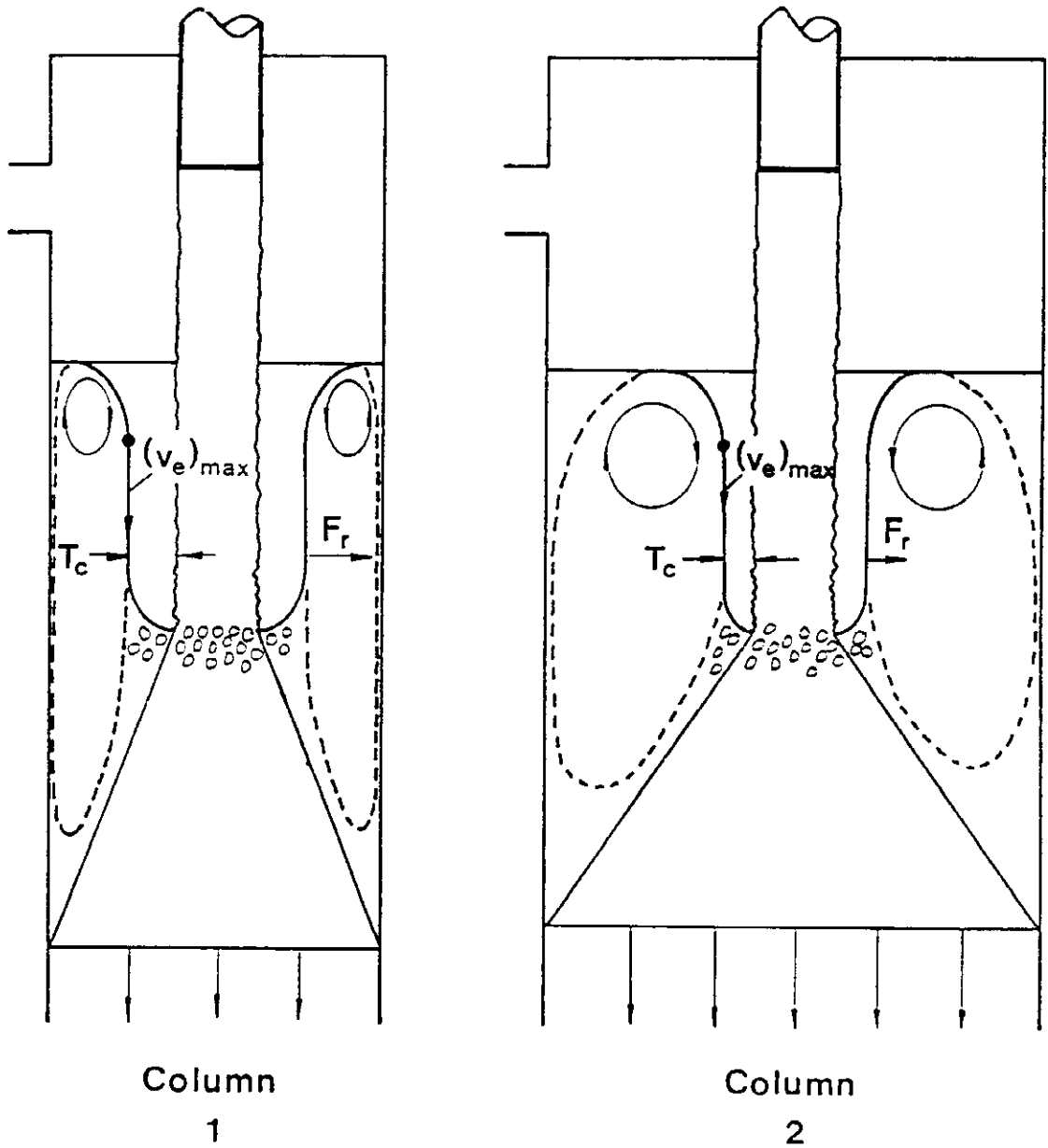
Column
1

Column
2

Figure 4.19 Schematic depicting effect of column diameter on
film thickness (constant jet diameter and velocity)

The results shown in both Figures 4.17 and 4.18 indicate that the column diameter does affect the gas film entrainment rate. Visual observation suggests that decreasing the column diameter increases the thickness of the entrained gas film. A possible explanation for this phenomenon is illustrated in Figure 4.19, which depicts the same jet plunging into two columns of differing diameters.

It is suggested in Figure 4.19 that the plunging jet generates a recirculating eddy inside the column whose volumetric flowrate is found when (4.19) is substituted into (4.17), i.e.

$$\frac{(Q_e)_{max}}{Q_L} = \frac{0 \cdot 37 \left\{ R_c^2 - \frac{1}{2} R_j^2 \right\}^{1/2}}{R_j} - 0 \cdot 64 \ . \tag{4.45}$$

In Figure 4.19 it can be seen that the gas film thickness T_c appears to be proportional to the magnitude[11] of the radial force F_r produced by the liquid recirculation inside the column, i.e.

$$T_c \propto F_r \ . \tag{4.46}$$

If the magnitude of F_r is related to the recirculating eddy maximum velocity $(v_e)_{max}$, such that F_r increases with increasing $(v_e)_{max}$, then

$$F_r \propto (v_e)_{max} \ . \tag{4.47}$$

The relationship between $(v_e)_{max}$ and the maximum volumetric liquid recirculating flowrate $(Q_e)_{max}$ is given by (4.24), from which

$$(v_e)_{max} \propto \frac{(Q_e)_{max}}{R_c^2} \ . \tag{4.48}$$

---

[11] the relative magnitudes of the radial force and the recirculating eddy maximum velocity are indicated by the length of the arrows in Figure 4.19

The maximum volumetric liquid recirculating flowrate can be calculated from (4.45) which can be simplified by assuming Q_L and R_j are constant as illustrated in Figure 4.19, and that for $R_c \gg R_j$ then

$$\left\{ R_c^2 - \frac{1}{2} R_j^2 \right\}^{1/2} \doteqdot R_c \, . \tag{4.49}$$

Therefore, from (4.49) we have

$$\left(Q_e \right)_{max} \propto R_c \, . \tag{4.50}$$

Finally, from (4.46) - (4.48) and (4.50), the relationship between T_c and R_c is given by

$$T_c \propto \frac{1}{R_c} \tag{4.51}$$

It is indicated by (4.51) that the gas film thickness, and hence the gas film entrainment rate, is inversely proportional to the column diameter. This result is consistent with the experimental observations given in Figure 4.17 and 4.18. Therefore it is suggested the column diameter influences the gas film entrainment rate by determining the magnitude of the recirculating eddy velocity, which ultimately controls the gas film thickness.

4.6.6 Effect of recirculating eddy velocity on the gas film thickness

The gas film thickness T_c was calculated from (4.35) using the experimental gas film entrainment values given in Appendix 5, and in Figure 4.20 T_c has been plotted against the recirculating eddy maximum velocity $(v_e)_{max}$.
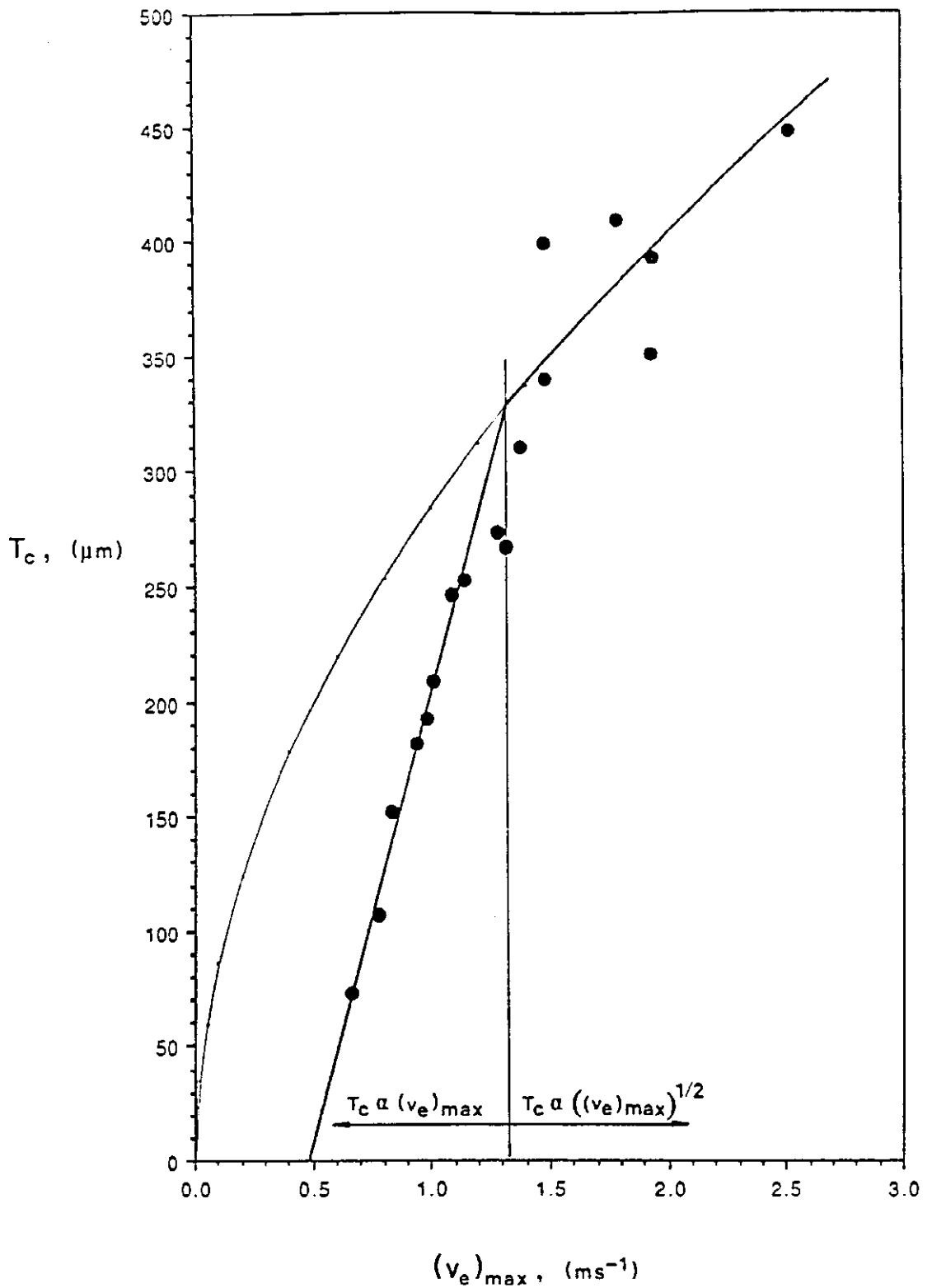
Figure 4.20   Gas film thickness vs recirculating eddy maximum velocity
(ρ_L = 1000 kg/m³ ; μ_L = 0.0009 Pa-s; $\mathfrak{S}$ = 0.063 N/m)
[see Appendix 5 for calculations]

It can be seen from Figure 4.20 that the curve is a straight line for values of $(v_e)_{max}$ less than approximately 1.1 m/s. For $(v_e)_{max}$ greater than 1.1 m/s the relationship is not linear.

A possible reason for the linear portion of the graph can be found by applying dimensional analysis to the forces which are controlling the film thickness, namely the viscous and interfacial forces. Dimensional analysis using only these two forces gives

$$T_c \propto \left\{ \frac{\sigma}{\mu_G g} \right\} (v_e)_{max} \quad . \tag{4.52}$$

Equation (4.52) implies that T_c is directly proportional to $(v_e)_{max}$ in the regime where viscous and interfacial forces dominate. From Figure 4.20 it appears this regime occurs when $(v_e)_{max} < 1.1$ m/s where a straight line (solid line) has been fitted through the data points.

The change in the shape of the curve in Figure 4.20 for recirculating velocities above 1.1 m/s is possibly because in this region the interfacial force becomes negligible and the inertial force controls the film thickness. A dimensional analysis considering only the viscous and inertial forces leads to a square-root relationship between the film thickness and maximum recirculating velocity, i.e.

$$T_c \propto \left\{ \frac{\mu_G}{\rho_L g} \right\}^{1/2} \left\{ (v_e)_{max} \right\}^{1/2} . \tag{4.53}$$

A square root relationship according to (4.53) has been applied to the data points in Figure 4.20 for $(v_e)_{max} > 1.1$ m/s. It can be seen from the graph that the resultant curve (dashed line) fits the data values reasonably well. Also, the curve can be extrapolated to a zero film thickness when $(v_e)_{max}$ is zero.

From the results shown in Figure 4.20 it is possible to conclude, therefore, that the relationship between the maximum recirculating eddy velocity and the gas film thickness, and hence the gas film entrainment rate, can be separated into two distinct regimes, namely one in which

viscous and interfacial forces dominate, and one in which viscous and inertial forces dominate. From the experimental data the transition between the two regimes occurs when $(v_e)_{max}$ is approximately equal to a value of 1.1 m/s for the water-teric 407 ($G = 62$ mN/m) system.

4.6.7 Comparison of experimental and predicted gas film thickness values

In Figure 4.21 the experimentally determined dimensionless film thickness T_c^* has been plotted against the logarithm of the induction trumpet capillary number, where both the dimensionless film thickness and the capillary number have been calculated using the mixture viscosity given by (6.33). It can be seen from the graph that the data points lie on curves of constant kinematic viscosity, and for low values of v_L the experimental values for T_c^* tend to be greater than those predicted by (4.40). It can also be seen there is closer agreement between the experimental results and the theoretical curve as the liquid kinematic viscosity is increased.

One possible reason for the results shown in Figure 4.21 is that for small values of $(Ca)_{trumpet}$, corresponding to low values of absolute viscosity, disturbances generated on the free surface of the induction trumpet are amplified and rupture the gas film prior to the formation of the constant film thickness region. Consequently, the measured values for T_c^* are greater than those predicted by (4.40) for the constant film thickness region. As $(Ca)_{trumpet}$ increases due to an increase in μ_L the disturbances are attenuated by the viscous forces and formation of the constant film thickness region is achieved, resulting in closer agreement between the measured and theoretical values for T_c^*.

It can be concluded from the results shown in Figure 4.21 that the stability of the induction trumpet surface is an important factor in determining the quantity of gas film which is entrained by the jet. Furthermore, under conditions of high liquid viscosity, thin film theory may be used to obtain an estimate of the gas film thickness.
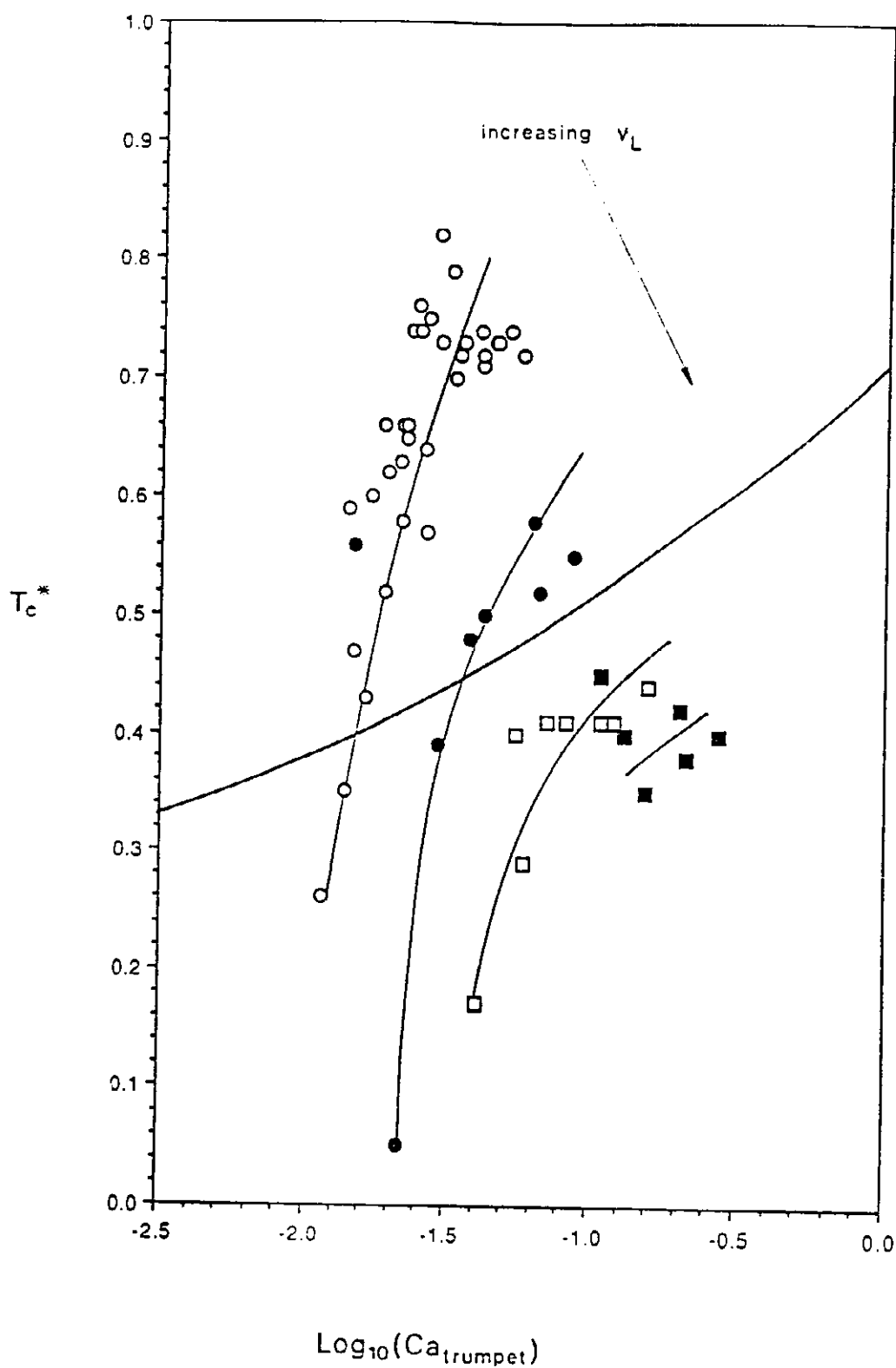
Figure 4.21   Dimensionless film thickness plotted against induction
              trumpet capillary number (ν_L = 9.7 x 10^{-7} (O);
              1.6 x 10^{-6} (●); 2.6 x 10^{-6} (□); 2.7 x 10^{-6} (■) m^2/s)
              [see Appendix 5 for calculations]

4.6.8 Prediction of the initiation of gas film entrainment

It was shown in Figure 4.20 that for the air-water system the data points for the viscous/interfacial force regime ($(v_e)_{max} < 1.1$ m/s) can be extrapolated to a zero film thickness when the recirculating liquid maximum velocity is approximately equal to 0.42 m/s. It seems reasonable, therefore, to interpret this value as the minimum maximum recirculating liquid velocity necessary before the initiation of entrainment of a gas film takes place.

It is not possible to compare the value of 0.42 m/s for $(v_e)_{max}$ obtained from this study with the results from Sheridan (1966) and McCarthy (1972) for air-water systems. Firstly, neither Sheridan nor McCarthy considered the significance of the recirculating eddy velocity on the initiation of entrainment. Secondly, for all three studies the surface roughness of the free jets was different, which would have a major influence on the mechanism initiating entrainment. For rough jets, such as those used in this study and by Sheridan (1966), the instabilities generated and then amplified on the induction trumpet surface could have caused the gas film to collapse, resulting in entrainment taking place. Also, with rough jets entrainment can occur in the form of gas being trapped within the undulations on the free surface of the jet which is then carried below the receiving liquid surface.

The initiation mechanism is different for smooth jets, such as those used by McCarthy (1972), where the gas film is not ruptured by surface instabilities, and entrainment is initiated only when the viscous and interfacial forces are overcome by the inertia associated with the motion of the induction trumpet free surface.

The difference between the initiation mechanisms for rough and smooth jets is highlighted by the results of McCarthy (1972), and Sheridan (1966). McCarthy (1972) reported that for very smooth water jets plunging into a quiescent liquid, entrainment was initiated at a jet velocity of approximately 7 m/s. This value is much higher than the values reported by Sheridan (1966) for rough jets.

4.6.8 Prediction of the initiation of gas film entrainment

It was shown in Figure 4.20 that for the air-water system the data points for the viscous/interfacial force regime ($(v_e)_{max} < 1.1$ m/s) can be extrapolated to a zero film thickness when the recirculating liquid maximum velocity is approximately equal to 0.42 m/s. It seems reasonable, therefore, to interpret this value as the minimum maximum recirculating liquid velocity necessary before the initiation of entrainment of a gas film takes place.

It is not possible to compare the value of 0.42 m/s for $(v_e)_{max}$ obtained from this study with the results from Sheridan (1966) and McCarthy (1972) for air-water systems. Firstly, neither Sheridan nor McCarthy considered the significance of the recirculating eddy velocity on the initiation of entrainment. Secondly, for all three studies the surface roughness of the free jets was different, which would have a major influence on the mechanism initiating entrainment. For rough jets, such as those used in this study and by Sheridan (1966), the instabilities generated and then amplified on the induction trumpet surface could have caused the gas film to collapse, resulting in entrainment taking place. Also, with rough jets entrainment can occur in the form of gas being trapped within the undulations on the free surface of the jet which is then carried below the receiving liquid surface.

The initiation mechanism is different for smooth jets, such as those used by McCarthy (1972), where the gas film is not ruptured by surface instabilities, and entrainment is initiated only when the viscous and interfacial forces are overcome by the inertia associated with the motion of the induction trumpet free surface.

The difference between the initiation mechanisms for rough and smooth jets is highlighted by the results of McCarthy (1972), and Sheridan (1966). McCarthy (1972) reported that for very smooth water jets plunging into a quiescent liquid, entrainment was initiated at a jet velocity of approximately 7 m/s. This value is much higher than the values reported by Sheridan (1966) for rough jets.

For systems where the viscous force prevents the collapse of the induction trumpet by disturbances amplified on the free surface, the recirculating eddy velocity can be used to obtain a relationship between the jet and column diameter, and the initiation velocity. Consider the expression derived earlier in (4.24) relating $(v_e)_{max}$ to the recirculating eddy maximum volumetric flowrate:-

$$(v_e)_{max} = \frac{4}{\pi R_c^2} (Q_e)_{max} \quad ,$$

where $(Q_e)_{max}$ is given by (4.17), i.e.

$$(Q_e)_{max} = \left\{ \frac{0.37}{C_T} - 0.64 \right\} Q_L \quad .$$

The Crayer-Curtet number, C_T, for a jet issuing into a stationary coaxial stream is given by (4.19):-

$$C_T = \frac{R_j}{\left\{ R_c^2 - \frac{1}{2} R_j^2 \right\}^{1/2}} \quad .$$

Substituting the expressions for $(Q_e)_{max}$ and C_T into (4.24) gives

$$(v_e)_{max} = \frac{4Q_L}{\pi R_c^2} \left\{ \frac{0.37 \left[R_c^2 - \frac{1}{2} R_j^2 \right]^{1/2}}{R_j} - 0.64 \right\} \quad . \qquad (4.54)$$

If $Q_L = \pi R_j^2 v_j$, then (4.54) becomes

$$(v_e)_{max} = 4 v_j \left\{ \frac{R_j}{R_c} \right\}^2 \cdot \left\{ \frac{0.37 \left[R_c^2 - \frac{1}{2} R_j^2 \right]^{1/2}}{R_j} - 0.64 \right\} \quad . \qquad (4.55)$$

If it is assumed that gas film entrainment is initiated once a critical recirculating eddy maximum velocity $(v_e)_{crit}$ is reached then (4.55) can be rewritten as

$$(v_e)_{crit} = 4(v_j)_{init}\left\{\frac{R_j}{R_c}\right\}^2\left\{\frac{0.37\left[R_c^2 - \frac{1}{2}R_j^2\right]^{1/2} - 0.64}{R_j}\right\}, \quad (4.56)$$

where $(v_j)_{init}$ is a function only of the liquid physical properties. Equation (4.56) can be simplified by making the approximation that for $R_c \gg R_j$,

$$\left\{R_c^2 - \frac{1}{2}R_j^2\right\}^{1/2} \doteqdot R_c. \quad (4.57)$$

Equation (4.56) then becomes

$$(v_e)_{crit} \doteqdot 4(v_j)_{init}\left\{\frac{R_j}{R_c}\right\}\cdot\left[0.37\left\{\frac{R_c}{R_j}\right\} - 0.64\right]. \quad (4.58)$$

Finally, for systems where the column diameter is constant, (4.58) can be rearranged to give the relationship between the jet diameter and the critical jet velocity $(v_j)_{init}$ for which entrainment is initiated, i.e.

$$\frac{1}{(v_j)_{init}} \doteqdot k_3 R_j - k_4 R_j^2, \quad (4.59)$$

where

$$k_3 = \frac{4 \times 0.37}{R_c^2 (v_e)_{crit}} \quad (4.60)$$

and

$$k_4 = \frac{4 \times 0.64}{R_c^2 (v_e)_{crit}}. \quad (4.61)$$

The validity of (4.59) can be checked using the experimental results given by Lin (1963) for an air-95 wt% glycerol solution. Lin measured the jet velocity at which entrainment was first observed for a number of different radius jets. His results are listed in Table 4.1 which also includes values of $(v_j)_{init}$ that have been calculated from (4.59).

TABLE 4.1 Comparison of initiation jet velocities as a function of jet radius calculated from (4.59) with the experimental results reported by Lin (1963) for the glycerol-air system

Jet Radius (m)	Constants in (4.59)[1] K_3 (10^3 sm^{-2})	K_4 (10^6 sm^{-3})	Initiation Jet Velocity From (4.59)[2] (m/s)	Lin (1963) (m/s)
0.0003			4.12	
0.0005			2.56	
0.0007			1.90	
0.0010			1.41	1.40
0.0015	0.850	0.140	1.04	1.04
0.0020	0.870	0.160	0.88	0.91
0.0025	0.863	0.153	0.80	0.83
0.0030	0.853	0.143	0.78	0.79
0.0035	0.845	0.135	0.80	0.77
0.0047	0.826	0.116	1.13	0.75
Average	0.851	0.141		
St. dev.	(0.015)	(0.015)		

[1] K_3 and K_4 values have been calculated by solving (4.59) simultaneously using the data values given by Lin (1963). The data point (R_j = 0.001 m, $(v_j)_{init}$ = 1.40 m/s) was used in conjunction with the appropriate data point to calculate the individual values for K_3 and K_4.

[2] The velocity values were calculated using the average values for K_3 and K_4.

It can be seen from the results given in Table 4.1 that K_3 and K_4 are approximately constant over the experimental range which is in accordance with (4.60) and (4.61), assuming that $(\upsilon_e)_{crit}$ and R_c are constant for the system. Therefore, the experimental results given by Lin (1963) should follow the relationship

$$\frac{1}{(\upsilon_j)_{init}} = (0.851 \times 10^3) R_j - (0.141 \times 10^6) R_j^2 \ , \qquad (4.62)$$

and in Figure 4.22 a comparison is made between the measured critical jet velocity and the prediction given by (4.62). It can be seen from the graph that the curve closely follows the experimental results for $R_j < 3.0$ mm. For larger values of R_j the curve deviates from the data points which is possibly because the assumption $\left\{ R_c^2 - \frac{1}{2} R_j^2 \right\}^{1/2} \doteq R_c$ no longer applies for $R_j > 3.0$ mm.

The values of K_3 and K_4 given in (4.62) could have been calculated directly from (4.60) and (4.61) respectively if the critical recirculating eddy maximum velocity $(\upsilon_e)_{crit}$ and the column radius were known. Alternatively, if K_3 and K_4 are known then (4.60) and (4.61) can be used to calculate $(\upsilon_e)_{crit}$ and R_c. If the average values of K_3 and K_4 listed in Table 4.1 are taken then $(\upsilon_e)_{crit}$ and R_c equal 0.17 m/s and 0.011 m respectively. No comparison can be made for the calculated value of R_c because Lin (1963) does not give a value for the column radius. However, the calculated value of $(\upsilon_e)_{crit}$ can be compared to measurements made by Wilkinson (1975) for air-glycerol/water solutions. He measured the linear velocity at which a horizontally rotating cylindrical roll began to entrain gas below the bath surface. From his results Wilkinson concluded that entrainment was initiated when a critical Capillary number equal to approximately 1.2, was reached. This value compares well with the present case, for which the critical Capillary number takes a value of 1.03 at the velocity of 0.17 m/s.
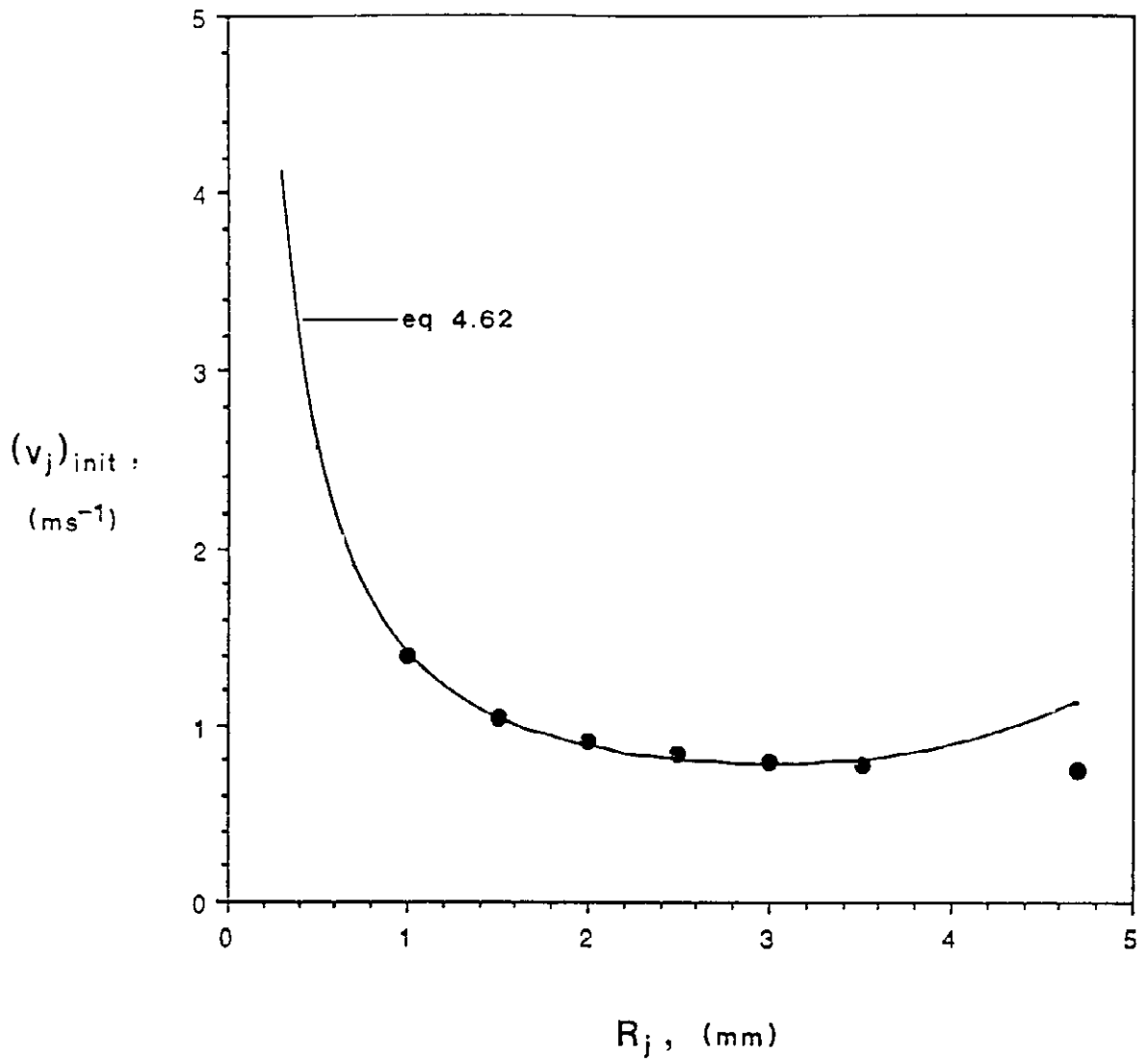
Figure 4.22   Comparison of experimental data of Lin (1963) and
the initiation jet velocity values predicted by
(4.62) for an air-95 wt% glycerol system

4.7 SUMMARY

The findings in this chapter can be summarised as follows:-

(i) The rate of entrainment for a rough plunging jet can be considered to be the sum of the quantity of gas which is trapped within the boundary of the jet at the point of impact with the receiving liquid, and also the quantity of gas present within the annular gas film located between the free surfaces of the jet and the receiving liquid at the point of impact. The flow of gas in the entrained film is not equal to the gas boundary layer moving with the jet surface.

(ii) The entrainment mechanism for the gas film component can be modelled using the velocity of the recirculating eddy generated within the receiving liquid by the action of the plunging jet. By predicting the magnitude of the velocity of the recirculating eddy, the effect of column diameter on the entrainment rate can be determined.

(iii) The rate of entrainment of the gas film can be calculated provided the film thickness is known. An estimate of the film thickness can be obtained from thin film theory provided the film does not rupture prior to attaining a constant thickness. A film of constant thickness is achieved only if the viscous forces present within the receiving liquid are sufficiently strong to dampen any disturbance generated on the induction trumpet surface. For systems where the film is ruptured prior to attaining a constant thickness the entrainment rate is greater than that predicted from thin film theory.

(iv) The experimental results indicate the initiation of gas film entrainment for smooth jets is controlled by the recirculating eddy velocity. The critical recirculating eddy velocity can be used to define a critical Capillary number for the induction trumpet which marks the initiation of gas film entrainment. For air – glycerol/water systems the critical Capillary number is approximately equal to unity.

Chapter 5

SUBMERGED JET EXPANSION
AND BUBBLE GENERATION

5.1 INTRODUCTION

Once the gas is entrained below the receiving liquid surface by the
plunging liquid jet it is dispersed as fine bubbles throughout the bulk
liquid flow. The size of the bubbles which are produced by this process
is determined by the ratio of the forces acting within the liquid phase
causing bubble breakup to the interfacial force which is tending to hold
the bubbles together. The ratio of these two forces is called the Weber
number and is defined as

$$We = \frac{\rho (\upsilon_m)^2 d}{\sigma} , \qquad (5.1)$$

where $(\upsilon)_m^2$ is the mean square velocity difference acting over a distance d.
Equation (5.1) can be used to define the critical Weber number We_{crit}
which corresponds to a maximum bubble diameter, $(d_b)_{max}$, which can exist
in a given velocity field, i.e.

$$We_{crit} = \frac{\rho (\upsilon_m)^2 (d_b)_{max}}{\sigma} . \qquad (5.2)$$

From (5.2) the maximum bubble diameter, and hence an estimate of the bubble diameter distribution, can be obtained provided values for We_{crit} and $\langle v_h \rangle^{\frac{1}{2}}$ are known.

In this chapter a model is developed to predict $(d_b)_{max}$ for the mixing zone at the top of the downcomer in the plunging jet bubble column. The model is based on (5.2) by assuming a value for the critical Weber number and the velocity fluctuation term is calculated from the energy dissipated by the jet within the submerged jet region. A model is also presented which predicts the expansion of the submerged jet based on the momentum values for the jet and the liquid inside the recirculating eddy surrounding the submerged jet.

5.2   LITERATURE REVIEW

In order to predict the maximum bubble diameter and size distribution generated within a plunging liquid jet bubble column, a knowledge of the region inside the downcomer where the bubbles are generated and the mechanism controlling their breakup is necessary. The breakup mechanism for bubbles and droplets is thought to be directly related to the critical Weber number and a review of the studies which have examined this idea is given in Section 5.2.1.

The critical Weber number criterion for bubble breakup can only be used if the intensity of the velocity fluctuations, which is a function of the energy dissipation rate within the liquid, is known. Inside a plunging liquid jet bubble column the energy dissipated by the submerged jet as it expands is responsible for the bubble breakup. For this reason a review of the studies investigating the expansion of a submerged jet is given in Section 5.2.2.

Finally, a review of the different types of bubble size distributions which have been reported by other workers is given in Section 5.2.3 in order to compare the results of the plunging jet system with alternative bubble generation devices.

5.2.1 Critical bubble Weber number

The fundamental work investigating the breakup and dispersion of droplets
and bubbles within a continuous liquid was carried out by Hinze (1955).
He described the external forces which acted to deform the surface of a
droplet or bubble as being either viscous stress or dynamic pressure set
up in the liquid phase. The deformation of the droplet or bubble from
these external forces then gave rise to internal viscous stresses as well
as dynamic pressures. In addition, the interfacial tension also gave
rise to a surface force which resisted the deformation of the droplet or
bubble. From these assumptions Hinze applied the definition of a
generalised Weber number presented earlier by Taylor (1934) and expressed
the Weber number as the ratio of the deforming forces to the restoring
forces acting on the droplet or bubble, i.e.

$$We = \frac{(F_{def}/A)}{(\sigma/d)} , \tag{5.3}$$

where F_{def} is the force per unit area acting to deform the droplet or
bubble and σ is the interfacial tension acting over a length scale equal
to the droplet or bubble diameter, d. For high Reynold numbers Hinze
concluded that the deformation of the droplet or bubble was caused by the
dynamic pressure forces of the turbulent motion of the liquid created as
a result of the velocity fluctuations acting over distances equal to the
diameter of the droplet or bubble. Under these conditions Hinze defined
the Weber number as

$$We = \frac{\rho_L (\upsilon_m)^2}{\sigma/d} , \tag{5.4}$$

where $(\upsilon_m)^2$ is the mean value of the squares of the velocity differences
over a distance equal to d. Hinze assumed the velocity fluctuations were
isotropic and were related to the energy input per unit mass and time by
the Kolmogoroff energy distribution law, i.e.

$$(\upsilon_m)^2 = C_1 (E_s d)^{2/3}. \tag{5.5}$$

In (5.5) E_s is the specific energy dissipation rate and C_1 is approximately equal to 2 according to Batchelor (1951). From (5.4) and (5.5) we have

$$We = 2\left(\frac{\rho_L}{G}\right) E_s^{2/3} d^{5/3}. \tag{5.6}$$

Hinze applied (5.6) to the data of Clay (1940) to determine the value of a critical Weber number corresponding to a maximum droplet diameter for a liquid-liquid dispersion contained between two coaxial cylinders, one of which, namely the inner one, rotated. On the basis of Clay's data Hinze found that We_{crit} was equal to 1.18.

Levich (1962) derived a similar expression to (5.3) which included the density of the dispersed phase. For bubbles dispersed within a continuous liquid phase the modified Weber number, We^*, was given by

$$We^* = \frac{(F_{def}/A)}{(G/d)}\left(\frac{\rho_G}{\rho_L}\right), \tag{5.7}$$

and following a similar analysis given by Hinze, (5.7) became

$$We^* = 2\left(\frac{\rho_L}{G}\right)E_s^{2/3} d^{5/3}\left(\frac{\rho_G}{\rho_L}\right)^{1/3}, \tag{5.8}$$

where ρ_L and ρ_G are the densities of the liquid and gas phases respectively. The modified definition of the Weber number given by Levich was found to give reasonable predictions for the maximum diameter for both bubbles in liquid systems and liquid droplets in gas systems.

Sevik and Park (1973) studied the splitting of bubbles and drops in the adjustment region of a high Reynolds number submerged water jet. They used the Weber number definition given by (5.3) and analysed the forces acting within the liquid stream on the bubbles to obtain the expression

$$We_{crit} = \left\{ (d_b)_{max} \left(\frac{\rho}{G}\right)^{3/5} E_s^{2/5} \right\}^{5/3} . \qquad (5.9)$$

Sevik and Park found experimentally that We_{crit} was equal to 1.26 which compared well with their calculated value of 1.24 based on the assumption the bubbles oscillated violently and eventually broke up when the characteristic frequency of the turbulence was equal to one of the resonant frequencies of the bubble.

Diagram removed for copyright reasons

Figure 5.1   Weber Number as a function of axis ratio
             for a bubble in a uniform velocity field
             (after Miksis et al, 1981)

Miksis et al (1981) computed the deformation of an axisymmetric bubble (or drop) in a flow field moving with a uniform velocity U. They assumed the flow was inviscid and incompressible and calculated the potential function on the bubble surface. They found that as the velocity was increased the bubble became oblate, spreading out in the direction normal to the direction of the flow and contracting in the direction of the flow. At a critical velocity the two poles of the bubble eventually touched each other and the bubble became unstable.

Miksis et al extended their analysis to determine the Weber number for which the bubble became unstable. They plotted the bubble Weber number against the axis ratio Υ (length of major axis/length of minor axis) as shown in Figure 5.1, where We_b was calculated using a bubble radius equivalent to the radius of a sphere with the same volume as the bubble. Miksis et al found that a maximum in the graph occurred at a bubble Weber number equal to 3.23. They interpreted this value to be the critical bubble Weber number, beyond which the bubble becomes unstable.

Lewis and Davidson (1982) predicted a critical bubble Weber number value for the breakup of a single bubble rising through a vertical liquid jet flowing upwards into a large volume of the same liquid. They analysed the deformation of an initially cylindrical bubble surrounded by an inviscid liquid in shear flow by calculating the pressure profile on the bubble surface for different values of the liquid shear rate ω_L. Their predictions are given in Figure 5.2 where it can be seen that the axis ratio became asymptotic at a critical shear rate qual to approximately 115 s^{-1}. At this point Lewis and Davidson assumed the bubble became unstable and broke up. From the predicted value of $(\omega_L)_{crit}$ Lewis and Davidson were able to calculate $(We_b)_{crit}$ by assuming that

$$(\upsilon_m)^2 = (\omega_L)^2 d_b^2 \; , \qquad\qquad (5.10)$$

which when substituted into (5.4) gave

$$We_b = \frac{\rho_L(\omega_L)^2(d_b)^3}{6} \; . \qquad\qquad (5.11)$$

Lewis and Davidson solved (5.11) for values of ω_L and their results are given in Figure 5.2. It can be seen from the graph that the bubble axis ratio became infinite when We_b approached 4.7. Lewis and Davidson found that this value was independent of the bubble diameter selected. They concluded, therefore, that $(We_b)_{crit}$ was equal to 4.7.

Diagram removed for copyright reasons

Figure 5.2 Theoretical distortion of a cylindrical
bubble due to shear flow calculated
by Lewis and Davidson (1982)

Lewis and Davidson related the critical bubble diameter to their experimental system by assuming that for a liquid jet flowing through an orifice

$$(\omega_L)_{crit} \doteq \frac{v_j}{1.1\, d_j} \quad ,$$

(5.12)

where v_j and d_j are the jet velocity and diameter respectively.

Equation (5.12) was then substituted into (5.11) to obtain an expression for the maximum stable bubble diameter, i.e.

$$(d_b)_{max} = \left\{ (We_b)_{crit}\ \frac{G}{\rho_L} \left(\frac{1.1\, d_j}{v_j}\right)^2 \right\}^{1/3} \quad ,$$

(5.13)

where $(We_b)_{crit}$ is equal to 4.7.

Rallinson (1984) examined the deformation of a bubble due to axisymmetric pure straining flow. He examined the stresses exerted on the bubble surface due to the internal and external fluid flow, and found there was a critical bubble Capillary number, $(Ca_b)_{crit}$, beyond which the bubble became unstable. Its value was given by

$$(Ca_b)_{crit} = 0.148 \left(\frac{\mu_G}{\mu_L}\right)^{-1/6} \quad ,$$

(5.14)

where μ_G is the absolute viscosity of the gas inside the bubble. Equation (5.14) is in good agreement with the results given by Hinch and Acrivos (1979) who found that for plane hyperbolic flows

$$(Ca_b)_{crit} = 0.145 \left(\frac{\mu_G}{\mu_L}\right)^{-1/6} \quad .$$

(5.15)

Hinch and Acrivos (1980) also found that for bubbles in simple shear flow,

$$(Ca_b)_{crit} = 0.054 \left(\frac{\mu_b}{\mu_L}\right)^{-2/3} . \qquad (5.16)$$

Ryskin and Leal (1984) obtained a numerical solution for the deformation of a bubble due to uniaxial extensional flow of an incompressible Newtonian liquid. They computed the shape of the bubble by balancing the total normal stresses and capillary pressure acting on the surface of the bubble and found that the Weber number for which the bubble became unstable was a function of the Reynolds number. Interpolation of their experimental results gave

$$\left\{\frac{1}{(We_b)_{crit}}\right\}^{10/9} = \left\{\frac{1}{2.76}\right\}^{10/9} + \left\{\frac{1}{0.247\,(Re_b)_{crit}}\right\}^{10/9}, \qquad (5.17)$$

where the bubble Reynolds number, and the corresponding critical bubble Weber number are given by

$$(Re_b)_{crit} = \frac{\rho_L \omega_L (d_b)^2_{max}}{2\mu_L} \qquad (5.18)$$

and

$$(We_b)_{crit} = \frac{\rho_L \omega_L^2 (d_b)^3_{max}}{6} \qquad (5.19)$$

Pandit and Davidson (1986) studied the breakup of bubbles rising through a vertical liquid jet flowing upwards through a horizontal orifice and into the large volume of the same liquid. They found that the number of smaller bubbles N_b formed by the breakup of a single large bubble in the flowing jet was correlated by:-

$$N_b = 2\cdot 38 \left\{ \frac{\Delta P (d_b)^3}{D_o^2 G} \right\}^{0\cdot 8},$$
(5.20)

where ΔP is the pressure drop across an orifice which has a diameter equal to D_o. Pandit and Davidson defined the critical Weber number for the jet produced by the orifice as

$$(We_b)_{crit} = 1\cdot 35 \left\{ \frac{\Delta P (d_b)^3_{crit}}{D_c G} \right\}.$$
(5.21)

They proceeded to calculate a value for $(We_b)_{crit}$ by assuming the minimum number of smaller bubbles formed by the breakup of a single large bubble having a diameter of $(d_b)_{crit}$ was equal to 2, i.e. $N_b = 2$. This value was substituted into (5.20) to find

$$\frac{\Delta P (d_b)^3_{crit}}{D_o^2 G} \doteqdot 0\cdot 8.$$
(5.22)

Substituting (5.22) into (5.21) gave a value for $(We_b)_{crit}$ of 1.1.

Walter and Blanch (1983) included the influence of the gas viscosity on the breakup of a bubble within a pseudoplastic liquid and suggested the critical bubble diameter was given by

$$(d_b)_{crit} = \frac{1\cdot 12\ G^{3/5}}{(E/V)^{2/5}\ \rho_L^{1/5}} \left\{ \frac{(\mu_L)_{ext}}{3\mu_G} \right\}^{1/10},$$
(5.23)

where E/V is the energy dissipation rate per unit volume and $(\mu_L)_{ext}$ is the extensional viscosity of the pseudoplastic liquid.

Davies (1987) compiled the experimental results of a number of studies and plotted the maximum drop diameter $(d_d)_{max}$ as a function of the local specific energy dissipation rate E_s, as shown in Figure 5.3.

Figure 5.3   Survey of maximum drop diameter as a function of the
local specific energy dissipation rate for different
types of devices (after Davies, 1987)

From the data given in Figure 5.3 Davies obtained a linear power law
relationship between E_s and $(d_d)_{max}$, over a range of 9 decades. It was
found by Davies the exponent for the energy dissipation was the same as
that given by Hinze (1955), and also that $\{(We_d)_{max}/2\}^{3/5}$ ranged between
0.5 and 1, which gave an average critical droplet Weber number of 1.3.

Hesketh et al (1987) studied the breakup of bubbles in a dilute dispersion flowing through a horizontal pipe. They used the definition of the Weber number given by (5.8) in order to predict the critical bubbble diameter, i.e.

$$(d_b)_{crit} = \left\{ \frac{(We^*_b)_{crit}}{2} \right\}^{3/5} \cdot \left\{ \frac{\sigma^{3/5}}{(\rho_L^2 \rho_G)^{1/5}} \right\} (E_s)^{-2/5} , \qquad (5.24)$$

where the specific energy dissipation rate E_s inside the pipe was calculated using the expression

$$E_s = \frac{2f j_L^3}{D_p} , \qquad (5.25)$$

where j_L is the liquid volumetric flux flowing through a pipe which has a diameter equal to D_p. The friction factor, f, is given by the Blasius equation

$$f = 0.079 \, Re^{-0.25} . \qquad (5.26)$$

Hesketh et al used (5.24) in conjunction with experimental measurements for $(d_b)_{max}$, to obtain a critical Weber number value of 1.1.

Table 5.1 contains a summary of the reported values of the critical Weber number found in the literature. For bubble-in-liquid systems the values range from 0.95 to 4.7, with the theoretical predictions of Miksis et al (1981), Lewis and Davidson (1982) and Ryskin and Leal (1984) all giving higher values for We_{crit} than those which were experimentally determined, which range from 1.1 to 1.24.

TABLE 5.1 Reported values for the critical Weber number

Author	Reported Critical Weber Number	Conditions
Hinze (1955)	0.5 – ∞	drop in viscous flow
	13 – ∞	drop in air stream
	1.1	emulsification in turbulent flow
Sevik and Park (1973)	1.24	bubble breakup by submerged liquid jet; the experimentally determined value of $(We_b)_{crit}$ was also predicted from resonant frequency of bubble
Miksis et al (1981)	3.23	predicted value for bubble/drop in axisymmetric uniform flow
Lewis and Davidson (1982)	4.7	cylindrical bubble in axisymmetric inviscid shear flow
Ryskin and Leal (1984)	0.95 (Re = 10) 2.15 (Re = 100) 2.76 (Re = ∞)	numerical prediction of bubble breakup in uniaxial extensional Newtonian flow
Pandit and Davidson (1986)	1.1	bubble breakup by submerged liquid jet
Davies (1987)	1.13	liquid in liquid systems
Hesketh et al (1987)	1.1	bubble breakup in the turbulent flow through a pipe

5.2.2 Submerged Liquid Jet Expansion

When a liquid jet plunges into a receiving liquid contained within a
vertical column the resulting submerged jet will expand to occupy the
entire cross-sectional area of the column as shown in Figure 5.4.
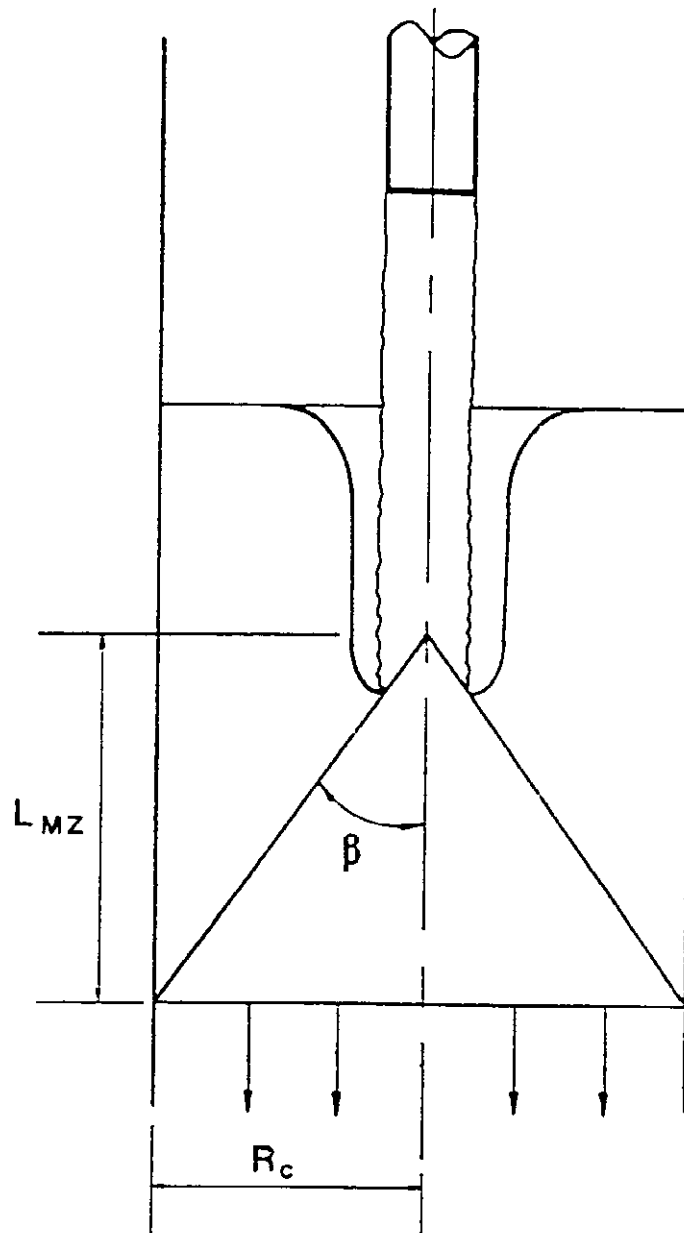
Figure 5.4   Expansion of a confined submerged jet

In Figure 5.4 β is known as the "jet angle", 2β being the angle subtended
at the apex of the cone occupied by the expanding liquid jet. There have
been a number of jet angle studies reported in the literature. Donald
and Singer (1959) reported a constant jet angle of $14^\circ \pm 2^\circ$ over a jet
Reynolds number range of 5,000 - 30,000. Their results compared to

earlier reported values of 14⁰ (Binnie, 1942), 16⁰ (Moss, 1947) and 20⁰
(Folsom, 1948). Donald and Singer also claimed that the receiving liquid
entered the submerged jet approximately perpendicular to the flow path,
which was contrary to the previously-held belief that the jet entrained
the surrounding liquid by a type of frictional effect. The implication
of this finding was that a momentum balance, and hence an energy balance,
could be defined for the system by considering only the liquid from the
jet source passing any transverse cross-section of the jet and ignoring
the flow of liquid surrounding the envelope of the submerged jet.

Table 5.2 contains a summary of jet angle studies reported in the
literature including values not already mentioned. The results show a
considerable variation suggesting that the jet angle measurements were
significantly influenced by the experimental conditions. With the
exception of Lane and Rice (1982), all of the studies listed in Table 5.2
are for unconfined jets.

TABLE 5.2 Measured values of jet angle for submerged jet

Author	Jet Angle (deg)	Comment
Binnie (1942)	14	
Moss (1947)	16	
Folsom (1948)	20	
Donald and Singer (1959)	14	
Sucui and Smigelschi (1976)	14	Jet angle determined by cone which contained the submerged biphasic region created by a liquid jet plunging into an unconfined liquid.
Unno and Inoue (1980)	24 - 29	Submerged liquid jet issuing from an orifice and passing upwards into a 150 mm diameter column.
Lane and Rice (1982)	22.25	Submerged jet circulating inside a closed system.

5.2.3 Bubble diameter distribution

The size distribution of bubbles formed by the breakup of larger bubbles in a turbulent field has been studied extensively by many workers (Lewis and Davidson, 1983; Unno and Inoue, 1980; Hesketh et al, 1987). They have all found the resultant bubble diameter distribution was skewed and best[12] described by a log-normal distribution. One possible reason for a skewed bubble diameter distribution is the probability of a bubble being broken increases with increasing diameter and the breakup of each large bubble results in the formation of many smaller bubbles. The generation of smaller bubbles at the expense of the larger ones would result in a skewed bubble diameter distribution. The presence of a bimodal bubble diameter distribution has also been reported and this is thought to be as a consequence of either the incomplete breakup of the feed bubbles or by the coalescence of bubbles in the turbulent shear field.

Mihail and Straja (1986) modelled the breakup and coalescence mechanisms to predict the maxima for the bimodal bubble diameter distribution. They defined the distributed product density function as $f(V_b,z,t)$, which gave the probability that at a time t, a bubble of volume V_b was at an axial position z. They obtained a population balance for the bubbles by taking the substantial derivative of the product density function, i.e.

$$\frac{Df}{Dt} = \begin{array}{c} \text{birth by} \\ \text{coalescence} \end{array} - \begin{array}{c} \text{death by} \\ \text{coalescence} \end{array}$$

$$+ \begin{array}{c} \text{birth by} \\ \text{breaking} \end{array} - \begin{array}{c} \text{death by} \\ \text{breaking} \end{array} \quad . \qquad (5.27)$$

By assuming the motion took place mainly in the axial direction and neglecting the radial and azimuthal velocities, the substantial derivative reduced to

$$\frac{Df}{Dt} = \frac{\partial f}{\partial t} + (v_b)_z \frac{\partial f}{\partial z} \quad . \qquad (5.28)$$

---

[12] Unno and Inoue (1980) describe their experimental results using a gamma distribution.

Mihail and Straja equated (5.27) and (5.28) and obtained expressions for the "birth" and "death" terms to obtain the resultant bubble size distribution for a given time and axial position. Preliminary results showed the model can successfully predict the existence and the positions of the two maxima in the bubble diameter distribution for an experimentally measured bimodal distribution.

In gas-liquid contacting operations it is common to report the mean bubble size as the mean volume-surface diameter $(d_b)_{vs}$ or Sauter mean diameter which is defined as

$$(d_b)_{vs} = \frac{\sum_{i=1}^{N} (n_i d_i^3)}{\sum_{i=1}^{N} (n_i d_i^2)} \quad , \tag{5.29}$$

where n_i is equal to the number of bubbles having a diameter equal to d_i. The Sauter mean diameter is useful when comparing the experimental results for different bubble diameter distributions. It can be applied directly to bimodal distributions without the need firstly to separate the two distributions and obtain the individual mean values.

Usually it is desirable to produce a two-phase mixture which has a uniform bubble diameter distribution, and the ratio of the standard deviation of the sample to the mean diameter is commonly used to give an indication of the range of bubble sizes. For a unimodal distribution the standard deviation and mean value are clearly defined and their ratio is easily calculated. For bimodal distributions the interpretation of the mean value and standard deviation are not clear and the ratio of the Sauter mean to the maximum bubble diameter, is used instead to indicate the spread of the distribution. Some of the reported values of this ratio are listed in Table 5.3. where it can be seen that the ratio ranges from 0.6 - 0.7 for both liquid-in-liquid and gas-in-liquid systems.

TABLE 5.3   Reported values of Sauter mean / maximum diameter ratio

Author	$\{(d_b)_{vm}\}/\{(d_b)_{max}\}$	System
Brown and Pitt (1972)	0.70	Kerosene in water dispersion
Zhang et al (1985)	0.62	Kerosene in water dispersion
Calabrese et al (1986)	0.6	Droplet breakup in a stirred tank
Hesketh et al (1987)	0.62	Bubbles in a pipeline (noted the existence of a bimodal bubble distribution)

5.3   THEORETICAL DEVELOPMENT

The development of a model to predict the maximum stable bubble diameter within the submerged jet region, or mixing zone of the downcomer section of a plunging jet bubble column can be divided into three main areas of research. The first requirement is to define the relationship between the forces acting within the mixing zone and the maximum stable bubble diameter. Secondly, expressions relating the forces acting on the bubbles to the variables of the system are required. Finally, the volume of the mixing zone, where the forces act to break up the bubbles, must be defined. Each of these aspects of the model are discussed in the following sections.

5.3.1   Expression for maximum bubble diameter

An expression for the maximum stable bubble diameter was obtained from the definition for the bubble Weber number defined by Levich (1962), i.e.

$$\left(We_b^*\right)_{crit} = 2 \left(\frac{\rho_L}{\rho_G}\right)\left(E_s\right)^{2/3}\left(d_b\right)_{max}^{5/3} \left(\frac{\rho_G}{\rho_L}\right)^{1/3} . \tag{5.30}$$

The maximum bubble diameter can be obtained from (5.30) provided the specific energy dissipation E_s, and a value for the critical bubble Weber number $(We_b^*)_{crit}$ are known.

Hesketh et al (1987) obtained experimentally a value of 1.1 for the critical Weber number, which agreed with the results from other studies. They supported their result with the argument that a bubble should break up when the forces distorting the bubble are just greater than the forces resisting the distortion, which they took to be when the Weber number is just greater than unity. In light of the experimental evidence and the argument presented by Hesketh et al (1987), a value of 1.1 has been chosen as a reasonable estimate for the critical bubble Weber number.

Substituting the value of 1.1 for $(We_b^*)_{crit}$ into (5.30) and rearranging, gives the following expression for the maximum bubble diameter, i.e.

$$(d_b)_{max} = \left(\frac{1\cdot1}{2}\right)^{3/5} \left\{\frac{\sigma^3}{(\rho_L)^2 \rho_G}\right\}^{1/5} (E_s)^{-2/5} \ . \tag{5.31}$$

Equation (5.31) can be used to calculate $(d_b)_{max}$ once an expression for the specific energy dissipation rate for the mixing zone is derived.

5.3.2 Specific energy dissipation rate for mixing zone

To predict the specific energy dissipation rate within the mixing zone the analysis used by Cunningham (1974) to predict the mixing losses for a liquid-jet gas pump has been applied. As shown in Figure 5.5, the liquid jet and the gas annulus enter the top of the pump as discrete phases. The gas and liquid phases are then intimately mixed in the throat before passing into the diffuser as a homogeneous bubbly mixture. The operating characteristics of the liquid-jet gas pump are very similar to those of a confined plunging jet system, i.e. the gas is entrained in the form of a sheath which surrounds the liquid jet. The gas sheath is then broken up and dispersed as bubbles by the intensive mixing within the submerged jet region just below the point of impact of the plunging jet. The gas and liquid then leave the mixing zone as a uniform bubbly mixture.

Liquid

Gas

Nozzle

Gas annulus

Free jet

Throat

Bubbly flow

Diffuser
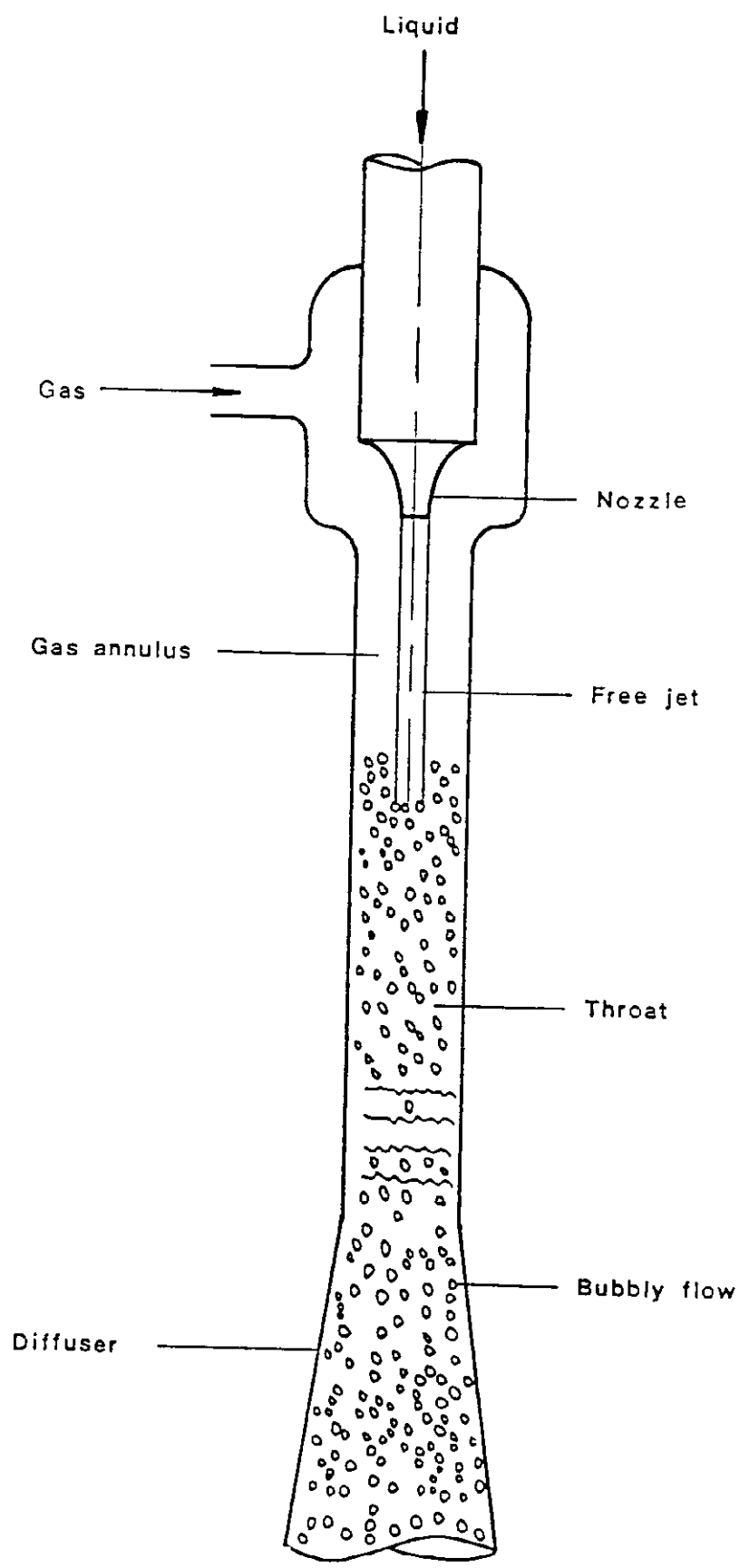
Figure 5.5 Schematic of the liquid-jet gas pump

Following Cunningham (1974), the calculated pressure rise inside the mixing zone of the plunging jet bubble column due to the momentum transfer from the liquid to the gas phase is given by (5.32):

$$P_1 - P_0 = \frac{\rho_L v_j^2}{2} \left\{ 2b - (2 + k_{MZ}) b^2 \left(1 + \frac{\rho_G Q_G}{\rho_L Q_L} \right) \left(1 + \frac{Q_G}{Q_L} \right) \right.$$

$$\left. + \frac{2 \frac{\rho_G}{\rho_L} \left(\frac{Q_G}{Q_L} \right)^2 b^2}{1 - b} \right\} , \qquad (5.32)$$

where b is the ratio of the cross-sectional area of the jet to the cross-sectional area of the column and k_{MZ} is the friction loss coefficient inside the mixing zone; P_0 and P_1 are the pressures at the inlet and outlet of the mixing zone respectively. From an energy balance, the pressure rise inside the mixing zone is also given by

$$P_1 - P_0 = \frac{\rho_L v_j^2}{2} \left\{ 1 - b^2 \left(1 + \frac{\rho_G Q_G}{\rho_L Q_L} \right) \left(1 + \frac{Q_G}{Q_L} \right)^2 + \frac{\rho_G}{\rho_L} \left(\frac{Q_G}{Q_L} \right)^3 \left(\frac{b}{1-b} \right)^2 \right\}$$

$$- \frac{Q_G}{Q_L} P_0 \ln \left(\frac{P_1}{P_0} \right) - \rho_L \left\{ (e_s)_{MZ} + (e_s)_{m1} \right\} , \qquad (5.33)$$

where $(e_s)_{MZ}$ and $(e_s)_{m1}$ are the specific energy dissipation terms for inside the mixing zone and mixing loss respectively. By recognising that

$$\rho_L (e_s)_{MZ} = \frac{\rho_L v_j^2}{2} k_{MZ} b^2 \left(1 + \frac{\rho_G Q_G}{\rho_L Q_L} \right) \left(1 + \frac{Q_G}{Q_L} \right) , \qquad (5.34)$$

equations (5.32) – (5.34) can be rearranged to obtain an expression for the irreversible specific energy dissipation attributed to the mixing of the gas and liquid phases, i.e.

$$(e_s)_{mL} = \frac{v_j^2}{2}\left\{ 1 - 2b - b^2\left(1 + \frac{\rho_G Q_G}{\rho_L Q_L}\right)\left(1 - \frac{Q_G}{Q_L}\right)^2 + 2b^2\left(1 + \frac{\rho_G Q_G}{\rho_L Q_L}\right)\left(1 + \frac{Q_G}{Q_L}\right) \right.$$

$$\left. - 2\left(\frac{\rho_G Q_G}{\rho_L Q_L}\right)\left(\frac{b^2}{1-b}\right) + \frac{\rho_G}{\rho_L}\left(\frac{Q_G}{Q_L}\right)^3\left(\frac{b}{1-b}\right)^2 \right\} \quad . \qquad (5.35)$$

The specific mixing loss can be used in conjunction (5.31) to predict the maximum bubble diameter once its dissipation rate $(E_s)_{ml}$ is known.

Assuming the mixing loss is uniformly dissipated throughout the mixing zone (submerged jet region), the specific dissipation rate is given by

$$(E_s)_{mL} = (e_s)_{ml}\frac{Q_L}{V_{MZ}} \quad , \qquad (5.36)$$

where Q_L is the volumetric flowrate of the liquid jet passing through the mixing zone volume V_{MZ}. This assumption is not strictly correct since the energy dissipation rate will be higher in the high shear regions of the mixing zone. However, (5.36) should give a reasonable approximation for the maximum bubble diameter when it is used in (5.31)

5.3.3   Estimation for mixing zone volume

If the volume of the mixing zone is assumed to be the same as the conical volume occupied by the submerged jet as it expands towards the walls of the column, then the expression for V_{MZ} is given by

$$V_{MZ} = \frac{\pi R_c^2 L_{MZ}}{3} \quad . \qquad (5.37)$$

As shown in Figure 5.4, the length of the mixing zone L_{MZ} can be calculated from the jet angle and the column radius using the expression

$$L_{MZ} = \frac{R_c}{\tan\beta} \qquad . \qquad\qquad (5.38)$$
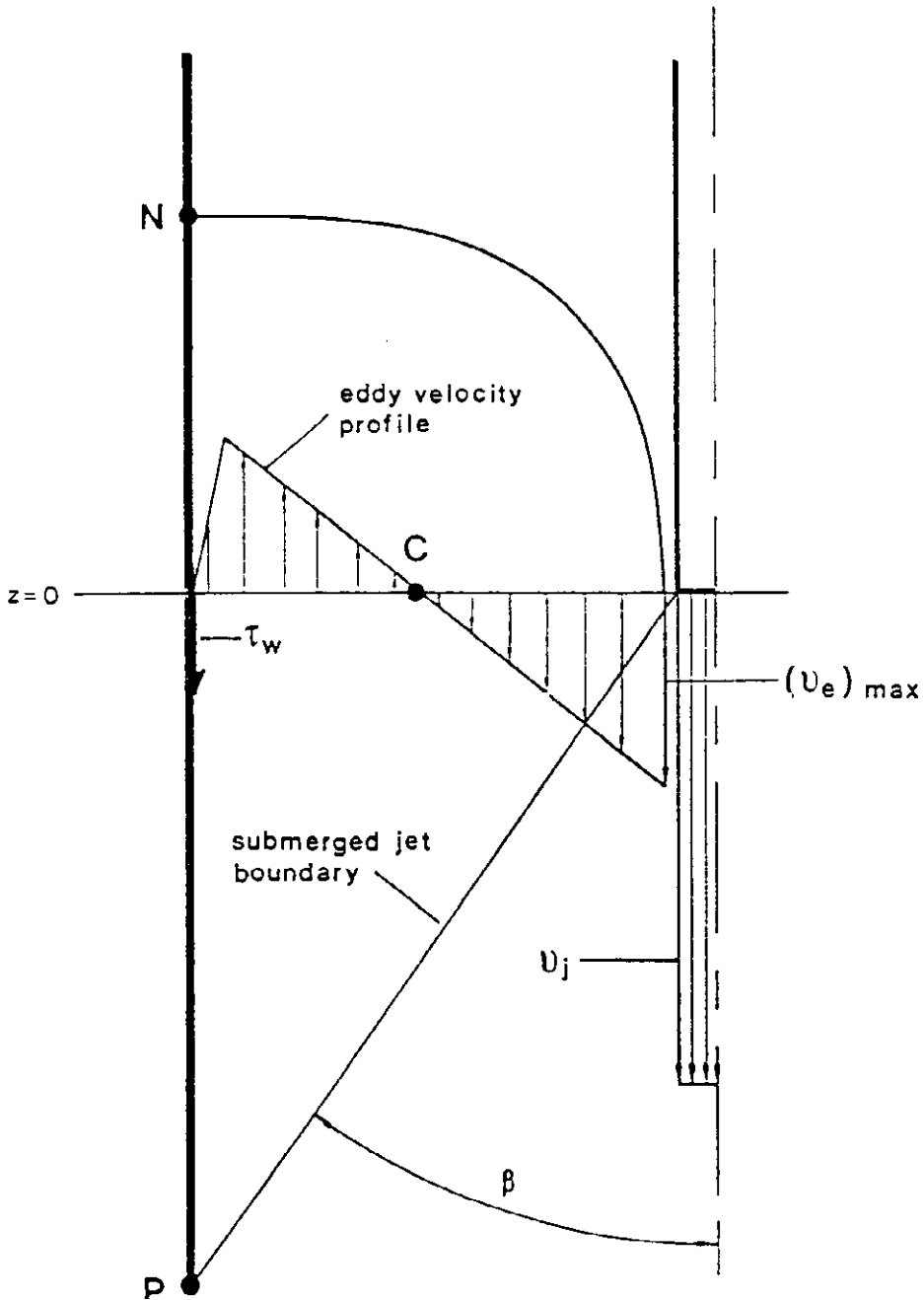
Figure 5.6 Velocity profile of jet and recirculating eddy at z=0

The submerged jet angle can be obtained by considering the radial transfer of momentum from the jet to the recirculating eddy. Radial momentum transfer from the jet will occur when there is a velocity gradient across the submerged jet-recirculating eddy boundary as shown in Figure 5.6.

It can be seen in Figure 5.6 the existence of a shear stress, τ_w, acting along the wall in the direction opposite to the motion of the recirculating eddy. If the wall shear stress did not exist the liquid inside the recirculating eddy would increase its velocity until a velocity gradient no longer existed across the recirculating eddy - submerged jet boundary. At this point the radial transfer of jet momentum to the eddy would be zero, and the recirculating eddy angular momentum is given by

$$\left(M_e\right)_{\tau_w = 0} = \rho_e Q_e \left\{\frac{v_j - 0}{2}\right\} . \tag{5.39}$$

In reality, a shear stress does act along the column wall, resulting in a difference between $(v_e)_{max}$ and v_j at the origin of the submerged jet, where $(v_e)_{max} < v_j$. The recirculating eddy angular momentum in this case is given by

$$\left(M_e\right)_{\tau_w \neq 0} = \rho_e Q_e \left\{\frac{(v_e)_{max} - 0}{2}\right\} . \tag{5.40}$$

The difference between (5.40) and (5.39) is the momentum loss from the recirculating eddy due to the shear stress acting against the liquid flow at the wall of the column, i.e.

$$2\pi R_c L_{MZ} \tau_w = \rho_e Q_e \left\{\frac{v_j - (v_e)_{max}}{2}\right\} , \tag{5.41}$$

where $2\pi L_{MZ}$ represents the surface over which the shear stress is acting.

For a liquid flowing through a circular conduit of radius R_c the shear stress is given by

$$T_w = - \frac{R_c}{2} \cdot \frac{dP}{dz} \quad , \tag{5.42}$$

where dP/dz is the pressure gradient along the length of the conduit. If ΔP is the change in pressure over the length of the mixing zone then

$$T_w = - \frac{R_c}{2} \cdot \frac{\Delta P}{L_{MZ}} \quad . \tag{5.43}$$

or

$$T_w = - \frac{\tan \beta}{2} \cdot \Delta P \quad . \tag{5.44}$$

Substituting (5.44) into (5.41) gives

$$\pi R_c L_{MZ} \tan \beta (-\Delta P) = \rho_e Q_e \left\{ \frac{v_j - (v_e)_{max}}{2} \right\} \quad , \tag{5.45}$$

which can be rearranged to give an expression for the jet angle, i.e.

$$\tan \beta = \frac{\rho_e Q_e \left\{ v_j - (v_e)_{max} \right\}}{2\pi R_c L_{MZ} (-\Delta P)} \quad . \tag{5.46}$$

The denominator in (5.46) represents the pressure force acting normal to the column wall in the opposite direction to the radial dissipation of jet momentum. An approximate expression for the pressure force in (5.46) can be obtained from the Euler number, N_{Eu}, which is defined as ratio of the frictional pressure force to the inertial force of the system. If the frictional pressure force is given by the denominator in (5.46), and the

inertial force is equivalent to the initial jet momentum, then the Euler number for the plunging jet system is given by

$$N_{Eu} = \eta \left\{ \frac{2\pi R_c L_{M2} (-\Delta P)}{M_j} \right\} , \qquad (5.47)$$

where η is a constant and its value depends on how effectively the jet momentum is converted into a pressure force. The initial jet momentum is equal to

$$M_j = \rho_L Q_L v_j . \qquad (5.48)$$

Witte (1969) also gives an expression for the Euler number, i.e.

$$N_{Eu} = \frac{\rho_L v_j^2}{P_o} , \qquad (5.49)$$

where P_o is the pressure in the headspace at the top of the downcomer. Equating (5.47) and (5.49) to obtain an expression for the pressure force, (5.46) becomes

$$\tan \beta = \eta \left(\frac{P_o}{\rho_L v_j^2} \right) \left(\frac{\rho_e}{\rho_L} \right) \left(\frac{Q_e}{Q_L} \right) \frac{\{ v_j - (v_e)_{max} \}}{v_j} . \qquad (5.50)$$

By recalling

$$(Q_e)_{max} = Q_L \left\{ \frac{0.37}{C_T} - 0.64 \right\} ,$$

where

$$C_T = \frac{R_j}{\{ R_c^2 - \frac{1}{2} R_j^2 \}^{1/2}} .$$

Equation (5.50) can be written as

$$\tan\beta = \eta\left(\frac{P_o}{\rho_L v_j^2}\right)\left(\frac{\rho_\varepsilon}{\rho_L}\right)\left\{\frac{0.37\left(R_c^2-\frac{1}{4}R_j^2\right)^{1/2}-0.64\,R_j}{R_j}\right\}\left\{\frac{v_j-(v_\varepsilon)_{max}}{v_j}\right\} \quad (5.51)$$

or

$$\beta = \frac{360}{2\pi}\tan^{-1}\left[\eta.\frac{P_o}{\rho_L v_j^2}.\frac{\rho_\varepsilon}{\rho_L}.\left\{\frac{0.37\left(R_c^2-\frac{1}{4}R_j^2\right)^{1/2}-0.64\,R_j}{R_j}\right\}\left\{\frac{v_j-(v_\varepsilon)_{max}}{v_j}\right\}\right], (5.52)$$

where the jet angle is given in degrees.

5.4 EXPERIMENTAL

The experimental setup used to study the size and bubble diameter distribution generated within the mixing zone at the top of the column consisted of a number of pressure tappings spaced 50 mm apart along the axial length of the column. These tappings were used to obtain the differential pressure profile from which the boundary of the mixing zone was determined. In addition to the pressure tappings located along the wall of the column there was another outlet situated 200 mm below the top pressure tapping. This outlet was used to draw the two phase mixture through the optical flow-through cell used to photograph the bubbles in order to determine the bubble diameter distribution.

The experimental procedure involved setting the gas and liquid flowrates to the desired values and then allowing the bubble column sufficient time to reach equilibrium operation. The column was assumed to be at equilibrium when the gas void fraction profile became constant with respect to time. The two-phase mixture was then drawn through the optical cell with the aid of a jet-ejector vacuum pump located upstream of the optical flow-through cell. The rate of bubbles passing between the parallel windows in the optical cell was adjusted by diluting the two-phase mixture with the clear liquid prior to it entering the optical

cell in order to minimise the number of overlapping bubbles appearing in
the photograph.

The differential pressure profile was constructed from the experimental
pressure readings. The boundary of the mixing zone was determined to be
the point where the differential reading first became constant which
marked the position where the pressure fluctuations due to flow
variations became insignificant. At this point the gas void fraction
became constant which indicated the onset of uniform two-phase flow. The
procedure and equipment used to take the bubble photographs is outlined
in Chapter 3. The bubble diameter distribution calculated from the
sample taken from the 200 mm sample port was assumed to be representative
of the bubbles generated inside the mixing zone.

5.5   RESULTS AND DISCUSSION

In this section the submerged jet angle measurements, which were
determined from the pressure profile readings given in Appendix 4, are
presented. The jet angle measurements are then compared to the predicted
values obtained from (5.52). From the jet angle measurements the volume
of the mixing zone and subsequent values for the maximum bubble diameter
have been calculated. These are compared with the experimental bubble
diameter measurements given in Appendix 3.

5.5.1   Axial wall pressure measurements

The general shape of the absolute pressure profiles along the axial
length of the bubble column were similar for all experimental runs. An
example of a typical curve is shown in Figure 5.7, where the total
pressure $P(z)$ normalised against the ambient atmospheric pressure P_{atm},
has been plotted as a function of length along the axis of the column.
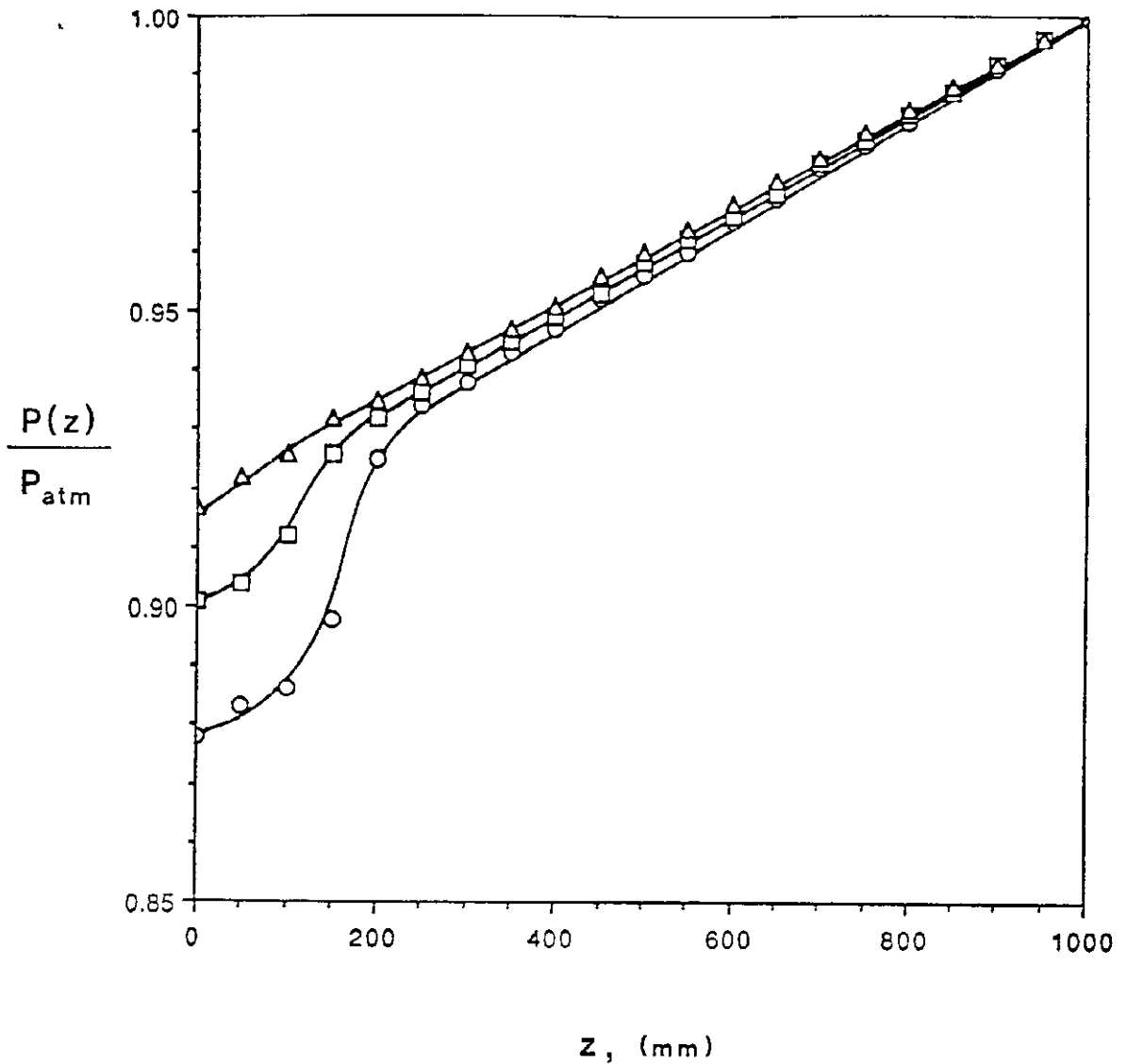
Figure 5.7 Normalised wall pressure profiles for 2.38 (Run 26),△;
4.76 (Run 17),□; and 7.12 mm (Run 8),○; mm diameter jet
[ρ_L = 1000 kg/m³; μ_L = 0.0009 Pa-s; σ = 0.062 N/m; no
baffles; D_j = 44 mm; v_j = 11.5 m/s]

It can be seen from Figure 5.7 that for each curve there is a distance
from the nozzle beyond which the normalised pressure is a linear function
of length. This region corresponds to the uniform two-phase flow zone
where the pressure gradient is constant due to the constant gas void
fraction,and any pressure variations due to velocity fluctuations within
the liquid are negligible.

Before uniform two-phase flow is achieved there is a region where the pressure profile is not linear. This region marks the mixing zone where a reversal in the direction of liquid flow takes place due to the presence of the recirculating eddy. Consequently, the negative dynamic pressure gradient counterbalances the increase in the hydrostatic pressure with increasing distance from the nozzle. The result is an absolute pressure profile gradient being less in the region of the recirculating eddy than for the uniform two-phase flow zone, and hence the sigmoidal shape in the normalised pressure profile along the column.

It can be seen from Figure 5.7 that the submerged jet reached the wall at lengths of 175, 148, and 72 mm for the 7.12, 4.76 and 2.38 mm diameter jets respectively. These distances were taken as the lengths of the mixing zone for the respective jet diameters, and from these readings the corresponding jet angles were calculated from (5.38). This procedure was repeated for all experimental runs.

TABLE 5.4   Effect of gas/liquid flow ratio on the measured jet angle (D_c = 74 mm; D_j = 4.76 mm; v_j = 11.5 m/s; ρ_L = 1000 kg/m³; σ = 0.063 N/m; μ_L = 0.0009 Pa-s)

Gas/Liquid Flow Ratio	Mixing Zone Length (mm)	Measured Jet Angle (deg)	Density Two-Phase Mixture (kg/m³)
0	150	13.9	999
0.126	170	12.3	800
0.296	216	9.8	620
0.645	260	8.1	474

5.5.2   Submerged jet angle

(a)   Effect of gas/liquid volumetric flow ratio

In Table 5.4 measured values for the submerged jet angle and the density of the two-phase mixture inside the recirculating eddy are listed as a function of the gas/liquid volumetric flow ratio.   It was assumed ρ_e was the same as the mixture in the uniform two-phase flow region which was obtained from the pressure readings given in Appendix 4.
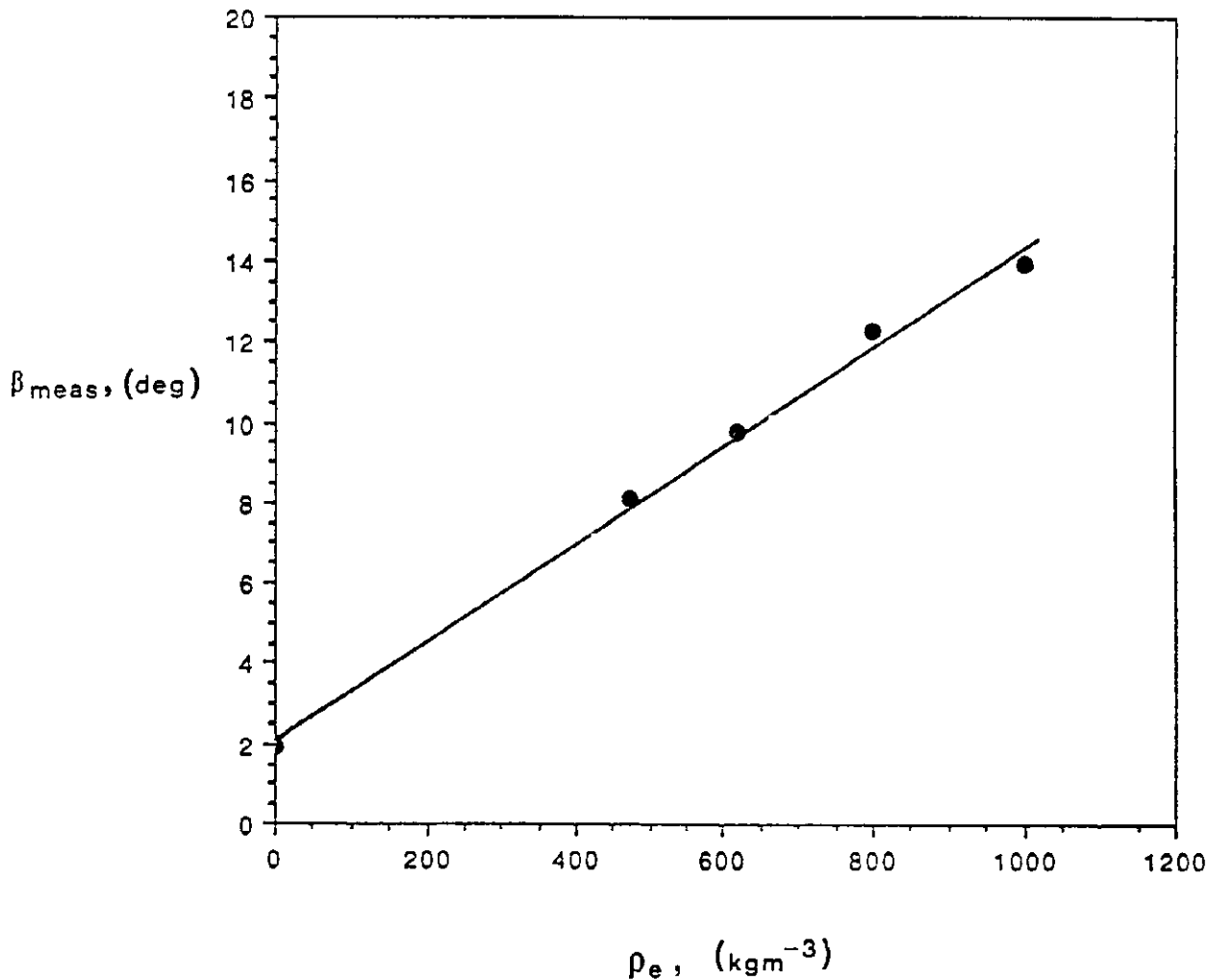
Figure 5.8   Measured jet angle vs recirculating eddy density
(Dc = 74 mm; no baffles; Dj = 4.76 mm; vj = 11.5 m/s;
ρ_L= 1000 kg/m^3; σ = 0.063 N/m; μL = 0.0009 Pa-s)

It can be seen from the results given in Table 5.4 that the jet angle decreases with decreasing mixture density inside the recirculating eddy. This trend is due to the reduction in the radial dissipation of jet momentum due to the increase in the density difference between the liquid inside the submerged jet and the recirculating eddy. When the jet angle is plotted against ρ_e as shown in Figure 5.8, the result is a straight line which is consistent with (5.52). The line can also be extrapolated to obtain a jet angle value of 2.1° when the recirculating eddy density is equal to zero, which is in agreement with the measured angle of 1.9° for the jet passing through air.

It has been shown in Figure 5.8 that the measured jet angle is directly proportional to the density of the mixture inside the recirculating eddy. To determine the effect of other system variables on the jet angle, the measured angle has been multiplied by the jet/eddy density ratio to account for the effect of having different recirculating eddy densities.

(b) Effect of column diameter

Table 5.5 contains values for the measured and corrected jet angle measurements as a function of column diameter.

TABLE 5.5 Effect of column diameter on the submerged jet angle
($Q_G/Q_L = 0.127$; $D_j = 4.76$ mm; $v_j = 11.5$ m/s;
$\rho_L = 1000$ kg/m³; $\sigma = 0.063$ N/m; $\mu_L = 0.0009$ Pa-s)

Column Diameter (mm)	Mixing Zone Length (mm)	Mixture Density (kg/m³)	Jet Angle Measured (deg)	Jet Angle Corrected (deg)	Maximum Recirculating Velocity (m/s)
44	148	847	8.5	10.0	1.488
74	170	800	12.3	15.4	0.970
95	157	759	16.8	22.1	0.776

It can be seen from Table 5.5 that the corrected jet angle increases with increasing column diameter, and when β_{corr} is plotted against D_c as shown in Figure 5.9, the graph is a straight line which is consistent with (5.52). Other features of the plot are: when the jet diameter is equal to D_c, the jet angle is zero; when D_J is less than D_c, negative values for the jet angle are obtained.
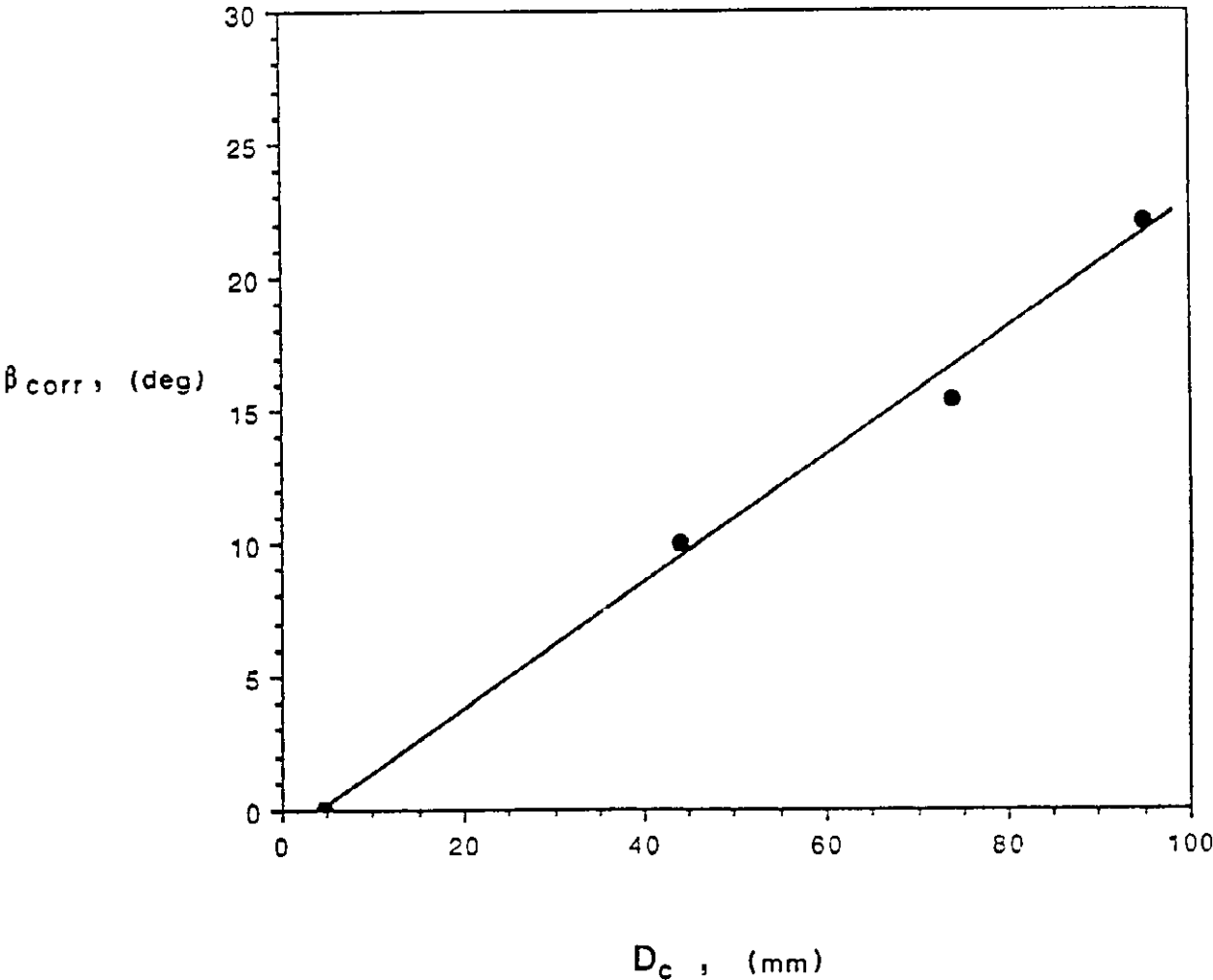
Figure 5.9   Corrected jet angle vs column diameter
(Q_G/Q_L = 0.127; D_J = 4.76 mm; v_J = 11.5 m/s;
ρ_L = 1000 kg/m³ ; σ = 0.063 N/m; μ_L = 0.0009 Pa-s)

In Figure 5.10 the corrected jet angle has been plotted against the
recirculating eddy maximum velocity, which is also given in Table 5.5.
From the graph it appears the curve can be extrapolated to obtain a 0°
value of jet angle when $(v_e)_{max}$ is equal to the jet velocity of
11.5 m/s. In this case the liquid at the boundary between the submerged
jet and the recirculating eddy are travelling at the same velocity, and
no radial jet momentum would be dissipated into the recirculating eddy.
Subsequently, there would be no expansion of the submerged jet.
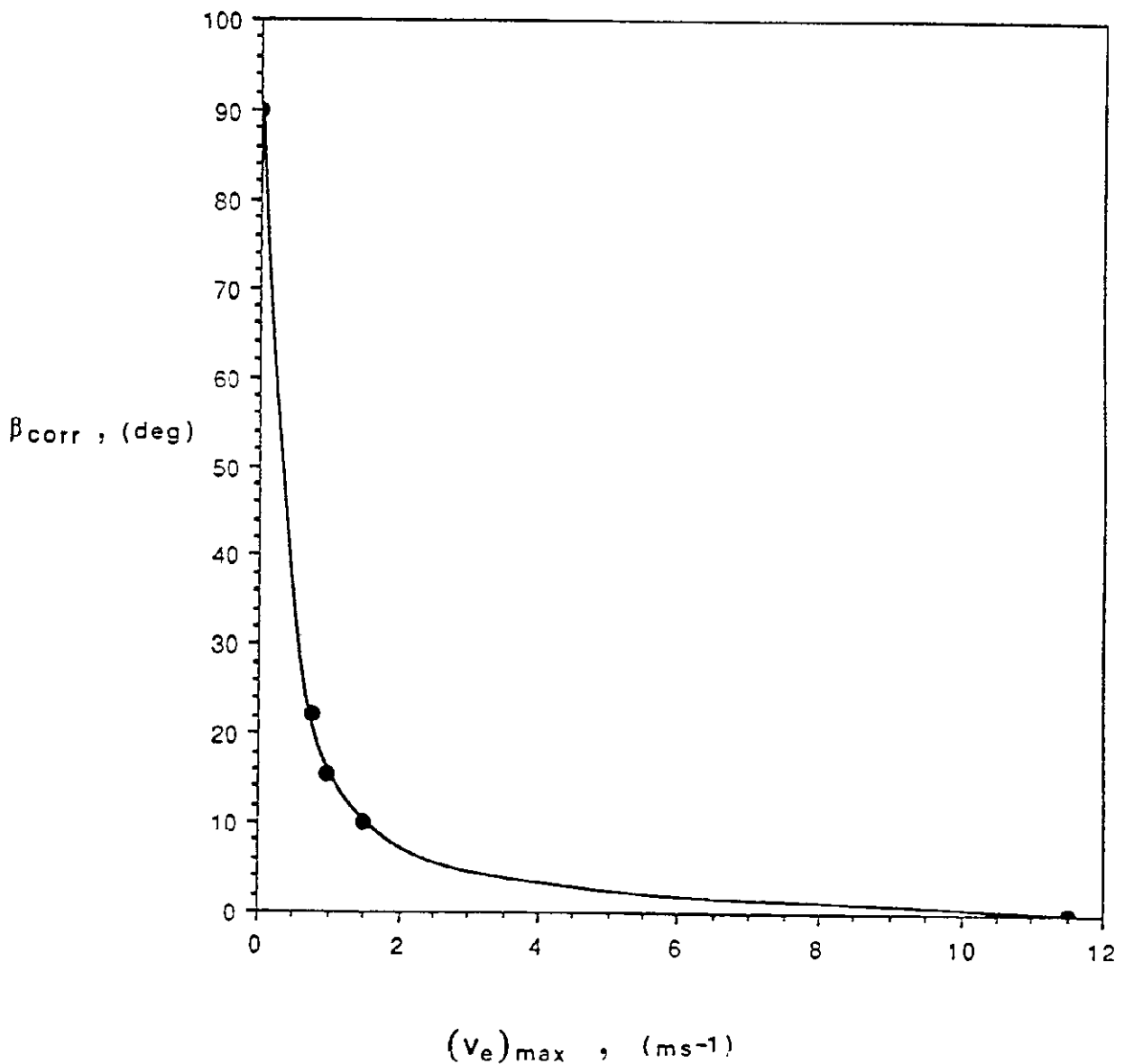
Figure 5.10 Corrected jet angle vs recirculating eddy maximum velocity
(No baffles; Q_G/Q_L = 0.127; D_j = 4.76 mm; v_j = 11.5 m/s;
ρ_L = 1000 kg/m³; σ = 0.063 N/m; μ_L = 0.0009 Pa-s)

It is also possible to extrapolate the curve given in Figure 5.10 to obtain a jet angle equal to 90° when $(v_e)_{max}$ is equal to zero. This result is consistent with (5.45) which can be rewritten as

$$\beta = \tan^{-1} \left\{ \frac{\rho_e Q_e \left[v_j - (v_e)_{max} \right]}{2\pi R_c L_{M2} (-\Delta P)} \right\} .$$

(5.53)

From (5.53) the jet angle will approach 90° when the length of the mixing zone approaches zero, i.e. the liquid inside the jet travels in the radial direction only. This condition corresponds to the jet striking a solid surface where the recirculating eddy maximum velocity is equal to zero.

(c) Effect of liquid density

Table 5.6 contains values for the jet angle for a range of liquid density values. It can be seen from the results the jet angle decreases with increasing liquid density, which is in consistent with (5.52).

TABLE 5.6 Effect of liquid density and absolute viscosity on the submerged jet angle (D_c = 44 mm; D_j = 4.76 mm; v_j = 11.5 m/s; σ = 0.063 N/m)

| Liquid | | Mixing Zone Length | Mixture Density | Jet Angle | |
| Absolute Viscosity | Density | | | Measured | Corrected |
(10^{-3}kg/(ms)	(kg/m³)	(mm)	(kg/m³)	(deg)	(deg)
0.871	1000	148	847	8.5	10.0
1.653	1064	198	929	6.4	7.3
2.854	1114	223	984	5.7	6.5

From (5.52) it can be seen that the jet angle should be inversely proportional to the square of the liquid density, and when β_{corr} is plotted against $1/(\rho_L)^2$ a straight line is obtained with a correlation coefficient equal to 0.966. Donald and Singer (1959) found that the jet angle was proportional to the kinematic viscosity of the liquid to the 0.1333 power, which suggests the jet angle is also a function of the absolute viscosity. Using the same value of the power exponent used by Donald and Singer, β_{corr} was plotted against $(1/\rho_L)^2(\mu_L)^{0.1333}$ and a straight line was obtained with a correlation coefficient equal to 0.989.

The improvement in the correlation coefficient obtained by including the absolute viscosity suggests a slight dependence of the jet angle on the liquid absolute viscosity which is not included in (5.52). It is possible the constant η in (5.49) has a functional dependence on the liquid viscosity, which is reasonable to expect since it is thought that η is a measure of the efficiency at which jet momentum is dissipated to generate a pressure force. The rate of dissipation is likely to be a function of the liquid absolute viscosity.

TABLE 5.7   Effect of jet diameter on jet angle for D_c = 44 and 74 mm (no baffles; v_j = 11.5 m/s; ρ_L = 1000 kg/m^3; σ = 0.063 N/m; μ_L = 0.0009 Pa-s)

Column Diameter (mm)	Jet Diameter (mm)	Mixing Zone Length (mm)	Mixture Density (kg/m^3)	Jet Angle Measured (deg)	Jet Angle Corrected (deg)
44	7.12	175	882	7.2	8.2
	4.76	148	847	8.5	10.0
	2.38	72	805	17.1	21.2
74	7.12	247	872	8.6	9.9
	4.76	170	800	12.3	15.4
	2.38	113	553	18.2	32.9

(d) Effect of jet diameter

Values for the submerged jet diameter for three different jet diameters
are listed in Table 5.7 for the 44 and 74 mm diameter columns. From the
results it can be seen that the jet angle decreases with increasing jet
diameter for both columns. In Figure 5.11 β_{corr} has been plotted against
the jet diameter.
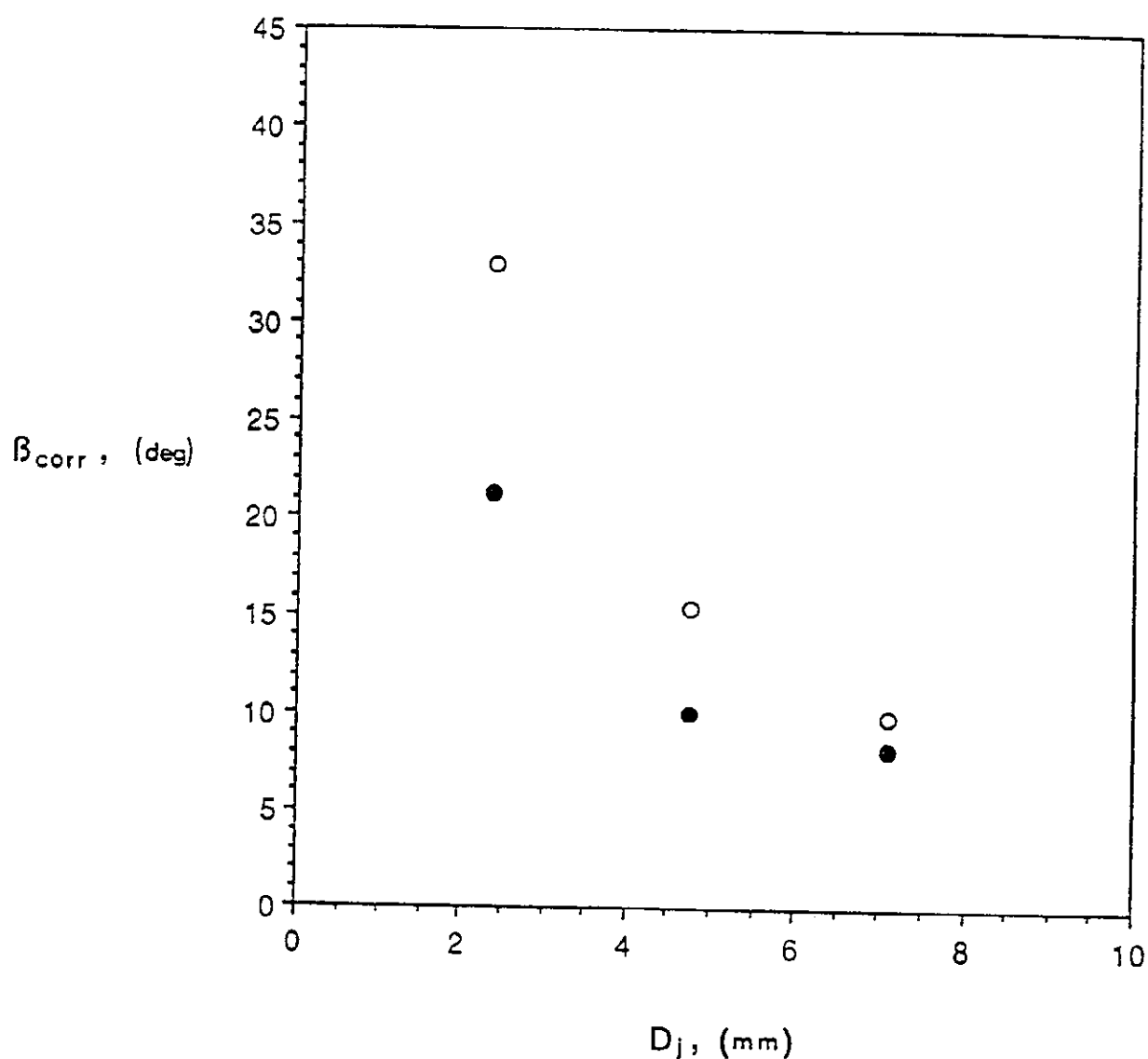
Figure 5.11 Corrected jet angle vs jet diameter for 44 ($\bullet$) and 74 (C) mm
diameter columns (no baffles; $\rho_L = 1000$ kg/m^3; $\sigma = 0.063$ N/m;
$\mu_L = 0.0009$ Pa-s)

It can be seen from Figure 5.11 that both curves appear to be hyperbolas with asymptote values for the corrected jet angle approaching 90° and 0° as the jet diameter approaches zero and the column diameter respectively. It is not possible to compare the trends shown in Figure 5.11 with those predicted from (5.52) as it applies only to systems where the Crayer-Curtet number is less than 0.5, which corresponds to the column diameter being at least twice the diameter of the jet. Clearly, this condition is not satisfied when the jet diameter approaches that of the column. However, it can be seen from (5.52) that as D_j approaches zero the jet angle approaches 90°, which is consistent with the experimental measurements.

(e) Effect of surface tension

The effect of surface tension on the jet angle is presented in Table 5.8 for the 4.76 mm and 7.12 mm diameter jets. It can be seen from the results that changing σ had no noticeable effect on either the two-phase mixture density or on the jet angle.

TABLE 5.8 Effect of surface tension on the jet angle for 4.76 and 7.12 mm diameter jets (D_c = 44 mm; v_j = 11.5 m/s; no baffles; ρ_L = 1000 kg/m³; μ_L = 0.0009 Pa-s)

Jet Diameter (mm)	Surface Tension (N/m)	Mixing Zone Length (mm)	Mixture Density (kg/m³)	Jet Angle Measured (deg)	Corrected (deg)
7.12	0.048	175	888	7.2	8.1
7.12	0.052	170	890	7.4	8.3
7.12	0.062	175	882	7.2	8.2
4.76	0.047	150	876	8.4	9.6
4.76	0.053	148	874	8.5	9.7
4.76	0.065	148	847	8.5	10.0

(f) Effect of jet velocity

Values for the jet angle as a function of the jet velocity are given in Table 5.9. From the results it can be seen the jet angle decreases with increasing jet velocity.

TABLE 5.9   Effect of jet velocity on the submerged jet angle
(D_c = 74 mm; D_j = 4.76 mm; ρ_L = 1000 kg/m³;
σ = 0.063 N/m; μ_L = 0.0009 Pa-s)

Velocity		$\dfrac{(v_e)_{max}}{v_j}$	Mixing Zone Length	Mixture Density	Jet Angle	
Jet	Eddy				Measured	Corrected
(m/s)	(m/s)		(mm)	(kg/m³)	(deg)	(deg)
15.0	1.276	11.76	248	822	8.5	10.3
11.5	0.976	11.78	170	800	12.3	15.4
7.8	0.663	11.77	74	750	26.7	35.6

The relationship between the the submerged jet angle and the jet velocity given in Table 5.9 can be compared to the prediction by examining the velocity terms appearing in (5.52), i.e.

$$\beta \simeq \left\{ \frac{v_j - (v_e)_{max}}{v_j^3} \right\} \, ,$$

or

$$\beta \simeq \left\{ 1 - \frac{(v_e)_{max}}{v_j} \right\} \, \frac{1}{v_j^2} \, . \qquad (5.54)$$

From Table 5.9 it can be seen that the ratio $\{(v_e)_{max}\}/v_j$ is constant.

Equation (5.54) can be rewritten as

$$\beta = K \frac{1}{v_j^2} \quad , \tag{5.55}$$

where K is a constant. From (5.55), the jet angle has been plotted
against $1/\{v_j\}^2$ in Figure 5.12 where it can be seen that the data points
have been fitted by a straight line passing through the origin with a
correlation coefficient equal to 0.995. This result is consistent with
(5.55).
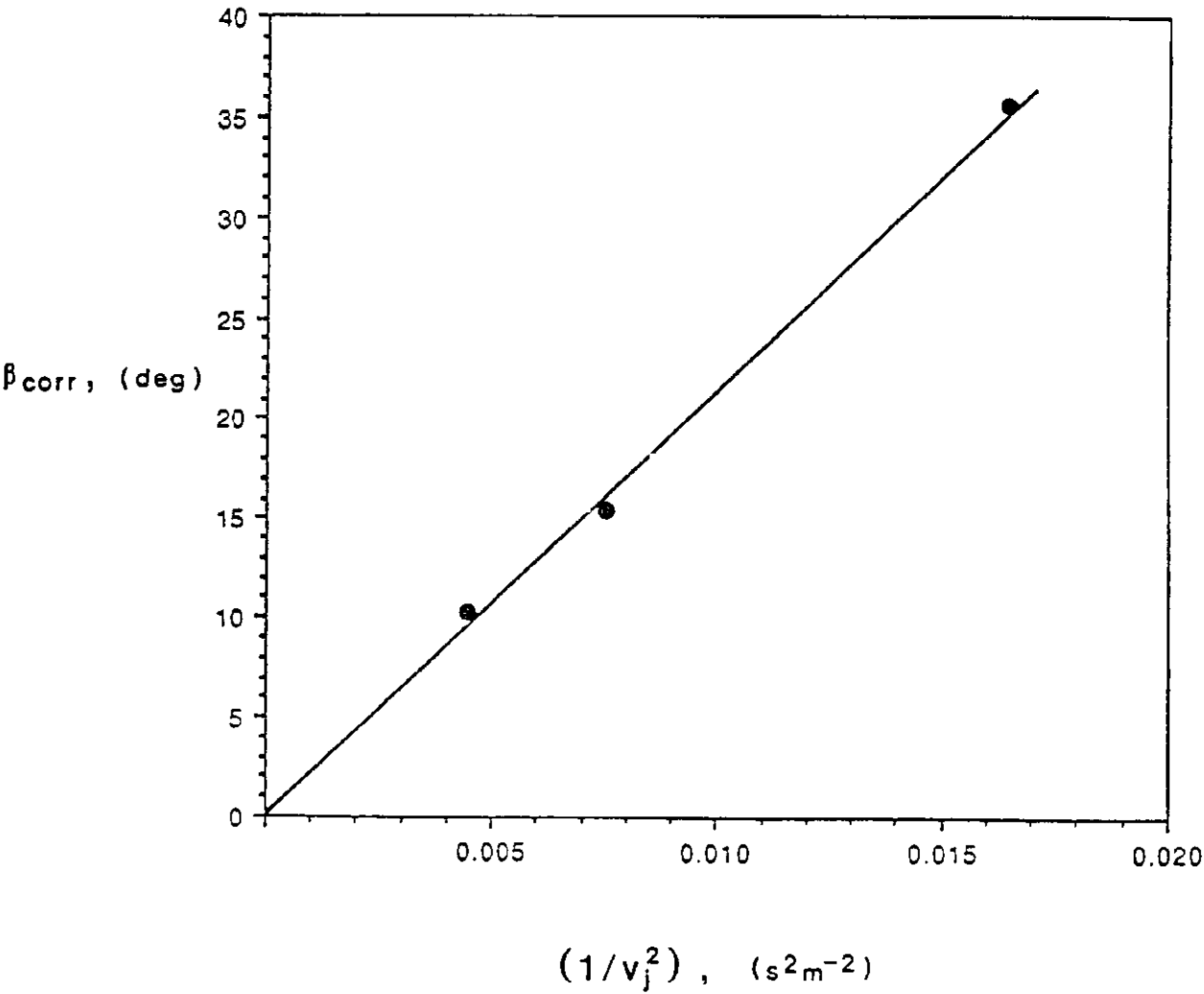
Figure 5.12   Corrected jet angle vs Inverse jet velocity function
(D_c = 74 mm; D_j = 4.76 mm; ρ_L = 1000 kg/m^3 ;
σ = 0.063 N/m; μ_L = 0.0009 Pa-s)

(g)   Jet angle constant

The value of η in (5.52) was found to be 0.089 by applying a least squares fit through the experimental jet angle measurements[13].

$$0.089\left[\frac{P_o}{\rho_L v_j^2}\right]\left[\frac{\rho_e}{\rho_L}\right]\left[\frac{0.37\sqrt{R_c^2 - \frac{1}{2}R_j^2} - 0.64R_j}{R_j}\right]\left\{\frac{v_j - (v_e)_{max}}{v_j}\right\}$$
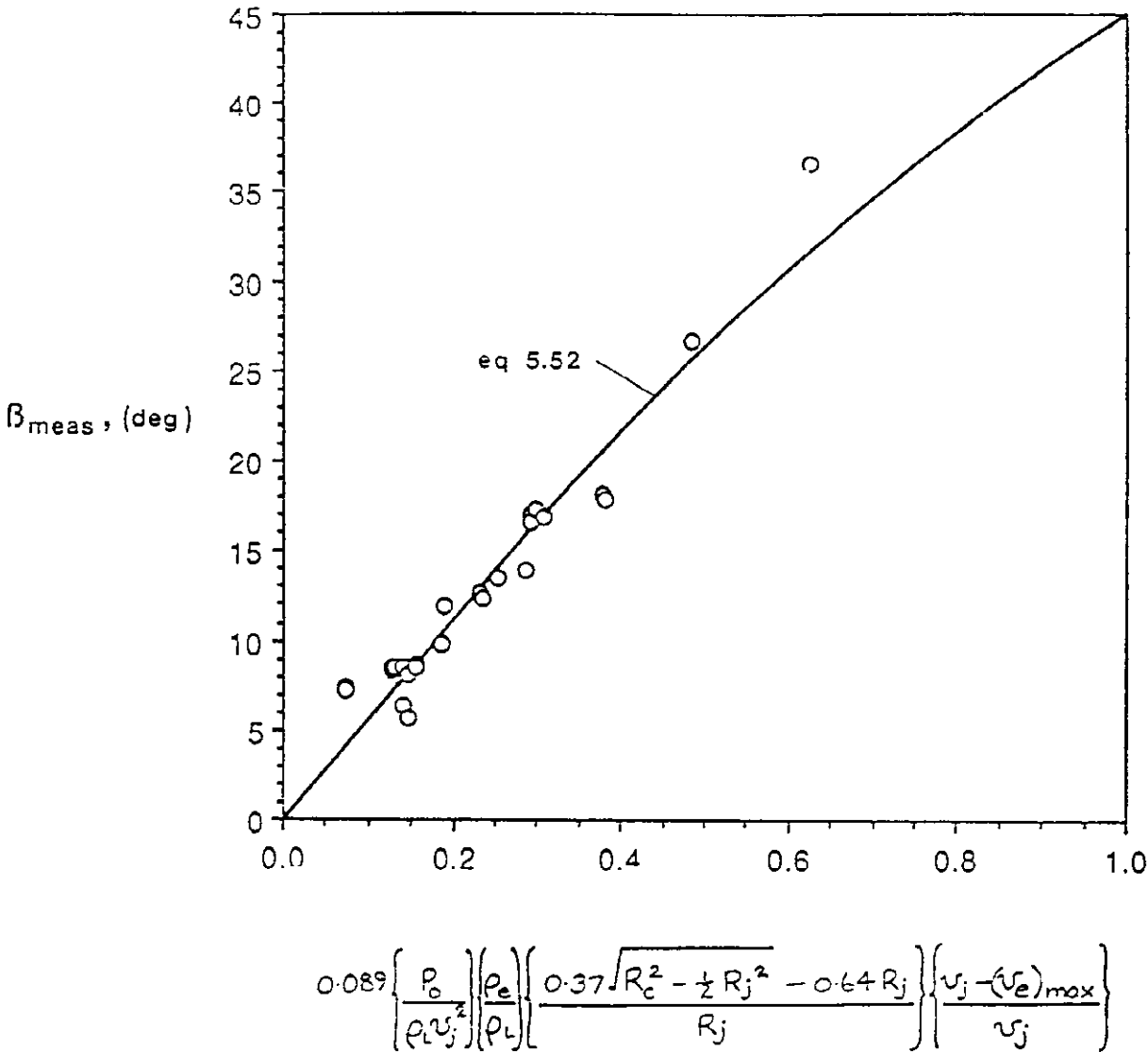
Figure 5.13   Comparison between measured and predicted jet angle values

If η is thought of as a measure of the efficiency at which the jet momentum is transferred into the recirculating eddy to produce a pressure

---

[13]Values for β_{meas} are given in Appendix 4.

force, its value can be compared to the mixing efficiencies of around 10 percent (0.1) obtained by Cunningham and Dopkin (1974), and Shimizu et al (1987) for the liquid-jet gas pump. Using a constant value of 0.089 in (5.52), the prediction[14] for the jet angle is shown in Figure 5.13 where it can be seen that the resultant curve is in good agreement with the experimental results.
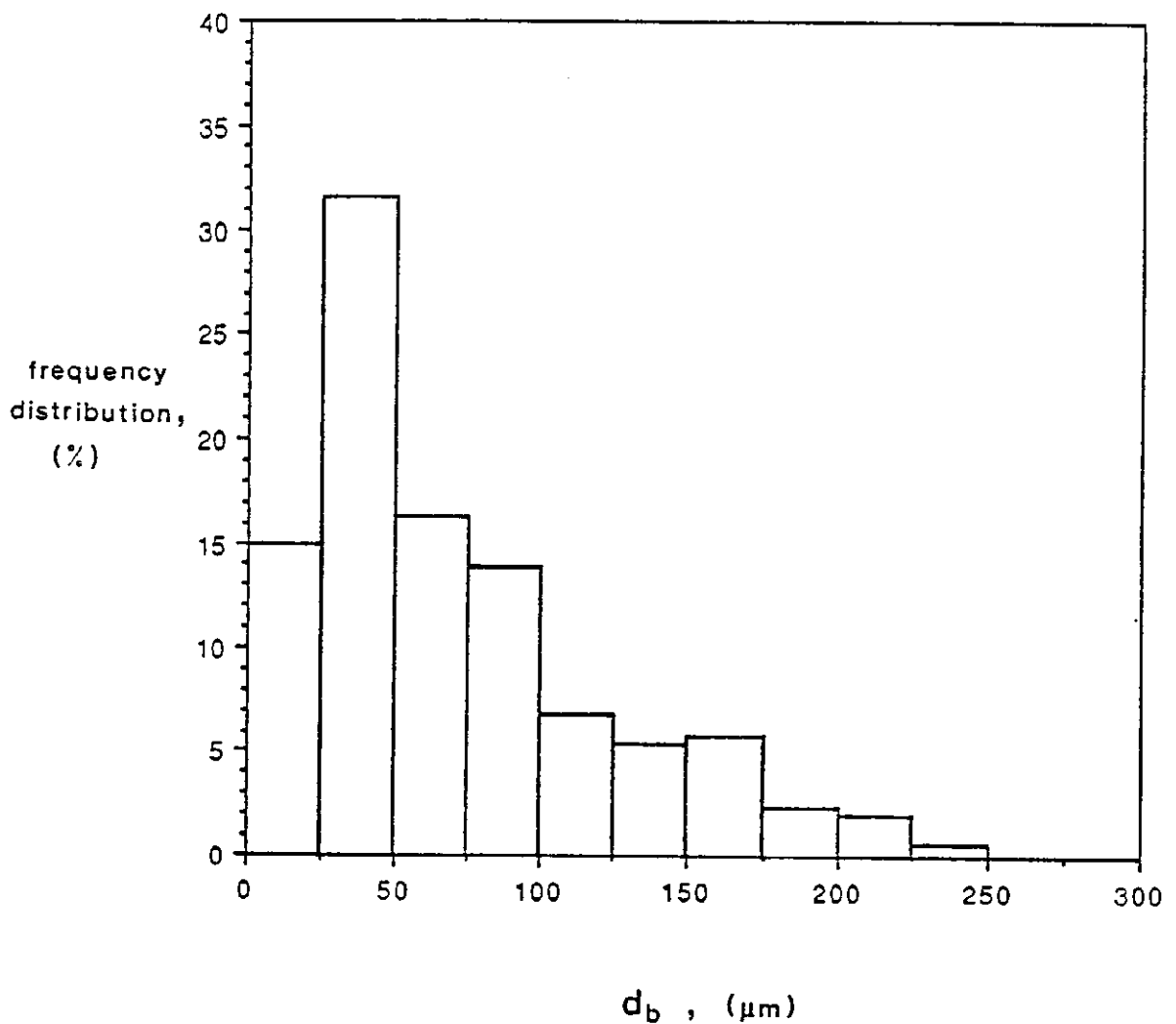
Figure 5.14 Frequency distribution curve for measured bubble diameter inside mixing zone (Run 2: D_c = 44 mm; ρ_L = 1000 kg/m^3; v_j = 11.5 m/s; D_j = 7.12 mm; μ_L = 0.001 Pa-s; σ = 0.048 N/m)

---

[14] Calculations for β_{corr} are given in Appendix 6

5.5.3 Bubble diameter distribution

The bubble diameter distribution generated within the mixing zone was
similar for all experimental runs. The frequency distributions were
bimodal, and could be reasonably represented by a log-normal
distribution. A typical frequency distribution curve obtained for an
experimental run is given in Figure 5.14, where it can be seen that the
distribution is bimodal.

The bimodal distribution could possibly be the result of the gas being
entrained into the mixing zone by two different entrainment mechanisms,
namely, that which is entrained as a film on the free surface of the
plunging jet, and that which is trapped within the boundary of the
plunging jet prior to impact. The gas inside the film would be subjected
to the high shearing forces acting at the submerged jet- recirculating
eddy boundary, while the gas inside the jet would be subjected to the
relatively lower-energy turbulent intensity fluctuations within the
submerged jet zone. The overall result of different forces acting on the
bubbles, depending on how the gas is entrained, is likely to produce a
bimodal bubble diameter distribution as shown by the experimental
results.

The experimental data from Figure 5.14 has been replotted on a log-
probability scale as shown in Figure 5.15. It can be seen that the
resultant curve consists of two straight lines, each having a different
slope. The observation that the plot is linear suggests the bubble
diameter distribution is log-normal, while the change in slope confirms
the presence of a bimodal distribution. The log-normal distribution is
most likely the result of the less stable larger bubbles being broken by
the shearing forces in the liquid, in preference to the more stable
smaller diameter bubbles. The preferential breakup of the larger bubbles
would result in a skewed bubble diameter distribution.
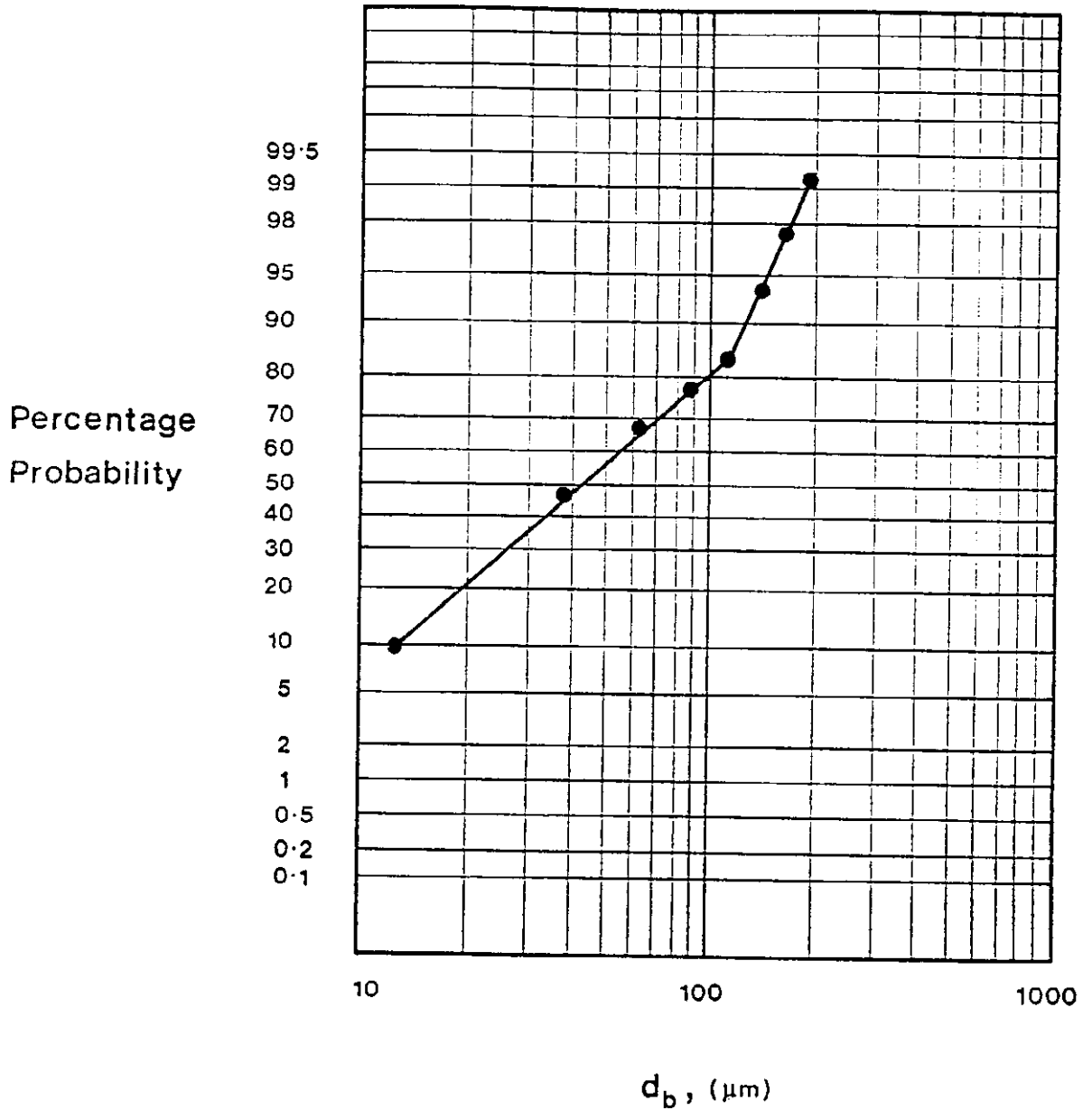
Figure 5.15 Log-probability plot of cumulative bubble diameter
distribution (Run 2: D_c = 44 mm; no baffles;
D_c = 7.12 mm; v_j = 11.5 m/s; ρ_L = 1000 kg/m³;
μ_L = 0.001 Pa-s; σ = 0.048 N/m)

5.5.4 Maximum bubble diameter

In this section the maximum bubble diameter, $(d_b)_{max}$, predicted by (5.31) is compared with the measured maximum value, $(d_b)_{99}$, which is the diameter that is greater than 99% of all the diameters in the cumulative distribution.

(a) Effect of gas-to-liquid volumetric flow ratio

Table 5.10 contains values for both the predicted and measured maximum bubble diameter for three different gas/liquid flow ratios.

TABLE 5.10 Effect of gas/liquid flow ratio on maximum bubble diameter
(D_c = 74 mm; no baffles; D_j = 4.76 mm; v_j = 11.5 m/s;
ρ_L = 1000 kg/m³; μ_L = 0.0009 Pa-s; σ = 0.063 N/m)

Gas/Liquid Flow Ratio	Bubble Diameter (µm)		Sauter Mean $(d_b)_{vs}$	$\dfrac{(d_b)_{vs}}{(d_b)_{99}}$
	Maximum			
	Measured $(d_b)_{99}$	Predicted $(d_b)_{max}$		
0.126	543	544	324	0.597
0.296	523	599	341	0.652
0.645	698	645	468	0.670

It can be seen from Table 5.10 that both the measured and predicted maximum bubble diameter increases with increasing Q_G/Q_L ratio. This is due to the volume of the mixing zone increasing with increasing gas-to-liquid ratio, while the energy input from the jet remains constant. The energy input per unit volume therefore decreases, which results in an increase in the maximum bubble diameter. The observation from Table 5.10 that the measured diameter is generally higher than the prediction is possibly due to the reduction in the turbulence intensity within the

mixing zone when bubbles are present. Bubble coalescence, which has not been accounted for in the model, could also account for the larger measured maximum bubble diameter.

(b) Effect of column diameter

Table 5.11 contains values for the measured and predicted maximum bubble diameter for three different diameter columns, with and without axial baffles installed.

TABLE 5.11 Effect of column diameter (and baffle installation) on the bubble diameter generated within the mixing zone (D_j = 4.76 mm; v_j = 11.5 m/s; ρ_L = 1000 kg/m^3; μ_L = 0.0009 Pa-s; σ = 0.063 N/m)

Column Diameter (mm)	Baffles Installed (Yes/No)	Bubble Diameter (µm)		Sauter Mean $(d_b)_{vs}$	$\dfrac{(d_b)_{vs}}{(d_b)_{99}}$
		Maximum			
		Measured $(d_b)_{99}$	Predicted $(d_b)_{max}$		
44	Yes	390	353	231	0.592
74		614	573	378	0.616
95		611	627	360	0.589
44	No	406	353	270	0.665
74		543	544	324	0.597
95		531	643	332	0.625

It can be seen from Table 5.11 that $(d_b)_{max}$ increases with increasing column diameter. This is due to the increase in the mixing zone volume with increasing column diameter while the energy input from the jet remains constant. Consequently, the energy dissipation rate per unit volume is less, which gives rise to the stable existence of larger diameter bubbles.

It can also be seen from Table 5.11 that the measured maximum diameter is greater than the prediction for the 44 mm diameter column irrespective of whether baffles were installed or not. This is possibly due to bubble coalescence. For the 74 mm and 95 mm diameter columns the motion of the bubbles is less and the probability of the bubbles having sufficient inertia to collide with each other and coalesce is significantly reduced. The absence of coalescence for the 74 and 95 mm diameter columns is indicated by the closer agreement between $(d_b)_{99}$ and $(d_b)_{max}$.

Finally, it can be seen from Table 5.11 that installing baffles inside the 74 and 95 mm diameter columns increased the measured maximum bubble diameter. The baffles possibly reduced the amount of liquid rotation inside the column which is generated by the jet. The rotational velocity component, not accounted for in the theory of bubble breakup, would increase the shear rate giving rise to smaller bubbles.

(c)   Effect of kinematic viscosity

Table 5.12 contains values for the measured and predicted maximum bubble diameter for three kinematic viscosity values.

TABLE 5.12   Effect of kinematic viscosity on the bubble diameter within the mixing zone (D_c = 44 mm; no baffles; D_j = 4.76 mm; v_j = 11.5 m/s; σ = 0.063 N/m)

Kinematic Viscosity (10^{-6} m²/s)	Bubble Diameter (μm)			$\dfrac{(d_b)_{vs}}{(d_b)_{99}}$
	Maximum		Sauter Mean $(d_b)_{vs}$	
	Measured $(d_b)_{99}$	Predicted $(d_b)_{max}$		
0.870	406	358	270	.665
1.558	318	381	187	.588
2.560	294	398	181	.616

It can be seen from Table 5.12 that $(d_b)_{99}$ decreases with increasing
liquid kinematic viscosity while $(d_b)_{max}$ increases with increasing ν_L.
The difference in the trends is possibly due to the effect of absolute
viscosity on the energy dissipation rate, causing bubble breakup to occur
within a volume less than that defined by (5.37). This effect would
increase with increasing absolute viscosity. Hence the increase in the
difference between the measured and predicted maximum diameter with
increasing ν_L.

(d) Effect of jet velocity

Table 5.13 contains values for the measured and predicted maximum bubble
diameter for three jet velocity values.

TABLE 5.13 Effect of jet velocity on the bubble diameter within the
the mixing zone (D_c = 74 mm; no baffles; D_j = 4.76 mm;
ρ_L = 1000 kg/m^3; μ_L = 0.0009 Pa-s; σ = 0.063 N/m)

Jet Velocity (m/s)	Bubble Diameter (μm) Maximum		Sauter Mean $(d_b)_{vs}$	$\dfrac{(d_b)_{vs}}{(d_b)_{99}}$
	Measured $(d_b)_{99}$	Predicted $(d_b)_{max}$		
15.0	584	473	349	.598
11.5	543	544	324	.597
7.8	718	630	430	.599

It can be seen from the table that $(d_b)_{max}$ increases with decreasing jet
velocity, which is expected since the energy input to the mixing zone is
proportional to the square of the jet velocity. Good agreement between
the measured and predicted values is obtained for jet velocity values of
11.5 and 7.8 m/s. For the higher jet velocity of 15 m/s, $(d_b)_{99}$ is

greater than the predicted diameter and this is possibly due to bubble
coalescence.

(e) Effect of jet diameter

Table 5.14 contains values for the measured and predicted maximum bubble
diameter for three jet diameters. The experiments were carried out using
the 44 mm and 74 mm diameter columns, with the installation of baffles
inside the 74 mm diameter column for some of the experiments.

TABLE 5.14 Effect of jet diameter on the bubble diameter
within the mixing zone (ρ_L = 1000 kg/m^3 ;
μ_L = 0.0009 Pa-s; σ = 0.063 N/m; v_j = 11.5 m/s)

Jet Diameter	Column Diameter	Baffles Installed	Bubble Diameter (μm)		Sauter Mean	$\dfrac{(d_b)_{vs}}{(d_b)_{99}}$
			Maximum			
			Measured	Predicted		
(mm)	(mm)	(Yes/No)	$(d_b)_{99}$	$(d_b)_{max}$	$(d_b)_{vs}$	
2.38	44	No	412	380	233	0.566
4.76			222	288	136	0.613
7.12			280	226	156	0.557
2.38	74	No	594	813	372	0.626
4.76			543	544	324	0.597
7.12			441	457	264	0.599
2.38	74	YES	716	796	488	0.682
4.76			614	573	378	0.616
7.12			488	457	314	0.605

It can be seen from the Table that for both columns the maximum bubble
diameter decreased with increasing jet diameter.   This is due to the

increase of the energy input into the mixing zone as a result of the higher mass flowrate associated with the increase in the jet diameter. It can also be seen from Table 5.14 that the measured maximum bubble diameter increased as a result of installing baffles inside the 74 mm diameter column. Possibly, the addition of baffles reduced the amount of rotation of the liquid inside the column, resulting in an increase in the bubble size.

(f)   Effect of surface tension

Table 5.15 contains values for the measured and predicted maximum bubble diameter for three surface tension values. It can be seen that, in most cases, $(d_b)_{99}$ followed the predicted trend where the bubble size increased with increasing surface tension. Also, the agreement between the predicted and measured maximum bubble diameter was improved with decreasing surface tension, where the likelihood of coalescence occurring was decreased.

TABLE 5.15   Effect of surface tension on the bubble diameter within the mixing zone (D_c = 44 mm; no baffles; v_j = 11.5 m/s; ρ_L = 1000 kg/m³; μ_L = 0.0009 Pas)

| Surface Tension (N/m) | Jet Diameter (mm) | Bubble Diameter (μm) | | Sauter Mean $(d_b)_{vs}$ | $\dfrac{(d_b)_{vs}}{(d_b)_{99}}$ |
| | | Maximum | | | |
		Measured $(d_b)_{99}$	Predicted $(d_b)_{max}$		
0.047	4.76	248	257	153	0.617
0.053		222	288	136	0.613
0.065		406	353	270	0.665
0.048	7.12	222	203	129	0.581
0.054		280	226	156	0.557
0.062		387	275	242	0.625

5.5.5 Bubble diameter ratio

From the results given in Tables 5.10 - 5.15 the average value for the bubble diameter ratio $\{(d_b)_{vs}\}/\{(d_b)_{99}\}$ was found to be 0.61, with a standard deviation of 0.03. This result is consistent with the literature values reported in Table 5.3.

5.6 SUMMARY

In this chapter a model has been developed to predict the maximum stable bubble diameter able to exist within the mixing zone of the plunging jet bubble column. The model was based on a critical Weber number equal to 1.1 where the specific energy dissipation term was given by the mixing loss derived by Cunningham (1974) for liquid-jet gas ejectors. The mixing loss was assumed to be dissipated within a volume equivalent to that of the submerged jet as it expanded to occupy the entire cross-sectional area of the bubble column.

The expansion of the submerged jet was predicted by equating the momentum loss of the recirculating eddy at the wall of the column with the radial dissipation of jet momentum. The radial dissipation of jet momentum to the recirculating eddy was assumed to be a function of the Euler number for the system based on the initial jet velocity and the pressure in the headspace at the top of the column.

The bubble diameter distributions generated in the mixing zone were found to be bimodal and followed a log-normal distribution. The measured maximum bubble diameter values, which were taken as the diameter which was greater than 99% of all the diameters in the cumulative distribution, were found, in the majority of cases, to agree within 10% of the predicted values. The experimental measurements also gave the bubble diameter ratio equal to 0.61 with a standard deviation of 0.03, which was consistent with the results reported in the literature.

Chapter 6

UNIFORM TWO-PHASE FLOW ZONE

6.1 INTRODUCTION

In the mixing zone of the plunging jet bubble column the gas and liquid
phases are intimately mixed to produce a uniform two-phase dispersion
which flows downwards and exits through the outlet at the base of the
column. The hydrodynamics of the uniform two-phase flow zone are
determined by the gas and liquid flowrates, liquid physical properties
and the initial bubble diameter distribution produced within the mixing
zone. There are a number of different flow regimes which can develop in
the uniform two-phase flow zone as illustrated in Figure 6.1.

At low gas flowrates "bubbly" flow exists in which small discrete bubbles
of different diameters move downward with the bulk liquid flow but not
generally at the same velocity as the liquid phase. The smaller bubbles
tend to collect towards the centre of the column where they exhibit a
faster downward velocity than the larger bubbles, which tend to
accumulate near the wall of the column. If the gas flowrate is increased
then the discrete bubbles coalesce and alternating gas and liquid
regions, or slugs, form inside the column. The gas slugs have
hemispherical caps which occupy nearly the entire diameter of the column.
These slugs are known as Dumitrescu[15] bubbles and the resulting flow is
known as slug flow. In most cases the drag and viscous forces are
sufficiently great to give the Dumitrescu bubbles a net downward

---

[15] see Dumitrescu (1943)

velocity. For even higher gas flowrates the length and velocity of the
slugs increases until the shearing forces present make them unstable. A
breakdown of the bubble occurs, resulting in a chaotic mixture of gas and
liquid packets. This type of flow behaviour is known as "churn-turbulent"
flow. Finally, for very high gas flowrates "annular" flow exists where
the liquid flows down the walls of the column and there is a gas core in
the centre.
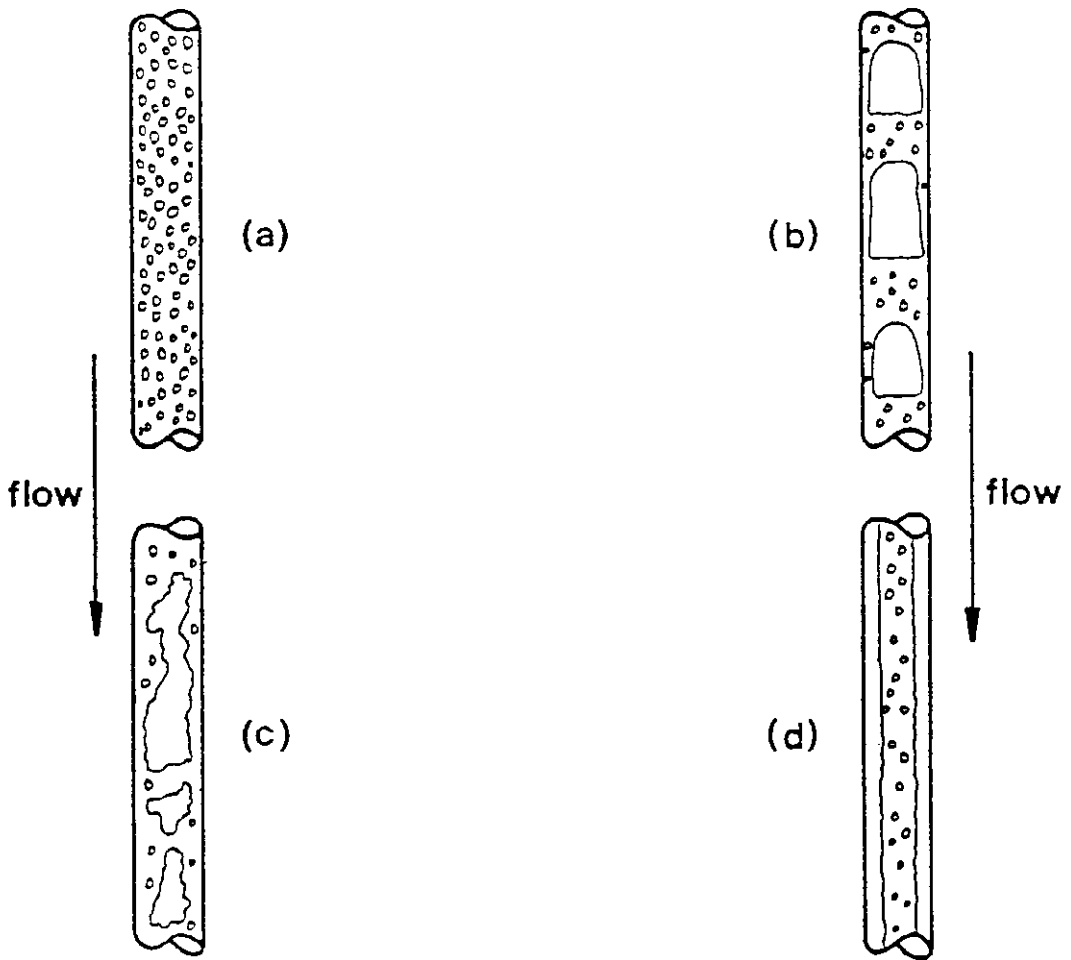
Figure 6.1   Flow pattern transitions for two-phase
             downward flow (a) bubbly (b) slug
             (c) churn-turbulent (d) annular

The abovementioned flows differ in their characteristics such as the pressure gradient, and the specific interfacial area. For a given gas-liquid flow ratio bubbly flow produces the greatest amount of interfacial area followed by churn-turbulent, slug and finally, annular flow. For bubbly flow the interfacial area is calculated from a knowledge of the bubble diameter distribution and the gas void fraction. A number of different studies have attempted to predict the gas void fraction for cocurrent gas-liquid downflow systems from experimental results (Friedel et al, 1980; Shah et al, 1983; Herbrechtsmeier et al, 1985).
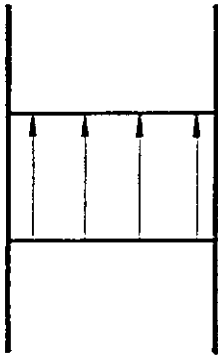
One-dimensional model (without local slip)
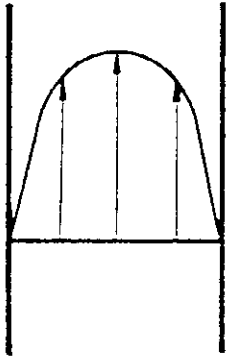
Two-dimensional model (without local slip)
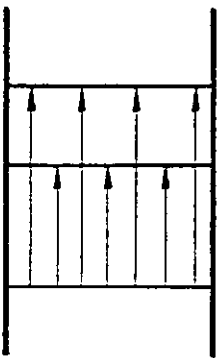
One-dimensional model (with local slip)
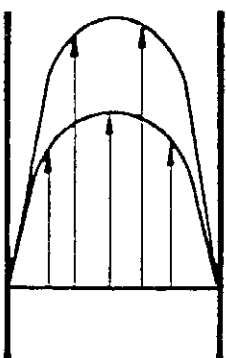
Two-dimensional model (with local slip)

Figure 6.2   Definition of gas and liquid velocity profiles
for different single mixture models

A number of theoretical models have also been developed to relate the gas void fraction to the system properties. The simplest form is the "single-mixture" model which assumes average fluid properties for each of the two phases with the mixture treated as a pseudofluid which obeys the continuity and momentum equations for single component flow. A number of different flow profiles have been assumed for the gas and liquid phases in the development of single-mixture models as illustrated in Figure 6.2.

The one-dimensional model (without local slip) defined in Figure 6.2 assumes that the gas and liquid phases behave as a single mixture moving at a uniform velocity throughout the system. Bankoff (1960) improved this model by allowing velocity variations to occur across the flow area by assuming a two-dimensional velocity profile. This model is given in Figure 6.2 as the two-dimensional model (without local slip). Wallis (1962) later developed the "one-dimensional drift-flux" model which allowed for local slip between the gas and liquid phases but it did not allow for velocity variations across the flow field. Zuber and Findlay (1965) combined the improvements developed by Bankoff (1960) and Wallis (1962) to develop the "two-dimensional drift-flux" model which included both the variation in radial velocity and also the local slip between the two phases. The main limitation with single mixture models, however, is that they do not consider the interaction between the gas and liquid phases which can have a significant influence on the system.

Such limitations were overcome by the development of the "separated-flow" model, first developed by Brodkey (1967), and later extended by Ishii and Zuber (1979), which included separate continuity, momentum and energy equations for the two phases. These equations were solved simultaneously, together with the interfacial rate equations, to determine how the two phases reacted with each other. Although separated-flow models are considerably more complex than the single mixture models, they do have the potential for predicting transitions in the type of flow pattern provided that the interfacial rate equations are accurately defined.

When operating a bubble column it is important to be able to ensure stable operation, and not only does bubbly flow give the best interfacial area characteristics, it also provides the most stable set of operating conditions. In the plunging jet bubble column the bubbles are typically

less than 1 mm in diameter and the downward superficial liquid velocity
is sufficiently high to ensure that the bubbles are carried downward and
discharged from the column through the opening at the base. For slug or
churn-turbulent flow the bubbles have much greater buoyancy and can rise
against the downflowing liquid. The result is a recirculation of the gas
phase inside the column, thereby reducing the gas handling capacity, and
in some cases can lead to the total collapse of the froth inside the
column. For this reason it is very important to know under what
conditions a transition from bubble to slug or churn-turbulent flow will
take place. This information is usually presented in the form of a flow-
pattern "map" which defines the boundaries where the different types of
flow exist under a given set of conditions.

Most flow-pattern maps have been obtained by performing a number of
experiments over a range of gas and liquid flowrates, fluid properties,
and column diameters and observing the flow pattern through a transparent
section of the column. The observed boundaries between the different
flow types is then mapped onto a two-dimensional plot by selecting
suitable co-ordinates for the two axes. To date no theoretical basis has
been applied to the selection of the co-ordinates, but instead most
researchers have relied on experimental data or dimensional arguments to
prepare their flow-pattern map. With dimensional flow-pattern maps
usually the volumetric or mass flowrates are used for the co-ordinate
axes. However, the use of dimensional co-ordinates restricts the use of
the map to other systems. Non-dimensional co-ordinates can be applied by
analysing the variables influencing the system. Some of the more common
dimensionless groups which have been used are:

$$\frac{j_G + j_L}{\{g D_c\}^{1/2}} \quad ; \quad \frac{j_G}{j_L} \quad ; \quad \frac{g \rho_L^2 D_c^3}{\mu_L^2} \quad ; \quad \frac{\rho_G}{\rho_L} \quad ; \quad \frac{\mu_G}{\mu_L} \quad ; \quad \frac{G \rho_L D_c}{\mu_L^2} \quad .$$

The advantage of developing a flow-pattern map based on a dimensionless
co-ordinate system is that it can possibly be applied to other
experimental conditions.

The aims of this chapter are to present a description of the different
models which have been used to calculate the gas void fraction for the
uniform two-phase flow region inside the bubble column. The description
is limited to the single mixture models of Wallis (1962) and Zuber and

Findlay (1965), and the separated flow model of Ishii and Zuber (1979).
A review of the different flow-pattern maps which have been developed for
downward flow is then given, with emphasis placed on the transition from
bubbly to slug or churn-turbulent flow. The influence of bubble diameter
on the flow transition is also discussed. Finally, the experimental gas
void fraction, bubble diameter and flow transitions for a range of
operating variables are compared with the predicted values from the
existing models.

6.2 SINGLE MIXTURE MODELS

6.2.1 One-dimensional drift-flux model

The one-dimensional drift-flux model developed by Wallis (1962) can be
used to predict the average gas void fraction of the system. The model
is based on the assumption that the shear stres at the wall can be
neglected and consequently the velocities for both the gas and liquid
phases are constant across the flow area. The model also assumes the
variables of the system are time and position independent (denoted by by
angle brackets, < >). Wallis defines a drift velocity, v', for each
phase which is the difference between the component linear velocity, v,
and the total volumetric flux, J, for the mixture, i.e.

$$\langle v_G' \rangle = \langle v_G \rangle - \langle J \rangle \quad ; \qquad (6.1a)$$

$$\langle v_L' \rangle = \langle v_L \rangle - \langle J \rangle \quad , \qquad (6.1b)$$

where $\langle v_G' \rangle$ and $\langle v_L' \rangle$ are the gas and liquid drift velocities
respectively. The gas and liquid linear velocities are given by:-

$$\langle v_G \rangle = \frac{\langle Q_G \rangle}{A \langle \epsilon \rangle} \quad ; \qquad (6.2a)$$

$$\langle \dot{v}_L \rangle = \frac{\langle Q_L \rangle}{A(1 - \langle \epsilon \rangle)} \quad , \tag{6.2b}$$

where A is the cross-sectional flow area and $\langle \epsilon \rangle$ is the gas void
fraction. The total volumetric flux, or the superficial velocity as it
is often called, is equal to the sum of the volumetric flux values for
the liquid and gas phases:-

$$\langle J \rangle = \langle j_G \rangle + \langle j_L \rangle \quad , \tag{6.3}$$

where $\langle j_G \rangle$ and $\langle j_L \rangle$ are given by

$$\langle j_G \rangle = \frac{\langle Q_G \rangle}{A} \quad , \tag{6.4a}$$

and

$$\langle j_L \rangle = \frac{\langle Q_L \rangle}{A} \quad . \tag{6.4b}$$

Wallis also defines drift flux terms $\langle j'_G \rangle$ and $\langle j'_L \rangle$ for the gas and
liquid phases respectively, as being equal to the drift velocity
multiplied by the fractional flow area occupied by the phase, i.e.

$$\langle j'_G \rangle = \langle v'_G \rangle \langle \epsilon \rangle \quad , \tag{6.5a}$$

and

$$\langle j'_L \rangle = \langle v'_L \rangle \left(1 - \langle \epsilon \rangle \right) \quad . \tag{6.5b}$$

By assuming there is no net drift through the plane moving at the
superficial velocity of the mixture, the system can be described by
analysing the flow equations for either the gas or liquid phases.
Considering the gas phase only, (6.5a) can be written using only the
volumetric flux terms and the gas void fraction, i.e.

$$\langle j_G' \rangle = \langle j_G \rangle (1 - \langle \epsilon \rangle) - \langle j_L \rangle \langle \epsilon \rangle \ . \tag{6.6}$$

Alternatively, using the linear velocity difference between the gas and
liquid phases, $\langle v_s \rangle$, and the gas void fraction:

$$\langle j_G' \rangle = \langle v_s \rangle (1 - \langle \epsilon \rangle) \langle \epsilon \rangle \ ; \tag{6.7}$$

where $\langle v_s \rangle$ is often called the slip velocity and is given by

$$\langle v_s \rangle = \langle v_G \rangle - \langle v_L \rangle \ . \tag{6.8}$$

Equation (6.6) is a general expression based on the principle of
continuity for the gas and liquid phases while (6.7) contains information
about the properties of the system through the slip velocity term.
Wallis (1969) obtained an alternative expression for the gas drift flux
for systems where the net force was zero, such as in one-dimensional
vertical flow where gravity was balanced by the pressure gradient and the
forces between the components. For this case the gas drift-flux is a
function of the gas void fraction and system properties only, i.e.

$$\langle j_G' \rangle = f (\epsilon, \text{system properties}) \ . \tag{6.9}$$

The major influence of the system properties is on the terminal velocity
of the bubbles, $(v_b)_\infty$, rising in an infinite fluid. In this case (6.9)
can be rewritten as

$$\langle j_G' \rangle = (v_b)_\infty \, f(\epsilon) \quad , \tag{6.10}$$

where $f(\epsilon)$ is a function of the gas void fraction only. Wallis equated (6.7) and (6.10) to obtain the expression

$$\frac{\langle v_s \rangle}{(v_b)_\infty} = g(\epsilon) \quad , \tag{6.11}$$

which relates the gas void fraction of the system to the slip velocity between the two phases and the terminal rise velocity of the bubbles. The gas drift flux for a given set of gas and liquid volumetric flux values is found by combining (6.7) and (6.11):

$$\langle j_G' \rangle = (v_b)_\infty \, g(\epsilon)(1 - \langle \epsilon \rangle)\langle \epsilon \rangle \quad , \tag{6.12}$$

where expressions for $g(\epsilon)$ are given in Table 6.1. which contains the updated list compiled by Deckwer and Schumpe (1987).

TABLE 6.1   Suggested forms of $g(\epsilon)$ reported in the literature

Author	$g(\epsilon)$
Richardson and Zaki (1954)	$\epsilon(1-\epsilon)^n$ $n=4.45+19.5d_b/D_c$ (Re<500), $n=2.39$ (Re>500), where $Re = (\rho_L j_L D_c)/\mu_L$.
Griffith and Wallis (1961)	$\epsilon(1-\epsilon)^n$ $n=2$ (small bubbles): $n=0$ (large bubbles).
Marrucci (1965)	$\dfrac{\epsilon(1-\epsilon)^2}{(1-\epsilon^{5/3})}$
Turner (1966)	$\epsilon(1-\epsilon)$
Davidson and Harrison (1966)	ϵ
Akita and Yoshida (1973)	$\dfrac{\epsilon}{(1-\epsilon)^4}$
Lockett and Kirkpatrick (1975)	$\epsilon(1-\epsilon)^{2.39}(1+2.55\epsilon^3)$
Mersman (1978)	$\dfrac{\epsilon}{(1-\epsilon)^4\sqrt{c_D}}$, c_D = bubble drag coeff.
Kara et al (1982)	$\epsilon(1-\epsilon)^m$, $m = -(5.392+1.899Re_L)$.
Shah et al (1983)	$\epsilon(1-\epsilon)^{1.74}$ (air-water). $\epsilon(1-\epsilon)^{2.39}(CN)^{-0.07}$ (air-alcohol soln) CN = No. C atoms.

A typical drift flux curve generated by (6.12) is illustrated in
Figure 6.3. Also shown in Figure 6.3 is the graphical solution to (6.6)
which relates the gas void fraction to the gas and liquid volumetric flux
values.
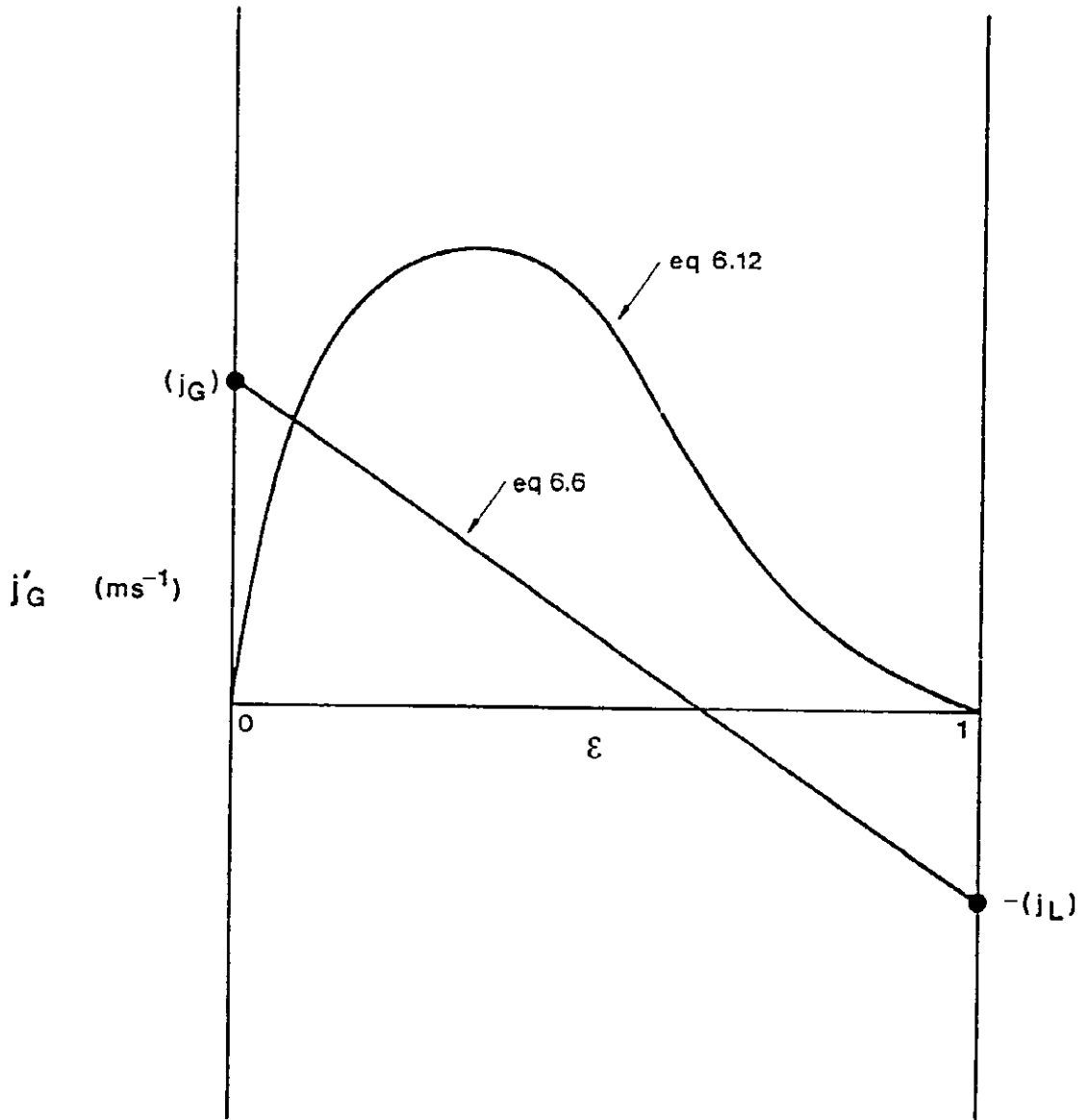
Figure 6.3 Drift flux solution for gas void fraction in
vertically-upward cocurrent gas-liquid flow

The graph shown in Figure 6.3 is constructed from (6.6) by drawing a line between the drift flux values for $\langle\epsilon\rangle$ equal to zero and unity, and realising that

(i)   when $\langle\epsilon\rangle = 0$, $\langle j_G{}'\rangle = \langle j_G\rangle(1-0) - \langle j_L\rangle 0 = \langle j_G\rangle$,

(ii) when $\langle\epsilon\rangle = 1$, $\langle j_G{}'\rangle = \langle j_G\rangle(1-1) - \langle j_L\rangle 1 = -\langle j_L\rangle$.

     (N.B.   The upward direction has been taken as positive)

The gas void fraction for a given gas and volumetric flux combination is obtained from the intersection of the continuity based drift-flux line given by (6.6) and the experimental curve.

6.2.2 Two-dimensional drift-flux model

Zuber and Findlay (1965) extended the one-dimensional drift-flux model developed by Wallis (1962) to account for variations in phase concentrations and velocities across the flow area. They accounted for the spatial variation in the gas void fraction and velocity profile by replacing the time and position average values used by Wallis with weighted mean values (denoted by [ ]) defined by

$$[F] = \frac{(\frac{1}{A})_A \int \epsilon F dA}{(\frac{1}{A})_A \int \epsilon dA} \equiv \frac{\langle\epsilon F\rangle}{\langle\epsilon\rangle} , \qquad (6.13)$$

where F is the quantity under consideration and is weighted for variations across the cross-sectional flow area A. By replacing the drift velocity expressions defined by Wallis (1962) with weighted mean values, Zuber and Findlay obtained

$$[v_G{}'] = [v_G] - [J] . \qquad (6.14a)$$

and

$$\left[v_L' \right] = \left[v_L \right] - \left[J \right] . \qquad (6.14b)$$

By applying the weighted mean definition given by (6.13), (6.14a) and (6.14b) can be rewritten as

$$\left[v_G' \right] = \frac{\langle \epsilon v_G \rangle}{\langle \epsilon \rangle} - \frac{\langle \epsilon J \rangle}{\langle \epsilon \rangle} , \qquad (6.15a)$$

and

$$\left[v_L' \right] = \frac{\langle \epsilon v_L \rangle}{\langle \epsilon \rangle} - \frac{\langle \epsilon J \rangle}{\langle \epsilon \rangle} \qquad (6.15b)$$

Zuber and Findlay (1965) define a Distribution Parameter C_o, as

$$C_o = \frac{\frac{1}{A} \int_A \epsilon J \, dA}{\left\{ \frac{1}{A} \int_A \epsilon \, dA \right\} \left\{ \frac{1}{A} \int_A J \, dA \right\}} = \frac{\langle \epsilon J \rangle}{\langle \epsilon \rangle \langle J \rangle} , \qquad (6.16)$$

which represents the ratio of the average of the product of the total volumetric flux and the gas void fraction, to the product of the averages of the two terms. Considering only the gas drift velocity expression given by (6.15a), $[v_G']$ is equal to

$$\left[v_G' \right] = \frac{\langle \epsilon v_G \rangle}{\langle \epsilon \rangle} - C_o \langle J \rangle , \qquad (6.17)$$

and realising that

$$\langle \epsilon v_G \rangle = \langle j_G \rangle , \qquad (6.18)$$

and

$$\left[\upsilon_L{}' \right] = \left[\upsilon_L \right] - \left[J \right] .$$

(6.14b)

By applying the weighted mean definition given by (6.13), (6.14a) and (6.14b) can be rewritten as

$$\left[\upsilon_G{}' \right] = \frac{\langle \epsilon \upsilon_G \rangle}{\langle \epsilon \rangle} - \frac{\langle \epsilon J \rangle}{\langle \epsilon \rangle} ,$$

(6.15a)

and

$$\left[\upsilon_L{}' \right] = \frac{\langle \epsilon \upsilon_L \rangle}{\langle \epsilon \rangle} - \frac{\langle \epsilon J \rangle}{\langle \epsilon \rangle}$$

(6.15b)

Zuber and Findlay (1965) define a Distribution Parameter C_o, as

$$C_o = \frac{\frac{1}{A} \int_A \epsilon J \, dA}{\left\{ \frac{1}{A} \int_A \epsilon \, dA \right\} \left\{ \frac{1}{A} \int_A J \, dA \right\}} = \frac{\langle \epsilon J \rangle}{\langle \epsilon \rangle \langle J \rangle} ,$$

(6.16)

which represents the ratio of the average of the product of the total volumetric flux and the gas void fraction, to the product of the averages of the two terms. Considering only the gas drift velocity expression given by (6.15a), $[\upsilon_G{}']$ is equal to

$$\left[\upsilon_G{}' \right] = \frac{\langle \epsilon \upsilon_G \rangle}{\langle \epsilon \rangle} - C_o \langle J \rangle ,$$

(6.17)

and realising that

$$\langle \epsilon \upsilon_G \rangle = \langle j_G \rangle ,$$

(6.18)

Equation (6.17) becomes:

$$\frac{\langle j_G \rangle}{\langle \epsilon \rangle} = C_o \langle J \rangle + \langle v'_G \rangle \qquad (6.19)$$

In order to use (6.19) to calculate $\langle \epsilon \rangle$ from the volumetric flux values and [v_G'], Zuber and Findlay (1965) attempted to predict values for C_o. In practice the Distribution parameter has been determined experimentally by plotting $\langle j_G \rangle / \langle \epsilon \rangle$ against $\langle J \rangle$ as shown in Figure 6.4. It can be seen from the figure that the resultant curve is a straight line which is in agreement with (6.19). The slope of this line is equal to C_o.
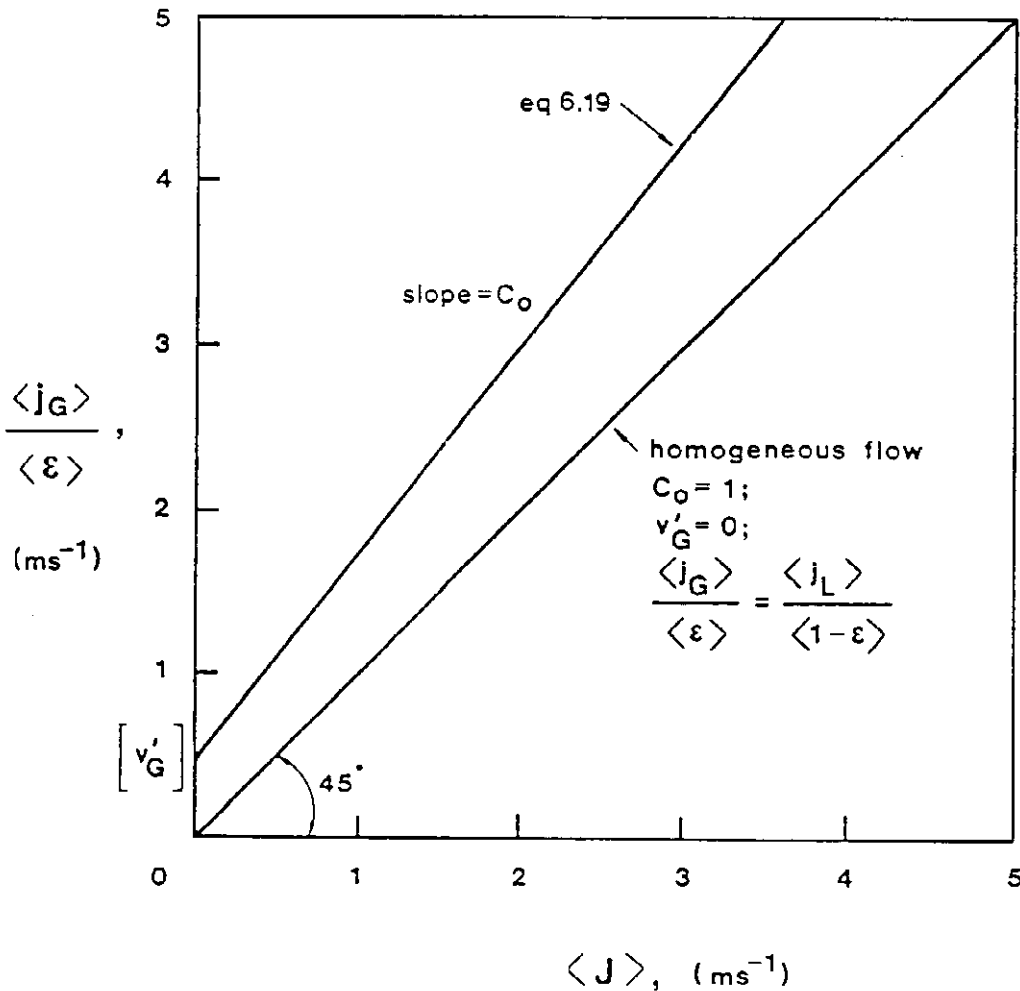
Figure 6.4   Zuber and Findlay drift flux plot

From their experimental observations Zuber and Findlay concluded that:-

(1) The value of C_o depended on the flow and concentration profiles;

(2) For fully established profiles, in axisymmetrical two-phase flow, C_o may range from 1.0 to 1.5 when the gas phase has a higher concentration in the centre of the flow than at the walls;

(3) When the gas phase is concentrated near the wall C_o can have a value less than unity;

(4) For fully established and constant profiles, C_o is constant.

TABLE 6.2   Experimentally found Distribution parameter values

Author	C_o	Conditions
Zuber and Findlay (1965)	1	Flat profile
	1.5	Peaked profile
Nassos and Bankoff (1967)	1.1	Cocurrent upflow (churn turbulent)
Bhaga and Weber (1972)	1.09	Cocurrent upflow
	2.28	Countercurrent gas upflow
Hatch (1973)	1.065	Cocurrent flow
Hills (1976)	1.16	Cocurrent upflow (churn-turbulent)
Merchuk and Stein (1981)	1.03	Cocurrent upflow
Clark and Flemmer (1984)	1.16	Upflow and downflow (bubbly)
Clark and Flemmer (1985)	0.934 (1 + 1.42)	Upflow
	1.521 (1 - 3.67)	Downflow
Clark and Flemmer (1986)	0.93	Cocurrent upflow (bubbly) for $\epsilon < 0.1$
	1.2	Cocurrent upflow (bubbly-slug trans) for $\epsilon > 0.1$

A number of studies have since attempted to quantify the values for the Distribution parameter and Table 6.2 contains a listing of experimentally determined values of C_0.

The vertical intercept in Figure 6.4 is equal to the weighted mean gas drift velocity $[v_G']$, which is equivalent to the unhindered bubble rise velocity $(v_b)_\infty$. For bubbly flow conditions where the bubble diameter is less than approximately 0.5 mm, $(v_b)_\infty$ is given by Stokes Law:

$$(v_b)_\infty = \frac{g(\rho_L - \rho_G) d_b^2}{18\mu_L} \quad , \qquad (6.20)$$

where d_b is the bubble diameter. For bubbly flow where the bubble diameter is greater than 0.5 mm, $(v_b)_\infty$ can be calculated from correlations given by either Peebles and Garber (1953), Wallis (1974) or Grace et al (1976). For churn-turbulent flow, the mean bubble rise velocity, $\{(v_b)_\infty\}_m$ can be calculated using

$$\left\{(v_b)_\infty\right\}_m = K\left\{\frac{\sigma g(\rho_L - \rho_G)}{\rho_L^2}\right\}^{1/4} \quad , \qquad (6.21)$$

where K is a constant and is approximately equal to either 1.53 (Harmathy, 1960), 1.41 (Levich, 1962) or 1.13 (Peebles and Garber, 1953).

For slug flow $(v_b)_\infty$ is given by Davies and Taylor (1950) as

$$(v_b)_\infty = \frac{2}{3}\left\{\frac{g r (\rho_L - \rho_G)}{\rho_L}\right\}^{1/2} . \qquad (6.22)$$

6.3 SEPARATED FLOW MODEL

The fundamental assumption made in single-mixture models is that each point in the mixture is occupied simultaneously by both phases without the presence of an interface. This assumption could certainly apply to gas mixtures but not to systems where a gas is dispersed within a

continuous liquid phase. In the latter case the interaction at the interface between the two phases has a major influence on the hydrodynamic properties of the system. To include the effect of interaction at the interface, a "two-fluid" model (Brodkey, 1967) was developed which considered the continuity, momentum, and energy equations for each phase separately. The interphase transfer of these properties was then defined in terms of the constitutive equations of the system.

The two-fluid model for dispersed gas systems has been extended by Ishii and Zuber (1979) for gravity dominated one-dimensional flow systems without transient effects or phase change. Their model assumes the axial component of the momentum equations for the dispersed (gas) and continuous (liquid) phases are given by

$$0 = -\epsilon \frac{dP}{dz} - \epsilon \rho_G g + (M_i)_G \qquad (6.23a)$$

and

$$0 = -(1-\epsilon) \frac{dP}{dz} - (1-\epsilon) \rho_L g + (M_i)_L , \qquad (6.23b)$$

where dP/dz is the pressure gradient in the axial direction within the mixture and is assumed to be the same for both phases.

In (6.23) $(M_i)_G$ and $(M_i)_L$ are the interfacial momentum terms for the gas and liquid phases respectively. For conservation of the mixture momentum, the sum of the interfacial momentum terms acting on the gas and liquid phases must equal zero, i.e.

$$(M_i)_G + (M_i)_L = 0 . \qquad (6.24)$$

From (6.23a), (6.23b) and (6.24), the pressure gradient within the mixture is given by (6.25), i.e.

$$\frac{dP}{dz} = -\rho_m g \quad , \tag{6.25}$$

where $\rho_m = \{\epsilon \rho_G + (1-\epsilon)\rho_L\}$ is the mean density of the mixture. From (6.23a) and (6.25),

$$(M_i)_G = \epsilon g(\rho_G - \rho_m) \tag{6.26a}$$

or

$$(M_i)_G = \epsilon g (1-\epsilon)(\rho_G - \rho_L) \quad . \tag{6.26b}$$

For systems where the dispersed gas phase comprises bubbles, the interfacial drag force acting on the gas phase is given by Zuber (1964) as

$$(M_i)_G = \frac{\epsilon(F_D)_b}{V_b} - \frac{\epsilon(1+2\epsilon)}{2(1-\epsilon)} \rho_L \frac{d}{dt}(v_G - v_L)$$

$$+ \frac{9\epsilon}{2r_b}\left\{\frac{\rho_L \mu_m}{\pi}\right\}^{1/2} \int_0^t \frac{d}{d\zeta}(v_G - v_L)\frac{d\zeta}{(t-\zeta)^{1/2}} \quad . \tag{6.27}$$

In (6.27) $(F_D)_b$ is the drag force acting on a single bubble which has a radius r_b and volume V_b. The absolute viscosity of the mxture is given by μ_m . The first term on the right-hand side accounts for the skin and form drag under steady state conditions. The second and third terms on the right-hand side are time dependent and relate to the acceleration of the apparent mass of the bubble, and the development of the surrounding boundary layer respectively.

For steady state conditions the time dependent terms disappear and (6.27) becomes

$$(M_i)_G = \frac{\epsilon(F_D)_b}{V_b} \; .$$

<div align="right">(6.28)</div>

Ishii and Zuber combined (6.26a) and (6.28) to obtain an expression for the steady state drag force:

$$(F_D)_b = g(1-\epsilon)(\rho_G - \rho_L) V_b \; .$$

<div align="right">(6.29)</div>

The steady state drag force is also given by

$$(F_D)_b = -\frac{1}{2} C_D \rho_L v_s^2 A_b \; ,$$

<div align="right">(6.30)</div>

where v_s is the slip velocity defined by (6.8), A_b is the projected area of the bubble and C_D is the bubble drag coefficient. From (6.29) and (6.30) the slip velocity is given by

$$v_s = \left\{ \frac{8g\, r_b\, (\rho_L - \rho_G)(1-\epsilon)}{3C_D\, \rho_L} \right\}^{1/2} \; ,$$

<div align="right">(6.31)</div>

where C_D is found by assuming that the drag coefficient for the bubble in the mixture is defined in the same manner as for a bubble in an infinite fluid. The drag coefficient $(C_D)_\infty$ for a bubble in an infinite fluid in the viscous regime is given by (6.32a):

$$(C_D)_\infty = \frac{24\left\{ 1 + 0.1(Re_b)_\infty^{0.75} \right\}}{(Re_b)_\infty} \; ,$$

<div align="right">(6.32a)</div>

where the bubble Reynolds number $(Re_b)_\infty$ is based on the liquid physical properties, the bubble diameter and the terminal velocity $(v_b)_\infty$ of the

bubble rising in an infinite fluid. The drag coefficient for a bubble in the two-phase mixture is equal to

$$C_D = \frac{24\left\{1 + 0.1 \left(Re_b\right)_{mixt}^{0.75}\right\}}{\left(Re_b\right)_{mixt}} ,$$ (6.32b)

where the mixture Reynolds number $(Re_b)_{mixt}$ is based on the liquid density ρ_L, the bubble diameter d_b, the slip velocity v_s, and the mixture viscosity μ_m . The mixture viscosity accounts for the effect that neighbouring bubbles have on each other by assuming around each bubble there exists a liquid boundary layer which restricts the motion of other bubbles. The net result of the restricted motion is an apparent increase in the viscosity of the system.

The mixture viscosity is assumed to be a function of the bubble concentration and viscosities of the liquid and gas phases. For dispersed bubble systems, μ_m is given by Ishii and Zuber (1979) as

$$\frac{\mu_m}{\mu_L} = \left(1-\epsilon\right)^{-\left\{2.5\left(\mu_G + 0.4\mu_L\right)/\left(\mu_G + \mu_L\right)\right\}} .$$ (6.33)

By substituting both (6.32a) and (6.32b) into (6.31) the approximate relationship for v_s is obtained:

$$v_s \doteq \left(v_b\right)_\infty \left(1-\epsilon\right)^{1/2} f(\epsilon) . \frac{1 + 0.1 \left(Re_b\right)_\infty^{0.75}}{1 + 0.1 \left(Re_b\right)_\infty^{0.75} \left\{f(\epsilon)\right\}^{6/7}} ,$$ (6.34)

where $f(\epsilon)$ is approximately equal to $\{(1-\epsilon)^{\frac{1}{2}} \mu_L\}/\mu_m$. By realising that $v_s = v_G'/(1-\epsilon)$ and $v_G' = j_G'/\epsilon$, (6.33) can be rewritten to obtain the gas drift-flux, i.e.

$$j_G' = \left(v_b\right)_\infty \epsilon \left(1-\epsilon\right)^{3/2} f(\epsilon) \frac{g\left(r_b^*\right)}{1 + g\left(r_b^*\right)\left\{f(\epsilon)\right\}^{6/7}} ,$$ (6.35)

where r_b^* is the non-dimensional bubble radius and is given by

$$r_b^* = r_b \left\{ \frac{\rho_L g (\rho_L - \rho_G)}{\mu_L^2} \right\}^{1/3} , \qquad (6.36)$$

and the function $g(r_b^*)$ for the viscous regime is equal to

$$g(r_b^*) = 0.55 \left\{ \left[1 + 0.08 (r_b^*)^3 \right]^{4/7} - 1 \right\}^{3/4} . \qquad (6.37)$$

Diagram removed for copyright reasons

Figure 6.5   Flow-regime map for cocurrent downward flow
proposed by Golan and Stenning (1969)

6.4 FLOW REGIME MAPS FOR COCURRENT DOWNWARD TWO-PHASE FLOW

Flow regime maps have been studied extensively for two-phase horizontal and vertically upward flow inside channels and reviews of these systems are given by Hewitt (1982), Rouhani and Sohal (1983), and Dukler and Taitel (1986). However, relatively few studies for cocurrent downward gas and liquid flow have been reported in the literature.

Golan and Stenning (1969) obtained experimental data for two-phase downflow using an inverted U-tube test section. From their results they obtained a flow regime map by plotting the superficial liquid velocity against the superficial gas velocity as shown in Figure 6.5. From the Figure the "oscillatory flow" regime represented a pulsating flow which was most likely caused by the inherently oscillatory characteristics of the U-tube arrangement.

Oshinowo and Charles (1974) produced a flow regime map for cocurrent downflow by plotting the square root of the inlet gas-to-liquid volume ratio, against the mixture Froude number Fr_{mixt}, divided by the square root of the property group N_P, which is defined as

$$N_P = \frac{\mu^*}{\left\{\rho^* \sigma^*\right\}^{1/2}} \quad , \tag{6.38}$$

where the dimensionless physical properties ρ^*, μ^* and σ^* were normalised against the physical properties for water. In (6.38) the Froude number is based on the column diameter and the total volumetric flux. Their flow regime map is shown in Figure 6.6.

Spedding and Nguyen (1980) examined systems for vertically upward and downward two-phase flow. A detailed analysis of their experimental results indicated the volumetric ratio and the Froude number, based on the column diameter and the total volumetric flux , were the most satisfactory parameters to use in flow regime mapping.

Figure 6.6   General flow regime map for two-phase vertical downflow
proposed by Oshinowo and Charles (1974)

Barnea et al (1982) modelled the transition from bubble to slug flow by
arguing that bubbles greater than a critical diameter $(d_b)_{crit}$, no longer
behaved as rigid spheres and readily coalesced to form gas slugs. They
assumed $(d_b)_{crit}$ was equal to twice the diameter at which Taylor bubbles
began to form (Brodkey, 1967), i.e.

$$(d_b)_{crit} = 2\left\{\frac{0\,46}{(\rho_L-\rho_G)g}\right\}^{1/2}.$$

(6.39)

Barnea et al proposed the bubble-to-slug transition occurred when the mean bubble diameter $(d_b)_m$ inside the pipe reached the value of $(d_b)_{crit}$, where $(d_b)_m$ was calculated using the correlation given by Calderbank (1958), i.e.

$$(d_b)_m = \left[0.415\left\{\frac{j_G}{j_G + j_L}\right\}^{1/2} + 0.725\right]\left\{\frac{\sigma}{\rho_L}\right\}^{3/5} E_s^{-2/5} \quad , \qquad (6.40)$$

where E_s is the specific energy dissipation rate, and for pipe flow it is given as

$$E_s = \left|\frac{dP}{dz}\right|\left\{\frac{j_G + j_L}{\rho_m}\right\} \quad , \qquad (6.41)$$

where

$$\frac{dP}{dz} = \frac{2f}{D_c}\rho_m (j_G + j_L)^2 \quad . \qquad (6.42)$$

The friction factor f in (6.42) is given by

$$f = 0.078\,(Re_p)^{-0.25} \quad , \qquad (6.43)$$

where the Reynolds number is based on the pipe diameter, liquid physical properties and total volumetric flux.

Finally, the transition from bubble-to-slug flow was fond by equating (6.39) and (6.40), i.e.

$$2\left\{\frac{0.46}{(\rho_L - \rho_G)g}\right\}^{1/2} = \left[0.415\left\{\frac{j_G}{j_G + j_L}\right\}^{1/2} + 0.725\right]\left\{\frac{\sigma}{\rho_L}\right\}^{3/5} E_s^{-2/5} \quad , \qquad (6.44)$$

Equation (6.44) is valid until maximum packing of the bubbles is reached, which, for spheres of equal diameter in a face-centred cubic arrangement, occurs when

$$\frac{j_G}{j_G + j_L} = 0.52 \quad . \tag{6.45}$$

Beyond this range Barnea et al predicted the transition from bubble-to-slug flow using the equation

$$j_L = j_G \left\{ \frac{1 - 0.52}{0.52} \right\} + (1 - 0.52)(v_b)_\infty \quad , \tag{6.46}$$

where $(v_b)_\infty$ was taken as the bubble rise velocity under churn-turbulent conditions, and is given by Harmathy (1960) as

$$(v_b)_\infty = 1.53 \left\{ \frac{g(\rho_L - \rho_G) G}{\rho_L} \right\}^{1/2} \quad . \tag{6.47}$$

Crawford et al (1985) studied the transition from bubble to intermittent flow in vertically downward systems where intermittent flow was either plug or churn-turbulent flow. They modified the correlation for upward flowing systems given earlier by Weisman and Kang (1981) to obtain the expression

$$\frac{j_G}{\{g D_c\}^{1/2}} = 0.18 \left[\frac{j_G + j_L}{\{g D_c\}^{1/2}} \right]^{1.6} . (0.65 - 0.3 [\cos \phi]^{0.3}) \quad , \tag{6.48}$$

where ϕ is the angle that the axis of the column is inclined to the horizontal plane.

6.5   BUBBLE COALESCENCE

Bach and Pilhofer (1978) discuss the influence of bubble coalescence on the operation of a countercurrent bubble column where the gas is introduced through a sparger at the base of the column.   Their results are shown in Figure 6.7.

Diagram removed for copyright reasons

Figure 6.7   Influence of bubble size on gas void fraction as a function of gas volumetric flux (after Bach and Pilhofer, 1978)

From Figure 6.7 it can be seen that there is a different relationship between the gas void fraction and the gas volumetric flux , for each bubble size.   Also, for a given gas volumetric flux the gas void fraction increases with decreasing bubble diameter.   This is due to the lower rise

velocities of the smaller diameter bubbles, resulting in their having a longer residence time inside the column. Consequently, the gas holdup is higher for the smaller diameter bubbles.

In Figure 6.7 each curve of constant bubble diameter passes through a maximum value of volumetric flux as indicated by the dotted line. This line is known as the "flooding line" and is the upper limit for the gas volumetric flux beyond which the liquid is carried in the same direction as the bubbles. In practice the flooding point for a given bubble diameter is rarely reached, and for increasing gas volumetric flux the operating point is continuously shifting to curves of larger bubble diameters. The heterogeneous flow containing the coalesced bubbles has a much greater gas handling capacity than the initial homogeneous flow.

Molerus (1987) has also examined the coalescence of bubbles inside a bubble column and the transition from homogeneous to heterogeneous flow. He defines a non-dimensional bubble diameter, $d_b{}^*$, as being equal to

$$d_b^* = \frac{d_b^3 g}{\nu_L^2} = 18 \, Re_b \left\{ 1 + 0.347 \left[L^* + \frac{1}{2}(L^*)^2 \right] \right\}$$

$$+ \; 3 \, (Re_b)^{3/2} + (Re_b)^2 \left\{ 0.3 + 0.424 \, L^* \right\}, \quad (6.49)$$

where L^* is the dimensionless length ratio and is given by

$$L^* = \frac{1}{\left\{ \Omega / [1-\Omega]^{1/3} - 1 \right\}} . \quad (6.50)$$

In (6.50) Ω is a packing parameter and has experimentally been found to equal 0.9. The Reynolds number for the bubble is based on the bubble diameter, liquid physical properties and the gas volumetric flux when there is no net liquid flow, i.e.

$$Re_b = \frac{\rho_L j_G d_b}{\mu_L} \quad . \tag{6.51}$$

Molerus also defined a dimensionless gas throughput Q_G^* as

$$Q_G^* = \frac{\rho_L^2}{\rho_L - \rho_G} \cdot \frac{j_G^3}{\mu_L g} \quad . \tag{6.52}$$

From (6.49) and (6.52) Molerus found the relationship between the gas void fraction and the dimensionless gas throughput for different bubble diameter values. His results are given in Figure 6.8.

Diagram removed for copyright reasons

Figure 6.8 Gas void fraction vs non-dimensional gas throughput inside a bubble column (after Molerus, 1987)

The solid curves in Figure 6.8 represent different values of d_b, and the broken line represents the flooding limit, beyond which homogeneous flow cannot exist. It can be seen from Figure 6.8 the experimental results (bolded line) follow the constant bubble diameter theoretical curve for low values of Q_G^*. At higher values of Q_G^* liquid recirculation was observed by Molerus, which corresponded to a significant increase in the measured bubble diameter.

The increase in the bubble diameter with increasing gas throughput observed by Molerus (1987), was thought to be as a result of the instability of the bubbly flow regime, resulting in an increase in the rate of bubble coalescence and the onset of heterogeneous flow. The onset of heterogeneous flow can be illustrated using the drift flux curve for cocurrent downflow as shown in Figure 6.9, which depicts a family of drift-flux curves corresponding to different size bubbles. The liquid volumetric flux is kept constant.

In Figure 6.9 the experimental drift-flux curve, accounting for bubble coalescence, is shown as the bolded line. The drift flux curve corresponding to the initial bubble diameter is given as the intersection of the measured gas void fraction and the line joining j_G and $-j_L$ when ϵ is equal to zero and one respectively. The experimental drift-flux curve follows the drift flux curve for the initial bubble diameter until a critical gas void fraction ϵ_{crit} is reached.

It can be seen from Figure 6.9 that when the gas void fraction is increased beyond ϵ_{crit}, coalescence takes place and a new drift flux curve, corresponding to a larger bubble diameter, is followed by the experimental data. The experimental drift flux curve is given by the intersection of the line joining j_G and $-j_L$, when ϵ is equal to zero and one respectively, with the drift-flux curve for the new bubble diameter. As the gas throughput is further increased more coalescence will take place and the experimental drift-flux curve will continue to change to drift-flux curves corresponding to larger bubble diameters.
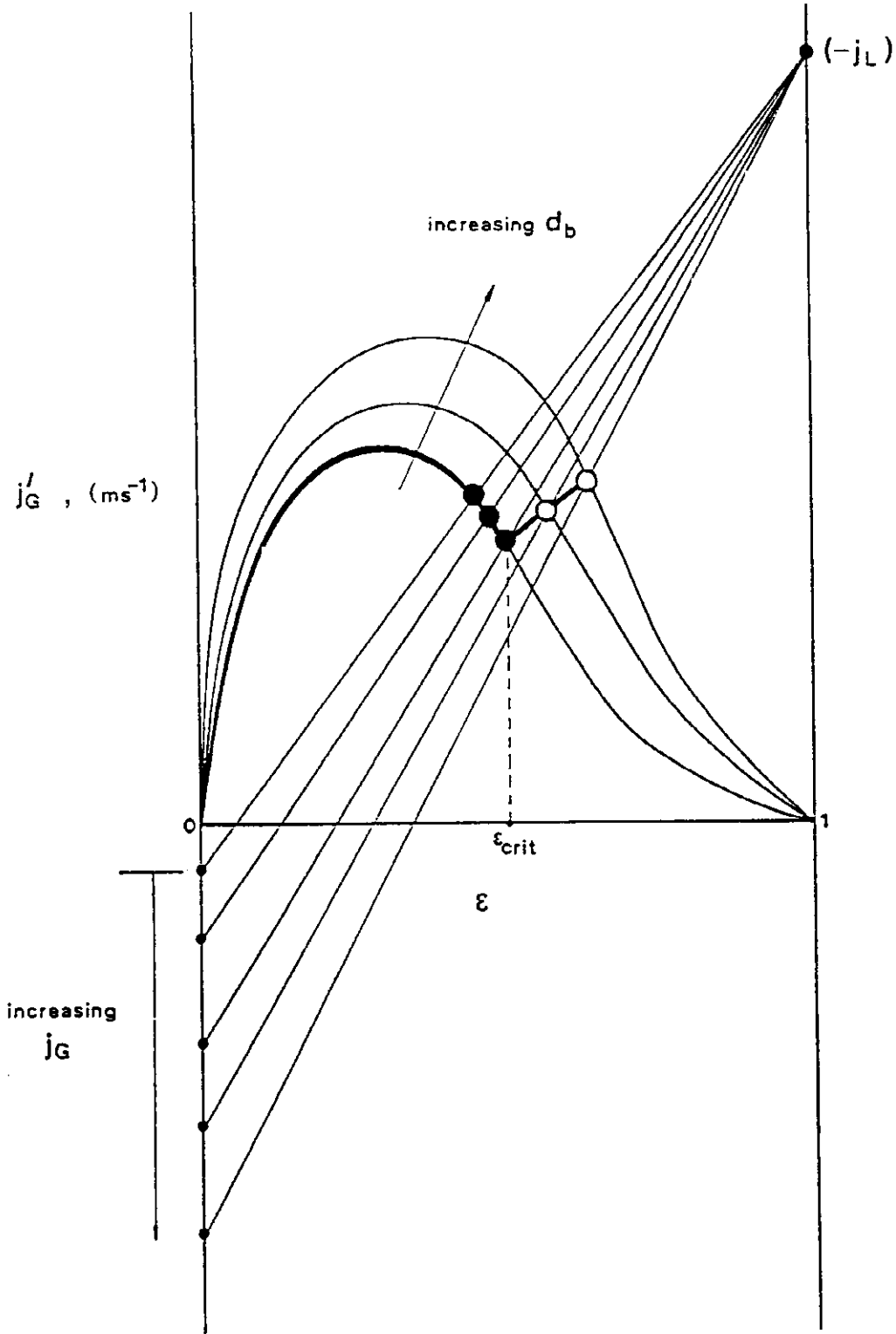
Figure 6.9   Drift flux curve showing effect of changing
bubble diameter on the gas void fraction

6.6   TRANSITION FROM HOMOGENEOUS TO HETEROGENEOUS FLOW

Iordache and Jinescu (1986) applied a kinetic model to predict the conditions under which the transition from homogeneous to heterogeneous flow takes place. The kinetic model is given by

$$\frac{d\phi}{dt} + v_b\,\frac{\partial\phi}{\partial z} = -a_o(\phi-\phi_\infty) + a_1 n\phi\left[v_b-(v_b)_\infty\right] \,, \quad (6.53)$$

where a_o and a_1 are constants, and $\phi(v_b)$ is the distribution function of the bubble velocity v_b within the dispersion containing n bubbles. In (6.53) the mean bubble velocity $(v_b)_m$ is given as

$$(v_b)_m = \frac{1}{n}\int_0^\infty v_b\,\phi(v_b)\,dv_b \;. \quad (6.54)$$

Iordache and Jinescu obtained the steady-state homogeneous solution to (6.53), and found that

$$\phi(v_b) = \frac{\phi_\infty(v_b)}{1+\dfrac{a_1}{a_o}\left[(v_b)_m-v_b\right]n} \,, \quad (6.55)$$

where $\phi_\infty(v_b)$ is the velocity distribution function in the absence of interactions between the bubbles. Equation (6.55) was found to be valid only for relatively high concentrations, otherwise the distribution function becomes negative which is impossible. The other condition when (6.55) becomes impossible to solve is when the denominator is zero, i.e.

$$\frac{a_1}{a_o}\left[(v_b)_m - v_b\right]n = 0 \,,$$

or

$$v_b = \frac{a_o}{a_1 n} + (v_b)_m \;. \quad (6.56)$$

Equation (6.56) corresponds to the condition which marks a transition in the flow regime. When this occurs (6.55) must be replaced by

$$\phi(v_b) = \frac{\phi_\infty(v_b)}{1 + \frac{a_i}{a_o}\{(v_b)_m - v_b\}n}$$

$$+ \quad bn\,\delta\left\{1 + \frac{a_i}{a_n}\left[(v_b)_m - v_b\right]n\right\} , \qquad (6.57)$$

where b is a constant and δ represents the Dirac delta function. The first term on the right hand side of (6.57) represents the homogeneous flow of discrete bubbles while the second term on the right hand side represents the collective flow of bubbles in a swarm. Iordache and Jinescu applied (6.56) to predict the point at which the transition from homogeneous to heterogeneous flow takes place.

Iordache and Jinescu also found that for homogeneous flow the gas void fraction was given implicitly by

$$\epsilon = \frac{(v_\epsilon)_m (1 - \epsilon^{1/3})}{(v_b)_m} , \qquad (6.58)$$

and for heterogeneous flow by

$$\epsilon = \frac{v_\epsilon (1-\epsilon)^{1/3}}{(v_b)_{max}}\left\{\frac{v_b}{(v_b)_\infty}\right\}_m , \qquad (6.59)$$

where $(v_b)_{max}$ is the maximum bubble rise velocity and $\{(v_b)_\infty\}_m$ is the mean velocity of the bubbles in the absence of interactions.

6.7   EXPERIMENTAL DESCRIPTION

The equipment used to determine the gas void fraction for the uniform
two-phase flow zone inside the plunging jet bubble column is illustrated
in Figure 3.4. The differential pressure between the 950 and 1000 mm
sampling ports was recorded once the column had reached equilibrium.
This measurement was then converted to give the gas void fraction
reading, using the method outlined in Section 3.4.3.

6.8   EXPERIMENTAL RESULTS AND DISCUSSION

The experimental results discussed in this section are used to examine
the effect of the operating variables, such as jet and column diameter,
and jet velocity, on the gas void fraction and stability of the uniform
two-phase region in the lower section of the bubble column. The raw
experimental data is contained in Appendix 1.

Note that in reporting the experimental results the upward direction has
been taken as being positive which is consistent with the previous
sections of this chapter. Therefore, the downward gas and liquid
volumetric fluxes have a negative sign. The absolute value of the liquid
volumetric flux has been used to calculate the Reynolds number for the
liquid phase.

6.8.1   Zuber and Findlay drift-flux plots

The ratio of the experimental gas volumetric flux divided by the gas void
fraction, j_G/ϵ, has been plotted against the total volumetric flux J in
Figure 6.10 for a typical experimental run. It can be seen from the
Figure that the data points fall on two straight lines. The two lines
represent the bubbly and churn-turbulent flow regimes inside the bubble
column. At low values of J (low values of j_G) the bubble concentration
inside the column is insufficient to promote coalescence and bubbly flow
exists. However, as J is increased, the bubble concentration is
sufficient to cause coalescence, and the onset of churn-turbulent flow.
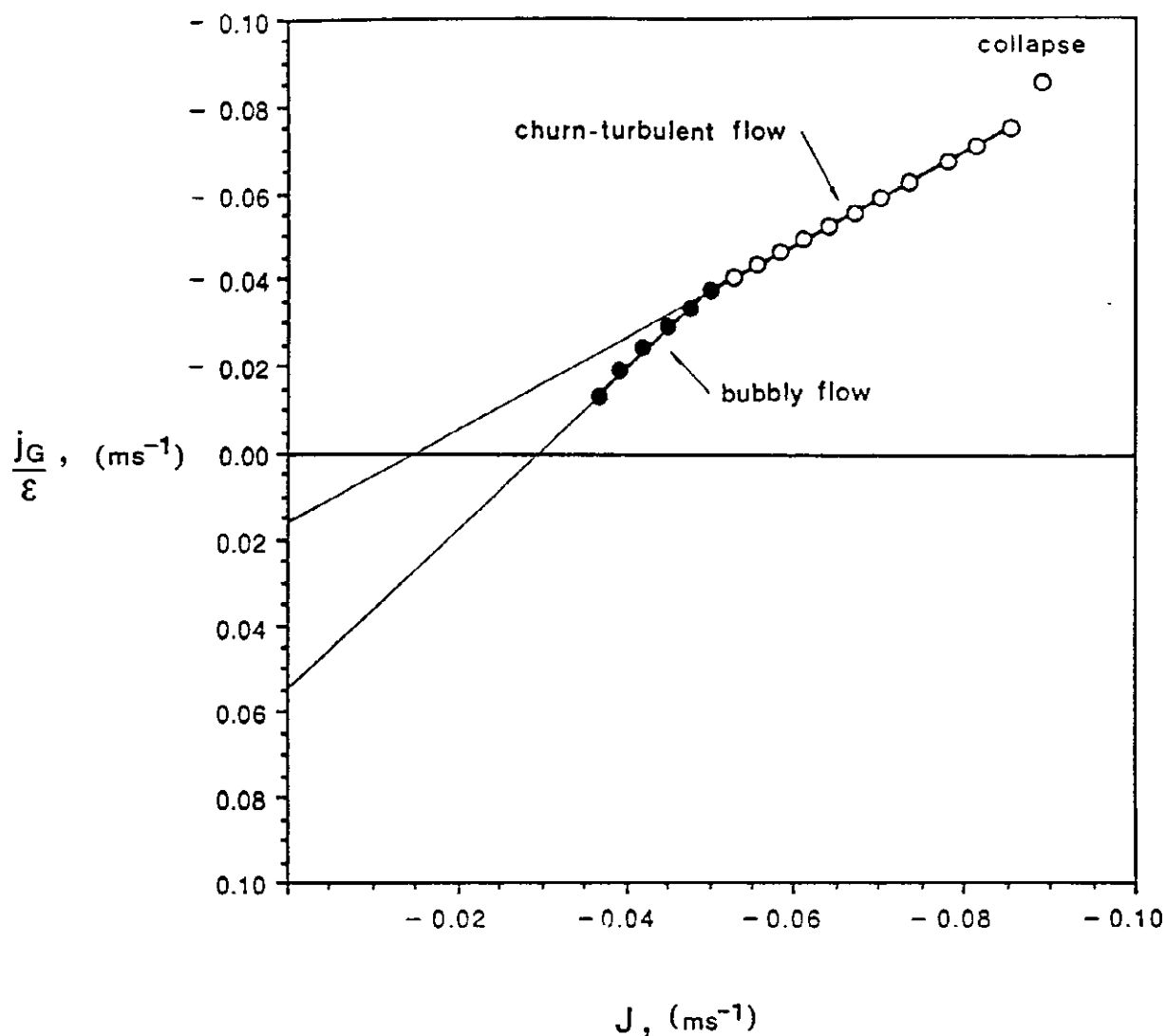
Figure 6.10   Zuber and Findlay drift-flux plot showing bubbly and churn-
turbulent regimes (Run 26; ϱ_L = 1000 kg/m³; μ_L = 0.001 Pa-s;
σ = 0.063 N/m; D_c = 44 mm; D_j = 2.38 mm; v_j = 11.5 m/s)

The Distribution parameter and the bubble rise velocity for both the
bubbly and churn-turbulent regimes are given by the slope and vertical
intercept respectively for the Zuber-Findlay drift-flux plot, i.e. when
j_G/ϵ is plotted against J.

Values for the Distribution parameter and the bubble rise velocity for the bubbly and churn-turbulent regimes for the experimental runs are listed in Table 6.3, where C_o and $(v_b)_\infty$ have been determined for each run using the same graphical procedure outlined in Figure 6.10.

TABLE 6.3 Experimentally determined Distribution parameter and bubble rise velocity for bubbly and churn-turbulent flow regimes (ρ_L = 1000 kg/m^3; μ_L = 0.001 Pa-s; σ = 0.063 N/m)

Run	Re_L [1]	Bubbly Regime		Churn-Turbulent Regime	
		C_o	$(v_b)_\infty$ (m/s)	C_o	$(v_b)_\infty$ (m/s)
8	14168	1.048	0.036	0.913	-0.005
16	9570	1.129	0.057	0.922	0.015
17	6502	1.172	0.058	0.923	0.013
18	4400	1.186	0.054	1.004	0.026
26	1613	1.964	0.060	1.050	0.015
75	3162	1.434	0.045	0.936	0.017
95	2502	1.668	0.039	0.998	0.014

[1] based on the liquid density and absolute viscosity, the absolute value for the liquid volumetric flux, and the column diameter.

6.8.2 Bubbly flow regime

(a) Distribution parameter

The values for the Distribution parameter listed in Table 6.3 for bubbly flow have been plotted against the liquid Reynolds number in Figure 6.11. It can be seen from the graph that C_o decreases from a value of approximately 2 at low Reynolds number, and rapidly decreases with increasing Re_L to approach a steady value of approximately unity for liquid Reynolds numbers greater than 10000.
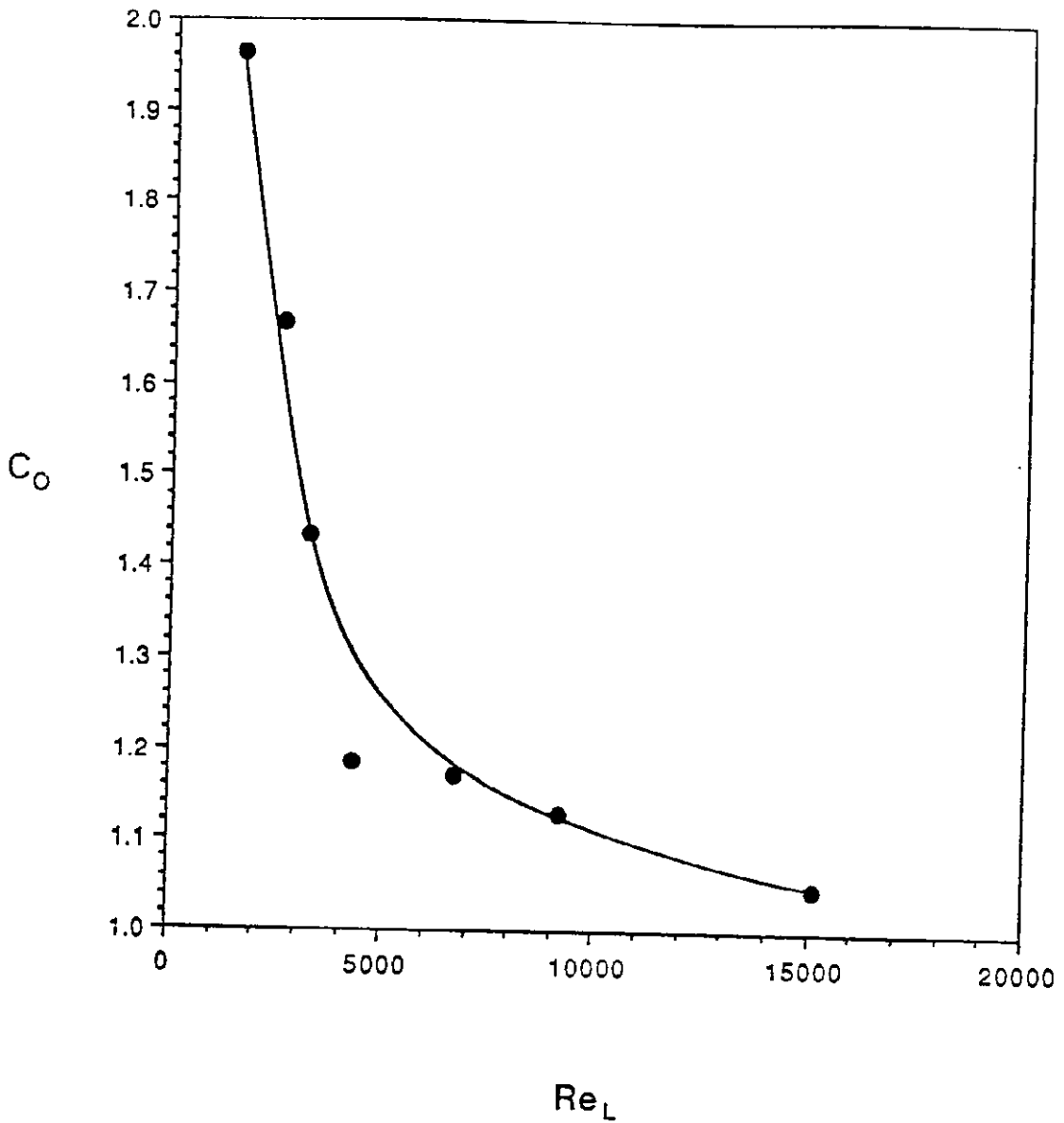
Figure 6.11   Distribution Parameter vs liquid Reynolds number for bubbly flow (ρ_L = 1000 kg/m^3; μ_L = 0.001 Pa-s; σ = 0.063 N/m)

It can also be seen from Figure 6.11 that the curve can be broadly divided into two separate regions, relating to laminar (Re_L < 5000) and turbulent (Re_L > 5000) liquid flow. For the laminar liquid flow regime the Distribution parameter is primarily determined by the parabolic velocity profile where the centreline velocity is higher than the mean

velocity. According to Zuber and Findlay (1965) this type of liquid
velocity profile will result in a value of C_0 greater than 1. The gas
phase will be unevenly distributed across the diameter of the column. As
the liquid volumetric flux through the column is increased, the velocity
profile becomes flatter resulting in a decrease in the value of C_0. The
results in Figure 6.11 suggest that for $Re_L > 10000$, the gas phase is
uniformly dispersed across the diameter of the column resulting in a
constant value of 1 for C_0.

(b) Bubble rise velocity

The bubble rise velocity values listed in Table 6.3 for the bubbly flow
regime, have been used in conjunction with Stokes Equation (6.20) to
determine the bubble diameter. The calculated bubble diameter values are
listed in Table 6.4. Also included in the Table are the Sauter mean
values for the measured bubble diameter distributions.

TABLE 6.4 Sauter mean and calculated bubble diameters for bubbly flow
(ρ_L = 1000 kg/m³; μ_L = 0.001 Pa-s; σ = 0.063 N/m)

Run	Bubble diameter (µm)	
	Sauter [1]	calculated [2]
8	285	240
16		296
17	289	300
18		300
26		320
75	424	300
95	474	280

[1] from measured bubble diameter distributions given in Appendix 3.
[2] calculated from (6.20) using $(v_b)_∞$ listed in Table 6.3.

It can be seen from Table 6.4 that the calculated values of the bubble diameter ranged from 240 to 320 μm with most of the values approximately equal to 300 microns. This value generally agreed with the bubble diameter measurements.
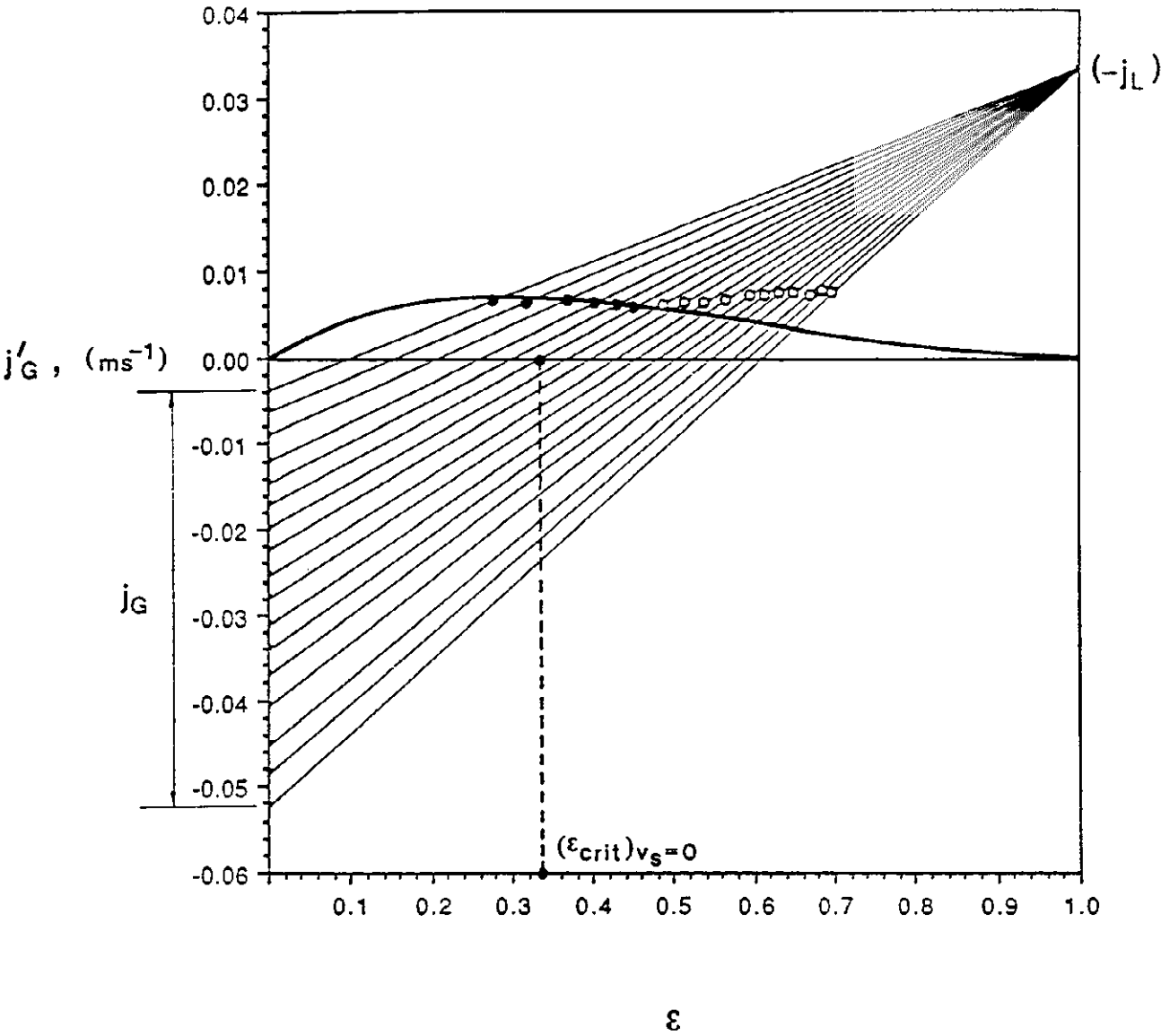
Figure 6.12   Experimental drift-flux curve showing regions of no observed coalescence (•), and coalescence (o) [Run 26; D_j = 2.38 mm; D_c = 44 mm; v_j = 11.5 m/s; ρ_L = 1000 kg/m³; μ_L = 0.001 Pa-s; σ = 0.063 N/m]

6.8.3 Transition from bubbly to churn-turbulent flow

The transition from bubbly to churn-turbulent flow is best illustrated by plotting the measured gas void fraction against the gas volumetric drift-flux, j_G', as shown in Figure 6.12. Also shown in Figure 6.12 are the gas, j_G, and liquid, j_L, volumetric flux data points which have been used to generate the experimental drift-flux curve, where the curve is given by the intersection of the line joining j_G (at $\epsilon=0$) and $-j_L$ (at $\epsilon=1$), and the measured gas void fraction.

In Figure 6.12 the solid circles (●) represent those data points where no coalescence was observed and they were used the generate the drift-flux curve (shown as the solid line) for the initial bubble diameter. The open circles (○) are those data points where coalescence was observed and they mark the onset of churn-turbulent flow. The point at which the line joining j_G and $-j_L$, and passing through the last data point prior to coalescence, intersects the horizontal axis of the graph is the critical gas void fraction, under no slip conditions, before bubble coalescence starts. It can be seen from Figure 6.12 that this occurs at a critical gas void fraction of approximately 0.34. Experimentally determined values of the critical gas void fraction (no slip condition) for the remaining runs are listed in Table 6.5.

TABLE 6.5   Critical gas void fraction (no slip) vs liquid Reynolds number (ρ_L = 1000 kg/m³; μ_L = 0.001 Pa-s; σ = 0.063 N/m)

Run	Re_L	ϵ_{crit}
8	14168	0.17
16	9570	0.20
17	6502	0.19
18	4400	0.17
26	1613	0.34
75	3162	0.21
95	2502	0.23

It can be seen from Table 6.5 that the average value of ϵ_{crit} is approximately equal to 0.20 for turbulent liquid flow (Re_L > 2000). The value of 0.2 for ϵ_{crit} is in agreement with the observations of Herbrechtsmeier and Schafer (1982) who reported the onset of coalescence, and the formation of large bubbles in a downflow reactor when the gas-to-liquid volumetric flow ratio was reduced below 0.25. If there was no slip between the gas and liquid phases then this ratio would correspond to a gas void fraction of twenty percent.

It can also be seen from Table 6.5 that a value of 0.34 was obtained under laminar liquid flow conditions (Re_L < 2000) which is higher than the value found for turbulent liquid flow. This result suggests the mechanism for coalescence is initiated at a lower gas phase concentration when liquid phase is turbulent. A possible reason for this result is that the probability of bubble coalescence taking place at lower gas phase concentrations is increased by the increased motion of the bubbles in turbulent flow.

The experimental drift-flux curves were used to determine the rate of bubble coalescence once the gas void fraction was increased beyond the critical gas void fraction value. Figure 6.13 contains the same experimental drift-flux data given in Figure 6.12 plotted on an expanded vertical scale. Also shown in the figure is the theoretical drift-flux curve which has been predicted from (6.35) using the appropriate calculated bubble diameter given in Table 6.4.

It can be seen from Figure 6.13 that the experimental data points follow the theoretical drift-flux curve for the initial bubble diameter prior to coalescence. However, when more gas is introduced to the system such that the gas void fraction is increased beyond ϵ_{crit}, the data values deviate from the curve. The deviation is caused by the onset of coalescence and the resulting increase in the bubble diameter. The system drift-flux curve now corresponds to a new equilibrium bubble diameter which is controlled by the rate of coalescence and the bubble breakup forces. Subsequent additions of gas to the column result in increases in the bubble diameter and changes in the drift-flux curve.
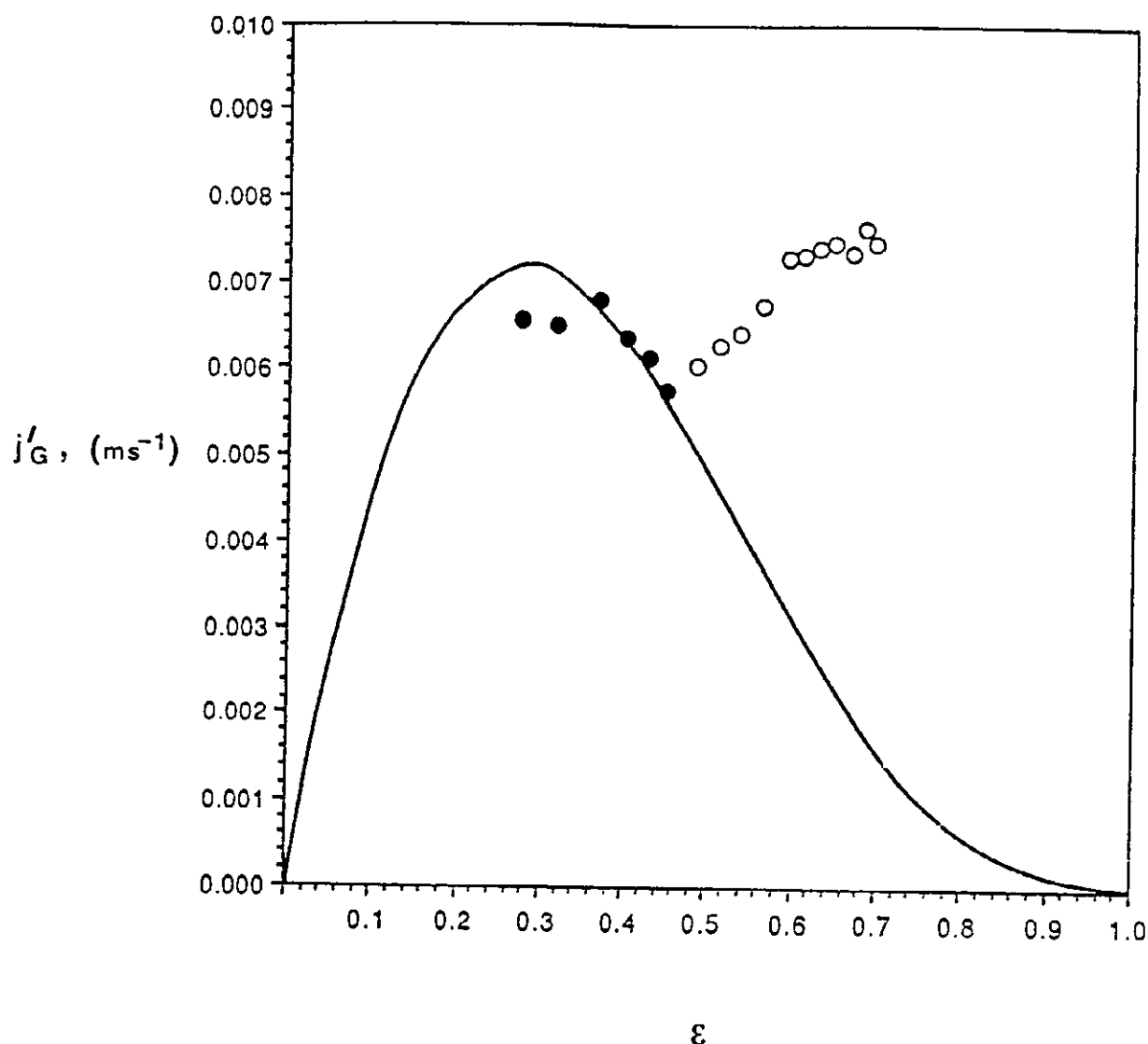
Figure 6.13   Experimental drift-flux curve (Run 26; D_j = 2.38 mm; D_c = 44 mm; v_j = 11.5 m/s; ρ_L = 1000 kg/m³; μ_L = 0.001 Pa-s; σ = 0.063 N/m)

It can be seen from Figure 6.13 that the experimental drift-flux curve in the region of bubble coalescence (open circles) increases linearly with increasing gas void fraction. The slope of this line can be thought of as a measure of the rate at which bubble coalescence occurs as a result of increasing gas void fraction. The gradient of the line fitted to the data points where coalescence was observed, j_G'/ϵ, was obtained from the

experimental drift-flux curves, and the resultant values for j_G'/ϵ have been plotted against the liquid Reynolds number as shown in Figure 6.14.
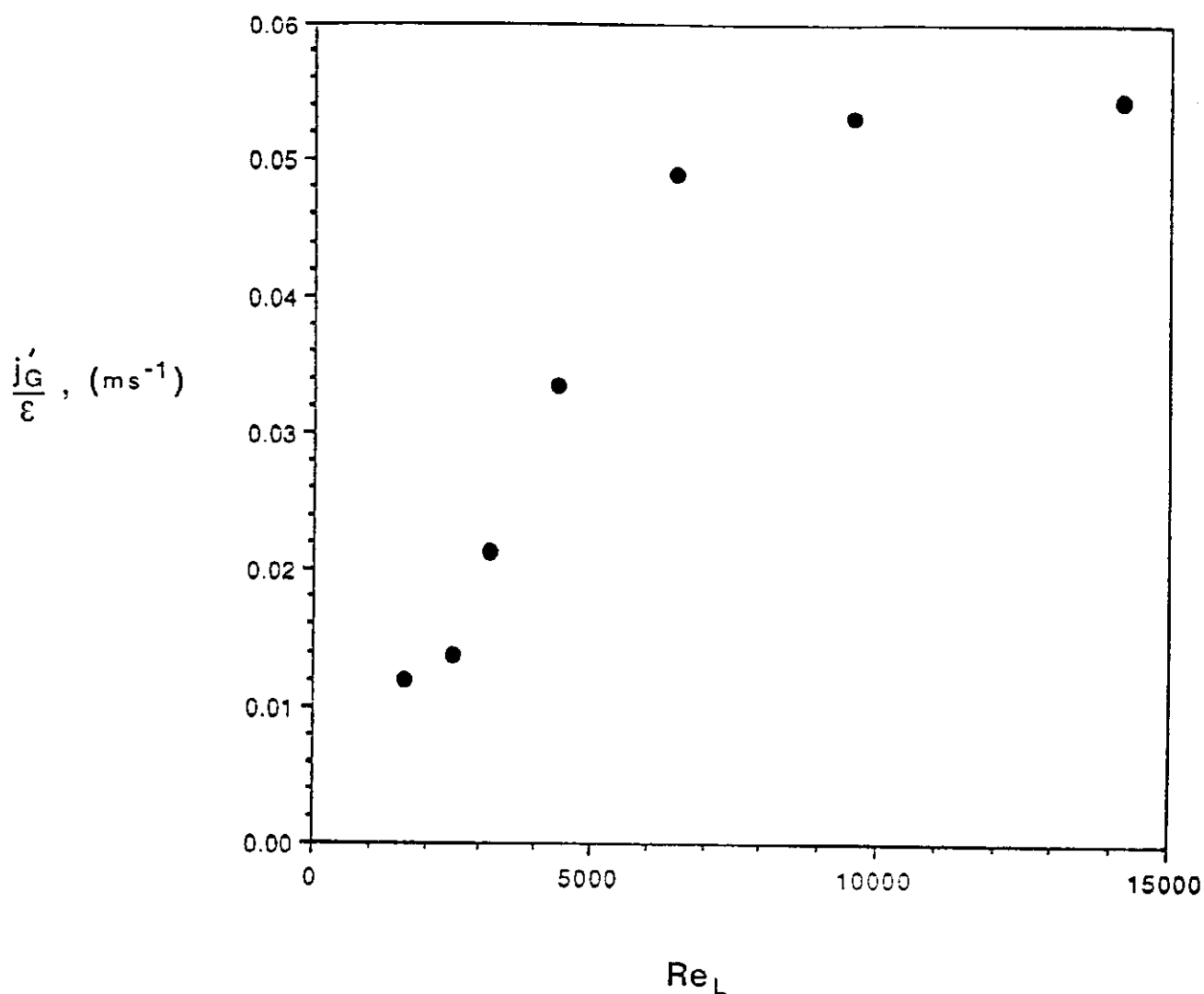
Figure 6.14 Gas drift-flux gradient vs liquid Reynolds number for bubble coalescing regime ($\rho_L = 1000$ kg/m³; $\mu_L = 0.001$ Pa-s; $\sigma = 0.063$ N/m)

It can be seen from Figure 6.14 that for liquid Reynolds numbers below approximately 6000 the data points follow a straight line. This result is consistent with (6.6) where $\langle j_G'/\epsilon \rangle$ is directly related to $\langle j_L \rangle$ if the intercept value, $\langle j_G \rangle (1-\langle \epsilon \rangle)/\langle \epsilon \rangle$, is assumed to be constant.

From Figure 6.14 it can be seen that the vertical intercept of the experimental curve is negative, which is also in agreement with (6.6) as $\langle j_G \rangle$ was always in the negative downward direction for the experimental runs.

It can also be seen from Figure 6.14 that j_G'/ϵ approaches a constant value as the liquid Reynolds number is increased beyond 6000, which suggests that the rate of bubble coalescence, and hence the rate of departure from the initial drift-flux curve, is constant when the liquid phase is fully turbulent. This is possibly due to an equilibrium being reached between the breakup and coalescing forces acting on the bubbles.

6.8.4 Churn-turbulent flow

As indicated in Section 6.8.3 the development of churn-turbulent flow is marked by the onset of bubble coalescence. The characteristics of the churn-turbulent flow can be modelled using the Zuber and Findlay (1965) drift-flux analysis once the Distribution parameter and the bubble rise velocity have been determined.

(a) Distribution parameter

The experimental values for the Distribution parameter, C_o, and the unhindered bubble rise velocity, $(V_b)_\infty$, for the churn-turbulent regime have already been given in Table 6.3. In Figure 6.15 C_o has been plotted against the liquid Reynolds number.

It can be seen from Figure 6.15 that the resultant curve is similar to that given in Figure 6.11 for the bubbly flow regime. The magnitude of the Distribution parameter, however, is less than those obtained for bubbly flow and reflects the observation that for churn-turbulent flow the larger bubbles preferentially rise near to the column wall. Consequently, the gas phase concentration is greater near the wall, resulting in lower values for C_o.

If the laminar-to-turbulent flow transition is assumed to occur at a liquid Reynolds number of approximately 3000, then it can be seen from the Figure 6.15 that the Distribution parameter is different for the laminar and turbulent liquid flow regimes. This is due to the difference in the liquid velocity profiles for the two flow regimes; where the turbulent regime will give a lower value for C_0 as a result of its flatter velocity profile.
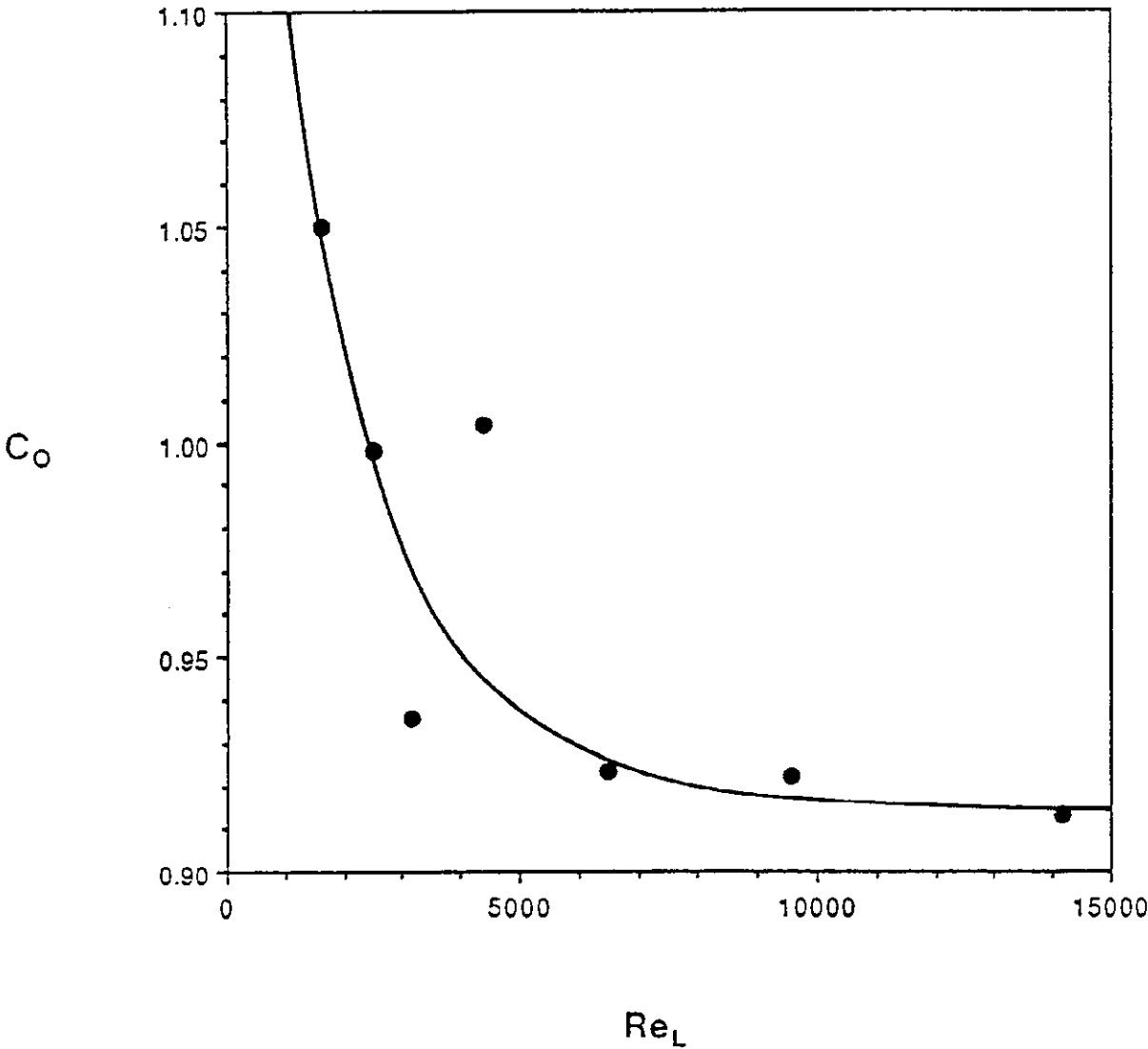
Figure 6.15 Distribution Parameter vs liquid Reynolds number for churn-turbulent flow (ρ_L = 1000 kg/m^3 ; μ_L = 0.001 Pa-s; σ = 0.063 N/m)

(b) Bubble rise velocity

From the results listed in Table 6.3 it can be seen that the mean value
of the unhindered bubble rise velocity for the churn-turbulent flow
regime was approximately equal to 0.017 m/s which is not in agreement
with the value of 0.2 m/s calculated from (6.21). The reason for this is
that in most of the experimental runs the maximum total volumetric flux
down the column was less than the rise velocity of the bubbles.
Consequently, the bubbles were able to return to the headspace at the top
of the downcomer. It is not clear as to how the recycling of the gas
phase can be included in the Zuber and Findlay drift-flux analysis. It
is clear from the experimental results, however, that the recycled gas
stream does influence the vertical intercept of the drift-flux plot, and
that its value is no longer $(v_b)_\infty$.

(c) Gas void fraction   .

In Figure 6.16 the measured gas void fraction, ϵ_{meas}, has been plotted
against the gas-to-liquid volumetric flow ratio for the churn-turbulent
flow regime. It can be seen from the graph the gas void fraction
increases with increasing value of the Q_G/Q_L ratio for each run. It can
also be seen that all of the experimental curves lie above the line
representing the no slip condition between the two phases. This result
suggests that slip, of varying amounts, was occurring for each run.
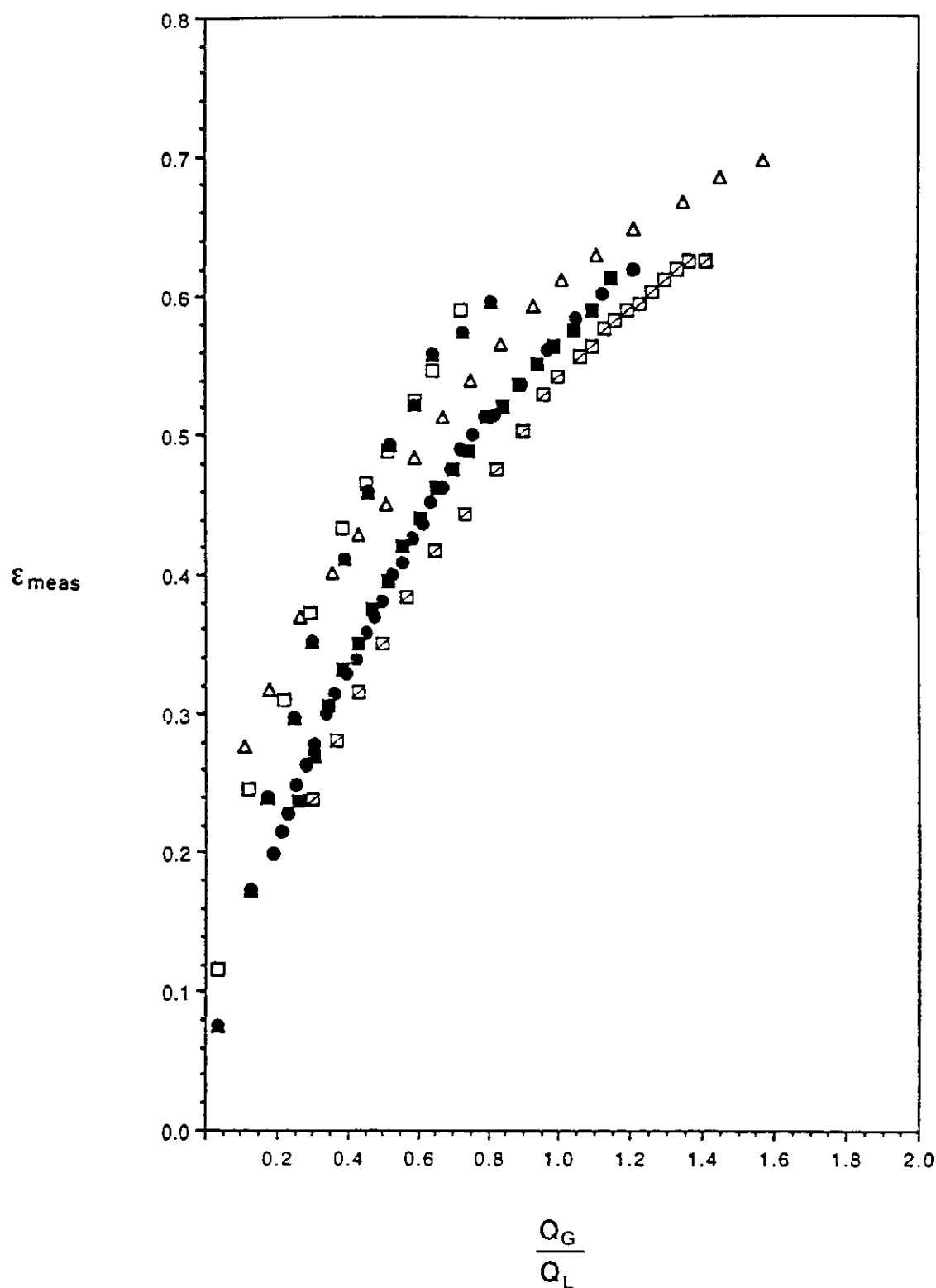
Figure 6.16 Measured void fraction, ε_{meas}, vs gas-to-liquid flow ratio [run 8 (⊠), 16 (■), 17 (●), 18 (○), 26 (△), 75 (▲), 95 (□); ρ_L = 1000 kg/m³; μ_L = 0.001 Pa-s; σ = 0.063 N/m]

It was thought that if the effect of the slip velocity, v_s, on the gas void fraction could be taken into account, then the modified experimental gas void fraction measurements should fall on a single curve. To test this idea a modified gas void fraction, ϵ_{mod}, was defined such that

$$\epsilon_{mod} = \epsilon_{meas} - \epsilon_{corr} \quad , \tag{6.60}$$

where ϵ_{corr} is the gas void fraction correction factor. An expression for ϵ_{corr} can be obtained by assuming that it is function only of the liquid volumetric flux and the bubble rise velocity, i.e.

$$\epsilon_{corr} = C_1 \left\{ \frac{(v_b)_\infty + j_L}{j_L} \right\} \quad , \tag{6.61}$$

where C_1 is a constant, and $(v_b)_\infty$ is the bubble rise velocity. By assuming a value[16] of 0.18 m/s for the bubble rise velocity, (6.61) becomes

$$\epsilon_{corr} = C_1 \left\{ \frac{0.18 + j_L}{j_L} \right\} \quad . \tag{6.62}$$

A value for C_1 was obtained by fitting (6.62) to the experimentally determined ϵ_{corr} values listed in Table 6.6 for the turbulent liquid regime ($Re_L > 2000$). By applying a least squares fit to the experimental results C_1 was found to be -0.045 with a standard deviation of 0.031. Substituting this value into (6.62) gives

$$\epsilon_{corr} = -0.045 \left\{ \frac{0.18 + j_L}{j_L} \right\} \quad . \tag{6.63}$$

---

[16]   The average bubble rise velocity of 0.18 m/s was obtained for the churn-turbulent regime from (6.21) using a value of 1.13 (Peebles and Garber, 1953) for K.

From (6.60), the gas void fraction correction factor is equal to the vertical axis intercept when the measured gas void fraction is plotted against the gas-to-liquid volumetric flow ratio, i.e. ϵ_{corr} is equal to the measured gas void fraction when the liquid volumetric flux is extrapolated to zero flow. The experimental curves given in Figure 6.16 were extrapolated to zero gas-to-liquid volumetric flow ratio to obtain the experimental values for ϵ_{corr} listed in Table 6.6.

The experimental values for the gas void fraction were applied to (6.60) to obtain the modified gas void fraction curves, and these are shown in Figure 6.17. It can be seen from the Figure that almost all of the data points fall on a single curve. Those points which do not lie on the curve correspond to laminar liquid flow conditions (Re_L < 2000), whereas for the remaining data points the flow is turbulent.

It is thought that, at low gas-to-liquid flow ratios, the parabolic velocity profile for laminar flow could result in a greater amounts of slip between the phases. This would result in a higher gas void fraction for laminar flow. As the gas-to-liquid flow ratio is increased the presence of bubbles would flatten the liquid velocity profile across the column, giving rise to closer slip velocity values for laminar and turbulent flow. This would lead to similar gas void fractions for laminar and turbulent flow when the gas-to-liquid flow ratio is increased as shown in Figure 6.17.
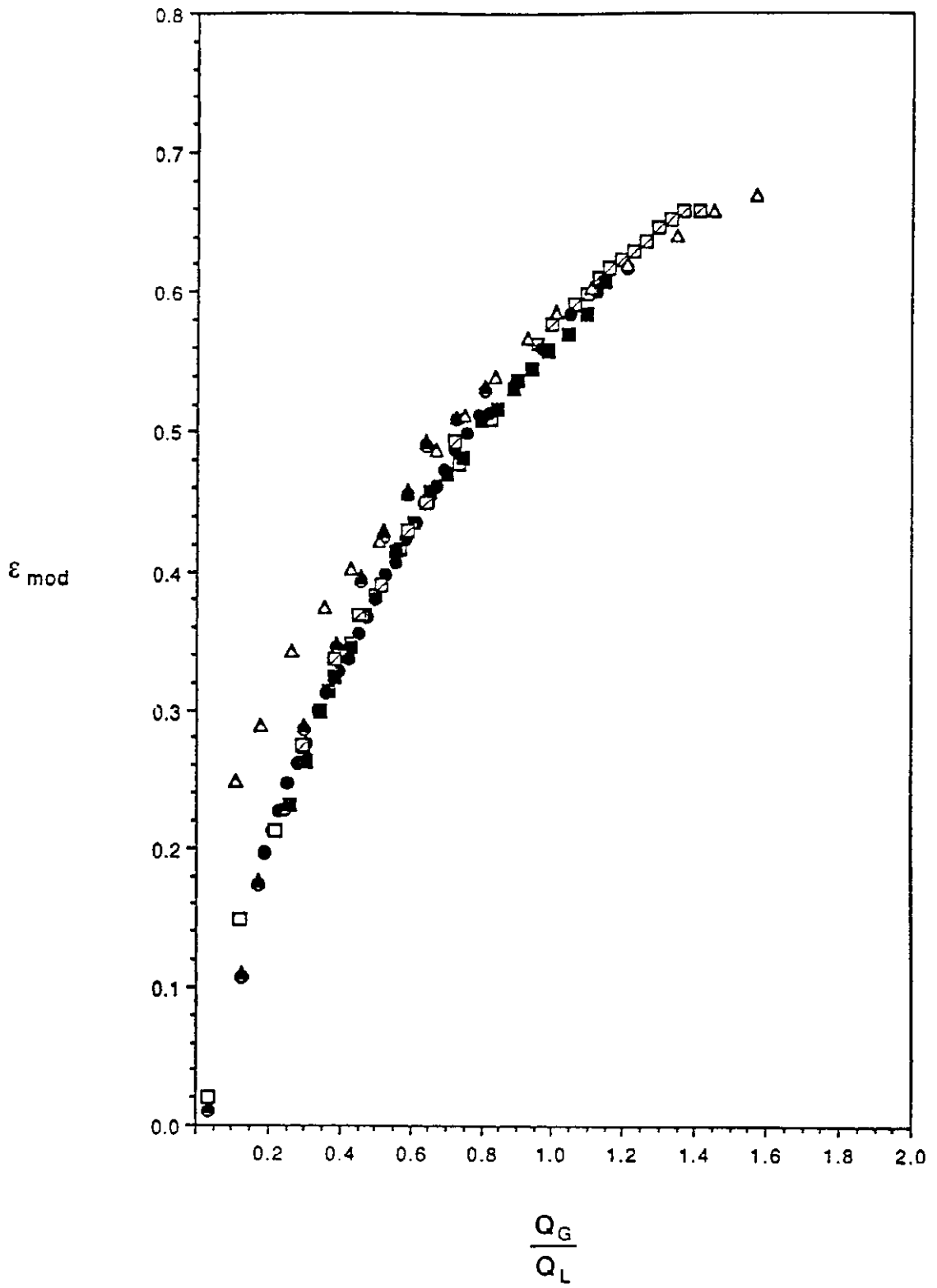
Figure 6.17 Modified gas void fraction ϵ_{mod}, plotted against gas/liquid flow ratio Q_G/Q_L, for runs 8 ($\boxtimes$), 16 ($\blacksquare$), 17 ($\bullet$), 18 ($\circ$), 26 ($\triangle$), 75 ($\blacktriangle$) and 95 ($\square$) (ρ_L = 1000 kg/m³; μ_L = 0.001 Pa s; σ = 0.063 N/m)

The experimental values for ϵ_{corr} are listed in Table 6.6 which also includes the predictions from (6.63).

TABLE 6.6 Experimental and predicted values for the gas void fraction correction factor, ϵ_{corr}. (ρ_L = 1000 kg/m³; μ_L = 0.001 Pa-s; σ = 0.063 N/m)

Run	Re_L	j_L (m/s)	C_1[1]	Correction factor Experimental	From (6.63)[2]
8	14168	-0.299	-0.083	-0.033	-0.018
16	9570	-0.174	-0.087	0.006	0.002
17	6502	-0.133	-0.028	0.002	0.016
18	4400	-0.090	-0.024	0.067	0.045
26	1613	-0.033		0.027	
75	3162	-0.047	-0.023	0.064	0.127
95	2505	-0.029	-0.023	0.097	0.234
		mean	-0.045		

[1] calculated from (6.62) using $-j_L$ and the experimental values for ϵ_{corr}
[2] calculated from (6.63) using C_1 equal to -0.045

In Figure 6.18 the gas void fraction correction factor has been plotted against the liquid volumetric flux where it can be seen that both the predicted and experimental values for the gas void fraction correction factor increase with decreasing liquid volumetric flux. The greatest deviation between the predicted curve and the experimental data occurs when the liquid flow is laminar. This observation suggests that the constant C_1 in (6.61) is a function of the type of flow within the liquid phase, where the value for C_1 is likely to be less for the laminar regime than that for the turbulent liquid flow regime.
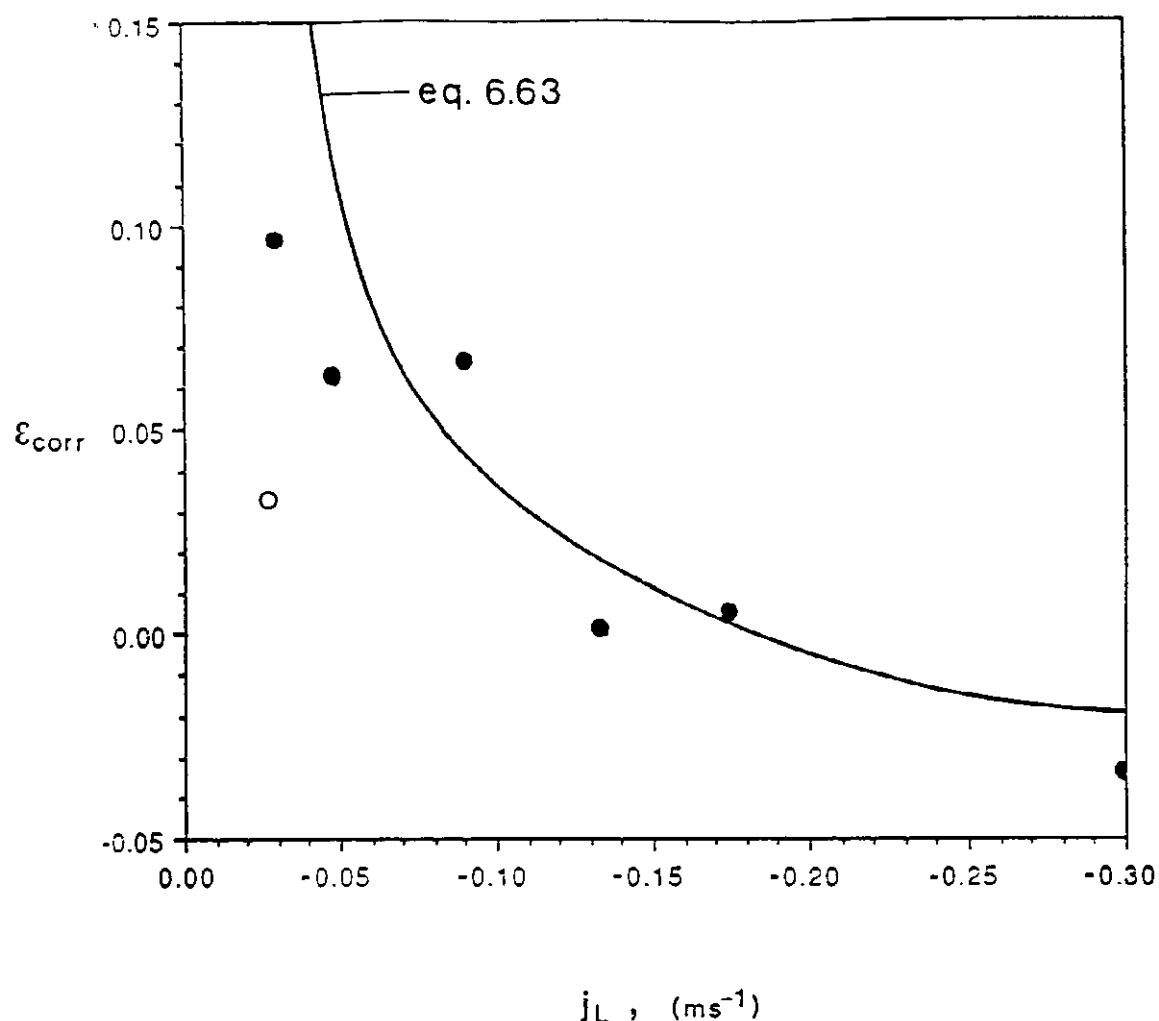
Figure 6.18 Void fraction correction factor vs liquid volumetric flux
[$Re_L > 2000$ (●), $Re_L < 2000$ (○); $\rho_L = 1000$ kg/m³;
$\mu_L = 0.001$ Pa-s; $\sigma = 0.063$ N/m]

6.9 SUMMARY

The following results have been obtained for the uniform two-phase flow
zone within the plunging jet bubble column:-

(1)   From the Zuber and Findlay (1965) drift-flux analysis the results
       indicate that for each experimental run a transition from bubbly

to churn-turbulent flow takes place. For bubbly flow, when the
liquid flow is laminar the Distribution parameter rapidly
decreases with increasing liquid Reynolds number to a value of
unity. For the liquid turbulent flow the Distribution parameter
is constant at a value approximately equal to unity.

(2)   For turbulent liquid flow when there is no slip between the gas
and liquid phases the onset of bubble coalescence, and the
transition from bubbly to churn-turbulent flow, occurs at a gas
void fraction value approximately equal to 0.2. For laminar
liquid flow under no slip conditions, the onset of coalescence
occurs at void fraction values greater than 0.3.

When slip takes place the experimental drift-flux curve can be
predicted using the separated flow model of Ishii and Zuber
(1979), provided that the initial bubble diameter is known. Under
these conditions the onset of coalescence for both laminar and
liquid flow occurs at higher gas void fraction values than when
the drift-flux is zero.

(3)   For the churn-turbulent flow regime the modified gas void fraction
can be used to collapse the data from all of the experimental runs
onto a single curve. The modified gas void fraction is defined
using a gas void fraction correction factor, which is directly
proportional to the ratio of the bubble rise velocity to the
liquid volumetric flux. The proportionality constant in the
expression for for ϵ_{corr} was found experimentally to equal
approximately -0.045 for turbulent liquid flow.

Chapter 7

OVERALL OPERATING CHARACTERISTICS

7.1   INTRODUCTION

The downcomer section of the plunging jet bubble column consists of four
main regions, namely the free jet, plunging jet, mixing zone and uniform
two-phase flow zone.   The hydrodynamics of each of these regions have
been examined separately in earlier chapters.   However, it is the
interactions between the processes occurring in these regions which
determines the operating characteristics of the overall system.

In this chapter the combined hydrodynamic characteristics of the
downcomer are discussed from the point of view of designing a downcomer
suitable for industrial application.   Emphasis is placed on the effect of
recirculation of both gas and liquid phases on the stable operating range
of the system.

7.2   FREE JET

The characteristics of the free jet are primarily determined by the
geometry of the nozzle and also the levels of turbulence present in the
jet delivery system, as described in Appendix 2.   The nozzle geometry and
level of upstream turbulence are set before the jet leaves the nozzle,
and determine whether the free jet will have a "rough" or "smooth"
surface.   In addition, once the jet leaves the nozzle the magnitude of

the disturbances on its free surface is increased by increasing the
frictional resistance of the gas phase. When the relative velocity
between the jet and the gas phase is low, this effect is negligible.
However, at high relative velocities the frictional resistance can
increase significantly the roughness of the jet surface, leading to an
increase in the overall rate of entrainment of the plunging jet.

From an operating viewpoint it is desirable to use rough jets because
they give higher rates of entrainment. Therefore, the gas volumetric
flux in the region of the free jet should be minimised by using the
maximum downcomer diameter possible. However, it should be noted that
the downcomer diameter has a significant influence on the characteristics
of the remaining regions, as discussed below.

The interaction between regions starts in the headspace through which the
free jet passes prior to plunging in the receiving gas-liquid phase. The
bubbles, which have risen against the bulk downward flow inside the
downcomer, accumulate in the headspace where they are re-entrained by the
plunging jet. The recycled gas associated with these bubbles effectively
reduces the capacity of the jet to entrain "new" gas feed.

If more gas is added to the downcomer, the length of the free jet
automatically increases, thereby increasing the effective diameter of the
jet at the plunge point, as discussed in Chapter 4. The increase in the
effective diameter of the jet increases its entrainment rate to handle
the addition of gas, and in this sense the jet is "self-regulating". If
the length of the free jet is increased the length of the two-phase
mixture inside the downcomer is reduced, thereby reducing the residence
time of the bubbles. Also associated with an increase in the free jet
length is an increase in the bubble diameter which reduces the
interfacial area inside the downcomer. Consequently it is important to
minimise the free jet length, which can be achieved by ensuring the rate
of recycled gas returning to the headspace is kept to a minimum.

7.3 PLUNGING JET

Entrainment takes place by two mechanisms described in Chapter 4. Part
of the entrained gas is trapped within the effective jet diameter, and
the remaining gas is contained in the film between the surfaces of the
free jet and the induction trumpet in the receiving liquid. These two
entrainment components are subjected to shearing forces of differing
magnitudes once they have entered the receiving liquid. The gas inside
the effective jet diameter enters the submerged jet region nearer to the
centre of the flow field where the radial velocity gradient is at a
minimum. Consequently, the bubbles produced in this region are larger
than those bubbles produced from the gas film entering the high shear
zone between the boundary of the submerged jet and the relatively slow
moving surrounding liquid. The smaller bubbles produced from the
filmwise component produce a high interfacial contact area, and are less
likely to be recycled into the headspace inside the downcomer.
Therefore, it is desirable to maximise this component of the entrainment
mechanism.

The thickness of the entrained film is determined by the magnitude of the
disturbances generated on the free surface of the induction trumpet.
When the disturbances are the same size as the thickness of the film the
gas will be cut off from the headspace above it and carried below the
liquid surface. The point at which the induction trumpet is truncated is
controlled by the physical properties of the liquid. If the disturbances
are large the induction trumpet will be truncated at a point closer to
the horizontal surface of the receiving liquid, resulting in a greater
rate of filmwise entrainment.

The rate of filmwise entrainment can be increased by increasing either
the velocity or diameter of the jet, both of which lead to an increase in
the volumetric flow through the jet. The filmwise entrainment rate is
proportional to the jet diameter while the volumetric flowrate through
the jet is proportional to the square of the jet diameter. Consequently,
if the jet diameter is increased in order to increase the entrainment
rate, the gas-to-liquid volumetric flow ratio will be decreased, thus
reducing the interfacial area. It is therefore better to increase the
entrainment rate by increasing the jet velocity thus maintaining the same
gas-to-liquid volumetric flow ratio as the entrainment rate and the

volumetric flow through the jet are both proportional to the jet velocity.

The rate of filmwise entrainment can also be increased by increasing the velocity of the free surface of the induction trumpet, which is equivalent to the recirculating eddy maximum velocity. The recirculating eddy maximum velocity increases with decreasing columnn diameter. Therefore the entrainment rate can be increased, for a fixed jet volumetric flowrate, by decreasing the diameter of the column.

7.4 MIXING ZONE

The mixing zone, which is primarily the region where the bubbles are generated, comprises the recirculating eddy and submerged jet streams.

The recirculating eddy is generated by the radial diffusion of jet momentum into the liquid surrounding the submerged jet. Momentum is dissipated by the jet in the radial direction due to the velocity and density difference across the submerged jet - surrounding liquid boundary. The velocity of the liquid surrounding the submerged jet increases due to a gain in momentum while the velocity of the liquid in the submerged jet decreases. Consequently, the submerged jet expands until it reaches the walls of the downcomer and the surrounding liquid forms a closed loop bounded by the submerged jet, the receiving liquid surface and the downcomer walls. Inside the surrounding liquid volume a circulating motion is developed, hence the name "recirculating eddy".

The recirculating eddy is a closed body of liquid separated from the liquid inside the submerged jet. Radial jet momentum will diffuse into the recirculating eddy as long as a velocity difference exists across the recirculating eddy - submerged jet boundary. If there is no momentum dissipation within the eddy, its velocity will increase until the velocity difference across the recirculating eddy - submerged jet boundary is equal to zero.

In practice recirculating eddy momentum is dissipated at the downcomer wall due to the shear stress acting against the direction of flow. The

area over which the shear stress acts depends on the downcomer diameter and the length along the downcomer where the submerged jet reaches the wall. This area can be reduced by either reducing the downcomer diameter or by increasing the submerged jet angle. However, by reducing the downcomer diameter the velocities inside the recirculating eddy are increased which will reduce the rate of dissipation of radial jet momentum and decrease the submerged jet angle.

The velocity profile generated within the recirculating eddy is important for two main reasons. Firstly, the velocity at the boundary of the eddy, which forms the free surface of the induction trumpet, controls the rate of filmwise entrainment. Secondly, the velocity profile, and in particular the boundary velocity of the recirculating eddy, influences the expansion of the submerged jet. It should be noted, however, that the recirculating eddy and the submerged jet are highly interactive: the rate of expansion of the submerged jet determines the velocity inside the recirculating eddy by defining the area over which the wall shear stress acts.

The volume in which jet energy is dissipated in the process of bubble generation is determined by the expansion of the submerged jet. The mean bubble diameter is directly related to the energy dissipation rate per unit submerged jet volume. Therefore, if small bubbles are required, it is necessary to reduce the volume of the submerged jet. However, it is not clear how this can be achieved because of the effect of variables such as column diameter and jet volumetric flowrate on the interaction between the recirculating eddy and the submerged jet.

The bubble diameter is a key variable in the operating characteristics of the downcomer section. In combination with the gas and liquid volumetric flux terms, the gas void fraction and the quantity of recycled gas are determined by the bubble size. Both the gas void fraction and the recycled gas component increase with increasing bubble diameter with the resultant increase in bubble rise velocity. The relative bubble rise velocity can be reduced by increasing the downward liquid volumetric flux, however this reduces the gas-to-liquid flow ratio into the column for a fixed gas input. In order to maximise the gas-to-liquid flow ratio whilst maintaining stable operation, it would be preferable to increase the downward volumetric liquid flux by decreasing the column diameter.

The density of the mixture is also determined by the relative velocity difference between the total downward volumetric flux and the bubble rise velocity, particularly inside the recirculating eddy where the bubble concentration appears to be higher than in the submerged jet region. Such a density difference would affect the rate of radial dissipation of jet momentum across the submerged jet – recirculating eddy boundary, thereby influencing the expansion of the submerged jet.

7.5   UNIFORM TWO PHASE FLOW ZONE

The interactions between the plunging jet and mixing zones result in a uniform two-phase downward flow which begins immediately below the submerged jet region.   The gas void fraction and type of flow in the uniform two-phase flow region depend on the gas and liquid volumetric flux, and the rise velocity of the bubbles.   At gas void fractions below approximately 0.3, bubbly flow occurs.   However, a gas void fraction of 0.3 represents a maximum gas-to-liquid volumetric flow ratio of 0.43.   In most applications the aim is to achieve a gas-to-liquid flow ratio of at least 1, which means that it is impractical to operate under ideal bubbly flow conditions.

For gas-to-liquid flow ratios of 1, the flow within the uniform two-phase flow zone becomes churn-turbulent, where the bubble rise velocity is of the order of 0.3 m/s (Harmathy, 1960).   It is important, therefore, when operating under churn-turbulent conditions to maintain the downward volumetric liquid flux inside the downcomer above 0.3 m/s to prevent gas from recycling to the top of the column.   In some cases the coalesced bubbles can bridge across the flow area to form a Dumitrescu bubble.   The rise velocity for a Dumitrescu bubble is given by

$$v_b = 0.496 \left\{ g R_c \right\}^{1/2} . \tag{7.1}$$

From (7.1) it can be seen that the velocity is a function of the column radius, and the downward superficial liquid volumetric flux required to prevent the Dumitrescu bubble returning to the headspace at the top of

the downcomer will need to be increased with increasing column radius.
For columns with a radius greater than approximately 40 mm, the minimum
downward liquid volumetric flux is determined by the rise velocity of the
Dumitrescu bubble. For columns with a radius less than 40 mm the minimum
liquid flux is approximately 0.3 m/s, which is equivalent to the rise
velocity of the churn turbulent bubbles.

7.6 STABILITY AND OPERATING RANGES

The operating range of gas throughput is controlled by the entrainment
characteristics of the plunging jet. As more gas is introduced the free
jet length will reach a new equilibrium value which gives the plunging
jet the required entrainment characteristics. For a fixed downcomer
length an increase in free jet length results in a corresponding decrease
in the volume of the two-phase flow region, which in turn results in a
decrease in the interfacial contact area. The minimum interfacial area
required to carry out the process will therefore limit the maximum
operating gas throughput for a fixed jet and downcomer system.

To overcome the reduction in interfacial area resulting from an increase
in the free jet length, the length of the uniform two-phase flow zone can
be increased by increasing the length of the downcomer. However, the
stability of operation inside the downcomer is determined by the flow
within the uniform two-phase flow zone, particularly the formation of
Dumitrescu bubbles due to coalescence. The presence of a Dumitrescu
bubble will restrict the flow of gas through the downcomer resulting in
an increase in pressure at the top of the froth phase. This will cause a
drop in the froth level, and in the extreme case, the complete collapse
of the system. To prevent the formation of Dumitrescu bubbles due to
coalescence, it is advisable to minimise the length of the uniform two-
phase flow zone where coalescence is most likely to occur. Also, the
rate of coalescence is increased with increasing initial bubble diameter,
and one of the effects of increasing the free jet length is an increase
in bubble diameter. Therefore, it is also advisable to operate the
downcomer with the shortest free jet length possible whilst still
maintaining the required gas throughput.

Chapter 8

CONCLUSIONS AND RECOMMENDATIONS

The results of this study have shown that the entrainment rate for a plunging liquid jet can be attributed to two different entrainment mechanisms: the gas contained within the boundary of the effective diameter of the jet at the plunge point, and the gas contained within the film between the induction trumpet and the free surface of the jet.

The rate of filmwise entrainment was obtained from the experimental results by extrapolating the total entrainment curve, plotted against the effective jet diameter, to the point of zero jet expansion. At this point the amount of gas contained within the effective jet diameter was zero and the measured entrainment rate could be attributed only to the filmwise component. The experimentally determined filmwise entrainment component was used to calculate the film thickness by realising that the flow inside the film was laminar, and that the boundary velocities were those of the free jet and the induction trumpet surface. It was assumed that the free surface of the induction trumpet followed the path of the "recirculating eddy" which consisted of the closed body of fluid circulating in the region between the boundary of the submerged jet and the downcomer wall. The velocity profile inside the eddy, and hence the velocity of the free surface of the induction trumpet, was found by applying the condition of solid body rotation to the liquid inside the recirculating eddy, whose volumetric flowrate was calculated using the empirical correlation proposed by Barchilon and Curtet (1964) for confined jets.

The calculated film thickness was found to be of the same order of magnitude as those predicted from thin film theory given by Levich (1962) for the constant thickness region of the film formed on a wire being withdrawn from a liquid bath. It was also found that the agreement between the predictions and the calculated film thickness was improved as the kinematic viscosity of the liquid was increased. This was because the increase in the viscous force prevented the gas film from rupturing prior to attaining a constant thickness. When the viscous force was not able to attenuate the disturbances on the induction trumpet free surface, the film was ruptured prior to attaining a region of constant thickness. This resulted in a greater rate of filmwise entrainment than was predicted from thin film theory.

It was also found from the experimental results that the initiation of filmwise entrainment depended on the free surface of the induction trumpet surface reaching a critical minimum velocity. This finding may be used to explain the wide range in the reported values of the minimum jet velocity necessary to initiate entrainment. The variation in the observed jet velocity seems likely to be due to the use of different diameter receiving vessels. The vessel diameter determines the jet velocity at which the induction trumpet surface reaches the critical velocity for the system under investigation. For the air-water system it was found that the critical velocity for the induction trumpet free surface was 0.4 m/s which was independent of the jet conditions and the downcomer diameter.

Once the gas was entrained it was assumed that the bubbles were formed within the volume occupied by the submerged jet where the volume was defined as the cone having a half angle of β and base equal to the diameter of the downcomer. The half angle was found experimentally by measuring the distance along the downcomer where the submerged jet reached the wall. The measured values for β were found to be in good agreement with those predicted from a model based on the rate of diffusion of jet momentum in the radial direction. The radial diffusion of jet momentum was found to be a function of the wall shear stress resisting the motion of the recirculating eddy and the Euler number for the jet-downcomer system, based on the jet velocity and the absolute pressure in the headspace at the top of the downcomer.

The maximum stable bubble diameter for the submerged jet volume was calculated from a model which used a critical Weber number value of 1.1, and assumed the energy dissipation rate per unit volume was equivalent to the energy mixing loss given by Cunningham (1974) for the throat section of a liquid-jet-gas-pump. This assumption was based on no heat generation within the submerged jet volume. In general it was found that the predicted maximum bubble diameter was in agreement with the measured value. It was also found that for the study the average value of the ratio of the Sauter mean to maximum diameter was 0.61, which was similar to reported values for mechanically agitated systems.

It was found that for turbulent liquid conditions in the uniform two-phase flow region inside the downcomer, a transition from bubbly to churn-turbulent flow occurred at a gas void fraction of approximately 0.2 when the gas drift flux was equal to zero. For all experimental runs, however, the gas drift flux was not zero and the flow transition was observed at gas void fraction values higher than 0.2, depending on the amount of drift between the gas and liquid phases. Under laminar liquid flow conditions the same transition took place at a much higher gas void fraction value.

The transition from bubbly to churn-turbulent flow was marked by a change in slope of the experimental line obtained from Zuber and Findlay (1965) drift-flux analysis. For the bubbly flow regime under laminar liquid conditions it was found that the distribution parameter C_o was greater than unity. As the liquid Reynolds number was increased the value of C_o rapidly decreased to approach unity under fully-turbulent flow. This trend indicated a more uniform distribution of the gas phase across the downcomer area as the liquid Reynolds number was increased.

For the churn-turbulent flow regime it was found that the experimental data for turbulent liquid flow could be collapsed onto a single curve when the modified gas void fraction was plotted against the gas-to-liquid volumetric flow ratio. The modified gas void fraction was obtained by applying a correction factor to the measured gas void fraction values to account for the difference in the bubble slip velocity between the experimental runs. There was also an indication that the constant in the correction factor was different for laminar liquid flow conditions.

Prior to the onset of bubble coalescence it was found that the experimental drift-flux curves could be fitted using the separated flow model proposed by Ishii and Zuber (1979) where the calculations were based on the Sauter mean diameter of the bubbles generated within the mixing zone of the downcomer. Once coalescence was initiated it was found that the experimental data departed from the original drift-flux curve and the drift-flux increased linearly with increasing gas void fraction. The slope of this line was found to increase with increasing liquid Reynolds number until a constant value was reached under fully turbulent liquid flow conditions.

The bubble diameter was found to play an important role in the overall operating characteristics of the downcomer. The interfacial area was maximised by generating the smallest sized bubbles possible and also by reducing the free jet length for a fixed downcomer length. The possibility of gas being recirculated to the headspace at the top of the downcomer was reduced by ensuring the volumetric liquid flux down the column was always greater than the rise velocity of the bubbles. It was found that the most stable operating conditions were obtained for the smallest diameter column used in conjunction with high throughput jets where the tip velocity was at least 10 m/s.

Recommendations for further work

This thesis has highlighted areas of research which require further examination:-

(1) experimental verification of the volumetric flowrate and velocity profile inside the recirculating eddy;

(2) measurement of the cross-sectional profile and velocity of the free surface of the induction trumpet;

(3) verification that the velocity of the free surface of the induction trumpet is equivalent to the recirculating eddy maximum velocity;

(4) measurement of the critical recirculating eddy maximum velocity required to initiate entrainment for a highly viscous liquid jet. The use of a highly viscous liquid would stabilise the induction trumpet against disturbance being generated on the free surface, and may provide a clearer picture of the mechanism which initiates entrainment;

(5) examination of the quantitative effect of introducing a rotational velocity component to the induction trumpet free surface on the rate of filmwise entrainment;

(6) determination of precisely where bubble breakup occurs once entrainment has been initiated and, once this region has been defined, calculation of the local energy dissipation rate;

(7) measurement of the radial gas void fraction profile in the mixing and uniform two-phase flow zone for both laminar and turbulent liquid flow conditions.

REFERENCES

Ahmed, N. (1983)
"Studies in the Flotation of Fine Particles", Dissertation, University of Newcastle, Australia.

Akita, K. and Yoshida, F. (1973)
"Gas Holdup and Volumetric Mass Transfer Coefficient in Bubble Columns: Effects of Liquid Properties", Ind. Eng. Chem. Process Des. Develop., 12: 76-80.

Allum, P. and Jameson, G.J. (1984)
"A Survey of Bubble Sizes in Industrial Flotation Cells", University of Newcastle, AMIRA Report, 226 pp.

Arai, T. and Hashimoto, H. (1986)
"Helical Surface Instability of Cylindrical Liquid Jet in Cocurrent Gas Stream", Bulletin of JSME, 29: 77-82.

Bach, H.F. and Pilhofer, T. (1978)
"Variation of Gas Holdup in Bubble Columns with Physical Properties of Liquids and Operating Parameters of Columns", Ger. Chem. Eng., 1: 270-275.

Bando, Y., Kuraishi, M., Nishimura, M., Hattori, M. and Asada, T. (1988)
"Cocurrent Downflow Bubble Column with Simultaneous Gas-Liquid Injection Nozzle", Journ. Chem. Eng. Japan, 21: 607-612.

Bankoff, S.G. (1960)
"A Variable Density Single-Fluid Model for Two-Phase Flow with Particular Reference to Steam-Water Flow", J. Heat Transf. (Trans. ASME), Series C, 82: 265-272.

Barchilon, M. and Curtet, R. (1964)
"Some Details of the Structure of an Axisymmetric Confined Jet with Backflow", Journ. Basic Eng., 86: 777-787.

Barnea, D., Shoham, O. and Taitel, Y. (1982)
"Flow Pattern Transition for Vertical Downward Two-Phase Flow", Chem. Eng. Sci., 37: 741-744.

Barnea, D. (1987)
"A unified model for predicting flow-pattern transitions for the whole range of pipe inclinations", Int. Journ. Multiphase Flow, 13: 1-12.

Batchelor, G.K. (1951)
Proc. Cambridge Phil. Soc., 41: 359.

Becker, H.A., Hottel, H.C. and Williams, G.C. (1962)
"Mixing and flow in ducted turbulent jets", Proc. 9th Int. Symp. Combustion, 7-20.

Bhaga, D. and Weber, M.E. (1972a)
"Holdup in Vertical Two and Three Phase Flow. Part 1 - Theoretical Analysis", Can. J. Chem. Eng., 50: 323-328.

Bhaga, D. and Weber, M.E. (1972b)
"Holdup in Vertical Two and Three Phase Flow. Part 2 - Experimental Investigation", Can. J. Chem. Eng., 50: 329-336.

Bin, A.K. (1988)
"Minimum air entrainment velocity of plunging liquid jets", Chem. Eng. Sci., 43: 379-389.

Binnie, A.M. (1942)
Engineering, 153: 503.

Bird, R.B., Stewart, W.E. and Lightfoot, E.N. (1960)
Transport Phenomena, John Wiley and Sons, Inc.

Bolton, B. and Middleman, S. (1980)
"Air Entrainment in a Roll Coating System", Chem. Eng. Sci., 35: 597-601.

Brodkey, R.S. (1967)
The Phenomena of Fluid Motions, Addison-Wesley Publishing Company, Reading, Massachusetts.

Brown, D.E. and Pitt, K. (1972)
"Drop Size Distribution of Stirred Non-Coalescing Liquid-Liquid System", Chem. Eng. Sci., 27: 577-583.

Buchholz, R., Tsepetonides, J., Steinemann, J. and Onken, V. (1983)
"Influence of gas distribution on interfacial area and mass transfer in bubble columns", Ger. Chem. Eng., 6: 105-113.

Buonopane, R.A., Gutoff, E.B., and Rimore, M.M.T. (1986)
"Effect of Plunging Tape Surface Properties on Air Entrainment Velocity", A.I.Ch.E. Journal, 32: 682-683.

Burley, R. and Jolly, R.P.S. (1984)
"Entrainment of Air into Liquids by a High Speed Continuous Solid Surface", Chem. Eng. Sci., 39: 1357-1372.

Calabrese, R.V., Chang, T.P.K. and Dang, P.T. (1986)
"Drop Breakup in Turbulent Stirred-Tank Contactors. Part I: Effect of Dispersed-Phase Viscosity", A.I.Ch.E. Journ., 32: 657-666.

Calderbank, P.H. (1958)
"Physical rate processes in industrial fermentation Part 1: The interfacial area in gas-liquid contacting with mechanical agitation", Trans. Instn Chem. Engrs., 36: 443-463.

Ciborowski, J. and Bin, A. (1972)
"Investigation of Aeration Effect of Free Liquid Jets", translated from Polish:. Inzynieria Chemiczna, II, 4: 557-77, by A. Hughes for B.H.P. Central Research Laboratories, May 1977.

Clark, N.N. and Flemmer, R. (1984)
"On Vertical Downward Two-Phase Flow", Chem. Eng. Sci., 39: 170-173.

Clark, N.N. and Flemmer, R.L. (1985)
"Predicting the Holdup in Two-Phase Bubble Upflow and Downflow using the Zuber and Findlay Drift-Flux Model", A.I.Ch.E. J., 31: 500-503.

Clark, N.N. and Flemmer, R. (1986)
"The Effect of Varying Gas Voidage Distributions on Average Holdup in Vertical Bubble Flow", Int. J. Multiphase Flow, 12: 299-302.

Clark, N.N., Atkinson, C.M. and Flemmer, R.L. (1987)
"Turbulent Circulation in Bubble Columns", A.I.Ch.E. J., 33: 515-518.

Clay, P.H. (1940)
Proc. Roy. Acad. Sci. (Amsterdam), 43: 852, 979.

Crawford, T.J., Weinberger, C.B. and Weisman, J. (1985)
"Two-Phase Flow Patterns and Void Fractions in Downward Flow. Part I: Steady-State Flow Patterns", Int. J. Multiphase Flow, 11: 761-782.

Cunningham, R.G. (1974)
"Gas Compression with the Liquid Jet Pump", Journ. Fluids Eng., Series I, 3: 203-215.

Cunningham, R.G. and Dopkin, R.J. (1974)
"Jet breakup and mixing throat lengths for the liquid jet gas pump", Journ. Fluids Eng. Series I, 3: 216-226.

Curtet, R. and Ricou, F.P. (1964)
"On the Tendency to Self-Preservation in Axisymmetric Ducted Jets", Journ. Basic Eng., 86: 735.

Davidson, J.F. and Harrison, D. (1966)
"The Behaviour of a Continuous Bubbling Fluidized Bed", Chem. Eng. Sci., 21: 731-738.

Davies, J.T. (1987)
"A Physical Interpretation of Drop Sizes in Homogenizers and Agitated Tanks, including the Dispersion of Viscous Oils", Chem. Eng. Sci., 42: 1671-1676.

Davies, R.M. and Taylor, Sir G.I. (1950)
"The Mechanics of Large Bubbles Rising Through Extended Liquids and Liquids in Tubes", Proc. Roy. Soc., 200A: 375-390.

De Frate, L.A. and Rush, F.E. (1969)
Preprint 39D. Symposium on selected papers, Part II, 64th National Meeting of the A.I.Ch.E., New Orleans, Louisianna, March 16-20.

Deckwer, W. and Schumpe, A. (1987)
"Bubble Columns - The State of the Art and Current Trends", Int. Chem. Eng., 27: 405-422.

Dobby, G.S., Yianatos, J.B. and Finch, J.A. (1986)
"Estimation of bubble diameter in flotation columns from drift-flux analysis", Unpublished report, 1986.

Donald, M.B. and Singer, H. (1959)
"Entrainment in Turbulent Fluid Jets", Trans. Instn. Chem. Engrs., 37: 255-267.

Dukler, A.E. and Taitel, Y. (1986)
"Flow Pattern Transitions in Gas-Liquid Systems: Measurement and Modelling", in Zuber, N., Hewitt, G. and Delhaye, J. (eds), Advances in Multiphase Flow, Vol. 2, pp. 1-94.

Dumitrescu, D.T. (1943)
"Flow past an air bubble in a vertical pipe", Z. F. Angew. Math. & Mech., 23: 139-149.

Folsom, R.G. and Ferguson, C.K. (1948)
Trans. Amer. Soc. Mech. Engrs., 71: 73

Freedman, W. and Davidson, J.F. (1969)
"Holdup and Liquid Circulation in Bubble Columns", Trans. Instn. Chem.
Engrs., 47: T251-T262.

Friedel, L., Herbrechtsmeier, P. and Steiner, R. (1980)
"Mean Gas Hold-Up in Downflow Bubble Columns", Ger. Chem. Eng., 3: 342-
346.

Funatsu, K., Hsu, Y. and Kamogawa, T. (1988)
"Gas Holdup and Gas Entrainment of a Plunging Water Jet with a Constant
Entrainment Guide", Can. J. Chem. Eng., 66: 19-28.

Grace, J.R., Wairegi, T. and Nguyen, T.H. (1976)
"Shapes and velocities of single drops and bubbles moving freely through
immiscible liquids", Trans. Instn. Chem. Engrs, 54: 167-173.

Glauert, M.B. and Lighthill, M.J. (1955)
Proc. Roy. Soc., Ser. A, 273: 188.

Golan, L.P. and Stenning, A.H. (1969)
"Two-Phase Vertical Flow Maps", Proc. Inst. Mech. Eng., 184: 108.

Griffith, P. and Wallis, G.B. (1961)
"Two-Phase Slug Flow", Journ. Heat Transf. (Trans. ASME), Series C, 83:
307-320.

Guy, C., Carreau, P.J. and Paris, J. (1986)
"Mixing Characteristics and Gas Holdup of a Bubble Column", Can. Journ.
Chem. Eng., 64: 23-35.

Harmathy, T.Z. (1960)
"Velocity of Large Drops and Bubbles in Media of Infinite and of
Restricted Extent", A.I.Ch.E. Journ., 6: 281-288.

Hatch, R.T. (1973)
"Experimental and Theoretical Studies of Oxygen Transfer in the Airlift Fermenter", Dissertation, Massachusetts Int. Technol., Cambridge, M.A.

Herbrechtsmeier, P., Schäfer, H. and Steiner, R. (1981)
"Gas Absorption in Downflow Bubble Columns for the Ozone-Water System", Ger. Chem. Eng., 4: 258-264.

Herbrechtsmeier, P. and Schäfer, H. (1982)
"Development of a Cascade Downflow Reactor as a High Performance Equipment for Physical Absorption and Desorption Processes", Ger. Chem. Eng., 5: 369-374.

Herbrechtsmeier, P., Schäfer, H. and Steiner, R. (1985)
"Influence of Operating Parameters on Interfacial Area in Downflow Bubble Columns", Ger. Chem. Eng., 8: 57-64.

Hesketh, R.P., Fraser Russell, T.W. and Etchells, A.W. (1987)
"Bubble Size in Horizontal Pipelines", A.I.Ch.E. Journ., 33: 663-667.

Hewitt, G.F. (1982)
"Liquid-Gas Systems", in Hetsroni, G. (ed.), Handbook of Multiphase Systems, McGraw-Hill, Washington.

Hikita, H., Asai, S., Tanigawa, K., Segawa, K. and Kitao, M. (1980)
"Gas hold-up in bubble columns", Chem. Eng. Journ., 20: 59-67.

Hills, J.H. (1974)
"Radial Non-Uniformity of Velocity and Voidage in a Bubble Column", Trans. Instn. Chem. Engrs., 52: 1-9.

Hills, J.H. (1976)
"The Operation of a Bubble Column at High Throughputs. I. Gas Holdup Measurements", Chem. Eng. Journ., 12: 89-99.

Hinze, J.O. (1955)
"Fundamentals of the Hydrodynamic Mechanism of Splitting in Dispersion Processes", A.I.Ch.E. Journ., 1: 289-295.

Hinch, E. J. and Acrivos, A. (1979)
"Steady Long Slender Droplets in Two-Dimensional Straining Motion",
Journ: Fluid. Mech., 91: 401-414

Hinch, E. J. and Acrivos, A. (1980)
"Long Slender Drops in a Simple Shear Flow", Journ. Fluid. Mech., 98:
305-328

Iodogawa, K., Ikeda, K., Fukuda, T. and Morooka, S. (1986)
"Behaviour of Bubbles of the Air-Water System in a Column under High
Pressure", Int. Chem. Eng., 26: 468-474.

Iordache, O. and Jinescu, G. (1986)
"The Stability of Flow in Bubble Columns", Chem. Eng. Sci., 41: 2585-
2588.

Ishii, M. and Zuber, N. (1979)
"Drag Coefficient and Relative Velocity in Bubbly, Droplet or Particulate
Flows", A.I.Ch.E. Journ., 25: 843-855.

Joshi, J.B. and Sharma, M.M. (1979)
"A Circulation Cell Model for Bubble Columns", Trans. Instn. Chem.
Engrs., 57: 244-251.

Joshi, J.B., Pandit, A.B. and Sharma, M.M. (1982)
"Mechanically Agitated Gas-Liquid Reactors", Chem. Eng. Sci., 37: 813-
844.

Kara, S., Kelkar, B.G., Shah, Y.T. and Carr, N.L. (1982)
"Hydrodynamics and Mixing in a Three-Phase Bubble Column", Ind. Eng.
Process Des. Dev., 21: 584-594.

Kato, Y., Nishinaka, M. and Morooka, S. (1975)
"Distribution of gas holdup in a bubble column", Kagaku Kogaku Ronbunshu,
1: 530.

Kennedy, B.S. and Burley, R. (1977)
"Dynamic Fluid Interface Displacement and Prediction of Air Entrainment",
Journ. Coll. Interface Science, 62: 48-62.

Kumagai, M. and Endoh, K. (1982)
"Effects of Kinematic Viscosity and Surface Tension on Gas Entrainment
Rate of an Impinging Liquid Jet", J. Chem. Eng. Japan, 15: 427-433.

Kumagai, M. and Endoh, K. (1983a)
"A Note on the Relationship between Gas Entrainment Curve and its
Starting Velocity", J. Chem. Eng. Japan, 16: 74-75.

Kumagai, M. and Endoh, K. (1983b)
"Mean Residence Time and Gas Holdup of Entrained Gas by an Impinging
Water Jet", J. Chem. Eng. Japan, 16: 357-363.

Lane, A.G.C. and Rice, P. (1982)
"The Flow Characteristics of a Submerged Bounded Jet in a Closed System",
Trans. I. Chem. E., 60: 245-248.

Latzko, Z. (1921)
Angew. Math. Mech., 1: 277.

Levich, V.G. (1962)
Physiochemical Hydrodynamics, Prentice-Hall, Englewood Cliffs, N.J.

Lewis, D.A. and Davidson, J.F. (1982)
"Bubble Splitting in Shear Flow", Trans. I. Chem. E., 60: 283-291.

Lewis, D.A. and Davidson, J.F. (1983)
"Bubble Sizes Produced by Shear and Turbulence in a Bubbly Column", Chem.
Eng. Sci., 38: 161-167.

Lin, T.J. (1963)
"Gas Bubble Entrainment by Plunging Laminar Liquid Jets", Ph.D. thesis,
Wayne State University, Detroit, Michigan.

Lin, T.J. and Donnelly, H.G. (1966)
"Gas Bubble Entrainment by Plunging Laminar Liquid Jets", A.I.Ch.E.
Journ., 12: 563-571.

Liu, C. and Barkelew, C.H. (1986)
"Numerical Analysis of Jet-stirred Reactors with Turbulent Flows and Homogeneous Reactions", A.I.Ch.E. Journal, 32: 1813-1820.

Lockett, M.J. and Kirkpatrick, R.D. (1975)
"Ideal Bubbly Flow and Actual Flow in Bubble Columns", Trans. Instn. Chem. Engrs., 53: 267-273.

McCarthy, M.J. (1972)
"Entrainment by Plunging Jets", Ph.D. thesis, University of Newcastle. N.S.W.

McCarthy, M.J. and Molloy, N.A. (1974)
"Review of Stability of Liquid Jets and the Influence of Nozzle", Chem. Eng. Journ., 7: 1-20.

McKeogh, E.J. and Ervine, D.A. (1981)
"Air Entrainment Rate and Diffusion Pattern of Plunging Liquid Jets", Chem. Eng. Sci., 36: 1161-1172.

Marrucci, G. (1965)
"Rising Velocity of a Swarm of Spherical Bubbles", Ind. Eng. Chem. Fund., 4: 224-225.

Merchuk, J.C. and Stein, Y. (1981)
"Local Holdup and Liquid Velocity in Air-Lift Reactors", A.I.Ch.E. Journ., 27: 377-388.

Mersmann, A. (1978)
"Design and Scale-up of Bubble and Spray Columns", Ger. Chem. Eng., 1: 1-11.

Mertes, A.T. (1938)
Patent 2,128,311. United States Patent Office.

Mihail, R. and Straja, J. (1986)
"A Theoretical Model Concerning Bubble Size Distributions", Chem. Eng. Journ., 33: 71-77.

Miksis, M., vanden-Broeck, J.M. and Keller, J.B. (1981)
"Axisymmetric Bubble or Drop in a Uniform Flow", J. Fluid Mech., 108: 89-100.

Molerus, O. (1987)
"Dependence of the Drag on Particles Concentration - A Basic Model and its Practical Applications", Chem. Eng. Sci., 42: 689-705.

Moss, E.T. (1947)
"The Mixing of Liquids by Injector Action", Trans. Instn. Chem. Engrs., 25: 191-198.

Nassos, G.P. and Bankoff, S.G. (1967)
"Slip Velocity Ratios in an Air-Water System Under Steady State and Transient Conditions", Chem. Eng. Sci., 22: 661-668.

Nishikawa, M., Yonezawa, Y., Kayamut, T., Koyama, K. and Nagata, S. (1976)
"Studies on Gas Holdup in Gas-Liquid Spouted Vessel", Journ. Chem. Eng. Japan, 9: 214-219.

Ogawa, S., Kobayashi, M., Tone, S. and Otake, T. (1982)
"Liquid Phase Mixing in the Gas-Liquid Jet Reactor with Liquid Jet Ejector", Journ. Chem. Eng. Japan, 15: 469-474.

Ohkawa, A., Shiokawa, Y., Sakai, N. and Endoh, K. (1985a)
"Gas Holdup in Downflow Bubble Columns with Gas Entrainment by a Liquid Jet", Journ. Chem. Eng. Japan, 18: 172-174.

Ohkawa, A., Shiokawa, Y., Sakai, N. and Imai, H. (1985b)
"Flow Characteristics of Downflow Bubble Columns with Gas Entrainment by a Liquid Jet", Journ. Chem. Eng. Japan, 18: 466-469.

Ohkawa, A., Kusabiraki, D., Kawai, Y., Sakai, N. and Endoh, K. (1986)
"Some Flow Characteristics of a Vertical Liquid Jet System Having Downcomers", Chem. Eng. Sci., 41: 2347-2361.

Ohkawa, A., Kawai, Y., Kusabiraki, D., Sakai, N. and Endoh, K. (1987) "Bubble size, interfacial area and liquid-phase mass transfer coefficient in downflow bubble columns with gas entrainment by a liquid jet", Journ. Chem. Eng. Japan, 20: 99-101.

Oshinowo, T. and Charles, M.E. (1974) "Vertical Two-Phase Flow. Part I. Flow Pattern Correlations", Can. Journ. Chem. Eng., 52: 25-35.

Otake, T., Tone, S., Kuboi, R., Takahashi, Y. and Nakao, K. (1981) "Dispersion of a Gas by a Liquid-Jet Ejector", Int. Chem. Eng., 21: 72-80.

Oyama, Y., Takashima, Y. and Idemura, H. (1953) Kagaku Kenkyusho Hokoku, 29: 344.

Pandit, A.B. and Davidson, J.F. (1986) "Bubble Break-up in Turbulent Liquid", Int. Conf. Bioreactor Fluid Dynamics, Cambridge, England, April 1986, pp. 109-120.

Peebles, F.N. and Garber, H.J. (1953) "Studies of the Motion of Gas Bubbles in Liquids", Chem. Engr. Progress, 49: 88-97.

Perry, R.T. (1967) "Fluid mechanics of entrainment through liquid-liquid and solid-liquid junctures", Ph.D. Thesis, University of Minnesota, Univ. Microfilms, No. 67-14, 639, Ann Arbor, Michigan.

Rajaratnam, N. (1976) Turbulent Jets, Amsterdam, Elsevier Scientific Publishing Company.

Rallinson, J.M. (1984) "The Deformation of Small Viscous Drops and Bubbles in Shear Flows", Ann. Rev. Fluid Mech., 16: 45-66.

Reilly, I.G., Scott, D.S., de Bruijn, T., Jain, A. and Piskorz, J. (1986) "A Correlation for Gas Holdup in Turbulent Coalescing Bubble Columns", Can. Journ. Chem. Eng., 64: 705-717.

234

Richardson, J.F. and Zaki, W.N. (1954)
"Sedimentation and Fluidization: Part I", Trans. Instn. Chem. Engrs, 32: 35-52. .

Rietema, K. and Ottengraph, S.P.P. (1970)
"Laminar Liquid Circulation a Bubble Street Formation in a Gas-Liquid System", Trans. Instn. Chem. Engrs, 48: T54-T62.

Rotte, J.W. (1969)
"Momentum, heat and mass transfer from continuous cylindrical bodies", Ph.D. Thesis, Delftse Universitaire Pers.

Rouhani, S.Z. and Sohal, M.S. (1983)
"Two-Phase Flow Patterns: A Review of Research Results", Progress in Nuclear Energy, 11: 219-259.

Ryskin, G. and Leal, L.G. (1984)
"Numerical Solution of Free-Boundary Problems in Fluid Mechanics. Part 3. Bubble Deformation in an Axisymmetric Straining Flow", J. Fluid Mech., 148: 37-43.

Schlichting, H. (1968)
Boundary Layer Theory, McGraw-Hill, New York.

Scriven, L.E. (1982)
"How Does Air Entrain at Wetting Lines?", A.I.Ch.E. Winter National Meeting, Orlando, Florida.

Sekizawa, T., Kubota, H. and Chung, W.C. (1983)
"Apparent Slip Velocity with Recirculating Turbulent Flow in Bubble Columns", Journ. Chem. Eng. Japan, 16: 327-330.

Sene, K.J. (1988)
"Air Entrainment by Plunging Jets", Chem. Eng. Sci., 43: 2615-2623.

Sevik, M. and Park, S.H. (1973)
"The Splitting of Drops and Bubbles by Turbulent Fluid Flow", Journ. Fluids Eng. (Trans. ASME), 95: 53-60.

Shah, Y.T., Kelkar, B.G., Goodbole, S.P. and Deskwer, W-D. (1982) "Design Parameters Estimation for Bubble Column Reactors", A.I.Ch.E. Journ., 28: 353-379.

Shah, Y.T., Kulkarni, A.A., Wieland, J.H. and Carr, N.L. (1983) "Gas Holdup in Two- and Three-Phase Downflow Bubble Columns", Chem. Eng. Journ., 26: 95-104.

Sheridan, A.T. (1966) "Surface Entrainment of Air by Water Jets", Nature, 209: 799-800.

Shimizu, Y., Nakamura, S., Kuzuhara, S. and Kurata, S. (1987) "Studies of the configuration and performance of annular type jet pumps", Journ. Fluids Eng., 109: 205-212.

Shirley, R.W. (1950) M.S. Thesis. University of Iowa, Ames.

Shyu, C.N. and Miyauchi, T. (1971) "Axial Dispersion in Gas Bubble Columns", Kagaku Kogaku Ronbunshu, 35: 663.

Spedding, P.L. and Nguyen, V.T. (1980) "Regime Maps for Air-Water Two-Phase Flow", Chem. Eng. Sci., 35: 779-793.

Spiers, R.P., Subbaraman, C.V. and Wilkinson, W.L. (1974) "Free Coating of a Newtonian Liquid onto a Vertical Surface", Chem. Eng. Sci., 29: 389-396.

Sucui, G.D. and Smigelschi, O. (1976) "Size of the Submerged Biphasic Region in Plunging Jet Systems", Chem. Eng. Sci., 31: 1217-1220.

Szekely, J. (1969) Trans. Met. Soc. A.I.M.E., 245: 341.

Taylor, Sir G.I. (1934) "The Formation of Emulsion in Definable Field of Flow", Proc. Roy. Soc. (London), Series A, 146: 501.

Thomas, N.H., Auton, T.R., Sene, K. and Hunt, J.C.R. (1984)
"Entrapment and Transport of Bubbles by Plunging Water", in W. Brutsaert
and G.J.H. Jirka (eds), Gas Transfer at Water Surfaces, D. Reidel
Publishing Company, 255-268.

Turner, J.C.R. (1966)
"On Bubble Flow in Liquids and Fluidized Beds", Chem. Eng. Sci., 21: 971-
974.

Ueyama, K. and Miyauchi, T. (1979)
"Properties of Recirculating Turbulent Two-Phase Flow in Gas Bubble
Columns", A.I.Ch.E. Journ., 25: 258-266.

Unno, H. and Inoue, I. (1980)
"Size Reduction of Bubbles by Orifice Mixer", Chem. Eng. Sci., 35: 1571-
1579.

van de Donk, J.A.C., van der Lans, R.G.J.M. and Smith, J.M. (1979)
"The Effect of Contaminants on the Oxygen Transfer Rate Achieved with a
Plunging Jet Contactor", 3rd Europe Conf. Mix., University of York, Paper
F1, 289-302.

van de Sande, E. (1974)
Air Entrainment by Plunging Water Jets, Ph.D. Thesis, Delftse
Universitaire Pers.

van de Sande, E. and Smith, J.M. (1973)
"Surface Entrainment of Air by High Velocity Water Jets", Chem. Eng.
Sci., 28: 1161-1168.

van de Sande, E. and Smith, J.M. (1976)
"Jet Break-up and Air Entrainment by Low Velocity Turbulent Water Jets",
Chem. Eng. Sci., 31: 219-224.

Viswanathan, K. and Subba Rao, D. (1983)
"Circulation in Bubble Columns", Chem. Eng. Sci., 38: 474-478.

Wachi, S., Morikawa, H. and Ueyama, K. (1987)
"Gas Holdup and Axial Dispersion in Gas-Liquid Concurrent Bubble Column",
Journ. Chem. Eng. Japan, 20: 309-316.

Wallis, G.B. (1962)
"A Simplified One-Dimensional Representation of Two-Component Vertical
Flow and its Application to Batch Sedimentation", Sympos. Interaction
Between Fluids and Particles, London 20-22 June, 1962, Instn. Chem.
Engrs, London, 9-16.

Wallis, G.B. (1969)
One-Dimensional Two-Phase Flow, McGraw-Hill, New York.

Wallis, G.B. (1974)
"The terminal speed of single drops or bubbles in an infinite liquid",
Int. Journ. Multiphase Flow, 1: 491-511.

Walter, J.F. and Blanch, H.W. (1983)
"Liquid Circulation Patterns and Their Effect on Gas Holdup and Axial
Mixing in Bubble Columns", Chem. Eng. Commun., 19: 243-262.

Weiland, P. and Onken, U. (1981)
"Differences in Behaviour of Bubble Columns and Airlift Loop Reactors",
Ger. Chem. Eng., 4: 174-181.

Weisman, J. and Kang, S.Y. (1981)
"Flow pattern transitions in vertical and upwardly inclined lines", Int.
Journ. Multiphase Flow, 7: 271-291.

Weisweiler, W. and Rosch, S. (1978)
"Interfacial Area and Bubble-Size Distribution in Jet Reactors", Ger.
Chem. Eng., 1: 212-218.

Weisweiler, W., Vavatzanidis, A. and Raible, L. (1982)
"Estimation of Physical Interfacial Area in a Momentum Transfer Tube of a
Jet Tube Reactor", Ger. Chem. Eng., 5: 380-387.

Whalley, P.B. and Davidson, J.F. (1974)
"Liquid Circulation in Bubble Columns", Instn. Chem. Engrs, Sympos.
Series. No. 38. Paper J5.

White, D.A. and Tallmadge, J.A. (1965)
"Theory of Drag Out of Liquids on Flat Plates", Chemical Engineering
Science, 20: 33-37.

Wijffels, J-B and Rietema, K. (1972a)
"Flow Patterns and Axial Mixing in Liquid-Liquid Spray Columns. Part I -
Theory", Trans. Instn. Chem. Engrs., 50: 224-232.

Wijffels, J-B and Rietema, K. (1972b)
"Flow Patterns and Axial Mixing in Liquid-Liquid Spray Columns. Part 2 -
Experiments", Trans. Instn. Chem. Engrs., 50: 233-239.

Wilkinson, W.L. (1975)
"Entrainment of Air by a Solid Surface Entering a Liquid/Air Interface",
Chem. Eng. Sci., 30: 1227-1230.

Witte, J.H. (1969)
"Mixing shocks in two-phase flow", J. Fluid Mech., 36: 639-655.

Yianatos, J.B., Laplante, A.R. and Finch, J.A. (1985)
"Estimation of Local Holdup in the Bubbling and Froth Zones of a Gas-
Liquid Column", Chem. Eng. Sci., 40: 1965-1968.

Zhang, S.H., Yu, S.C., Zhou, Y.C. and Su, Y.F. (1985)
"A Model for Liquid-Liquid Extraction Column Performance - The Influence
of Drop Size Distribution on Extraction Efficiency", Can. Journ. Chem.
Eng., 63: 212-226.

Zuber, N. (1964)
"On the dispersed two-phase flow in the laminar flow regime", Chem. Eng.
Sci., 19: 897-917.

Zuber, N. and Findlay, J.A. (1965)
"Average Volume Concentration in Two-Phase Flow Systems", Journ. Heat
Transf. (Trans. ASME), Series C, 453-468.

Appendix 1

SUMMARY OF CONDITIONS

AND EXPERIMENTAL RESULTS

In this appendix a summary of the conditions for the experimental runs performed in this study is presented. Also included in this appendix are the measurements for the volumetric gas entrainment rate, free jet length and gas void fraction for each run.

TABLE A1.1 :   Summary of conditions for the experimental runs

RUN NUMBER	COLUMN DIAMETER (mm)	NOZZLE DIAMETER (mm)	LIQUID FLOWRATE (L/min)	SURFACE TENSION (mN/m)	LIQUID DENSITY (kg/m3)	LIQUID VISCOSITY) (mPas)
1	44.2	7.12	36.035	48	996.5	.8513
2	44.2	7.12	27.555	48	996.5	.8513
3	44.2	7.12	18.740	48	997.0	.8327
4	44.2	7.12	36.035	54	996.2	.8513
5	44.2	7.12	27.555	54	997.3	.9111
6	44.2	7.12	18.740	55	997.5	.8705
7	44.2	7.12	36.035	62	997.5	.8705
8	44.2	7.12	27.555	62	997.5	.8705
9	44.2	7.12	18.740	62	997.5	.9325
10	44.2	4.76	16.011	47	996.5	.8327
11	44.2	4.76	12.249	47	996.5	.8705
12	44.2	4.76	8.324	48	996.5	.8904
13	44.2	4.76	16.011	53	996.5	.8513
14	44.2	4.76	12.249	53	996.5	.8327
15	44.2	4.76	8.324	53	996.5	.8513
16	44.2	4.76	16.011	63	996.2	.8327
17	44.2	4.76	12.249	65	996.8	.8705
18	44.2	4.76	8.324	62	997.3	.9111
19	44.2	2.38	4.004	48	997.5	.9325
20	44.2	2.38	3.062	49	997.3	.9111
21	44.2	2.38	2.082	49	997.9	.9548
22	44.2	2.38	4.004	53	997.5	.9325
23	44.2	2.38	3.062	54	997.5	.9325
24	44.2	2.38	2.082	54	997.0	.8904
25	44.2	2.38	4.004	60	997.3	.9111
26	44.2	2.38	3.062	61	997.5	.9325
27	44.2	2.38	2.082	60	997.5	.9325
28	44.2	7.12	36.035	64	1064	1.653
29	44.2	7.12	27.555	63	1064	1.653
30	44.2	7.12	18.740	62	1064	1.653
31	44.2	4.76	16.011	63	1061	1.653
32	44.2	4.76	12.249	64	1061	1.653
33	44.2	4.76	8.324	62	1061	1.653
34	44.2	2.38	4.004	64	1061	1.653
35	44.2	2.38	3.062	64	1061	1.653
36	44.2	2.38	2.082	64	1061	1.653
37	44.2	7.12	36.035	53	1114	2.854
38	44.2	7.12	27.555	53	1114	2.854
39	44.2	7.12	18.740	53	1114	2.854
40	44.2	4.76	16.011	63	1114	2.854
41	44.2	4.76	12.249	65	1114	2.854
42	44.2	4.76	8.324	62	1114	2.854
43	44.2	2.38	4.004	63	1116	2.854
44	44.2	2.38	3.062	62	1116	2.854
45	44.2	2.38	2.082	63	1116	2.854
46	44.2	7.12	36.035	24	784.0	2.12
47	44.2	7.12	27.555	24	784.0	2.12
48	44.2	7.12	18.740	24	784.0	2.12
49	44.2	4.76	16.011	24	784.0	2.12
50	44.2	4.76	12.249	24	784.0	2.12
51	44.2	4.76	8.324	24	784.0	2.12
55	44.2	7.12	12.249	54	997.3	.9111

TABLE A1.1 (cont'd) : Summary of conditions for the experimental runs

RUN NUMBER	COLUMN DIAMETER (mm)	NOZZLE DIAMETER (mm)	LIQUID FLOWRATE (L/min)	SURFACE TENSION (mN/m)	LIQUID DENSITY (kg/m3)	LIQUID VISCOSITY) (mPas)
56	44.2	2.38	8.324	54	997.3	.9111
64	44.2(B)	4.76	12.249	65	998.6	1.053
65	44.2	4.76(*)	12.249	65	998.6	1.053
67	44.2	4.76(*)	12.249	65	999.1	.9325
68	44.2	4.76(*)	12.249	65	999.1	.9111
69	44.2	4.76(*)	12.249	64	998.9	.9548
70	44.2	4.76(*)	12.249	64	998.9	.9325
71	74.3	7.12	36.035	65	998.0	.9325
72	74.3	7.12	27.555	63	998.0	.8904
73	74.3	7.12	18.740	63	998.0	.9779
74	74.3	4.76	16.011	65	998.9	1.109
75	74.3	4.76	12.249	63	998.8	1.081
76	74.3	4.76	8.324	64	998.8	1.081
77	74.3	2.38	4.004	63	998.2	1.002
78	74.3	2.38	3.062	64	998.2	1.002
80	74.3(B)	7.12	36.035	63	998.2	1.002
81	74.3(B)	7.12	27.555	61	998.0	.9779
82	74.3(B)	7.12	18.740	63	998.0	.9779
83	74.3(B)	4.76	16.011	67	998.8	1.081
84	74.3(B)	4.76	12.249	67	998.8	1.081
85	74.3(B)	4.76	8.324	67	998.8	1.081
86	74.3(B)	2.38	4.004	65	998.4	1.027
87	74.3(B)	2.38	3.062	62	998.4	1.027
88	74.3(B)	2.38	2.082	63	998.4	1.027
91	95.4	7.12	36.035	65	998.4	1.027
92	95.4	7.12	27.555	65	998.9	1.109
93	95.4	7.12	18.740	63	998.8	1.081
94	95.4	4.76	16.011	63	998.8	1.081
95	95.4	4.76	12.249	63	998.8	1.081
96	95.4	4.76	8.324	63	998.8	1.081
97	95.4	2.38	4.004	63	998.9	1.109
100	95.4(B)	4.76	16.011	62	998.4	1.027
101	95.4(B)	4.76	12.249	62	998.4	1.027

TABLE A1.2 Run 1 data

'GAS FLOWRATE (L/min)	JET LENGTH (m)	GAS VOID FRACTION
9.500		.179
11.610		.210
13.680	.009	.240
15.790	.013	.272
17.900	.018	.304
20.330	.023	.336
23.020	.030	.366
25.650	.038	.395
27.820	.045	.418
29.600	.052	.442
30.890	.058	.453
33.680	.067	.472
35.480	.076	.490
37.570	.082	.506
39.490	.093	.522
41.460	.108	.538
43.600	.122	.554
45.650	.138	.568
47.700	.157	.580
49.600	.179	.594
51.600	.215	.615
53.640	.235	.622
55.590	.264	.632

TABLE A1.2 Run 2 Data

GAS FLOWRATE (L/min)	JET LENGTH (m)	GAS VOID FRACTION
9.220	.015	.236
11.270	.023	.273
13.270	.033	.309
15.310	.043	.342
17.350	.055	.374
19.700	.073	.411
22.260	.094	.443
24.850	.119	.477
26.930	.141	.499
28.630	.171	.519
29.870	.190	.531
31.610	.209	.543
32.530	.228	.552
33.460	.242	.559
34.260	.260	.568
35.240	.271	.580
36.200	.292	.586
37.080	.308	.593
38.040	.325	.603
39.000	.343	.610
39.950	.355	.617
41.270	.373	.623
42.030	.398	.630
43.080	.408	.632
43.980	.430	.635
45.900	.465	.637

TABLE A1.2 Run 3 Data

GAS FLOWRATE (L/min)	JET LENGTH (m)	GAS VOID FRACTION
3.590	.008	.157
4.420	.010	.194
5.350	.020	.223
6.260	.028	.252
7.090	.038	.282
8.060	.052	.305
8.950	.061	.327
9.830	.077	.354
10.910	.094	.381
11.870	.111	.396
12.840	.129	.420
13.790	.151	.434
14.780	.169	.453
15.840	.196	.471
16.730	.225	.489
17.920	.244	.505
19.000	.274	.522
20.090	.302	.539
21.430	.340	.554
22.660	.373	.567
23.920	.397	.583
25.050	.438	.597
25.900	.473	.608
26.740	.495	.617
27.540	.530	.621
28.180	.545	.621
28.730	.560	.614

TABLE A1.2 Run 4 Data

GAS FLOWRATE (L/min)	JET LENGTH (m)	GAS VOID FRACTION
9.422		.163
11.523		.205
13.577	.010	.225
15.658	.014	.251
17.736	.018	.280
20.151	.022	.317
22.788	.028	.362
25.449	.035	.373
27.580	.042	.402
29.355	.050	.428
30.634	.056	.447
33.414	.067	.466
35.210	.074	.469
37.223	.086	.487
39.142	.096	.504
41.113	.109	.522
43.243	.124	.542
45.299	.130	.546
47.221	.152	.552
49.194	.168	.503
51.262	.197	.371
53.199	.223	.020
55.174	.255	

TABLE A1.2   Run 5 Data

GAS FLOWRATE (L/min)	JET LENGTH (m)	GAS VOID FRACTION
7.224	.007	.189
8.201	.010	.208
9.097	.012	.232
10.005	.015	.253
11.115	.021	.277
12.102	.026	.289
13.090	.030	.310
14.064	.037	.335
15.098	.042	.358
16.190	.049	.363
17.102	.054	.370
18.317	.065	.396
19.419	.074	.414
20.556	.086	.433
21.942	.096	.439
23.205	.108	.457
24.487	.124	.471
25.656	.136	.477
26.547	.150	.489
27.409	.168	.501
28.224	.179	.514
28.869	.191	.515
29.419	.198	.528
32.081	.227	.526
32.993	.245	.536
33.781	.254	.520
34.773	.272	.498
35.706	.290	.432
36.589	.305	.345
37.527	.320	.119

TABLE A1.2   Run 6 Data

GAS FLOWRATE (L/min)	JET LENGTH (m)	GAS VOID FRACTION
4.342	.009	.195
5.254	.017	.232
6.152	.025	.265
6.967	.035	.301
7.906	.046	.332
8.790	.059	.343
9.656	.076	.363
11.335	.100	.392
11.674	.105	.407
12.280	.117	.414
12.623	.122	.422
13.274	.131	.437
13.554	.141	.445
14.537	.159	.466
15.120	.172	.470
15.592	.176	.481
16.188	.190	.490
17.169	.211	.507
17.632	.222	.514
18.695	.250	.531
19.764	.278	.533
21.088	.305	.529
22.288	.355	.442
23.533	.378	.351

TABLE A1.2 Run 7 Data

GAS FLOWRATE (L/min)	JET LENGTH (m)	GAS VOID FRACTION
9.468		.184
11.566		.216
13.632	.012	.246
15.723	.015	.276
17.816	.022	.306
20.248	.027	.334
22.877	.034	.372
25.547	.044	.401
27.691	.052	.425
29.498	.060	.449
30.783	.068	.459
33.589	.080	.478
35.345	.094	.499
37.364	.116	.521
39.276	.121	.538
41.253	.127	.558
43.370	.158	.577
45.379	.178	.596
47.308	.202	.608
49.279	.233	.621
51.322	.265	.630
53.259	.295	.633
55.189	.338	.615

TABLE A1.2 Run 8 Data

GAS FLOWRATE (L/min)	JET LENGTH (m)	GAS VOID FRACTION
9.133	.017	.240
11.150	.025	.281
13.131	.037	.316
15.149	.050	.352
17.159	.064	.384
19.505	.080	.419
22.002	.104	.444
24.575	.133	.476
26.628	.160	.503
28.323	.192	.530
29.528	.231	.544
31.248	.250	.558
23.187	.261	.566
33.071	.282	.578
33.857	.300	.585
64.858	.317	.591
35.792	.336	.596
36.674	.352	.603
37.625	.369	.613
38.562	.388	.620
39.499	.407	.625
40.781	.430	.625
41.542	.440	.625
42.543	.460	.613

TABLE A1.2   Run 9 Data

GAS FLOWRATE (L/min)	JET LENGTH (m)	GAS VOID FRACTION
3.558	.008	.155
4.378	.011	.190
5.299	.021	.229
6.201	.028	.259
7.025	.039	.289
7.974	.051	.321
8.853	.064	.345
9.729	.078	.367
10.803	.095	.390
11.758	.111	.411
12.715	.128	.434
13.651	.147	.453
14.655	.166	.467
15.697	.190	.489
16.572	.223	.504
17.732	.256	.522
18.793	.291	.531
19.870	.327	.547
21.183	.385	.575
22.391	.405	.578
23.625	.448	.594
24.739	.495	.608
25.562	.548	.607
26.367	.610	.450

TABLE A1.2   Run 10 Data

GAS FLOWRATE (L/min)	JET LENGTH (m)	GAS VOID FRACTION
4.481		.217
5.424		.257
6.351	.003	.287
7.194	.006	.318
8.167	.010	.350
9.068	.013	.373
9.970	.018	.393
11.067	.026	.414
12.048	.028	.455
13.036	.033	.465
14.014	.038	.488
15.040	.043	.507
16.134	.051	.529
17.063	.058	.543
18.270	.067	.554
19.376	.083	.575
20.490	.103	.595
21.863	.123	.606
23.117	.140	.623
24.388	.164	.632
25.545	.188	.638
26.428	.207	.631
27.275	.235	.581

TABLE A1.2   Run 11 Data

GAS FLOWRATE (L/min)	JET LENGTH (m)	GAS VOID FRACTION
2.591		.186
3.314	.004	.224
4.129	.007	.265
4.592	.009	.287
5.321	.015	.317
6.054	.022	.344
6.722	.027	.372
7.446	.036	.398
8.156	.045	.421
8.891	.055	.454
9.601	.067	.471
10.454	.075	.493
11.242	.096	.506
12.015	.113	.531
12.760	.133	.538
13.586	.148	.562
14.308	.170	.576
15.107	.193	.586
15.948	.217	.600
16.629	.240	.612
17.810	.263	.623
18.880	.288	.612
19.966	.328	.468

TABLE A1.2   Run 12 Data

GAS FLOWRATE (L/min)	JET LENGTH (m)	GAS VOID FRACTION
1.852	.006	.229
2.541	.017	.287
2.825	.021	.312
3.248	.030	.339
3.696	.041	.374
4.033	.049	.388
4.481	.062	.421
4.796	.073	.437
5.188	.086	.453
5.543	.094	.463
5.903	.105	.480
6.215	.118	.490
6.555	.132	.501
6.902	.146	.514
7.624	.180	.539
8.459	.225	.565
9.001	.249	.581
9.757	.282	.604
10.549	.320	.613
11.307	.365	.557

TABLE A1.2 Run 13 Data

GAS FLOWRATE (L/min)	JET LENGTH (m)	GAS VOID FRACTION
2.635		.138
4.205		.204
4.478	.008	.216
5.422	.010	.257
6.351	.011	.287
7.196	.013	.317
8.168	.015	.342
9.070	.018	.373
9.971	.022	.398
11.071	.027	.412
12.058	.031	.436
13.047	.038	.455
14.014	.045	.475
15.047	.053	.492
16.133	.066	.526
17.047	.077	.544
18.251	.093	.562
19.348	.109	.583
20.458	.135	.599
21.829	.157	.615
23.072	.180	.634
24.336	.210	.648
25.498	.230	.655
26.379	.248	.661
27.250	.267	.655
28.064	.290	.630
28.712	.315	.624
29.268	.320	.216

TABLE A1.2 Run 14 Data

GAS FLOWRATE (L/min)	JET LENGTH (m)	GAS VOID FRACTION
2.590	.010	.191
3.317	.010	.230
4.126	.012	.268
4.586	.014	.291
4.911	.015	.307
5.315	.017	.324
5.677	.021	.337
6.048	.025	.353
6.368	.029	.363
6.714	.033	.378
7.068	.040	.393
7.438	.042	.400
7.816	.046	.413
8.146	.052	.425
8.454	.058	.436
8.881	.064	.445
9.755	.080	.474
10.830	.104	.498
11.786	.122	.519
12.741	.149	.538
13.678	.175	.560
14.679	.203	.580
15.728	.231	.595
16.612	.258	.614
17.785	.285	.632
18.855	.315	.650
19.935	.350	.647
21.293	.385	.600
22.509	.420	.437
23.767	.460	.186

TABLE A1.2 Run 15 Data

GAS FLOWRATE (L/min)	JET LENGTH (m)	GAS VOID FRACTION
1.212	.010	.169
2.545	.018	.295
2.980	.025	.332
3.255	.030	.345
3.555	.039	.366
4.040	.052	.402
4.490	.064	.426
4.805	.072	.445
5.200	.087	.461
5.549	.099	.477
5.913	.112	.493
6.226	.125	.502
6.564	.141	.516
6.909	.162	.527
7.269	.175	.539
7.635	.196	.546
7.957	.210	.559
8.255	.228	.570
8.668	.252	.581
9.019	.264	.602
9.357	.286	.597
9.779	.305	.602
10.186	.324	.601
10.564	.348	.577
10.948	.377	.521

TABLE A1.2 Run 16 Data

GAS FLOWRATE (L/min)	JET LENGTH (m)	GAS VOID FRACTION
4.620		.238
5.350		.269
6.090	.008	.306
6.760	.010	.331
7.490	.012	.352
8.210	.015	.375
8.950	.019	.397
9.660	.023	.421
10.530	.027	.441
11.320	.032	.463
12.110	.036	.476
12.870	.040	.488
13.720	.045	.514
14.460	.050	.522
15.290	.057	.538
16.130	.068	.551
16.820	.075	.565
17.800	.087	.577
18.610	.100	.592
19.470	.115	.614
20.510	.135	.620
21.480	.157	.633
22.430	.175	.620

TABLE A1.2 Run 17 Data

TABLE A1.2 Run 18 Data

GAS FLOWRATE (L/min)	JET LENGTH (m)	GAS VOID FRACTION
2.550		.199
2.840		.215
3.130	.006	.229
3.420	.007	.250
3.720	.008	.264
4.060	.009	.278
4.510	.011	.301
4.830	.013	.315
5.230	.016	.330
5.590	.020	.339
5.950	.024	.358
6.270	.029	.369
6.610	.035	.382
6.960	.040	.400
7.320	.046	.409
7.690	.051	.426
8.020	.056	.438
8.320	.062	.452
8.740	.069	.464
9.090	.075	.475
9.440	.082	.490
9.860	.090	.501
10.270	.099	.514
10.660	.108	.515
11.600	.131	.537
12.540	.154	.562
13.470	.178	.586
14.460	.203	.603
15.490	.235	.620
16.360	.255	.639
17.500	.293	.620
18.570	.315	.495

GAS FLOWRATE (L/min)	JET LENGTH (m)	GAS VOID FRACTION
1.190	.005	.175
1.820	.011	.244
2.500	.023	.308
2.780	.028	.328
3.060	.034	.353
3.340	.042	.373
3.630	.049	.395
3.960	.056	.412
4.410	.068	.433
4.720	.080	.454
5.100	.092	.470
5.450	.105	.488
5.810	.116	.500
6.110	.130	.513
6.440	.144	.524
6.780	.162	.539
7.130	.176	.551
7.490	.195	.552
7.810	.211	.564
8.100	.231	.576
8.510	.252	.584
8.850	.266	.597
9.180	.296	.603
9.590	.316	.606
9.990	.346	
10.370	.362	

TABLE A1.2 Run 19 Data

GAS FLOWRATE (L/min)	JET LENGTH (m)	GAS VOID FRACTION
1.184		.305
1.691	.004	.364
2.221	.010	.412
2.767	.018	.454
3.335	.030	.498
3.955	.043	.538
4.395	.058	.558
4.704	.080	.576
5.088	.097	.591
5.433	.114	.608
5.787	.130	.620
6.094	.145	.636
6.424	.160	.648
6.764	.178	.660
7.116	.188	.671
7.478	.200	.685
7.794	.220	.695
8.089	.228	.704
8.500	.245	.712
8.845	.253	.726
9.185	.265	.732
9.604	.273	.732
10.007	.285	.732
10.389	.298	.720
10.773	.310	.695
11.156	.318	.620

TABLE A1.2 Run 20 Data

GAS FLOWRATE (L/min)	JET LENGTH (m)	GAS VOID FRACTION
.369		.252
.598	.002	.306
.881	.007	.352
1.178	.013	.382
1.432	.021	.413
1.682	.029	.439
1.944	.040	.464
2.206	.054	.491
2.468	.071	.516
2.745	.088	.545
3.021	.105	.570
3.306	.121	.594
3.590	.144	.607
3.918	.161	.620
4.355	.189	.650
4.664	.212	.667
5.049	.235	.676
5.392	.257	.695
5.746	.272	.704
6.054	.285	.708
6.379	.318	.704
6.718	.340	.645
7.069	.368	

TABLE A1.2 Run 21 Data

GAS FLOWRATE (L/min)	JET LENGTH (m)	GAS VOID FRACTION
.066	.010	.325
.155	.015	.343
.252	.019	.371
.354	.025	.388
.447	.034	.404
.574	.050	.424
.716	.069	.448
.843	.086	.470
.977	.105	.490
1.126	.123	.517
1.239	.153	.539
1.366	.167	.557
1.484	.180	.575
1.603	.200	.589
1.718	.218	.611
1.853	.238	.626
1.974	.258	.639
2.103	.265	.645
2.234	.275	.655
2.355	.293	.670
2.476	.305	.689
2.621	.315	.673
2.758	.338	.655
2.886	.348	.620
3.015	.368	.592
3.160	.385	.573
3.288	.420	

TABLE A1.2 Run 22 Data

GAS FLOWRATE (L/min)	JET LENGTH (m)	GAS VOID FRACTION
1.183	.002	.319
1.690	.003	.370
2.219	.011	.414
2.764	.024	.458
3.332	.039	.499
3.950	.063	.538
4.389	.080	.562
4.699	.095	.579
5.083	.113	.596
5.431	.124	.606
5.783	.140	.626
6.091	.158	.640
6.418	.173	.651
6.758	.187	.660
7.111	.200	.676
7.473	.214	.682
7.790	.230	.701
8.084	.245	.712
8.495	.258	.721
8.841	.268	.728
9.179	.283	.732
9.597	.294	.720
10.001	.315	.682
10.383	.328	.601

TABLE A1.2   Run 23 Data

GAS FLOWRATE (L/min)	JET LENGTH (m)	GAS VOID FRACTION
.363		.275
.590	.003	.319
.869	.012	.360
1.161	.017	.390
1.412	.027	.415
1.658	.037	.442
1.915	.050	.476
2.174	.064	.496
2.433	.083	.523
2.705	.096	.549
2.978	.115	.570
3.258	.133	.595
3.538	.151	.613
3.862	.172	.632
4.291	.211	.642
4.594	.230	.673
4.973	.254	.685
5.314	.270	.694
5.662	.295	.701
5.965	.313	.698
6.287	.338	.638
6.624	.358	.563

TABLE A1.2   Run 24 Data

GAS FLOWRATE (L/min)	JET LENGTH (m)	GAS VOID FRACTION
.067	.013	.332
.158	.017	.350
.257	.024	.375
.361	.035	.393
.456	.047	.412
.585	.065	.426
.731	.081	.451
.861	.102	.483
.996	.127	.513
1.148	.145	.542
1.263	.165	.558
1.393	.194	.589
1.513	.221	.601
1.635	.232	.617
1.749	.250	.627
1.888	.263	.649
2.015	.272	.658
2.146	.291	.671
2.278	.306	.680
2.401	.330	.658
2.523	.348	.614
2.671	.360	.586
2.814	.371	.570
2.936	.436	

TABLE A1.2 Run 25 Data

GAS FLOWRATE (L/min)	JET LENGTH (m)	GAS VOID FRACTION
1.169		.327
1.669	.006	.387
2.193	.017	.429
2.731	.030	.476
3.295	.043	.513
3.906	.068	.557
4.339	.089	.577
4.641	.108	.600
5.023	.127	.620
5.363	.144	.637
5.712	.156	.651
6.016	.174	.665
6.340	.192	.676
6.676	.206	.689
7.024	.226	.704
7.380	.243	.708
7.697	.263	.708
7.986	.278	.645
8.392	.318	.482

TABLE A1.2 Run 26 Data

GAS FLOWRATE (L/min)	JET LENGTH (m)	GAS VOID FRACTION
.361		.276
.585	.003	.317
.862	.010	.370
1.152	.023	.402
1.400	.030	.430
1.644	.041	.451
1.899	.057	.485
2.155	.075	.514
2.412	.091	.539
2.682	.108	.566
2.952	.132	.595
3.231	.148	.613
3.510	.167	.631
3.830	.192	.649
4.256	.227	.669
4.558	.258	.685
4.932	.288	.698
5.265	.324	.657
5.607	.355	.544

25

TABLE A1.2 Run 27 Data

GAS FLOWRATE (L/min)	JET LENGTH (m)	GAS VOID FRACTION
.066	.012	.326
.155	.016	.341
.252	.022	.363
.353	.034	.401
.446	.053	.417
.572	.071	.432
.715	.094	.456
.842	.114	.478
.974	.136	.513
1.122	.167	.531
1.234	.189	.553
1.361	.214	.583
1.479	.238	.605
1.597	.258	.627
1.711	.275	.642
1.845	.298	.664
1.966	.313	.670
2.093	.337	.642
2.221	.373	.570

TABLE A1.2 Run 28 Data

GAS FLOWRATE (L/min)	JET LENGTH (m)	GAS VOID FRACTION
9.640		.166
11.780	.006	.199
13.870	.007	.233
16.000	.009	.261
18.140	.014	.291
20.610	.020	.314
23.270	.027	.349
25.990	.035	.380
28.160	.042	.407
29.980	.052	.438
31.260	.059	.449
34.090	.070	.473
35.910	.079	.493
37.970	.090	.531
39.860	.110	.563
41.770	.130	.590
43.950	.149	.607
45.980	.168	.646
47.910	.194	.672
49.900	.220	.701
51.900	.255	.707
53.940	.283	.713
55.830	.323	.707

TABLE A1.2   Run 29 Data

GAS FLOWRATE (L/min)	JET LENGTH (m)	GAS VOID FRACTION
9.210	.012	.226
11.240	.020	.259
13.230	.031	.298
15.260	.045	.331
17.290	.057	.362
19.630	.077	.396
22.160	.102	.433
24.700	.131	.463
26.770	.164	.495
28.460	.199	.513
29.660	.216	.537
31.370	.248	.555
32.280	.255	.566
33.200	.278	.578
34.000	.297	.593
34.970	.316	.604
35.880	.337	.613
36.750	.358	.622
37.710	.373	.631
38.650	.395	.637
39.530	.418	.637

TABLE A1.2   Run 30 Data

GAS FLOWRATE (L/min)	JET LENGTH (m)	GAS VOID FRACTION
3.590	.007	.140
4.410	.011	.189
5.340	.018	.205
6.250	.028	.236
7.080	.039	.268
8.040	.049	.292
8.920	.063	.313
9.800	.075	.338
10.880	.092	.365
11.830	.110	.387
12.790	.133	.411
13.730	.152	.432
14.730	.170	.447
15.790	.194	.465
16.660	.224	.491
17.840	.237	.500
18.900	.267	.526
19.980	.293	.538
21.280	.340	.573
22.510	.377	.585
23.730	.435	.603
24.840	.498	
25.660	.545	

TABLE A1.2 Run 31 Data

GAS FLOWRATE (L/min)	JET LENGTH (m)	GAS VOID FRACTION
4.603		.212
5.337		.237
6.073	.003	.262
6.741	.006	.289
7.468	.007	.307
8.176	.011	.329
8.914	.014	.354
9.628	.017	.377
10.485	.019	.395
11.277	.025	.414
12.055	.029	.430
12.805	.033	.449
13.631	.040	.471
14.358	.044	.489
15.161	.050	.510
15.999	.057	.527
16.675	.063	.548
17.609	.077	.566

TABLE A1.2 Run 32 Data

GAS FLOWRATE (L/min)	JET LENGTH (m)	GAS VOID FRACTION
2.558		.177
2.847		.197
3.137	.004	.211
3.436	.005	.221
3.732	.007	.234
4.073	.008	.256
4.523	.010	.280
4.848	.011	.304
5.604	.018	.328
6.281	.023	.365
6.971	.031	.388
7.706	.038	.419
8.332	.047	.434
9.105	.058	.462
9.873	.067	.478
10.665	.086	.505
11.437	.099	.535
12.208	.118	.554
12.977	.137	.574
13.705	.159	.578
14.434	.182	.598
15.213	.212	.616
16.043	.245	.640
16.848	.273	.640
17.615	.305	.652

TABLE A1.2   Run 33 Data

GAS FLOWRATE (L/min)	JET LENGTH (m)	GAS VOID FRACTION
1.193	.003	.130
1.824	.010	.204
2.499	.018	.272
2.778	.023	.305
3.190	.029	.333
3.347	.032	.344
3.633	.039	.368
3.962	.047	.392
4.403	.056	.416
4.709	.069	.439
5.093	.081	.459
5.444	.088	.475
5.799	.100	.482
6.104	.113	.498
6.432	.128	.511
6.768	.148	.524
7.119	.165	.533
7.475	.189	.545
7.786	.212	.557
8.075	.240	.562
8.483	.257	.571
8.816	.291	.586
9.142	.318	.593
9.549	.348	.606
9.933	.385	.619
10.296	.440	.618
10.684	.470	.618

TABLE A1.2   Run 34 Data

GAS FLOWRATE (L/min)	JET LENGTH (m)	GAS VOID FRACTION
1.168	.003	.270
1.666	.006	.336
1.926	.010	.372
2.185	.013	.399
2.720	.023	.442
2.993	.029	.465
3.277	.033	.487
3.558	.040	.517
3.879	.050	.539
4.304	.071	.573
4.439	.083	.588
4.772	.107	.609
5.114	.125	.629
5.307	.137	.641
5.649	.163	.656
5.806	.193	.664
5.942	.210	.676

TABLE A1.2   Run 35 Data

GAS FLOWRATE (L/min)	JET LENGTH (m)	GAS VOID FRACTION
.364	.002	.184
.589	.005	.250
.866	.010	.307
1.158	.016	.349
1.406	.022	.384
1.650	.030	.419
1.906	.041	.455
2.159	.060	.485
2.415	.074	.519
2.684	.091	.545
2.951	.118	.581
3.227	.142	.602
3.501	.174	.623
3.817	.203	.644
4.059	.248	.653
4.236	.275	.670
4.374	.305	.679

TABLE A1.2   Run 36 Data

GAS FLOWRATE (L/min)	JET LENGTH (m)	GAS VOID FRACTION
.067	.009	.183
.157	.013	.216
.255	.019	.271
.358	.023	.306
.452	.032	.336
.580	.047	.365
.722	.067	.406
.849	.088	.439
.983	.116	.459
1.132	.140	.495
1.243	.179	.527
1.368	.203	.557
1.486	.227	.583

TABLE A1.2   Run 37 Data

GAS FLOWRATE (L/min)	JET LENGTH (m)	GAS VOID FRACTION
9.710		.171
11.830		.199
13.930		.238
16.100		.263
18.250	.010	.296
20.650	.017	.339
23.350	.022	.373
26.100	.027	.385
28.280	.033	.413
30.080	.040	.451
31.320	.047	.468
34.150	.055	.482
35.980	.065	.535
38.020	.076	.558
39.950	.086	.580
41.960	.100	.603
44.070	.117	.636
46.090	.140	.647
48.040	.160	.664
49.860	.210	.659

TABLE A1.2   Run 38 Data

GAS FLOWRATE (L/min)	JET LENGTH (m)	GAS VOID FRACTION
9.210	.008	.232
11.250	.013	.271
13.250	.021	.314
15.270	.029	.347
17.290	.039	.385
19.630	.054	.421
22.160	.073	.466
24.710	.097	.507
26.710	.122	.580
28.360	.150	.613
29.550	.170	.652
32.200	.205	

TABLE A1.2 Run 35 Data

GAS FLOWRATE (L/min)	JET LENGTH (m)	GAS VOID FRACTION
.364	.002	.184
.589	.005	.250
.866	.010	.307
1.158	.016	.349
1.406	.022	.384
1.650	.030	.419
1.906	.041	.455
2.159	.060	.485
2.415	.074	.519
2.684	.091	.545
2.951	.118	.581
3.227	.142	.602
3.501	.174	.623
3.817	.203	.644
4.059	.248	.653
4.236	.275	.670
4.374	.305	.679

TABLE A1.2 Run 36 Data

GAS FLOWRATE (L/min)	JET LENGTH (m)	GAS VOID FRACTION
.067	.009	.183
.157	.013	.216
.255	.019	.271
.358	.023	.306
.452	.032	.336
.580	.047	.365
.722	.067	.406
.849	.088	.439
.983	.116	.459
1.132	.140	.495
1.243	.179	.527
1.368	.203	.557
1.486	.227	.583

TABLE A1.2 Run 37 Data

GAS FLOWRATE (L/min)	JET LENGTH (m)	GAS VOID FRACTION
9.710		.171
11.830		.199
13.930		.238
16.100		.263
18.250	.010	.296
20.650	.017	.339
23.350	.022	.373
26.100	.027	.385
28.280	.033	.413
30.080	.040	.451
31.320	.047	.468
34.150	.055	.482
35.980	.065	.535
38.020	.076	.558
39.950	.086	.580
41.960	.100	.603
44.070	.117	.636
46.090	.140	.647
48.040	.160	.664
49.860	.210	.659

TABLE A1.2 Run 38 Data

GAS FLOWRATE (L/min)	JET LENGTH (m)	GAS VOID FRACTION
9.210	.008	.232
11.250	.013	.271
13.250	.021	.314
15.270	.029	.347
17.290	.039	.385
19.630	.054	.421
22.160	.073	.466
24.710	.097	.507
26.710	.122	.580
28.360	.150	.613
29.550	.170	.652
32.200	.205	

TABLE A1.2 Run 39 Data

GAS FLOWRATE (L/min)	JET LENGTH (m)	GAS VOID FRACTION
3.600	.004	.127
4.430	.008	.169
5.360	.014	.193
6.270	.021	.230
7.110	.027	.259
8.070	.036	.277
8.950	.045	.305
9.830	.058	.333
10.910	.070	.359
11.870	.082	.383
12.830	.102	.402
13.770	.118	.423
14.770	.138	.449
15.820	.155	.465
16.700	.180	.485
17.870	.208	.507
18.920	.243	.524
20.000	.268	.546
21.290	.310	.591
22.500	.365	.600
23.710	.430	.600
24.770	.520	.600

TABLE A1.2 Run 40 Data

GAS FLOWRATE (L/min)	JET LENGTH (m)	GAS VOID FRACTION
4.703		.176
5.034		.194
5.449	.003	.202
5.821	.005	.221
6.201	.007	.230
6.532	.008	.244
6.887	.008	.255
7.229	.009	.268
7.630	.009	.272
8.018	.010	.280
8.356	.010	.292
8.667	.011	.297
9.089	.012	.315
9.473	.013	.319
9.835	.015	.330
10.276	.015	.341
10.706	.017	.353
11.110	.018	.362
11.516	.021	.370
11.916	.023	.382
12.295	.025	.393
12.696	.028	.426
13.053	.030	.414
13.506	.033	.414
13.870	.035	.442
14.262	.037	.447
14.591	.040	.459
15.034	.044	.473
15.481	.047	.459

TABLE A1.2   Run 41 Data

GAS FLOWRATE (L/min)	JET LENGTH (m)	GAS VOID FRACTION
2.646		.126
4.214	.003	.202
4.683	.006	.225
5.012	.008	.239
5.424	.011	.254
5.793	.013	.269
6.170	.016	.285
6.495	.018	.302
7.052	.023	.314
7.183	.024	.327
7.577	.028	.342
7.964	.031	.351
8.297	.034	.360
8.605	.039	.380
9.038	.043	.386
9.398	.048	.403
10.193	.058	.426
11.015	.073	.450
11.804	.088	.470
12.600	.104	.487
13.376	.125	.521
14.119	.148	.528
14.861	.173	.549

TABLE A1.2   Run 42 Data

GAS FLOWRATE (L/min)	JET LENGTH (m)	GAS VOID FRACTION
2.574	.010	.205
3.295	.024	.259
4.083	.033	.310
4.533	.044	.342
4.675	.048	.348
4.849	.053	.364
5.032	.058	.371
5.244	.063	.383
5.394	.066	.386
5.596	.073	.393
5.744	.077	.394
5.959	.084	.411
6.130	.087	.414
6.274	.094	.422
6.453	.102	.430
6.609	.108	.438
6.800	.112	.447
6.934	.116	.449
7.127	.125	.458
7.316	.133	.460
7.530	.139	.467
7.680	.149	.482
7.859	.156	.482
8.001	.164	.503
8.133	.173	.493
8.299	.179	.496
8.522	.195	.501
8.710	.205	.505
8.904	.217	.523
9.054	.232	.527
9.204	.246	.527
9.392	.253	.527
9.548	.270	.535
9.800	.285	.538
9.996	.305	.515
10.195	.326	.510

TABLE A1.2 Run 43 Data

GAS FLOWRATE (L/min)	JET LENGTH (m)	GAS VOID FRACTION
1.199	.003	.235
1.454	.005	.276
1.708	.007	.310
1.975	.008	.344
2.237	.011	.371
2.499	.014	.411
2.776	.018	.447
3.048	.021	.486
3.335	.025	.517
3.621	.033	.543
3.945	.051	.568
4.388	.073	.579
5.527	.098	.590
4.869	.133	.600
5.215	.218	.607

TABLE A1.2 Run 44 Data

GAS FLOWRATE (L/min)	JET LENGTH (m)	GAS VOID FRACTION
.374	.002	.140
.606	.004	.204
.890	.006	.266
1.187	.011	.316
1.440	.016	.364
1.688	.021	.410
1.946	.028	.452
2.202	.042	.503
2.461	.058	.539
2.733	.074	.571
3.007	.103	.595
3.285	.145	.612

TABLE A1.2 Run 45 Data

GAS FLOWRATE (L/min)	JET LENGTH (m)	GAS VOID FRACTION
.069	.008	.083
.162	.012	.142
.262	.016	.190
.368	.020	.218
.464	.024	.252
.593	.031	.305
.739	.043	.344
.866	.063	.408
1.002	.077	.448
1.153	.100	.484
1.265	.135	.521

TABLE A1.2 Run 46 Data

GAS FLOWRATE (L/min)	JET LENGTH (m)	GAS VOID FRACTION
9.130		.191
11.168		.219
13.185	.005	.247
15.234	.008	.279
17.282	.010	.309
19.645	.012	.339
22.217	.015	.368
24.830	.019	.398
26.956	.021	.423
28.696	.025	.445
29.944	.027	.456
32.659	.030	.478
34.420	.034	.493
36.438	.036	.514
38.342	.039	.531
40.237	.043	.542
42.307	.047	.566
44.157	.050	.584
46.067	.053	.592
48.054	.058	.616
50.108	.063	.623
52.132	.070	
54.048	.078	

TABLE A1.2 Run 47 Data

GAS FLOWRATE (L/min)	JET LENGTH (m)	GAS VOID FRACTION
8.936	.007	.242
10.933	.008	.279
12.891	.011	.314
14.887	.016	.348
16.889	.022	.378
19.203	.029	.415
21.729	.037	.443
24.279	.046	.477
26.347	.053	.502
28.037	.062	.534
29.231	.069	.537
31.733	.081	.564
33.413	.094	.584
35.343	.118	.596
37.180	.142	.606
39.085	.170	.590

TABLE A1.2 Run 48 Data

GAS FLOWRATE (L/min)	JET LENGTH (m)	GAS VOID FRACTION
3.495	.007	.182
5.219	.011	.238
6.942	.022	.291
8.766	.034	.341
10.722	.049	.379
12.633	.070	.423
14.582	.097	.461
16.535	.127	.491
18.779	.174	.528
21.213	.232	.558
23.688	.286	.584
25.707	.327	.607
27.369	.378	.630
28.556	.405	.646
31.127	.455	.662
32.797	.504	.670
34.679	.553	.622

TABLE A1.2 Run 49 Data

GAS FLOWRATE (L/min)	JET LENGTH (m)	GAS VOID FRACTION
3.541		.172
4.351		.208
5.274	.003	.240
6.181	.005	.269
7.014	.007	.296
7.969	.009	.322
8.858	.010	.351
10.828	.013	.396
12.765	.018	.439
14.737	.022	.481
16.718	.028	.517
19.015	.035	.559
21.524	.043	.590
24.068	.053	.630
26.129	.067	.662

TABLE A1.2 Run 50 Data

GAS FLOWRATE (L/min)	JET LENGTH (m)	GAS VOID FRACTION
2.523	.002	.175
4.027	.005	.251
5.202	.007	.302
6.097	.009	.334
6.915	.013	.362
7.856	.018	.392
8.731	.023	.423
9.603	.028	.448
10.676	.033	.472
11.632	.038	.493
12.592	.044	.512
13.533	.054	.533
14.538	.065	.556
15.597	.078	.572
16.485	.095	.592
17.655	.106	.610
18.729	.138	.628
19.817	.160	.646
21.170	.184	.660
22.388	.205	.670

TABLE A1.2 Run 51 Data

GAS FLOWRATE (L/min)	JET LENGTH (m)	GAS VOID FRACTION
2.490	.007	.253
3.970	.025	.339
4.417	.031	.367
5.126	.045	.403
5.829	.058	.445
6.473	.078	.478
7.174	.093	.498
7.859	.116	.518
8.566	.150	.542
9.253	.171	.568
10.078	.201	.588
10.845	.233	.605
11.597	.257	.622
12.322	.284	.639
13.138	.303	.653
13.842	.333	.662
14.683	.355	.670
15.452	.387	.686
16.127	.410	.698
17.040	.440	.710
17.873	.478	.721

TABLE A1.2 Run 55 Data

GAS FLOWRATE (L/min)	JET LENGTH (m)	GAS VOID FRACTION
1.197	.008	.130
1.711	.016	.184
2.248	.022	.226
2.800	.035	.270
3.377	.044	.301
4.005	.060	.335
4.451	.071	.362
4.765	.084	.379
5.156	.093	.382
5.509	.101	.395
5.866	.114	.408
6.177	.127	.419
6.510	.141	.429
6.853	.156	.444
7.208	.166	.457
7.572	.186	.476
7.890	.199	.490
8.186	.214	.487
8.597	.235	.491
8.944	.253	.503
9.278	.275	.512
9.699	.288	.518
10.097	.312	.531
10.473	.335	.536

TABLE A1.2 Run 56 Data

GAS FLOWRATE (L/min)	JET LENGTH (m)	GAS VOID FRACTION
5.269		.406
6.988		.475
8.805		.546
9.677	.011	.580
10.749	.014	.594
11.704	.016	.614
12.663	.018	.634
13.608	.022	.651
14.615	.025	.668
15.681	.029	.694
18.857	.037	.725
19.976	.040	.725
21.361	.043	.594

TABLE A1.2 Run 64 Data

GAS FLOWRATE (L/min)	JET LENGTH (m)	GAS VOID FRACTION
1.695		.112
3.312		.235
3.938		.266
5.149		.313
6.031		.345
6.838	.020	.361
7.763	.028	.388
8.427	.042	.404
9.478	.060	.426
10.532	.060	.450
11.462	.070	.474
12.390	.090	.495
14.299	.060	.551
16.216	.080	.577

TABLE A1.2 Run 51 Data

GAS FLOWRATE (L/min)	JET LENGTH (m)	GAS VOID FRACTION
2.490	.007	.253
3.970	.025	.339
4.417	.031	.367
5.126	.045	.403
5.829	.058	.445
6.473	.078	.478
7.174	.093	.498
7.859	.116	.518
8.566	.150	.542
9.253	.171	.568
10.078	.201	.588
10.845	.233	.605
11.597	.257	.622
12.322	.284	.639
13.138	.303	.653
13.842	.333	.662
14.683	.355	.670
15.452	.387	.686
16.127	.410	.698
17.040	.440	.710
17.873	.478	.721

TABLE A1.2 Run 55 Data

GAS FLOWRATE (L/min)	JET LENGTH (m)	GAS VOID FRACTION
1.197	.008	.130
1.711	.016	.184
2.248	.022	.226
2.800	.035	.270
3.377	.044	.301
4.005	.060	.335
4.451	.071	.362
4.765	.084	.379
5.156	.093	.382
5.509	.101	.395
5.866	.114	.408
6.177	.127	.419
6.510	.141	.429
6.853	.156	.444
7.208	.166	.457
7.572	.186	.476
7.890	.199	.490
8.186	.214	.487
8.597	.235	.491
8.944	.253	.503
9.278	.275	.512
9.699	.288	.518
10.097	.312	.531
10.473	.335	.536

TABLE A1.2 Run 56 Data

GAS FLOWRATE (L/min)	JET LENGTH (m)	GAS VOID FRACTION
5.269		.406
6.988		.475
8.805		.546
9.677	.011	.580
10.749	.014	.594
11.704	.016	.614
12.663	.018	.634
13.608	.022	.651
14.615	.025	.668
15.681	.029	.694
18.857	.037	.725
19.976	.040	.725
21.361	.043	.594

TABLE A1.2 Run 64 Data

GAS FLOWRATE (L/min)	JET LENGTH (m)	GAS VOID FRACTION
1.695		.112
3.312		.235
3.938		.266
5.149		.313
6.031		.345
6.838	.020	.361
7.763	.028	.388
8.427	.042	.404
9.478	.060	.426
10.532	.060	.450
11.462	.070	.474
12.390	.090	.495
14.299	.060	.551
16.216	.080	.577

TABLE A1.2   Run 65 Data

GAS FLOWRATE (L/min)	JET LENGTH (m)
4.258	.008
6.022	.023
7.753	.050
9.462	.080
11.437	.119
13.279	.163
15.285	.211
17.289	.274
19.400	.358

TABLE A1.2   Run 66 Data

GAS FLOWRATE (L/min)	JET LENGTH (m)
4.250	.011
6.021	.028
7.745	.049
9.448	.078
11.445	.116
13.299	.160
15.301	.218
17.300	.278
19.418	.353

TABLE A1.2   Run 67 Data

GAS FLOWRATE (L/min)	JET LENGTH (m)
4.203	.008
5.968	.019
7.680	.043
9.379	.072
11.331	.111
13.162	.157
15.138	.215
17.116	.288
19.204	.367

TABLE A1.2   Run 68 Data

GAS FLOWRATE (L/min)	JET LENGTH (m)
4.206	.008
5.968	.019
7.672	.045
9.362	.081
11.314	.127
13.128	.185
15.103	.248
17.073	.325
19.167	.390

TABLE A1.2   Run 69 Data

GAS FLOWRATE (L/min)	JET LENGTH (m)
4.274	.006
6.061	.012
7.792	.041
9.515	.078
11.500	.138
13.339	.215
15.330	.295
17.330	.378
19.448	.465

TABLE A1.2   Run 70 Data

GAS FLOWRATE (L/min)	JET LENGTH (m)
4.168	.008
5.908	.017
7.597	.037
9.269	.090
11.182	.183
12.967	.278
14.916	.355
16.872	.435
18.938	.520

TABLE A1.2   Run 71 Data

GAS FLOWRATE (L/min)	JET LENGTH (m)	GAS VOID FRACTION
1.730		.047
3.539		.102
5.291	.003	.147
7.039	.005	.193
8.881	.009	.238
10.856	.012	.280
12.791	.016	.328
14.916	.019	.369
16.740	.024	.398
19.007	.032	.429
21.519	.038	.454
24.056	.050	.474
26.083	.065	.500
27.692	.110	.529
28.804	.220	.492
29.924	.280	.429

TABLE A1.2   Run 72 Data

GAS FLOWRATE (L/min)	JET LENGTH (m)	GAS VOID FRACTION
1.701		.066
3.474	.003	.130
5.189	.005	.183
6.897	.011	.230
8.706	.019	.276
10.638	.031	.316
12.533	.047	.356
14.461	.059	.388
16.393	.075	.424
18.634	.093	.457
21.059	.119	.492
23.526	.153	.519
25.513	.183	.544
27.148	.220	.565
28.320	.235	.576
29.396	.285	.595
31.164	.328	.606
32.822	.380	.607
34.632	.440	.582

TABLE A1.2 Run 73 Data

GAS FLOWRATE (L/min)	JET LENGTH (m)	GAS VOID FRACTION
.833		.058
1.688	.005	.109
2.577	.011	.160
3.432	.018	.213
4.213	.026	.244
5.110	.043	.280
5.976	.063	.318
6.769	.076	.351
7.684	.094	.380
8.529	.115	.408
9.371	.135	.432
10.411	.153	.452
11.328	.175	.479
12.250	.208	.501
13.153	.240	.514
14.115	.260	.528
15.143	.295	.544
15.991	.330	.598
17.119	.363	.636
18.149	.407	.579
19.192	.470	.590
20.495	.517	.589

TABLE A1.2 Run 74 Data

GAS FLOWRATE (L/min)	JET LENGTH (m)	GAS VOID FRACTION
.794		.078
2.202	.002	.162
4.249	.006	.268
5.159	.009	.313
6.041	.017	.344
6.841	.025	.387
7.761	.032	.419
8.623	.037	.450
9.479	.044	.482
10.920	.052	.513
12.412	.065	.544
14.345	.085	.594
16.247	.145	.588
18.374	.320	.607

TABLE A1.2 Run 75 Data

GAS FLOWRATE (L/min)	JET LENGTH (m)	GAS VOID FRACTION
.471		.077
1.660	.005	.174
2.270	.012	.241
3.272	.022	.297
3.880	.034	.353
5.067	.057	.413
5.927	.077	.461
6.710	.098	.493
7.616	.135	.523
8.264	.165	.558
9.283	.205	.576
10.285	.258	.598
11.208	.305	

TABLE A1.2 Run 76 Data

GAS FLOWRATE (L/min)	JET LENGTH (m)	GAS VOID FRACTION
.581	.017	.185
1.116	.026	.243
1.386	.055	.320
1.738	.094	.332
1.919	.097	.329
2.194	.152	.384
2.486	.175	.430
2.723	.203	.429
3.339	.270	.496

TABLE A1.2   Run 77 Data

GAS FLOWRATE (L/min)	JET LENGTH (m)	GAS VOID FRACTION
.599	.017	.391
1.084	.029	.466
1.622	.038	.504
2.171	.088	.542
2.755	.178	.579
3.294	.350	.598

TABLE A1.2   Run 78 Data

GAS FLOWRATE (L/min)	JET LENGTH (m)	GAS VOID FRACTION
.421	.037	.443
.742	.107	.481
1.015	.142	.524
1.431	.260	.555
1.762	.365	.589

TABLE A1.2   Run 80 Data

GAS FLOWRATE (L/min)	JET LENGTH (m)	GAS VOID FRACTION
1.726	.002	.042
3.533	.004	.086
5.284	.007	.130
7.016	.010	.172
8.850	.012	.229
10.814	.013	.269
12.731	.016	.317
14.683	.024	.356
16.643	.034	.360
18.900	.040	.420
21.371	.048	.470
23.877	.062	.466
25.857	.100	.487
27.317	.270	.454

TABLE A1.2   Run 81 Data

GAS FLOWRATE (L/min)	JET LENGTH (m)	GAS VOID FRACTION
1.700		.065
3.473	.002	.127
5.181	.006	.181
6.885	.013	.232
8.698	.023	.268
10.617	.036	.319
12.507	.047	.361
14.150	.065	.405
16.321	.084	.432
18.497	.117	.470
20.841	.185	.492
23.249	.275	.467
25.206	.345	.426
26.849	.380	.401
28.036	.405	.388

TABLE A1.2 Run 82 Data

GAS FLOWRATE (L/min)	JET LENGTH (m)	GAS VOID FRACTION
.832	.002	.058
1.685	.008	.106
2.569	.015	.160
3.417	.028	.216
4.197	.043	.257
5.072	.064	.303
5.930	.091	.339
6.693	.115	.381
7.567	.155	.404
8.410	.205	.432
9.232	.275	.447

TABLE A1.2 Run 83 Data

GAS FLOWRATE (L/min)	JET LENGTH (m)	GAS VOID FRACTION
.795		.070
2.200	.006	.163
4.242	.008	.266
5.149	.017	.313
6.026	.023	.354
6.823	.028	.383
7.746	.037	.426
8.601	.045	.442
9.456	.052	.463
10.891	.065	.498
12.377	.084	.529
14.246	.170	.566

TABLE A1.2 Run 84 Data

GAS FLOWRATE (L/min)	JET LENGTH (m)	GAS VOID FRACTION
.635		.102
1.670	.009	.200
2.285	.018	.244
3.296	.028	.299
3.912	.040	.360
5.102	.058	.410
5.963	.088	.446
6.752	.120	.485
7.666	.145	.522
8.298	.215	.547
9.319	.270	.554

TABLE A1.2 Run 85 Data

GAS FLOWRATE (L/min)	JET LENGTH (m)	GAS VOID FRACTION
.587	.022	.072
1.129	.042	.278
1.404	.058	.285
1.937	.120	.347
2.220	.165	.372
2.751	.225	.438

TABLE A1.2   Run 86 Data

GAS FLOWRATE (L/min)	JET LENGTH (m)	GAS VOID FRACTION
.603	.018	.393
1.091	.030	.459
1.632	.040	.486
2.190	.062	.520
2.786	.085	.557
3.349	.138	.584
3.874	.205	.607

TABLE A1.2   Run 87 Data

GAS FLOWRATE (L/min)	JET LENGTH (m)	GAS VOID FRACTION
.425	.035	.439
.747	.088	.506
1.025	.122	.521
1.445	.133	.557
1.786	.182	.585

TABLE A1.2   Run 91 Data

GAS FLOWRATE (L/min)	JET LENGTH (m)	GAS VOID FRACTION
5.14		.143
8.646	.007	.216
12.446	.013	.288
16.328	.025	.349
20.988	.040	.419
25.461	.057	.479
28.315	.077	.523

TABLE A1.2   Run 92 Data

GAS FLOWRATE (L/min)	JET LENGTH (m)	GAS VOID FRACTION
1.652		.078
3.373	.003	.145
5.039	.010	.197
6.700	.017	.244
8.459	.024	.292
10.342	.042	.328
12.184	.055	.369
14.062	.067	.408
15.942	.090	.443
18.122	.130	.476
20.478	.160	.513
22.865	.210	.541

TABLE A1.2   Run 93 Data

GAS FLOWRATE (L/min)	JET LENGTH (m)	GAS VOID FRACTION
.804	.002	.078
1.626	.013	.144
2.480	.025	.196
3.303	.043	.247
4.059	.065	.286
4.905	.100	.332
5.734	.140	.369
6.493	.175	.397
7.369	.210	.431
8.178	.245	.462
8.986	.273	.477

TABLE A1.2   Run 94 Data

GAS FLOWRATE (L/min)	JET LENGTH (m)	GAS VOID FRACTION
1.653	.003	.169
2.974	.010	.256
3.876	.017	.288
5.067	.024	.337
6.727	.038	.392
8.479	.060	.446
10.360	.087	.502
12.185	.134	.543
14.015	.190	.581
15.895	.300	.531

TABLE A1.2   Run 95 Data

GAS FLOWRATE (L/min)	JET LENGTH (m)	GAS VOID FRACTION
.463	.003	.117
1.631	.018	.247
2.828	.037	.310
3.820	.052	.372
.987	.085	.434
5.826	.114	.466
6.595	.172	.488
7.472	.325	.526
8.099	.438	.548
9.103	.590	.591

TABLE A1.2   Run 96 Data

GAS FLOWRATE (L/min)	JET LENGTH (m)	GAS VOID FRACTION
.453	.057	.249
1.270	.153	.352
2.150	.320	.435
3.085	.520	.573

TABLE A1.2 Run 97 Data

GAS FLOWRATE (L/min)	JET LENGTH (m)	GAS VOID FRACTION
.766		.452
1.219	.020	.573
2.077	.238	.601
2.865	.393	.479

TABLE A1.2 Run 100 Data

GAS FLOWRATE (L/min)	JET LENGTH (m)	GAS VOID FRACTION
1.633	.007	.177
3.233	.017	.259
3.845	.020	.294
5.027	.028	.337
6.678	.040	.385
8.240	.050	.426
10.300	.060	.485
12.128	.075	.523
13.982	.115	.560
15.825	.225	.582

TABLE A1.2 Run 101 Data

GAS FLOWRATE (L/min)	JET LENGTH (m)	GAS VOID FRACTION
.444	.005	.096
1.571	.022	.254
2.746	.035	.320
3.719	.055	.372
4.862	.070	.423
5.696	.091	.444
6.287	.129	.485
7.161	.189	.515
7.793	.270	.541
8.793	.353	.567

Appendix 2

PROPERTIES OF THE FREE JET

In this appendix the results of preliminary experiments examining the influence of the throat length of the nozzle on the gas entrainment rate for the plunging liquid jet are presented. Also reported in this appendix are the measurements for the expansion in the jet diameter as a function of the free jet length.

.

A2.1 INTRODUCTION

The entrainment characteristics of a plunging liquid jet are a function
of the jet velocity and diameter at the point of impact with the
receiving liquid. As illustrated in Figure A2.1 the jet diameter after
it leaves the nozzle is determined by the relaxation of the velocity
profile inside the jet and also by the interaction of the free surface of
the jet with the surrounding atmosphere (McMarthy and Molloy, 1974).
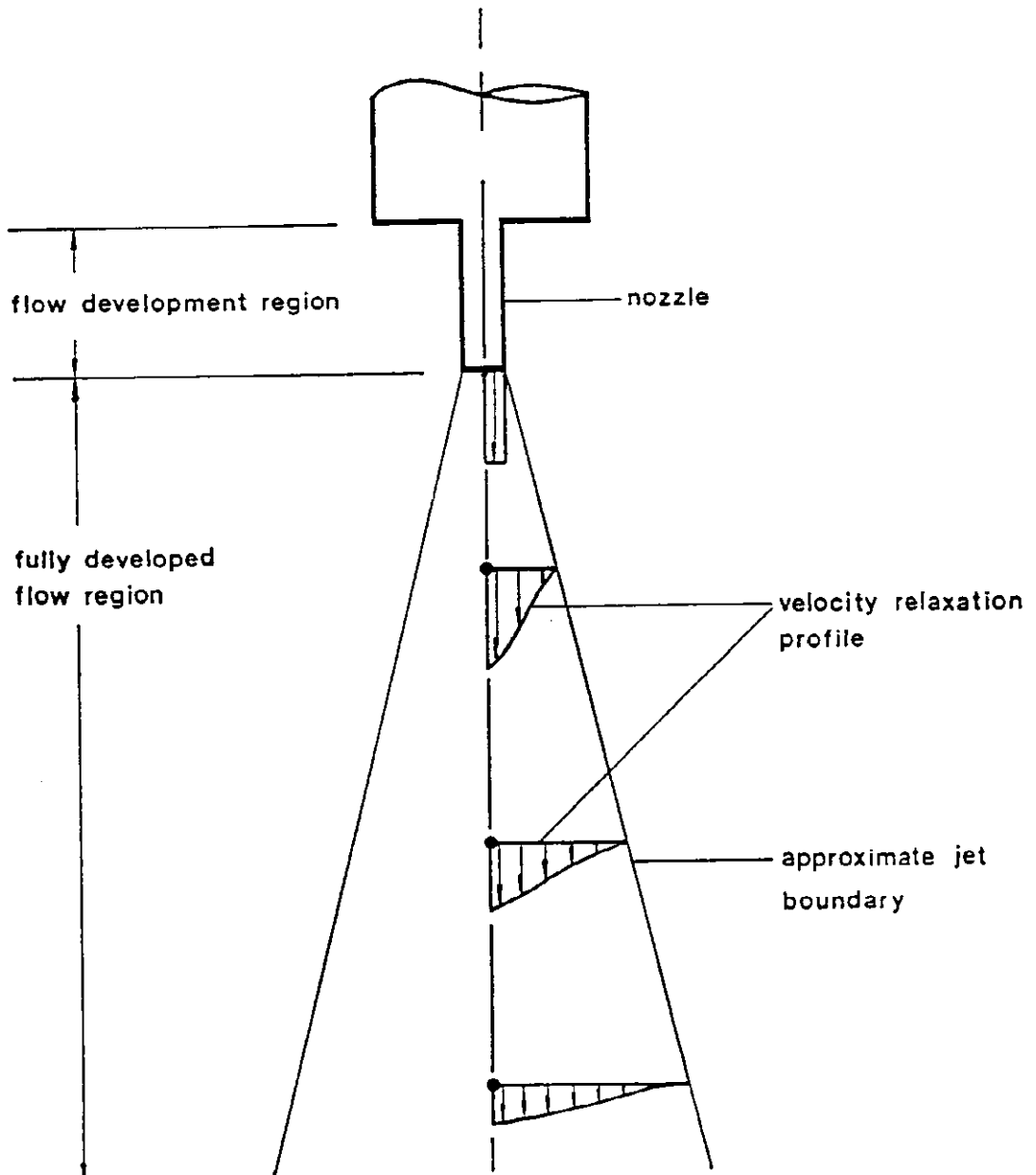
Figure A2.1 Velocity profile transitions within the liquid jet

The velocity relaxation inside the jet occurs as a result of the change from a pipe flow velocity profile, when the liquid is inside the nozzle, to a plug flow velocity profile once the jet has left the confines of the nozzle. Further downstream the velocity profile changes from plug flow to parabolic flow due to the interaction of the outer boundary of the jet with the surrounding atmosphere. This interaction slows the velocity of the jet at its free surface resulting in an expansion in the jet diameter.

Associated with the velocity relaxation within the jet once it leaves the nozzle is a lateral movement of the free surface of the jet which extends beyond the original boundary of the jet diameter. The lateral motions of the liquid create undulations on the jet surface which increase in magnitude with increasing free jet length. The irregular nature of the jet surface created by the undulations is often called the "surface roughness" and jets which exhibit this characteristic are called rough jets. The surface roughness is strongly influenced by the upstream conditions of the jet delivery system. Disturbances such as swirl generated by a pump, vibration from a motor or irregularities on the inside surface of the pipework are all amplified once the liquid passes through the nozzle, resulting in an increase in the surface roughness.

The jets used in this study were intended to simulate those types of jets suitable for industrial applications. Industrial jets would normally have rough surfaces created by the disturbances generated within the delivery system. They would also need to give the maximum rate of gas entrainment. In order to achieve these prerequisites in the jet design a preliminary set of experiments was performed.

The aims of the experiments reported in Appendix 2 were therefore, firstly, to determine the nozzle design which gave the maximum rate of gas entrainment and secondly, to measure the jet diameter as a function of the free jet length for all jets used in this study. This data was then used to quantify the entrainment measurements given in Chapter 4.

A2.2 EFFECT OF THROAT LENGTH ON JET EXPANSION AND ENTRAINMENT RATE

The effect of the nozzle throat length on the jet expansion and rate of entrainment was measured for the nozzles listed in Table A2.1. It can be seen from the table that while the nozzle diameter was held constant at 4.76 mm, the normalised throat length ratio ranged from 0.7 - 16.4.

TABLE A2.1 Nozzle dimensions [1]

Run	D_N (mm)	$\dfrac{L_N}{D_N}$
17	4.76	16.39
65	4.76	13.24
67	4.76	6.81
68	4.76	3.28
69	4.76	1.89
70	4.76	0.74

[1] Symbols are defined in Figure 3.3

A2.2.1 Gas entrainment rate

The normalised entrainment rates as a function of the normalised jet lengths for the nozzles given in Table A2.1 are given in Figure A2.2. The jet velocity at the nozzle was constant at 11.5 m/s.
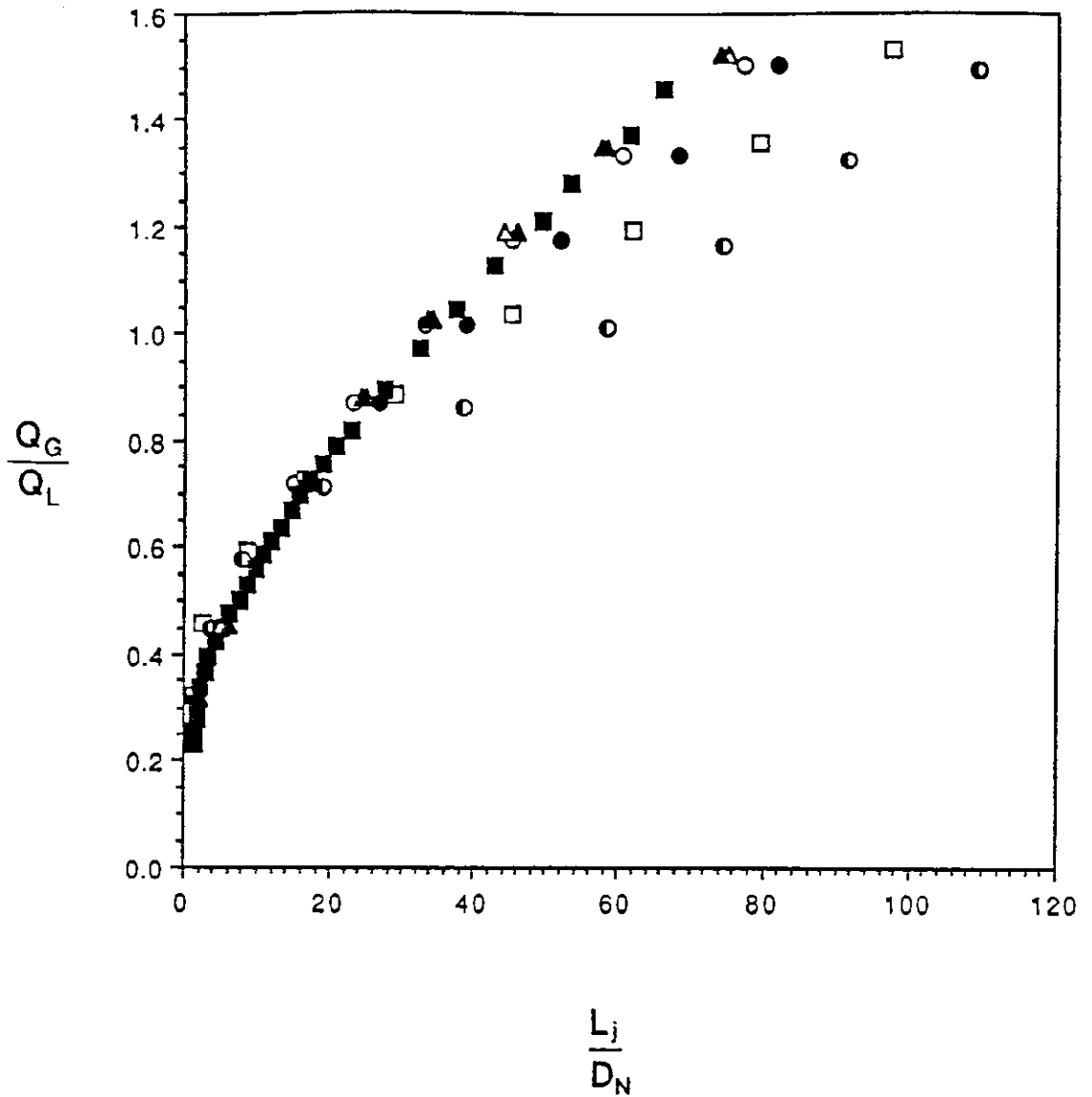
Figure A2.2 Normalised entrainment rate vs normalised jet length
[L_N/D_N = 16.4($\triangle$); 13.2($\blacktriangle$); 6.8($\bigcirc$); 3.8($\bullet$); 1.9($\square$);
0.7($\mathbb{C}$); ρ_L = 1000 kg/m³; μ_L = 0.001 Pa-s; σ = 0.063N/m]

It can be seen from Figure A2.2 that for jet lengths less than
approximately 15 nozzle diameters, the entrainment rate was independent
of the throat length of the nozzle. Beyond 15 nozzle diameters, however,
the entrainment rate varied with throat length. In this region the
nozzle with the shortest throat length corresponded to the lowest rate of
entrainment. The entrainment rate then increased with increasing throat

length, until at a throat length of approximately 7 nozzle diameters, the entrainment rate became independent of the throat length.

The data presented in Figure A2.2 can be compared to the results of other studies. McCarthy (1972) also studied the influence of the throat length of the nozzle on the rate of gas entrainment. He found that for a jet length of 30 nozzle diameters there was a maximum when the entrainment rate was plotted against the nozzle throat length as shown in Figure A2.3.

Figure A2.3   Entrainment rate vs normalised nozzle throat length
(after McCarthy, 1972)

From Figure A2.3 it can be seen that for throat length values below 8
nozzle diameters the entrainment rate increased steadily, reflecting the
increase in scale of the disturbances on the surface of the jet. For
throat lengths between 8 and 40 nozzle diameters there was an elevated
entrainment region which corresponded to the appearance of transverse
oscillations of the jet axis. Above throat lengths of 40 nozzle
diameters the transverse oscillations of the jet axis disappeared and the
entrainment rate became constant as a result of the fully developed pipe
flow within the nozzle.
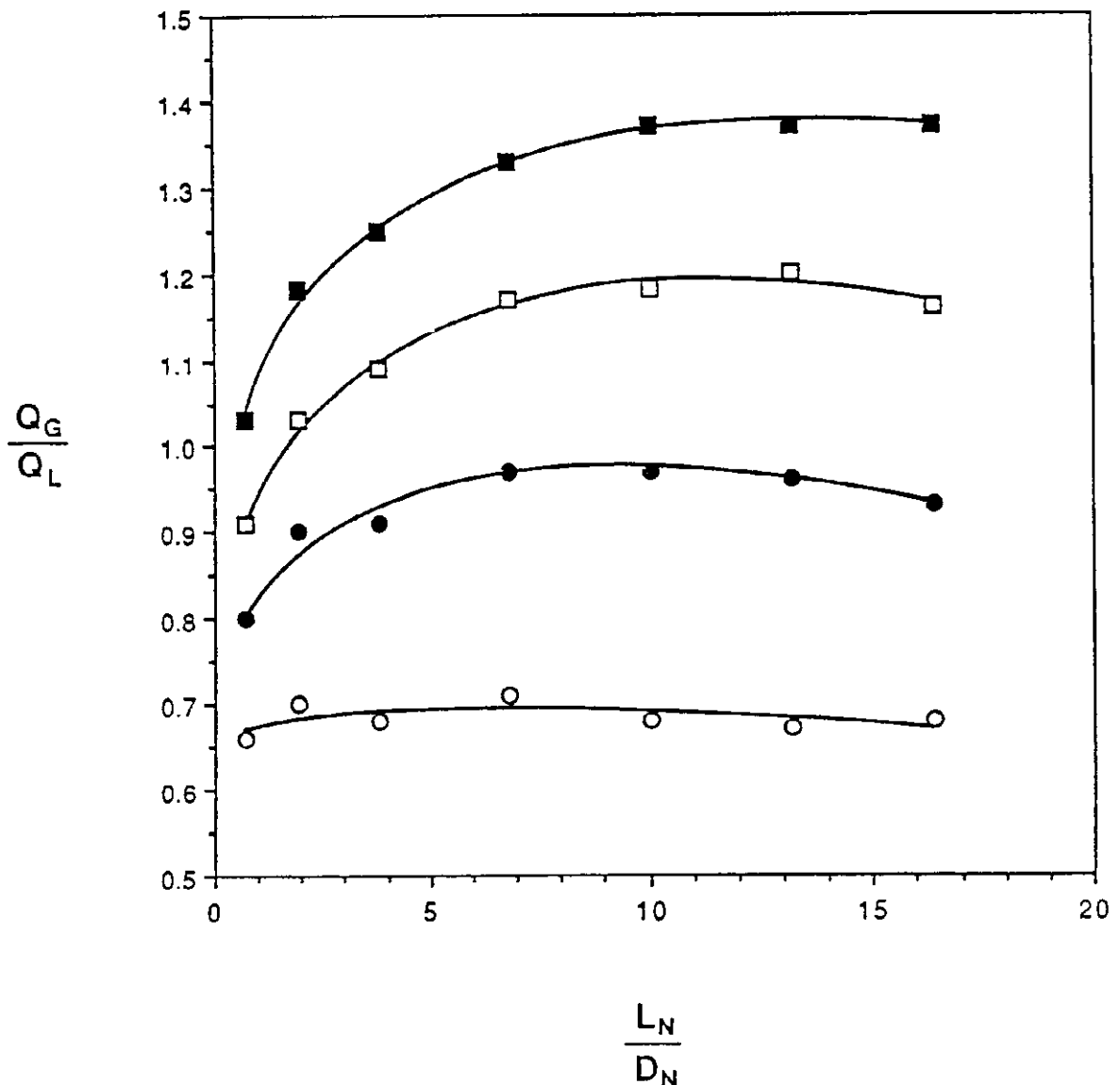
Figure A2.4 Normalised entrainment rate vs normalised throat length
[L_J/D_N = 15(O); 30(●); 45(□); 60(■)]

In Figure A2.4 the entrainment measurements from Figure A2.2 have been replotted as a function of the normalised throat length. It can be seen from the Figure that for for a normalised jet length of 15 the normalised gas entrainment rate was independent of the throat length. For normalised jet lengths above 15 it can be seen that the normalised entrainment rate varied with changing throat length. In the range of throat lengths examined a maximum value in the normalised entrainment rate was observed. As can be seen from Figure A2.4 the maximum entrainment rate varied with throat length for the different normalised jet length values.

It can be concluded that the results that for a given free jet length above a normalised value of 15 there was an optimum throat length which gave a maximum in the gas entrainment rate. The results also indicated that the optimum throat length increased with increasing normalised free jet length.

The reason why the normalised entrainment rate was independent of throat length, for normalised jet length values less than 15, can be found from Arai and Hashimoto (1986). They described the stability of a liquid jet as being divided into three different regions as illustrated in Figure A2.5, where the transition boundaries have been plotted as a function of the jet Weber number. Arai and Hashimoto based the Weber number on the gas density, the nozzzle diameter, and the jet velocity relative to the surrounding gas, i.e.

$$We_j = \frac{D_N \rho_G (v_j - v_G)^2}{6} .$$

(A2.1)

In Figure A2.5 Region I is where the surface of the jet is relatively smooth; Region II is where the surface is disturbed and unstable surface waves propagate along the continuous liquid jet; Region III is where the liquid jet breaks into droplets. Arai and Hashimoto observed, both visually and using frequency response techniques, the transition between the three regions outlined above.

Figure A2.5 Transition boundaries for 1 mm diameter liquid jet
            given by Arai and Hashimoto (1986)

Using the definition for the jet Weber number given by (A2.1), the
nozzles listed in Table A2.1 have a Weber number equal to 10. From
Figure A2.5 it can be seen that when We_j is equal to 10 the transition
from a smooth jet to one which surface waves dominate the surface occurs
at a free jet length of approximately 15 jet diameters. This value
corresponds to the normalised length where the experimental entrainment

curves in Figure A2.2 start to deviate from each other. From this
observation it is possible to conclude that the position along the jet
surface where waves begin to develop is independent of the nozzle
conditions. However, the amplitude of the surface waves once they have
developed is a function of the nozzle throat length which results in
different rates of entrainment.
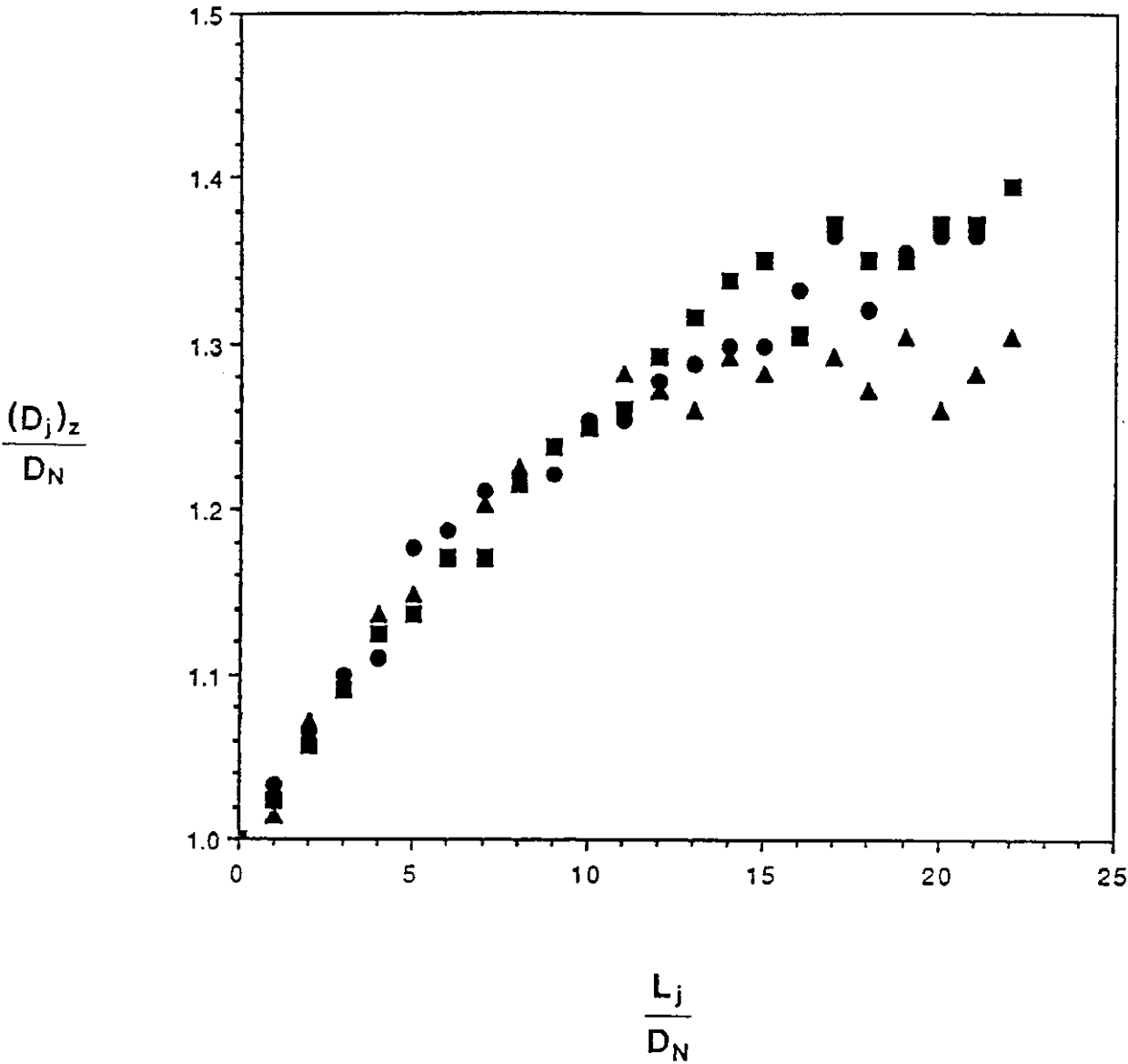
Figure A2.6 Normalised jet diameter vs normalised jet length
[L_N/D_N = 13.24(●); 6.81(■); 3.78(▲)]

A2.2.2 Jet expansion

The normalised jet diameter has been plotted against the normalised jet
length as shown in Figure A2.6 for three different nozzle throat lengths.
It can be seen from the graph that the expansion in the jet diameter with
increasing jet length was the same when the normalised throat length was
greater than 7. This could possibly be due to the existence of fully-
developed turbulent flow within the troat nozzle, which resulted in the
same amplitude of the surface disturbances. When the normalised throat
length was less than 7, possibly the flow was not fully developed.
Consequently the amplitude of the surface disturbances were less than
that for fully developed flow, which resulted in a reduction in the
overall expansion of the jet.

It can also be seen from Figure A2.6 that the difference in the rate of
jet expansion was not noticeable, however, until after a normalised free
jet length of approximately 13, when the surface of the free jet changed
from being smooth to rough. At this point the disturbances on the
surface were amplified, resulting in a greater change in the jet diameter
with jet length for each nozzle.

A2.3 JET DIAMETER MEASUREMENT

From the experimental results presented in Section A2.2, the maximum
entrainment rate was obtained for nozzles which had a normalised throat
length greater than 13. Consequently, the nozzles used for all further
entrainment studies had a normalised throat length of at least 13. A
list of the nozzle dimensions used is given in Table 3.4. For these
nozzles the effective jet diameter was measured, using the procedure
outlined in Section 3.4.1, for a range of experimental conditions. A
summary of the experimental conditions is given in Table A2.2 and the jet
expansion measurements are given in Table A2.3.

TABLE A2.2 :   Summary of conditions for the jet expansion measurements

JET NUMBER	NOZZLE DIAMETER (mm)	THROAT LENGTH (mm)	JET VELOCITY (m/s)	SURFACE TENSION (mN/m)	LIQUID DENSITY (kg/m3)	LIQUID VISCOSITY) (mPas)
1	7.12	124	15.1	48	996.5	.8513
2	7.12	124	11.5	48	996.5	.8513
3	7.12	124	7.8	48	997.0	.8327
4	7.12	124	15.1	54	996.2	.8513
5	7.12	124	11.5	54	997.3	.9111
6	7.12	124	7.8	55	997.5	.8705
7	7.12	124	15.1	62	997.5	.8705
8	7.12	124	11.5	62	997.5	.8705
9	7.12	124	7.8	62	997.5	.9325
10	4.76	78	15.0	47	996.5	.8327
11	4.76	78	11.5	47	996.5	.8705
12	4.76	78	7.8	48	996.5	.8904
13	4.76	78	15.0	53	996.5	.8513
14	4.76	78	11.5	53	996.5	.8327
15	4.76	78	7.8	53	996.5	.8513
16	4.76	78	15.0	63	996.2	.8327
17	4.76	78	11.5	65	996.8	.8705
18	4.76	78	7.8	62	997.3	.9111
19	2.38	36	15.0	48	997.5	.9325
20	2.38	36	7.8	49	997.9	.9548
21	2.38	36	15.0	53	997.5	.9325
22	2.38	36	11.5	54	997.5	.9325
23	2.38	36	7.8	54	997.0	.8904
24	2.38	36	15.0	60	997.3	.9111
25	2.38	36	11.5	61	997.5	.9325
26	2.38	36	7.8	60	997.5	.9325
27	4.76	78	15.0	63	1061	1.653
28	4.76	78	11.5	64	1061	1.653
29	4.76	78	7.8	62	1061	1.653
30	4.76	78	15.0	63	1114	2.854
31	4.76	78	11.5	65	1114	2.854
32	4.76	78	7.8	62	1114	2.854
33	4.76	78	15.0	24	784.0	2.12
34	4.76	63	11.5	65	998.6	1.053
35	4.76	32	11.5	65	999.1	.9325
36	4.76	18	11.5	65	999.1	.9111
37	4.76	9	11.5	64	998.9	.9548
38	4.76	4	11.5	64	998.9	.9325

TABLE A2.3 : Normalised jet diameter measurements

NORMALISED JET LENGTH	JET NUMBER					
	1	2	3	4	5	6
0	1.000	1.000	1.000	1.000	1.000	1.000
1	1.040	1.020	1.011	1.034	1.031	1.015
2	1.100	1.051	1.043	1.094	1.062	1.046
3	1.145	1.084	1.075	1.138	1.092	1.092
4	1.190	1.130	1.075	1.182	1.123	1.092
5	1.236	1.162	1.106	1.227	1.169	1.123
6	1.280	1.177	1.122	1.256	1.215	1.139
7	1.295	1.177	1.138	1.271	1.200	1.169
8	1.295	1.208	1.138	1.330	1.246	1.184
9	1.341	1.240	1.185	1.360	1.277	1.246
10	1.341	1.240	1.153	1.404	1.308	1.246
11	1.341	1.303	1.185	1.434	1.339	1.231
12	1.416	1.287	1.201	1.389	1.339	1.262
13	1.446	1.334	1.216	1.434	1.339	1.277
14	1.431	1.318	1.216	1.464	1.354	1.293
15	1.462	1.350	1.216	1.434	1.385	1.308
16	1.462	1.318	1.216	1.449	1.385	1.354
17	1.537	1.350	1.248	1.471	1.369	1.324
18	1.506	1.318	1.296	1.522	1.447	1.338
19	1.492	1.397	1.279	1.552	1.447	1.400
20	1.521	1.350	1.296	1.507	1.416	1.369
21	1.567	1.366	1.233	1.507	1.462	1.354
22	1.582	1.382	1.248	1.552	1.477	1.385
23	1.612	1.334	1.233	1.522	1.569	1.369
24	1.582	1.334	1.201	1.552	1.523	1.354
25	1.627	1.318	1.226	1.567	1.493	1.324
26	1.582	1.350	1.248	1.582	1.460	1.354
27	1.619	1.303	1.264	1.567	1.508	1.369
28	1.612	1.366	1.264	1.625	1.538	1.385
29						
30						

TABLE A2.3 (contd) : Normalised jet diameter measurements

NORMALISED JET LENGTH	JET NUMBER					
	7	8	9	10	11	12
0	1.000	1.000	1.000	1.000	1.000	1.000
1	1.001	1.014	1.020	1.031	1.027	1.016
2	1.074	1.076	1.035	1.084	1.027	1.044
3	1.089	1.092	1.066	1.123	1.069	1.030
4	1.133	1.107	1.066	1.149	1.097	1.058
5	1.148	1.138	1.082	1.201	1.097	1.100
6	1.207	1.170	1.128	1.228	1.153	1.114
7	1.207	1.201	1.128	1.267	1.168	1.100
8	1.237	1.247	1.159	1.280	1.168	1.142
9	1.252	1.264	1.159	1.280	1.168	1.142
10	1.266	1.232	1.174	1.306	1.181	1.170
11	1.280	1.279	1.174	1.358	1.224	1.170
12	1.310	1.264	1.174	1.306	1.238	1.142
13	1.325	1.295	1.159	1.319	1.252	1.183
14	1.354	1.295	1.159	1.398	1.266	1.170
15	1.310	1.295	1.190	1.358	1.280	1.197
16	1.339	1.310	1.190	1.437	1.280	1.183
17	1.354	1.341	1.205	1.398	1.280	1.197
18	1.443	1.341	1.205	1.385	1.294	1.211
19	1.399	1.326	1.236	1.398	1.294	1.170
20	1.428	1.373	1.190	1.385	1.294	1.211
21	1.413	1.341	1.252	1.450	1.308	1.253
22	1.443	1.326	1.205	1.502	1.280	1.211
23	1.399	1.310	1.174	1.515	1.323	1.239
24	1.384	1.295	1.174	1.555	1.336	1.211
25	1.399	1.326	1.159	1.528	1.379	1.197
26	1.413	1.341	1.174			
27	1.413	1.264	1.205			
28	1.369	1.310	1.174			
29						
30						

TABLE A2.3 (contd) : Normalised jet diameter measurements

NORMALISED JET LENGTH	JET NUMBER					
	13	14	15	16	17	18
0	1.000	1.000	1.000	1.000	1.000	1.000
1	1.033	1.010	1.021	1.004	1.018	1.008
2	1.061	1.052	1.062	1.059	1.044	1.050
3	1.117	1.080	1.048	1.086	1.085	1.079
4	1.144	1.066	1.062	1.114	1.085	1.079
5	1.185	1.108	1.062	1.128	1.113	1.107
6	1.213	1.136	1.103	1.141	1.113	1.120
7	1.241	1.150	1.117	1.169	1.153	1.107
8	1.282	1.150	1.131	1.188	1.153	1.150
9	1.295	1.150	1.117	1.211	1.181	1.150
10	1.295	1.178	1.144	1.238	1.181	1.150
11	1.364	1.207	1.159	1.224	1.235	1.150
12	1.364	1.193	1.186	1.251	1.262	1.192
13	1.378	1.207	1.159	1.279	1.262	1.206
14	1.392	1.235	1.159	1.293	1.275	1.206
15	1.419	1.263	1.186	1.293	1.289	1.206
16	1.419	1.249	1.200	1.306	1.329	1.192
17	1.475	1.263	1.186	1.334	1.303	1.206
18	1.447	1.277	1.172	1.320	1.344	1.249
19	1.475	1.263	1.186	1.320	1.329	1.206
20	1.447	1.249	1.144	1.376	1.329	1.220
21	1.502	1.263	1.159	1.348	1.316	1.192
22	1.502	1.291	1.172	1.348	1.329	1.206
23	1.488	1.249	1.200	1.417	1.316	1.220
24	1.516	1.249	1.159	1.348	1.357	1.192
25	1.475	1.305	1.172	1.348	1.329	1.178
26		1.305		1.376		1.178
27				1.403		1.220
28						
29						
30						

TABLE A2.3 (contd) : Normalised jet diameter measurements

NORMALISED JET LENGTH	JET NUMBER					
	19	20	21	22	23	24
0	1.000	1.000	1.000	1.000	1.000	1.000
1	.996	1.008	1.005	1.005	1.017	1.015
2	1.034	1.028	1.066	1.024	.997	1.034
3	1.053	1.028	1.066	1.080	1.017	1.071
4	1.053	1.008	1.106	1.062	1.037	1.052
5	1.053	1.047	1.127	1.100	1.037	1.089
6	1.073	1.067	1.127	1.080	1.037	1.108
7	1.110	1.047	1.186	1.119	.997	1.089
8	1.092	1.087	1.166	1.100	1.057	1.108
9	1.092	1.067	1.146	1.119	1.037	1.146
10	1.073	1.087	1.207	1.119	1.077	1.128
11	1.092	1.125	1.227	1.138	1.097	1.146
12	1.092	1.128	1.207	1.138	1.117	1.146
13	1.110	1.165	1.227	1.138	1.097	1.165
14	1.110	1.106	1.247	1.175	1.077	1.183
15	1.169	1.106	1.267	1.156	1.077	1.202
16	1.149	1.125	1.267	1.214	1.117	1.183
17	1.092	1.125	1.267	1.195	1.097	1.202
18	1.092	1.165	1.186	1.214	1.097	1.222
19	1.130	1.165	1.307	1.195	1.117	1.222
20	1.110	1.185	1.307	1.195	1.117	1.202
21	1.130	1.125	1.327	1.232	1.137	1.240
22	1.110	1.185	1.327	1.232	1.117	1.259
23	1.110	1.165	1.367	1.232	1.117	1.222
24	1.110	1.185	1.327	1.175	1.117	1.222
25	1.130	1.185	1.307	1.195	1.137	1.222
26	1.130	1.165	1.347	1.214	1.156	1.259
27	1.130	1.185	1.347	1.214	1.117	1.240
28	1.149	1.110				
29	1.110	1.165				
30	1.130	1.110				
31	1.188	1.185				
32	1.169	1.165				
33	1.149	1.224				
34	1.188	1.244				
35	1.169	1.284				

TABLE A2.3 (contd) : Normalised jet diameter measurements

NORMALISED JET LENGTH	JET NUMBER					
	25	26	27	28	29	30
0	1.000	1.000	1.000	1.000	1.000	1.000
1	1.016	1.010	1.006	1.011	1.013	1.027
2	1.036	1.031	1.094	1.055	1.043	1.041
3	1.074	1.072	1.109	1.099	1.074	1.096
4	1.074	1.051	1.122	1.099	1.104	1.124
5	1.094	1.093	1.152	1.113	1.119	1.151
6	1.055	1.093	1.195	1.128	1.119	1.151
7	1.133	1.093	1.225	1.157	1.149	1.207
8	1.094	1.113	1.195	1.216	1.180	1.193
9	1.133	1.113	1.195	1.245	1.149	1.221
10	1.133	1.155	1.210	1.259	1.194	1.235
11	1.153	1.155	1.254	1.231	1.165	1.263
12	1.191	1.155	1.268	1.245	1.180	1.276
13	1.153	1.155	1.298	1.274	1.180	1.305
14	1.191	1.196	1.254	1.259	1.180	1.290
15	1.191	1.175	1.298	1.274	1.165	1.305
16	1.153	1.175	1.268	1.289	1.180	1.276
17	1.172	1.196	1.298	1.377	1.194	1.263
18	1.191	1.216	1.313	1.304	1.210	1.290
19	1.191	1.196	1.298	1.274	1.194	1.332
20	1.191	1.196	1.341	1.333	1.180	1.290
21	1.172	1.196	1.327	1.347	1.180	1.290
22	1.153	1.258	1.298	1.347	1.194	1.276
23	1.191	1.175	1.268	1.347	1.180	1.305
24	1.211	1.237	1.371	1.347	1.194	1.318
25	1.231	1.216	1.268	1.304	1.180	1.318
26	1.231	1.258	1.268	1.333	1.165	1.263
27	1.231	1.237	1.298	1.319	1.165	1.332
28		1.258				
29		1.258				
30		1.258				
31		1.258				
32		1.258				
33		1.258				
34		1.299				
35		1.237				

TABLE A2.3 (contd) : Normalised jet diameter measurements

NORMALISED JET LENGTH	JET NUMBER					
	31	32	33	34	35	36
0	1.000	1.000	1.000	1.000	1.000	1.000
1	1.019	1.008	1.043	1.033	1.013	1.024
2	1.049	1.064	1.096	1.065	1.036	1.057
3	1.049	1.078	1.190	1.099	1.058	1.091
4	1.092	1.091	1.229	1.110	1.080	1.125
5	1.107	1.134	1.270	1.176	1.092	1.137
6	1.122	1.134	1.310	1.187	1.103	1.170
7	1.151	1.148	1.350	1.210	1.103	1.170
8	1.151	1.176	1.350	1.221	1.125	1.215
9	1.180	1.190	1.363	1.221	1.114	1.238
10	1.180	1.176	1.376	1.254	1.136	1.249
11	1.195	1.204	1.403	1.254	1.114	1.260
12	1.195	1.204	1.444	1.277	1.158	1.293
13	1.209	1.176	1.417	1.288	1.125	1.316
14	1.180	1.204	1.430	1.298	1.169	1.339
15	1.209	1.218	1.457	1.298	1.158	1.350
16	1.195	1.176	1.484	1.332	1.158	1.305
17	1.253	1.232	1.470	1.365	1.125	1.373
18	1.224	1.246	1.537	1.321	1.136	1.350
19	1.239	1.204	1.497	1.354	1.147	1.350
20	1.239	1.232	1.510	1.365	1.147	1.373
21	1.268	1.246	1.537	1.365	1.169	1.373
22	1.268	1.190	1.617		1.169	1.395
23	1.209	1.176	1.564			
24	1.253	1.190	1.591			
25	1.239	1.218	1.550			
26	1.239	1.190				
27	1.253	1.232				
28						
29						
30						

TABLE A2.3 (contd) : Normalised jet diameter measurements

NORMALISED JET LENGTH	JET NUMBER					
	37	38	39	40	41	42
0	1.000	1.000	1.000			
1	1.015	1.039	1.026			
2	1.071	1.064	1.076			
3	1.092	1.127	1.114			
4	1.137	1.189	1.127			
5	1.148	1.202	1.127			
6	1.170	1.227	1.152			
7	1.204	1.240	1.152			
8	1.226	1.265	1.139			
9	1.238	1.290	1.127			
10	1.249	1.302	1.152			
11	1.282	1.327	1.139			
12	1.271	1.365	1.152			
13	1.259	1.327	1.152			
14	1.293	1.327	1.114			
15	1.282	1.308	1.114			
16	1.304	1.327	1.127			
17	1.293	1.315	1.089			
18	1.271	1.315	1.089			
19	1.304	1.315	1.089			
20	1.259	1.340	1.101			
21	1.282	1.340	1.064			
22	1.304	1.315	1.089			
23		1.290	1.076			
24		1.315	1.064			
25						

Appendix 3

BUBBLE SIZE MEASUREMENT

In this appendix the measured bubble diameter distributions
for the mixing, and uniform two-phase flow zones are
reported. Also included in this appendix are the Sauter mean
diameter, and maximum bubble diameter which has been taken as
the value which is greater than 99% of all the measured
bubble diameters in the cumulative frequency distribution.

TABLE A3.1 : Summary of experimental bubble diameter results

Run	Qg/Ql	Max diameter		Sauter mean	
		Mixing zone	Two-phase zone	Mixing zone	Two-phase zone
2	.118	222	221	129	138
5	.116	280	271	156	169
8	.117	387	449	242	285
11	.129	248	364	153	236
14	.129	222	386	136	245
17	.127	406	412	270	289
23	.127	412	543	233	384
32	.127	318	324	187	209
41	.131	294	418	181	264
64	.125	390	409	231	263
72	.114	441	487	264	312
74	.126	584	639	349	420
75(1)	.126	543	640	324	424
75(2)	.296	523	584	341	408
75(3)	.645	698	726	468	445
76(1)	.125	718	747	430	506
78	.131	594	738	372	552
81	.114	519	767	314	466
84	.127	614	794	378	479
87	.130	716	773	488	557
95(1)	.125	531	694	332	472
101	.124	611	586	360	419

All diameter values given in microns

Gas-to-liquid volumetric flow ratio is at gas inlet conditions

Max diameter is the size corresponding to the 99% value on the cumulative frequency distribution for the measured diameters

TABLE A3.2 : Percentage frequency distribution of bubble diameter
measurements for mixing zone (200 mm sample port)

SIZE BAND (μm)	RUN NUMBER					
	2	5	8	11	14	17
0 - 25	9.88	7.67	2.62	4.95	4.56	2.97
25 - 50	36.63	26.99	23.28	23.63	24.48	24.75
50 - 75	21.40	19.94	21.97	16.21	20.75	17.16
75 - 100	9.88	16.26	10.16	22.25	17.84	10.89
100 - 125	9.88	11.04	7.54	12.09	13.28	5.28
125 - 150	6.17	7.36	10.16	6.59	8.30	6.27
150 - 175	1.65	4.29	5.57	5.22	5.39	2.64
175 - 200	2.06	1.53	3.28	4.40	3.32	5.94
200 - 225	1.65	2.15	3.28	1.92	1.24	5.28
225 - 250	.82	.92	1.97	1.92	.41	3.30
250 - 275	.00	.61	1.64	.55	.41	1.98
275 - 300	.00	1.23	2.62	.27	.00	3.30
300 - 325	.00	.00	2.30	.00	.00	3.96
325 - 350	.00	.00	.66	.00	.00	2.31
350 - 375	.00	.00	1.64	.00	.00	1.65
375 - 400	.00	.00	.66	.00	.00	.99
400 - 425	.00	.00	.66	.00	.00	1.32
425 - 450	.00	.00	.00	.00	.00	.00
450 - 475	.00	.00	.00	.00	.00	.00
475 - 500	.00	.00	.00	.00	.00	.00
Total	100.00	100.00	100.00	100.00	100.00	100.00

SIZE BAND (μm)	RUN NUMBER			
	23	32	41	64
0 - 25	4.93	7.05	7.26	10.50
25 - 50	24.01	24.36	21.55	28.61
50 - 75	15.13	22.12	15.74	18.37
75 - 100	9.87	12.50	14.29	10.50
100 - 125	10.20	9.62	9.20	7.87
125 - 150	7.89	7.69	11.14	3.94
150 - 175	8.22	4.49	7.02	5.25
175 - 200	7.24	3.53	3.39	5.25
200 - 225	3.95	3.85	4.84	2.62
225 - 250	2.30	1.60	2.91	1.84
250 - 275	1.32	.64	.73	1.05
275 - 300	1.64	.64	1.21	1.31
300 - 325	.66	1.28	.73	.52
325 - 350	.33	.32	.00	.79
350 - 375	.33	.32	.00	.26
375 - 400	.33	.00	.00	.52
400 - 425	1.32	.00	.00	.52
425 - 450	.33	.00	.00	.26
450 - 475	.00	.00	.00	.00
475 - 500	.00	.00	.00	.00
Total	100.00	100.00	100.00	100.00

TABLE A3.2 (cont'd) : Percentage frequency distribution of bubble
measurements for mixing zone

SIZE BAND (µm)	RUN NUMBER					
	72	74	75(1)	75(2)	75(3)	76(1)
0 - 50	15.50	21.86	15.00	9.84	8.10	3.14
50 - 100	26.10	32.51	28.53	32.68	23.05	12.04
100 - 150	19.12	13.93	20.59	9.45	18.69	13.09
150 - 200	17.05	9.56	11.47	13.78	10.28	7.85
200 - 250	9.82	6.83	8.53	9.45	7.48	15.71
250 - 300	4.65	5.46	4.71	8.27	6.85	12.04
300 - 350	3.10	4.64	3.53	5.51	5.30	14.14
350 - 400	2.58	1.09	2.06	3.94	3.74	3.66
400 - 450	1.29	1.64	3.24	2.36	2.80	4.71
450 - 500	.78	.27	.59	3.54	2.80	5.24
500 - 550	.00	.82	.88	.39	4.05	1.57
550 - 600	.00	.55	.88	.39	2.18	3.66
600 - 650	.00	.27	.00	.39	1.87	1.05
650 - 700	.00	.27	.00	.00	1.87	.52
700 - 750	.00	.27	.00	.00	.31	1.57
750 - 800	.00	.00	.00	.00	.62	.00
800 - 850	.00	.00	.00	.00	.00	.00
850 - 900	.00	.00	.00	.00	.00	.00
900 - 950	.00	.00	.00	.00	.00	.00
950 -1000	.00	.00	.00	.00	.00	.00
Total	100.00	100.00	100.00	100.00	100.00	100.00

SIZE BAND (µm)	RUN NUMBER					
	78	81	84	87	95(1)	101
0 - 50	10.58	20.39	9.83	16.96	18.26	12.50
50 - 100	28.85	24.92	24.28	24.70	33.53	28.21
100 - 150	11.54	11.97	17.92	13.69	11.38	18.59
150 - 200	11.54	13.27	10.98	8.04	7.78	9.62
200 - 250	6.41	8.09	8.09	3.87	7.19	8.97
250 - 300	9.62	8.09	8.09	5.65	6.89	5.45
300 - 350	4.81	4.21	4.62	4.46	5.99	6.73
350 - 400	6.41	4.85	5.78	4.46	4.19	3.21
400 - 450	4.81	2.27	4.62	4.46	1.80	1.92
450 - 500	1.92	.32	2.31	2.98	.90	1.92
500 - 550	2.24	1.62	1.45	2.68	1.80	1.92
550 - 600	.32	.00	.87	3.27	.30	1.28
600 - 650	.96	.00	.58	2.08	.00	.32
650 - 700	.00	.00	.58	1.49	.00	1.28
700 - 750	.00	.00	.00	.60	.00	.00
750 - 800	.00	.00	.00	.30	.00	.00
800 - 850	.00	.00	.00	.30	.00	.00
850 - 900	.00	.00	.00	.30	.00	.00
900 - 950	.00	.00	.00	.00	.00	.00
950 -1000	.00	.00	.00	.00	.00	.00
Total	100.00	100.00	100.00	100.00	100.00	100.00

TABLE A3.3 : Percentage frequency distribution of bubble diameter
measurements for uniform-two-phase-flow zone

SIZE BAND (μm)	RUN NUMBER					
	2	5	8	11	14	17
0 - 25	14.97	9.87	5.50	6.73	3.38	5.78
25 - 50	31.63	29.93	17.15	23.55	26.46	26.19
50 - 75	16.33	16.78	15.86	18.96	16.62	17.69
75 - 100	13.95	13.16	11.00	11.93	11.38	10.54
100 - 125	6.80	10.53	7.77	7.03	9.23	4.76
125 - 150	5.44	4.61	5.18	5.20	4.62	4.08
150 - 175	5.78	4.93	4.85	6.12	4.31	2.38
175 - 200	2.38	3.62	3.24	4.28	3.69	4.08
200 - 225	2.04	2.30	3.24	3.98	4.92	1.70
225 - 250	.68	1.64	2.59	2.45	5.85	4.42
250 - 275	.00	1.97	6.80	3.36	1.54	3.06
275 - 300	.00	.66	4.21	1.22	3.38	3.06
300 - 325	.00	.00	5.83	2.14	.62	3.74
325 - 350	.00	.00	1.94	1.53	1.54	2.38
350 - 375	.00	.00	1.29	.92	.92	2.04
375 - 400	.00	.00	1.29	.31	1.23	2.38
400 - 425	.00	.00	.65	.31	.31	1.36
425 - 450	.00	.00	.65	.00	.00	.34
450 - 475	.00	.00	.97	.00	.00	.00
475 - 500	.00	.00	.00	.00	.00	.00
Total	100.00	100.00	100.00	100.00	100.00	100.00

SIZE BAND (μm)	RUN NUMBER			
	23	32	41	64
0 - 25	3.18	5.81	7.43	14.09
25 - 50	30.04	28.44	24.77	29.90
50 - 75	13.07	18.65	16.41	18.56
75 - 100	4.59	10.40	10.53	10.65
100 - 125	2.12	12.54	8.98	3.78
125 - 150	2.47	4.89	4.95	3.78
150 - 175	2.47	3.98	5.26	2.41
175 - 200	1.41	3.98	4.95	1.37
200 - 225	1.77	2.75	3.41	3.44
225 - 250	2.47	1.83	2.79	1.72
250 - 275	2.12	2.14	3.10	3.09
275 - 300	3.89	1.83	1.55	.69
300 - 325	4.24	1.83	.93	3.09
325 - 350	4.24	.92	.31	.69
350 - 375	4.59	.00	.93	1.03
375 - 400	3.18	.00	1.86	.34
400 - 425	4.59	.00	1.24	1.03
425 - 450	4.24	.00	.62	.34
450 - 475	1.41	.00	.00	.00
475 - 500	1.06	.00	.00	.00
Total	97.17	100.00	100.00	100.00

TABLE A3.3 (cont'd) : Percentage frequency distribution of bubble
measurements for uniform-two-phase-flow zone

SIZE BAND (μm)	RUN NUMBER					
	72	74	75(1)	75(2)	75(3)	76(1)
0 - 50	23.84	17.34	23.46	23.93	14.48	9.22
50 - 100	28.81	34.37	28.79	23.93	28.96	14.56
100 - 150	14.24	13.93	7.41	8.59	12.12	6.31
150 - 200	9.93	5.57	5.56	7.36	10.77	5.34
200 - 250	6.95	4.02	4.01	2.15	6.40	4.37
250 - 300	4.97	6.19	5.56	8.90	8.42	6.31
300 - 350	3.31	4.95	8.33	5.83	4.71	7.28
350 - 400	3.64	2.48	5.25	5.21	4.71	10.68
400 - 450	2.32	2.79	3.70	5.21	2.02	8.74
450 - 500	1.32	3.41	2.78	3.37	1.68	11.17
500 - 550	.66	1.55	1.23	2.45	1.35	4.37
550 - 600	.00	2.17	1.54	3.07	1.01	1.94
600 - 650	.00	.31	1.85	.00	1.35	2.91
650 - 700	.00	.31	.62	.00	.67	5.34
700 - 750	.00	.62	.00	.00	.67	.49
750 - 800	.00	.00	.00	.00	.34	.49
800 - 850	.00	.00	.00	.00	.34	.49
850 - 900	.00	.00	.00	.00	.00	.00
900 - 950	.00	.00	.00	.00	.00	.00
950 -1000	.00	.00	.00	.00	.00	.00
Total	100.00	100.00	100.00	100.00	100.00	100.00

SIZE BAND (μm)	RUN NUMBER					
	78	81	84	87	95(1)	101
0 - 50	18.15	20.18	25.47	4.73	11.38	7.07
50 - 100	20.97	22.59	24.53	16.73	17.07	26.26
100 - 150	10.89	7.53	8.70	8.36	13.01	6.40
150 - 200	3.23	7.53	4.35	4.73	2.44	6.06
200 - 250	2.02	8.43	4.04	2.55	2.44	7.41
250 - 300	2.42	9.34	5.59	5.82	6.50	5.05
300 - 350	2.02	6.63	8.39	4.73	6.50	8.08
350 - 400	4.44	4.82	4.04	3.27	8.13	9.09
400 - 450	2.82	3.92	5.90	8.73	11.38	8.42
450 - 500	6.45	2.11	2.80	6.18	6.50	8.08
500 - 550	8.47	1.81	2.48	12.00	4.88	5.39
550 - 600	6.85	1.20	.62	7.64	6.50	2.36
600 - 650	4.84	.90	.62	4.00	.81	.34
650 - 700	3.63	1.51	.31	5.82	1.63	.00
700 - 750	2.42	.30	.62	2.91	.81	.00
750 - 800	.40	.60	.62	1.82	.00	.00
800 - 850	.00	.30	.31	.00	.00	.00
850 - 900	.00	.30	.62	.00	.00	.00
900 - 950	.00	.00	.00	.00	.00	.00
950 -1000	.00	.00	.00	.00	.00	.00
Total	100.00	100.00	100.00	100.00	100.00	100.00

Appendix 4

AXIAL PRESSURE PROFILE AND SUBMERGED
JET ANGLE MEASUREMENTS

In this appendix the measured axial wall pressure profiles
for experimental runs are reported. Also included in this
appendix are values for the submerged jet angle which have
been determined from the pressure profiles.

TABLE A4.1 : Pressure summary and submerged jet angle measurements

RUN NUMBER	Qg/Ql	PRESSURE		TWO-PHSE DENSITY	MIXING ZONE LENGTH	SUBMERGED JET ANGLE
		ATM (kN/m2) #1	HDSPCE (kN/m2) #2	(kg/m3) #3	(mm) #4	(deg) #5
2	.118	101.19	89.29	888	175	7.2
5	.116	101.19	90.23	890	170	7.4
8	.117	103.19	89.61	882	175	7.2
11	.129	101.19	89.48	876	150	8.4
14	.129	103.59	91.29	874	148	8.5
17	.127	103.19	91.84	847	148	8.5
23	.127	103.19	92.71	805	72	17.1
32	.127	101.33	91.37	929	198	6.4
41	.131	101.86	90.19	984	223	5.7
64	.125	101.59	91.42	849	148	8.5
72	.114	102.79	93.12	872	247	8.6
74	.126	101.33	92.29	822	248	8.5
75(0)		101.19	90.78	999	150	13.9
75(1)	.126	101.19	92.74	800	170	12.3
75(2)	.296	101.19	94.64	620	216	9.8
75(3)	.645	101.19	96.71	474	260	8.1
76(0)		101.19	90.98	1000	50	36.6
76(1)	.125	101.19	94.04	750	74	26.7
78	.131	101.86	96.78	553	113	18.2
81	.114	103.19	93.42	869	248	8.5
84	.127	100.79	92.48	796	166	12.6
87	.13	101.06	95.67	563	115	17.9
95(0)		101.46	91.36	1000	125	16.6
95(1)	.125	101.46	94.73	759	157	16.9
95(2)	.295	101.46	95.81	618	198	13.5
95(3)	.645	101.46	98.35	455	227	11.9
101	.124	101.86	94.73	743	153	17.3

#1   used to normalise pressure readings given in Table A4.2

#2   pressure in headspace of downcomer (Po in eq 5.52)

#3   calculated from differential pressure readings for uniform two-phase flow zone (assumed to be same as eddy density)

#4   distance from tip of nozzle where wall pressure gradient becomes constant

#5   taken as inverse tan (column radius/mixing zone length)

Table A4.2 : Normalised Absolute Axial Wall Pressure Profiles

DISTANCE FROM NOZZLE (mm)	RUN NUMBER					
	2	5	8	11	14	17
0	.878	.880	.878	.895	.898	.901
50	.881	.883	.883	.899	.901	.904
100	.889	.891	.886	.907	.909	.912
150	.918	.919	.898	.923	.924	.926
200	.929	.929	.925	.929	.930	.932
250	.933	.934	.934	.933	.935	.936
300	.938	.938	.938	.938	.939	.941
350	.942	.943	.943	.942	.943	.945
400	.947	.947	.947	.947	.948	.949
450	.951	.952	.952	.951	.952	.953
500	.956	.956	.956	.956	.956	.958
550	.960	.960	.960	.960	.961	.962
600	.964	.965	.965	.964	.965	.966
650	.969	.969	.969	.969	.969	.970
700	.973	.974	.974	.973	.974	.975
750	.978	.978	.978	.978	.978	.979
800	.982	.982	.982	.982	.982	.983
850	.987	.987	.987	.987	.987	.987
900	.991	.991	.991	.991	.991	.992
950	.996	.996	.996	.996	.996	.996
1000	1.000	1.000	1.000	1.000	1.000	1.000

DISTANCE FROM NOZZLE (mm)	RUN NUMBER					
	23	32	41	64	72	74
0	.917	.892	.884	.899	.902	.909
50	.922	.897	.889	.903	.906	.912
100	.926	.901	.893	.909	.910	.916
150	.932	.909	.903	.925	.914	.921
200	.935	.925	.920	.931	.920	.931
250	.939	.931	.926	.936	.931	.937
300	.943	.936	.932	.940	.939	.942
350	.947	.941	.936	.945	.944	.946
400	.951	.945	.941	.949	.949	.950
450	.956	.950	.946	.953	.953	.954
500	.960	.954	.951	.957	.957	.958
550	.964	.959	.956	.962	.962	.962
600	.968	.963	.961	.966	.966	.967
650	.972	.968	.966	.970	.970	.971
700	.976	.972	.971	.974	.974	.975
750	.980	.977	.976	.979	.979	.975
800	.984	.982	.980	.983	.983	.983
850	.988	.986	.985	.987	.987	.987
900	.992	.991	.990	.991	.991	.992
950	.996	.995	.995	.996	.996	.996
1000	1.000	1.000	1.000	1.000	1.000	1.000

Table A4.2 (cont) : Normalised Absolute Axial Wall Pressure Profiles

DISTANCE FROM NOZZLE (mm)	RUN NUMBER					
	75(0)	75(1)	75(2)	75(3)	76(0)	76(1)
0	.895	.914	.933	.949	.898	.929
50	.900	.917	.932	.949	.902	.928
100	.904	.921	.935	.949	.907	.932
150	.910	.926	.938	.949	.913	.935
200	.919	.934	.944	.953	.919	.939
250	.925	.939	.950	.958	.925	.944
300	.930	.944	.955	.960	.930	.948
350	.935	.948	.959	.963	.935	.952
400	.940	.952	.962	.966	.940	.956
450	.945	.956	.965	.969	.945	.959
500	.950	.960	.968	.973	.950	.963
550	.955	.964	.971	.977	.955	.967
600	.960	.968	.974	.981	.960	.970
650	.965	.972	.977	.984	.965	.974
700	.970	.976	.981	.986	.970	.978
750	.975	.980	.984	.988	.975	.981
800	.980	.984	.987	.991	.980	.985
850	.985	.988	.990	.993	.985	.989
900	.990	.992	.993	.995	.990	.993
950	.995	.996	.997	.998	.995	.996
1000	1.000	1.000	1.000	1.000	1.000	1.000

DISTANCE FROM NOZZLE (mm)	RUN NUMBER					
	78	81	84	87	95(0)	95(1)
0	.948	.901	.914	.942	.902	.926
50	.946	.906	.918	.944	.907	.929
100	.949	.909	.922	.947	.912	.932
150	.952	.914	.926	.950	.916	.936
200	.954	.918	.934	.953	.921	.940
250	.958	.930	.940	.956	.928	.945
300	.961	.939	.944	.960	.934	.950
350	.964	.944	.948	.963	.940	.955
400	.967	.949	.952	.965	.945	.959
450	.969	.953	.956	.968	.950	.962
500	.972	.957	.960	.971	.955	.966
550	.975	.962	.964	.974	.960	.970
600	.978	.966	.968	.977	.965	.974
650	.980	.970	.972	.980	.970	.977
700	.983	.974	.976	.983	.975	.981
750	.986	.979	.980	.986	.980	.985
800	.989	.983	.984	.988	.985	.989
850	.992	.987	.988	.991	.990	.992
900	.994	.991	.992	.994	.995	.996
950	.997	.996	.996	.997	1.000	1.000
1000	1.000	1.000	1.000	1.000	1.000	1.000

Table A4.2 (cont) : Normalised Absolute Axial Wall Pressure Profiles

DISTANCE FROM NOZZLE (mm)	RUN NUMBER		
	95(2)	95(3)	101
0	.940	.965	.927
50	.940	.965	.930
100	.945	.965	.934
150	.948	.965	.937
200	.951	.965	.941
250	.954	.967	.946
300	.957	.968	.951
350	.961	.970	.955
400	.966	.972	.959
450	.969	.975	.963
500	.972	.977	.967
550	.975	.980	.970
600	.978	.983	.974
650	.981	.986	.978
700	.984	.988	.981
750	.988	.991	.985
800	.991	.993	.989
850	.994	.995	.993
900	.997	.998	.996
950	1.000	1.000	1.000
1000	1.000	1.000	1.000

Appendix 5

CALCULATIONS FOR CHAPTER 4

In this appendix the calculations for the thickness of the
entrained gas film, the jet Weber number, and the induction
trumpet Capillary number are reported.

TABLE A5.1 :   Data for Figure 4.16 (Weber no vs film entr rate)

RUN NUMBER	NOZZLE DIAMETER (mm)	LIQUID FLOWRATE (L/min)	SURFACE TENSION (mN/m)	LIQUID DENSITY (kg/m3)	JET WEBER NUMBER	NORM(1) FILM ENTRAIN.
1	7.12	36.035	48	996.5	33633	.278
2	7.12	27.555	48	996.5	19666	.210
3	7.12	18.740	48	997.0	9101	.178
4	7.12	36.035	54	996.2	29887	.303
5	7.12	27.555	54	997.3	17495	.259
6	7.12	18.740	55	997.5	7946	.191
7	7.12	36.035	62	997.5	26064	.296
8	7.12	27.555	62	997.5	15241	.208
9	7.12	18.740	62	997.5	7049	.147
10	4.76	16.011	47	996.5	22694	.360
11	4.76	12.249	47	996.5	13282	.293
12	4.76	8.324	48	996.5	6006	.171
13	4.76	16.011	53	996.5	20125	.355
14	4.76	12.249	53	996.5	11779	.270
15	4.76	8.324	53	996.5	5440	.161
16	4.76	16.011	63	996.2	16925	.342
17	4.76	12.249	65	996.8	9607	.271
18	4.76	8.324	62	997.3	4654	.142
19	2.38	4.004	48	997.5	11129	.299
20	2.38	3.062	49	997.3	6374	.268
21	2.38	2.082	49	997.9	2949	
22	2.38	4.004	53	997.5	10079	.382
23	2.38	3.062	54	997.5	5785	.140
24	2.38	2.082	54	997.0	2673	
25	2.38	4.004	60	997.3	8901	.334
26	2.38	3.062	61	997.5	5121	.161
27	2.38	2.082	60	997.5	2407	
28	7.12	36.035	64	1064	26933	.345
29	7.12	27.555	63	1064	15999	.243
30	7.12	18.740	62	1064	7519	.214
31	4.76	16.011	63	1061	18026	.305
32	4.76	12.249	64	1061	10386	.268
33	4.76	8.324	62	1061	4951	.110
34	2.38	4.004	64	1061	8878	.367
35	2.38	3.062	64	1061	5192	.018
37	7.12	36.035	53	1114	34051	.373
38	7.12	27.555	53	1114	19911	.225
39	7.12	18.740	53	1114	9209	.165
40	4.76	16.011	63	1114	18927	.382
41	4.76	12.249	65	1114	10737	.289
42	4.76	8.324	62	1114	5198	.191
43	2.38	4.004	63	1116	9486	.201
44	2.38	3.062	62	1116	5637	.082
46	7.12	36.035	24	784.0	52921	.228
47	7.12	27.555	24	784.0	30944	.201
48	7.12	18.740	24	784.0	14313	.145
49	4.76	16.011	24	784.0	34965	.249
50	4.76	12.249	24	784.0	20465	.169
51	4.76	8.324	24	784.0	9451	.230
55	7.12	12.249	54	997.3	3457	.064

TABLE A5.1 (cont): Data for Figure 4.16 (Weber no vs film entr rate)

RUN NUMBER	NOZZLE DIAMETER (mm)	LIQUID FLOWRATE (L/min)	SURFACE TENSION (mN/m)	LIQUID DENSITY (kg/m3)	JET WEBER NUMBER	NORM(1) FILM ENTRAIN.
56	2.38	8.324	54	997.3	42745	.708
64	4.76	12.249	65	998.6	9624	.267
65	4.76	12.249	65	998.6	9624	.247
66	4.76	12.249	65	998.6	9624	.255
67	4.76	12.249	65	999.1	9629	.264
68	4.76	12.249	65	999.1	9629	.259
69	4.76	12.249	64	998.9	9778	.270
71	7.12	36.035	65	998.0	24874	.248
72	7.12	27.555	63	998.0	15006	.160
73	7.12	18.740	63	998.0	6941	.065
74	4.76	16.011	65	998.9	16449	.175
75	4.76	12.249	63	998.8	9932	.110
76	4.76	8.324	64	998.8	4515	.035
77	2.38	4.004	63	998.2	8485	
78	2.38	3.062	64	998.2	4885	
91	7.12	36.035	65	998.4	24884	.226
92	7.12	27.555	65	998.9	14558	.111
93	7.12	18.740	63	998.8	6946	.036
95	4.76	12.249	63	998.8	9932	

(1) measured film entrainment rates were obtained by extrapolating the experimental entrainment rate vs jet diameter curves to zero jet expansion. The measured rate was normalised by dividing by the liquid volumetric rate.

TABLE A5.2 : Data for Figure 4.20 (eddy velocity vs film thkness)

RUN NUMBER	NOZZLE DIAMETER (mm)	COLUMN DIAMETER (mm)	LIQUID FLOWRATE (L/min)	EDDY(1) FLOWRATE (L/min)	EDDY(2) VELOCITY (m/s)	FILM(3) THKNESS (μm)
1	7.12	44	36.035	58.791	2.578	434
2	7.12	44	27.555	44.956	1.971	353
3	7.12	44	18.740	30.574	1.341	297
4	7.12	44	36.035	58.791	2.578	455
5	7.12	44	27.555	44.956	1.971	393
6	7.12	44	18.740	30.574	1.341	308
7	7.12	44	36.035	58.791	2.578	448
8	7.12	44	27.555	44.956	1.971	351
9	7.12	44	18.740	30.574	1.341	267
10	4.76	44	16.011	44.353	1.945	403
11	4.76	44	12.249	33.932	1.488	342
12	4.76	44	8.324	23.059	1.011	234
13	4.76	44	16.011	44.353	1.945	401
14	4.76	44	12.249	33.932	1.488	327
15	4.76	44	8.324	23.059	1.011	226
16	4.76	44	16.011	44.353	1.945	393
17	4.76	44	12.249	33.932	1.488	340
18	4.76	44	8.324	23.059	1.011	209
19	2.38	44	4.004	24.806	1.088	239
20	2.38	44	3.062	18.970	.832	217
21	2.38	44	2.082	12.899	.566	
22	2.38	44	4.004	24.806	1.088	283
23	2.38	44	3.062	18.970	.832	136
24	2.38	44	2.082	12.899	.566	
25	2.38	44	4.004	24.806	1.088	246
26	2.38	44	3.062	18.970	.832	152
27	2.38	44	2.082	12.899	.566	
28	7.12	44	36.035	58.791	2.578	475
29	7.12	44	27.555	44.956	1.971	375
30	7.12	44	18.740	30.574	1.341	320
31	4.76	44	16.011	44.353	1.945	365
32	4.76	44	12.249	33.932	1.488	321
33	4.76	44	8.324	23.059	1.011	175
34	2.38	44	4.004	24.806	1.088	273
35	2.38	44	3.062	18.970	.832	20
37	7.12	44	36.035	58.791	2.578	486
38	7.12	44	27.555	44.956	1.971	357
39	7.12	44	18.740	30.574	1.341	278
40	4.76	44	16.011	44.353	1.945	405
41	4.76	44	12.249	33.932	1.488	331
42	4.76	44	8.324	23.059	1.011	243
43	2.38	44	4.004	24.806	1.088	182
44	2.38	44	3.062	18.970	.832	86
46	7.12	44	36.035	58.791	2.578	413
47	7.12	44	27.555	44.956	1.971	364
48	7.12	44	18.740	30.574	1.341	279
49	4.76	44	16.011	44.353	1.945	346
50	4.76	44	12.249	33.932	1.488	260
51	4.76	44	8.324	23.059	1.011	292
55	7.12	44	12.249	19.984	.876	149

TABLE A5.2 (cont): Data for Figure 4.20 (eddy veloc vs film thkness)

RUN NUMBER	NOZZLE DIAMETER (mm)	COLUMN DIAMETER (mm)	LIQUID FLOWRATE (L/min)	EDDY(1) FLOWRATE (L/min)	EDDY(2) VELOCITY (m/s)	FILM(3) THKNESS (μm)
56	2.38	44	8.324	51.570	2.261	463
64	4.76	44	12.249	33.932	1.488	
65	4.76	44	12.249	33.932	1.488	
66	4.76	44	12.249	33.932	1.488	
67	4.76	44	12.249	33.932	1.488	
68	4.76	44	12.249	33.932	1.488	
69	4.76	44	12.249	33.932	1.488	
71	7.12	44	36.035	58.791	2.578	409
72	7.12	74	27.555	88.082	1.365	310
73	7.12	74	18.740	59.904	.929	182
74	4.76	74	16.011	81.755	1.267	273
75	4.76	74	12.249	62.545	.970	192
76	4.76	74	8.324	42.504	.659	73
77	2.38	74	4.004	43.488	.674	
78	2.38	74	3.062	33.257	.516	
91	7.12	95	36.035	154.585	1.454	399
92	7.12	95	27.555	118.207	1.112	253
93	7.12	95	18.740	80.392	.756	107
95	4.76	95	12.249	82.556	.776	

(1) calculated from (4.45).

(2) calculated from (4.24).

(3) calculated from (4.35) using the measured film entrainment rates.

TABLE A5.3 :   Data for Figure 4.21 (Capill no vs dmls film thkns)

RUN NUMBER	GAS(1) VOID FRACTION	LIQUID VISCOSITY (mPa-s)	MIXT(2) VISCOSITY (mPa-s)	CAP(3) NUMBER TRUMPT	LOG CAPILL NUMBER	DIMLSS(4) FILM THKNSS
1	.218	.851	1.097	.059	-1.230	.807
2	.174	.851	1.036	.043	-1.371	.772
3	.151	.833	.986	.028	-1.560	.807
4	.233	.851	1.119	.053	-1.272	.837
5	.206	.911	1.155	.042	-1.375	.814
6	.160	.871	1.042	.025	-1.595	.815
7	.228	.871	1.137	.047	-1.325	.818
8	.172	.871	1.058	.034	-1.473	.760
9	.128	.933	1.074	.023	-1.634	.696
10	.265	.833	1.144	.047	-1.325	.844
11	.227	.871	1.135	.036	-1.445	.823
12	.146	.890	1.048	.022	-1.656	.711
13	.262	.851	1.165	.043	-1.369	.833
14	.213	.833	1.066	.030	-1.524	.812
15	.139	.851	.993	.019	-1.723	.705
16	.255	.833	1.128	.035	-1.458	.829
17	.213	.871	1.115	.026	-1.593	.825
18	.124	.911	1.045	.017	-1.769	.636
19	.230	.933	1.221	.028	-1.558	.649
20	.211	.911	1.164	.020	-1.704	.690
21		.955	.955	.011	-1.958	
22	.276	.933	1.301	.027	-1.574	.744
23	.123	.933	1.067	.016	-1.784	.451
24		.890	.890	.009	-2.030	
25	.250	.911	1.226	.022	-1.653	.666
26	.139	.933	1.087	.015	-1.829	.500
27		.933	.933	.009	-2.056	
28	.257	1.653	2.234	.090	-1.046	.639
29	.195	1.653	2.062	.065	-1.190	.601
30	.176	1.653	2.013	.044	-1.361	.629
31	.234	1.653	2.167	.067	-1.175	.573
32	.211	1.653	2.104	.049	-1.311	.585
33	.099	1.653	1.838	.030	-1.523	.414
34	.268	1.653	2.271	.039	-1.413	.560
35	.018	1.653	1.683	.022	-1.660	.055
37	.272	2.854	3.931	.191	-.719	.504
38	.184	2.854	3.503	.130	-.885	.449
39	.142	2.854	3.330	.084	-1.075	.435
40	.276	2.854	3.957	.122	-.913	.482
41	.224	2.854	3.688	.084	-1.074	.467
42	.160	2.854	3.405	.056	-1.256	.433
43	.167	2.854	3.434	.059	-1.227	.311
44	.076	2.854	3.090	.041	-1.382	.177
46	.186	2.120	2.610	.280	-.552	.441
47	.167	2.120	2.552	.210	-.679	.450
48	.127	2.120	2.432	.136	-.867	.428
49	.199	2.120	2.656	.215	-.667	.422
50	.145	2.120	2.483	.154	-.813	.375
51	.187	2.120	2.615	.110	-.958	.498
55	.060	.911	.971	.016	-1.802	.505

TABLE A5.3 (cont):   Data for Figure 4.21 (Capill no vs dmls flm thkns)

RUN NUMBER	GAS(1) VOID FRACTION	LIQUID VISCOSITY (mPa-s)	MIXT(2) VISCOSITY (mPa-s)	CAP(3) NUMBER TRUMPT	LOG CAPILL NUMBER	DIMLSS(4) FILM THKNSS
56	.415	.911	1.581	.066	-1.179	.766
64	.211	1.053	1.342	.031	-1.513	
65	.198	1.053	1.321	.030	-1.520	
66	.203	1.053	1.329	.030	-1.517	
67	.209	.933	1.187	.027	-1.566	
68	.206	.911	1.155	.026	-1.578	
69	.213	.955	1.221	.028	-1.547	
71	.199	.933	1.171	.046	-1.333	.736
72	.138	.890	1.038	.022	-1.648	.815
73	.061	.978	1.043	.015	-1.813	.578
74	.149	1.109	1.308	.026	-1.593	.663
75	.099	1.081	1.203	.019	-1.732	.556
76	.034	1.081	1.120	.012	-1.938	.266
77		1.002	1.002	.011	-1.970	
78		1.002	1.002	.008	-2.093	
91	.184	1.027	1.266	.028	-1.548	.920
92	.100	1.109	1.235	.021	-1.675	.675
93	.035	1.081	1.121	.013	-1.871	.364
95		1.081	1.081	.013	-1.875	

(1) calculated using the gas-to-liquid volumetric flow ratio

(2) calculated from (6.33)

(3) calculated from (4.41) using the mixture viscosity

(4) calculated from (4.40) using the mixture viscosity

Appendix 6

PREDICTION OF SUBMERGED JET ANGLE

In this appendix the calculations are given for prediction of
the submerged jet angle given by (5.52).

TABLE A6.1 Prediction of the submerged jet angle

RUN	EDDY FLOWRATE (L/min) #1	EDDY VELOCITY (m/s) #2	Po (kN/m2) #3	EULER NUMBER #4	X AXIS #5	JET ANGLE (deg) #6
2	44.956	1.971	89.29	.675	.073	4.2
5	44.956	1.971	90.23	.679	.073	4.2
8	44.956	1.971	89.61	.678	.072	4.1
11	33.932	1.488	89.48	.677	.128	7.3
14	33.932	1.488	91.29	.694	.131	7.5
17	33.932	1.488	91.84	.694	.127	7.2
23	18.970	.832	92.71	.705	.292	16.3
32	12.249	1.488	91.37	.691	.139	7.9
41	33.932	1.488	90.19	.682	.145	8.2
64	33.932	1.488	91.42	.691	.127	7.2
72	88.082	1.365	93.12	.700	.154	8.8
74	81.755	1.267	92.29	.410	.141	8.0
75(0)	62.545	.970	90.78	.690	.288	16.1
75(1)	62.545	.970	92.74	.705	.236	13.3
75(2)	62.545	.970	94.64	.719	.186	10.6
75(3)	62.545	.970	96.71	.735	.146	8.3
76(0)	42.504	.659	90.98	1.495	.625	32.0
76(1)	42.504	.659	94.04	1.546	.484	25.9
78	33.257	.516	96.78	.736	.377	20.7
81	88.082	1.365	93.42	.706	.155	8.8
84	62.545	.970	92.48	.699	.233	13.1
87	33.257	.516	95.67	.723	.378	20.7
95(0)	82.556	.776	91.36	.691	.294	16.4
95(1)	82.556	.766	94.73	.720	.307	17.1
95(2)	82.556	.776	95.81	.724	.252	14.1
95(3)	82.556	.776	98.35	.744	.190	10.8
101	82.556	.776	94.73	.716	.299	16.7

#1 calculated from (4.45)

#2 calculated from (4.24)

#3 pressure in headspace of the column

#4 based on the pressure in the headspace of the column and the jet velocity

#5 given by

$$0.089 \left\{ \frac{P_o}{\rho_L v_j^2} \right\} \left\{ \frac{\rho_e}{\rho_L} \right\} \left\{ \frac{0.37\sqrt{R_c^2 - \frac{1}{4}R_j^2} - 0.64 R_j}{R_j} \right\} \left\{ \frac{v_j - (v_e)_{max}}{v_j} \right\}$$

#6 calculated from (5.52) where η is 0.089